THREE-DIMENSIONAL FINITE ELEMENT ANALYSIS OF EARTH PRESSURE BALANCE TUNNELLING

LIM KEN CHAI

(B.Eng.(Hons.), NUS)

A THESIS SUBMITTED

FOR THE DEGREE OF DOCTOR OF PHILOSOPHY

DEPARTMENT OF CIVIL ENGINEERING

NATIONAL UNIVERSITY OF SINGAPORE

2003

This thesis is dedicated to my mother and father

for their support and love

Acknowledgements

First and foremost, I am deeply grateful to *Associate Professor Lee Fook Hou*, my main supervisor, who has provided a motivating, passionate and critical atmosphere during the many discussions we had. His excellent guidance has enabled me to understand first hand on the complex issues revolving around this research work and has given me the courage to clear the issues step-by-step and see the light at the end of this tunnelling work.

I also wish to thank *Associate Professor Phoon Kok* Kwang who as my second supervisor provided constructive comments during the research time as well as the preliminary version of this thesis.

This study would never be able to get going if not for the funding and research scholarship from Econ Corporation Limited and the National University of Singapore respectively. I am grateful to these institutes for providing me the financial support. Also, special thanks to Land Transport Authority of Singapore who has kindly agreed to let me access their field logbooks and instrumented data for C704 tunnelling works.

The knowledge, joy and satisfaction that I have benefited during discussions with research pals from Center for Soft ground Engineering and Center for Protective Technology are immeasurable. Thanks to pals like Swee Huat, Deon, Sze Han, Ashish,Wai Kit, Tiong Guan, Poh Ting, Lee Yeong, Joo Kai and William Cheang. Without you guys, this research period will be soulless.

Last but not least, I would like to express my thanks to Byron Chong, Danny Ang, Chee Meng, Michael Wong, Flanagan Eng, Joewaye Foo and my family who have given me the moral support, without whom completion of this thesis would not have been possible. Yes, it's a jump on the Singapore River if you know what I mean. Get ready the Tiger!

Table of Contents

Summary

This study investigates the viability of applying three-dimensional finite element analyses to the prediction of ground movement arising from earth pressure balance tunnelling. It seeks to address two of the issues involved in three-dimensional finite element analysis, namely (i) the feasibility of conducting three-dimensional analysis without resorting to inordinate amounts of computer resources and time, and (ii) the usefulness of three-dimensional analysis in predicting field movements and its advantages compared to two-dimensional analysis.

To answer the first issue, two Krylov subspace iterative solvers namely element-by-element Preconditioned Conjugate Gradient (PCG) and Quasi-Minimal Residual (QMR) were examined and discussed over the direct method of solving stiffness matrix arising from geotechnical domains. It also examines the performance of the Jacobi Preconditioner when used with two Krylov subspace iterative methods. The number of iterations needed for convergence was shown to be different for drained, undrained and consolidation problems, even for similar condition numbers. The key to the problem was due to differences in the eigenvalue distribution, which cannot be completely described by the condition number alone.

For drained problems involving large stiffness ratios between different material zones, ill-conditioning is caused by these large stiffness ratios. Since Jacobi preconditioning operates on degrees-of-freedom, it effectively homogenises the different spatial sub-domains. The undrained problem, modelled as a nearly incompressible problem, is much more resistant to Jacobi preconditioning, because its ill-conditioning arises from

the large stiffness ratios between volumetric and distortional deformational modes, many of which involve the similar spatial domains or sub-domains. The consolidation problem has two sets of degrees-of-freedom, namely displacement and pore pressure. Some of the eigenvalues are displacement dominated whereas others are excess pore pressure dominated. Jacobi preconditioning compresses the displacement-dominated eigenvalues in a similar manner as the drained problem, but pore-pressure-dominated eigenvalues are often over-scaled. Convergence can be accelerated if this over-scaling is recognised and corrected for.

The second issue was addressed through a back-analysis of an actual three-dimensional tunnel heading problem, namely the tunnelling operation of Contract 704 of the Northeast Mass Rapid Transit Line. This back-analysis exercise leads to the following findings:

(i) Various construction sequences due to Earth Pressure Balance tunnelling were translated to a set of parametric studies to determine their influences on the ground response. It is important to consider parameters such as excavation step-length, face pressure and drainage conditions at the tunnel excavated boundary. On the other hand, grout stiffness and tunnel boring machine weight were found not to be significant factors.

(ii) Conventional soil parameters obtained from triaxial and oedometer results have over-estimated the ground response in relation to the field results. Application of a non-linear small strain and elastic anisotropy soil within the yield surface of modified Cam Clay yield much better results.

(iii) A comparative study between two-dimensional and three-dimensional finite element analyses were examined over a range of stiff and soft soils. A

graphical approach depicting two-dimensional ground loss and face area contraction to the three-dimensional ground responses was crafted to isolate ground response for different stages of tunnelling excavations i.e. pre- and post- excavations. By equating the three-dimensional ground settlement corresponding to a given tunnel heading standoff, the two-dimensional ground relaxation ratio or face area contraction can be found respectively. In terms of trough width, the stress-transfer effect of the soil in front of the tunnel heading gives a narrower three-dimensional trough width as compared to the two-dimensional one. For soft soils, depending upon the in-situ K_0 value, when the tunnel is near the monitored section (either ahead or behind), the three-dimensionally computed trough may be narrower or wider than the two-dimensionally computed trough. This is due to the effect of face pressure, which is simulated in the three-dimensional analyses but not in the two-dimensional analyses.

Key Words: Krylov subspace, iterative, ill-conditioning, three-dimensional finite element analysis, Earth Pressure Balance tunnelling, ground loss.

Nomenclature

b	denotes load vector of real *ndf*-space
c’	effective stress parameters, cohesion
e_{cs}	void ratio at Critical state
e_o	initial void ratio
i	distance to the point of inflexion of the trough width
k_{s1}'	effective bulk moduli of the upper or first layer soil
k_{s2}'	effective bulk moduli of lower or second soil layer
k	an empirical constant for trough width
k	denotes the permeability matrix
k_1	parameter to take into account the “doming” effect across the tunnel face, $0 < k_1 < 1$
k	permeability (isotropically)
k_1	coefficients of permeability of the upper or first soil layer for consolidation analyses
k_2	The coefficients of permeability of the lower or second soil layer for consolidation analyses
k_x	permeability in x-direction
k_y	permeability in y-direction
k_s'	effective bulk modulus of soil skeleton
k_w	bulk modulus of water
$\kappa(A)$	condition number of global stiffness matrix A
m	is a matrix equivalent of the Kronecker delta
m	the OCR exponent of the empirical formulation of G_0

m_{pij}^{-1}	under-scaled preconditioning factors
n	an empirical constant for trough width
n	effective stress exponent of the empirical formulation of G_0
n	number of joints in the lining ring where $n > 4$
ndf	denotes the number of degrees-of-freedom
p_{t}	denotes the nodal pore water pressure at the current time step
q	deviator stress
q_f	the deviator stress at failure
r	tunnel radius
t	standardised normal random variable
w	natural water content
x	denotes unknown displacement vector of real *ndf*-space
x	the distance from the centreline of the tunnel driving axis
$x^{(0)}$	is the initial guess
$x^{(n)}$	is the approximate solution vector after n iterations
x, y, z	Cartesian ordinates in X, Y and Z directions
x_s and x_f	respectively the starting and final locations of the tunnel face

A	global stiffness matrix
A^*	preconditioned global matrix
A_{e}	equivalent to element stiffness matrix K_e
B	denotes the matrix of shape function derivatives for displacement
C	is the flow matrix

C	constant of the empirical formulation of G_0
C_c	Compression Index
C_r	Recompression/Swelling Index
C_u	undrained shear strength
D	elastic modulus matrix or stress-strain matrix
D	diameter of the tunnel
E_h	the horizontal elastic Young's modulus
E_v	the vertical elastic Young's modulus
E	initial Young's modulus
E	denotes the shape function derivatives for excess pore water pressure
E_1'	elastic Young's modulus for first layer of soil
E_2'	elastic Young's modulus for second layer of soil
E_c	liner modulus
E_g	grout modulus
EI	flexural rigidity
Ep	excess pitch
F_p	normalised face pressure
G'	shear modulus
G_0	the initial tangential stiffness
G_∞	the tangential stiffness at very large strain
H	horizontal displacement
I	2nd moment of area of a continuous concrete lining with the same dimensions
I_j	2nd moment of area of each joint

I_{eff}	effective 2nd moment of area of a continuous concrete lining with the same dimensions
K	Bulk Modulus
K	an empirical constant dependent on ground conditions
K'	effective bulk modulus
K_1	represents the constraints arising from incompressibility
K_e	the effective stress stiffness matrix
$\mathrm{K_o}$	coefficient of earth pressure at rest
K_s'	represents the stiffness matrix of the soil skeleton
K_w	the bulk modulus of water and n is the porosity of the soil structure
L	is the link matrix
L	length of shield
LI	Liquidity Index
LL	Liquid limit
L_{shield}	length of the shield machine
M	critical state parameter
M^{-1}	the Jacobi or diagonal preconditioner of global matrix A
$\overline{N}$	denotes the shape function for excess pore water pressure
$\mathrm{N_c}$	number of iterations needed for relative residual norm ($R_r^{(n)}$) to fall below 1×10^{-6}
$\mathrm{N_d}$	total number of degrees-of-freedom for drained or undrained case
N_{broms}	stability number used by Broms and Bennermark (1967)
$R_i^{(n)}$	relative “improvement” norm

$R_E^{(n)}$	relative energy error norm
$R_r^{(n)}$	relative residual norm
PI	Plasticity Index
PL	Plastic Limit
R_{sr}	the step ratio $\frac{Z_{excav}}{L_{shield}}$
S'	effective stiffness matrix for consolidation matrix
S_0	the initial tangential stiffness of the q vs ε_s curve
S_∞	the tangential stiffness at very large strain
S	settlement obtained from numerical results
S_{max}	maximum settlement obtained from numerical results
T	tridiagonal matrix
V_i	trough volume
V_f	face volume Loss
V_o	tunnel opening volume (πr^2)
Y_0	the depth from the ground surface to the springline level
Z	tunnel driving in z-direction of the Cartesian-ordinates.
Z_{excav}	excavation step sizes

2-D	two-dimensional
3-D	three-dimensional
EPB	earth pressure balance
EPCG	element-by-element PCG
EQMR	element-by-element quasi-minimal residual

FE	finite element
FEA	Finite element analysis
FEM	finite element model
HCC	hyperbolic small strain modified Cam Clay model
HMCEA	hyperbolic small strain coupled with elastic anisotropy formulated within modified Cam Clay
MCC	modified Cam Clay
MCEA	modified Cam Clay with elastic anisotropy factor
MINRES	minimum residual
PCG	Preconditioned conjugate gradient
QMR	quasi-minimal residual
SYMMLQ	symmetric LQ
TBM	tunnel boring machine

$\langle \cdot, \cdot \rangle$	denotes the inner product
$\| \cdot \|_2$	denotes the matrix 2-norm
$\lvert u \rvert_{max}$	maximum displacement magnitude
$\lvert p \rvert_{max}$	maximum pore pressure magnitude
$\max_j \lvert \cdot \rvert$	the maximum absolute value term over index-*j*
F()	represent the cumulative distribution function of a standardised normal random variable

Δf	denotes the nodal load increment
Δp	denotes the excess pore water pressure increment
Δu	denotes the displacement increment
Δt	denotes the time step
Δ_x	distance of step-size adopted in the step-by-step incremental finite element analysis

λ_{max}	maximum eigenvalue
λ_{min}	minimum eigenvalue
$\sigma_{\max}$	maximum singular value
$\sigma_{\min}$	minimum singular value
σ_s	Overburden Pressure at tunnel axis
σ_τ	Tunnel supporting pressure at tunnel axis
ν	Poisson’s ratio
ν'	effective Poisson’s ratio
ϕ'	effective stress parameters, internal friction angle
ε_∞	the shear strain at yielding
ε_s	deviator strain
ε_s	the shear strain
ε	percentage ground loss
γ_{bulk}	bulk unit weight
γ_w	unit weight of water
α^2	anisotropy factor

δ_x	maximum inward axial displacement of soil at the tunnel face
δ	settlement magnitude
δ_{max}	maximum settlement
κ	slope of the isotropic unload-reload line
λ	slope of the isotropic normal compression line

List of Tables

List of Figures

1 Introduction

1.1 Background: Tunnels in Urban Environment

Since historical times, tunnels have been constructed for the protection of goods, people or to provide alternative source of public transportation. In 1806, Isambard Brunel pioneered the use of a shield machine for tunnelling. It was constructed underneath the Thames in London. The tunnel was finally completed after more than 5 instances of serious flooding. Today, in London, more than 150km of deep-bored tunnels were used for subways. In Tokyo and the surrounding districts, the underground is crowded with urban tunnels for underground railways, water supply, communications and other uses. These are just two of many cases in which congested urban environment has necessitated the use of underground tunnels. Mair (1996) noted that, in an urban environment, constraints of existing tunnels or deep foundations often results tunnels having to be constructed close beneath or near such structures.

Likewise, the increase in demand and complexity of Singapore's infrastructures has prompted the use of tunnelling for mass transportation. For instance, the newly opened Northeast line (NEL) lies completely underground and Earth-Pressure Balance (EPB) shields were used extensively in its construction. These modern shields utilize closed-face rotary cutters to excavate the soils. Movements into the shield were prevented because of continuous heading support through pressurized tunnel heading and early grout replacement at the tail voids. Notwithstanding this, however, some ground movement is unavoidable. For instance, in the construction of the NEL, the allowable ground loss is 1%.

The new NEL line passes through densely built up areas where excess ground movements can have serious consequences on the structures on top and around the tunnel. During tunnel construction, ground deformation is often unavoidable since the removal of the soil from within the tunnel and the exposure of the tunnel sides and face results in a change of stress and pore pressure distribution in the ground. The effects are essentially three-dimensional (3-D) in nature. There is thus significant interest in the prediction of the ground deformation and its effects on surrounding buildings and foundations.

1.2 Effects of Tunnelling on surrounding ground and structures

An examination of field records of subsidence near soft ground tunnelling operations by Attewell (1977) indicates that a major proportion of total soil deformation occurs after construction. He presented a case study on a factory building. The structural damage to the buildings can be related to the tunnel centre line and its position on the settlement profile.

Boscardin and Cording (1989) presented a graphical relationship between structural damage and the crucial parameters of angular distortion and horizontal tensile ground strain. O'Reilly and New (1991) conducted a review of ground movements associated with tunnelling. They suggested that ground settlement by itself does not damage structures and is therefore likely to be an unreliable measure of damage potential. On the other hand, differential ground movements give rise to the angular distortion and horizontal ground strains that eventually caused damages. In particular they pointed out that it is the hogging curvature and tensile strain beneath structures that give the best measures of risk of damages.

Hellings (1994) presented a case study of a tunnel excavation during 1930's near the Mansion house in London. The building suffered damages in the form of ground lowering and crack joints. The settlements reached as much as 200 mm and the crack joint width grew to about 25 mm. Major and costly repairs were required and the effects of the damages are still evident. This indicates that it is important to control not only the stability of the tunnel heading but also the deformations that the construction of the tunnel generates in the adjacent ground.

1.3 Prediction of ground movement above tunnels

The discussion above highlights the deleterious effects of excessive ground deformation. In a congested, highly urbanized setting, these issues often assume added importance owing to the proximity of buildings and structures to the tunnels and the serious consequences and economic losses which can result from excessive ground deformation. For these reasons, prediction of ground movements arising from tunnelling works is now often a standard requirement in the design and construction of new tunnels. For example, estimation of ground movement and an assessment of the risk that these movements pose to surrounding buildings is now virtually a standard requirement for tunnelling works in Singapore.

Prediction of tunnelling-induced ground movement cannot be readily achieved by means of first-principle, two-dimensional (2-D) finite element (FE) analysis. This is because ground deformation will largely cease once the lining has been installed and tail void grouting has been completed. Although the tunnel can be very long, only a very short segment is unsupported at any one point of time. This is the segment around the tunnel boring machine (TBM), which lies between the tunnel face and the lined segment. 2-D FE analysis, which simulates the soil being fully removed before the lining is installed effectively, assumes a very long unsupported span of tunnel, which is unduly conservative. To temper this excessive conservatism, displacement is often prescribed on the tunnel walls in accordance with an assumed ground loss ratio. Once a ground loss ratio is assumed, ground settlement can be predicted either empirically (often assuming a normal distribution curve for the ground settlement profile) or numerically using FE analysis. Whichever method is adopted, it is important to note that the starting point of the prediction is, in fact, an assumption of the magnitude of ground loss. Thus, the prediction is never strictly based on first principles.

It is evident from the above discussion that the tunnelling problem is essentially a three-dimensional (3-D) problem that is influenced by the ground behaviour at the tunnel face and the free span between the face and the lined segment. Such a problem cannot be analysed from a first principle standpoint using 2-D analysis which takes no account of tunnel face and length of the free span. This study is an attempt to model the construction of a tunnel by EPB method using 3-D finite element analysis, thereby obviating the necessity to assume a certain ratio of ground loss. This method is chosen based on its flexibility in modelling different stages in the construction sequence and its ability to predict stress and displacement patterns. However, realistic 3-D analysis using commercially available codes such as ABAQUS often requires very high levels of computer resources and time [e.g. Dasari (1996), Komiya et al. (1999) and is not a viable option for most engineering design and consultancy setups. In order to create a framework which can potentially allow sufficiently realistic and refined 3-D FE analysis to be undertaken by engineering design and consultancy setups, a new suit of iterative algorithms is developed based on the pre-conditioned conjugate gradient

(PCG) and quasi-minimal residual (QMR) approaches which are implemented on personal computer (PC) platforms. This will be elaborated upon in more detail in Chapter 3.

1.4 Objectives and Scope of this Study

The objectives of this study are as follows:

- To study the possibility of analysing tunnelling problems involving realistically large ground domains using 3-D FE analysis. As mentioned earlier, the main obstacle in the way of solving large problems on PC-based platforms is the large amount of computer resources and, more importantly, time needed. To overcome this problem, a new suit of iterative solvers for 3-D geotechnical FE analysis is developed which demonstrates robust convergence characteristics under a wide range of geotechnical scenarios.
- To demonstrate the viability of the developed software by using it to back-analyse the ground movement around a monitored EPB-tunnelling project in weathered residual soil in Singapore using 3-D FE analysis. Various constitutive soil models will be used and compared with field results and to assess their ability to back-predict the field measurements. Finally, a comparison of performance is also made between the full 3-D FE analysis and some pseudo-3-D analyses; the latter involving 2-D FE analyses which attempt to model some aspects of the 3-D behaviour of the tunnelling problem.

This thesis is divided into six chapters. The first and second chapters introduce the background of the study and a literature review, which examines the issues that drive the current study. In the process of the literature review, the effects of tunnelling will be discussed and a review of previous research works will be presented, together with an examination of the current state-of-the-art and existing knowledge gaps.

Chapter 3 will cover the first objective of the thesis as mentioned beforehand. Over here, the linear algebraic equations resulting from the assembly of the finite element stiffness equations will be reviewed through three solution algorithms, viz. the frontal method, Element-by-Element (EBE) Preconditioned Conjugate Gradient (PCG) and EBE Quasi Minimal Residual Method (QMR). The latter two algorithms will hereafter be termed collectively as "iterative Krylov subspace solvers". Thereafter, this chapter will examine the performance of iterative Krylov subspace solvers in some idealised geotechnical problems, with emphasis on the convergence characteristics of these solvers. The performance of iterative solvers on different large 3-D finite element analyses will be presented and discussed.

Chapters 4 and 5 will address the second objective of this thesis. Chapter 4 presents the field results of an EPB tunnelling project in Singapore's residual granitic soil and summarises the ground behaviours when a EPB tunnelling machine performs in a stiff residual soil. In Chapter 5, the field results will be backed-analysed with 3-D FE analysis using various constitutive soil models, including the Mohr Coulomb model, modified Cam Clay (MCC) and some non-linear small strain and anisotropic models. The 3-D FE analyses with the developed software will attempt to simulate as closely as possible, the construction sequences for the EPB tunnelling method, especially in the tunnel face and tail void area to capture the salient characteristics of 3-D tunnelling. The performance of a small-strain MCC coupled with elastic anisotropy will also be examined. In the final section, the prediction of 3-D FE analysis is compared with those of some “pseudo-3-D FE analysis” that involve using 2-D FE analysis with some of the 3-D features simulated. By so doing, the conditions needed to obtain reasonably “3-D” answers from these pseudo-3-D analyses will be clarified.

Finally Chapter 6 will draw the thesis to an end by summarising the main findings and conclusions of this research. Future research areas are also recommended in the concluding chapter.

2 Literature Review

2.1 Tunnelling using Earth Pressure Balance (EPB) machine

Bored tunnels are often constructed by one of several methods. These are open or close-faced shields, slurry shields and Earth-Pressure Balance shields, [e.g. Schmidt (1982), Maidl et al. (1996)]. In cohesive ground conditions, the Earth-Pressure Balance (EPB) machine offers some advantages over other types of machines because cohesive soils often have significant plasticity and low permeability, which allows the EPB machine to transfer the plenum pressure effectively. Modern examples of using EPB shields with full-face support to control ground movement include the San Francisco clean water project (1981), Singapore MRT contract 301A North-south line (1985) and Taiwan, Taipei Metro contract 201A (1998). EPB shields have also been used in Japan successfully. EPB shields have several advantages over slurry shield machines because it has no problem of slurry recycling and treatment plant. This in turn saves on space and cost, and has less impact on the environment. This method is currently used extensively for the construction of bored tunnels in residual soils for the North-East line (NEL), where the site referred to in this thesis is located. For this reason, only this method is described in detail below.

The operational principle of the EPB machine is to drive the shield in cohesive and non-cohesive soils with the tunnel face being supported by the shield’s cutting wheel as shown in Figure 2.1. As shown in this figure, the soil that is removed from the face by the cutting bits on the rotating cutter head does not fall into the excavation chamber. Instead the soil is pressed through the openings of the cutting wheel into the excavation chamber where it is then mixed with admixtures to increase its plasticity.

The thrust force of the shield is transferred via the pressure bulkhead and the soil slurry onto the tunnel face. This mechanism allowed a controlled entry of soil into the excavation chamber. Balance is reached when the pressure applied by the bulkhead provided by the shield is equal to the external lateral earth-pressure.

If the applied pressure is higher than the earth pressure, consolidation may occur around the tunnel face whilst soil movement into the excavation chamber may be accentuated. If the applied pressure is lowered than the earth pressure, the tunnel face will deform towards the cutter head and that may increase face loss and ground surface settlement. As the hydraulic jacks thrust the shield forward, segmental lining is erected concurrently at the tailskin of the shield. Tail voids are generally filled with cement grout to minimise further settlement.

2.2 Surface Settlement caused by shield tunnelling

One of the most important effects of shallow bored tunnels is ground surface settlement arising from the inward movement of the soil into the tunnel. Cording and Hansmire (1975) defined the ground loss as the volume of soil that displaces across the perimeter of a tunnel. It is often defined in terms of volume lost per unit length of tunnel constructed. The percentage (%) of ground loss is defined as ratio of the volume loss to the total tunnel volume per unit length. Volume loss can be classified into 4 main types

1. Ahead of the tunnel face

2. In the shield area

3. Behind the shield

4. Long term movement

Figures 2.2 and 2.3 illustrate the types of volume loss for shield tunnelling.

2.2.1 Volume loss at Tunnel face

Volume loss at the tunnel face, as shown in Figure 2.2, is caused by the inward axial movement of the soil into the excavated space and is closely related to tunnel heading stability. Tunnel heading stability in soft soil is usually defined in terms of overload factor N_{broms} (Broms & Bennermark, 1967), such that

$$N = \left(\frac{\sigma_S - \sigma_\tau}{C_u} \right) \qquad (2.1)$$

Where σ_s = Overburden Pressure at tunnel axis

σ_τ = Tunnel supporting pressure at tunnel axis

C_u = Undrained shear strength

Broms (1967) conducted extrusion tests for soft clay and concluded that, the overload factor must be less than 6to ensure stability and limit ground movement.

Lee and Rowe (1991) presented a volume loss definition for the tunnel face for finite element computations. They showed that the face volume loss, V_f, is related to geometry constraint as shown below:

$$V_f = \left(\pi r^2\right) k_1 \frac{\delta_x}{\Delta x} \qquad (2.2)$$

Where r = tunnel radius

k_1 = parameter to take into account the “doming” effect across the tunnel face, $0 < k_1 < 1$

δ_x = maximum inward axial displacement of soil at the tunnel face.

Δ_x = distance of step-size adopted in the step-by-step incremental finite element analysis.

Clough and Schmidt (1977) observed that the tunnel face ground loss contributed from one-quarter to one-third of the total volume loss. In view of this, the EPB machines’ full tunnel face support should reduce the total volume loss significantly as the tunnel is advancing.

2.2.2 Voids in the shield area

Ground loss around the shield arises mainly from two causes. The first is the over-cut invariably incurred by the over-sized face cutter, which allows the shield lining to move forward without experiencing excessive soil drag. This over-sized cutter reduces friction and improves the steering of the shield lining. The inward movement of the soil behind the over-sized cutters forms the shield volume loss.

Cording and Hansmire (1975) suggested that volume loss over the shield as shown in Figure 2.3 could also arise from the shield deviation from its prescribed tunnel alignment. The shield loss due to deviation from design grade, V_s, can be estimated from the relationship proposed by Nelson (1985), i.e.

$$V_s = \frac{\pi RL}{2}.(Ep) \qquad (2.3)$$

Where R = radius of shield

L = length of shield

Ep = excess pitch

Grouting around the shield can reduce the ground loss. Maidl et al (1996) suggested "sufficient support of the whole ring area is achieved by filling it with a free-flowing pressure-controlled material. This injection material must not be too liquid in order not to flow into the excavation chamber. On the other hand it has to be liquid enough to completely fill the gap, which is constantly changing as the shield advances."

2.2.3 Voids behind the shield (tail void)

The third cause of ground loss is tail void, which is defined as the area between the outside diameter of the shield and the lining. The advancing shield leaves, in its wake, an annulus between the surrounding ground and the extrados of the lining. To reduce the settlement behind the shield, the ring annulus has to be grouted as soon as possible during tunnelling.

2.2.4 Long Term Losses

Long-term losses around soft ground are caused by volume changes arising from consolidation of soil around the tunnel lining due to pore pressure changes during tunnelling or drainage into the tunnel. Peck (1969) highlighted that delayed settlements due to consolidation may have a much greater area extent than those caused by the tunnelling operation themselves. Palmer and Belshaw (1980) described a 2.5 m tunnel driven through soft to firm lacustrine clay. As the tunnel face approaches to within 1 m, the porewater pressure rose by about 10 %, but the pressure dropped by as much as 40 % when it passes through.

2.3 Previous Studies on Ground Response to Tunnelling

In this section, the literature survey reviews tunnel related research, which are categorised into three main types, namely analytical, empirical and numerical studies. Their findings are summarised in Tables 2.1, 2.2, and 2.3 respectively.

2.3.1 Empirical and Experimental research

Schmidt (1969) suggested that using a Gaussian distribution curve could fit the surface transverse settlement trough due to tunnelling. Two parameters, namely the ground loss ε and the standard deviation i of the curve, are needed to fit the surface settlement. The percentage ground loss ε is defined as follows:

$$\varepsilon = \frac{V_i}{V_o} \times 100\% \tag{2.4}$$

where V_i = Trough volume

V_o = Tunnel opening volume (πr^2)

r = Radius of tunnel

Peck (1969) suggested that i can be related to the tunnel radius r and the depth to the springline of tunnel z by the relation as follows:

$$\frac{i}{r} = \left(\frac{z}{2r}\right)^n \tag{2.5}$$

where n is an empirical constant.

Based on the shape of the normal distribution curve, Peck (1969) showed that the maximum settlement δ_{max} is given by

$$\delta_{\max} = \frac{0.314\varepsilon D^2}{i} \tag{2.6}$$

where D is the diameter of the tunnel. The settlement at various points of the trough is then given by

$$\delta = \delta_{\max} \exp\left(\frac{-x^2}{2i^2}\right) \tag{2.7}$$

in which x is the distance from the centreline.

Peck (1969) suggested that ε is usually in the range of 1~2 % for stiff clay and 2~5 % for soft clay. However, ε is likely to be dependent upon tunnelling machine and technology. With current tunnelling technology, it is likely that Peck's (1969) suggested ε-values are on the high side. For instance, the Land Transport Authority's (LTA) specifications for maximum ground loss due to tunnelling is 1 %. Mair et al (1993) suggested that subsurface settlement profiles could also be reasonably approximated in the form of a Gaussian distribution in the same way as surface settlement profiles.

Schmidt (1969) and Peck (1969) noted that there is a bow wave effect ahead of the tunnelling as seen in Figure 2.4. This bow wave is, in fact, the development of surface settlement trough above and ahead of the advancing heading. Attewell and Goodman (1982) noted from field studies that the 3-D surface settlement profile is often such that the transverse settlement curve is approximately a normal distribution curve while the longitudinal profile (along the tunnel axis) is approximately a cumulative normal distribution curve.

Subsequently, O'Reilly and New (1991) assumed that ground loss createss a radial movement towards the centre of the tunnel i.e. at the axis of excavation and that all ground deformations takes place at constant volume. The vertical δ and horizontal H displacements for any points with co-ordinates x, y, z are given by:

$$\delta_{(y,z)} = \frac{V_s}{Kz\sqrt{(2\pi)}} \exp\left[F\left(\frac{x - x_s}{Kz}\right) - F\left(\frac{x - x_f}{Kz}\right)\right] \tag{2.8}$$

$$H_{(y,z)} = \frac{y}{z}\delta_{(y,z)} \tag{2.9}$$

$$H_{(x,z)} = \frac{V_s}{Kz\sqrt{(2\pi)}}\left[\exp\left(\frac{-(x - x_s)^2 - y^2}{2(Kz)^2}\right) - \exp\left(\frac{-(x - x_f)^2 - y^2}{2(Kz)^2}\right)\right] \tag{2.10}$$

Where x_s and x_f are respectively the starting and final locations of the tunnel face, $i = Kz$, where K is an empirical constant dependent on ground conditions. Function $F(\ )$ represent the cumulative distribution function of a standardised normal random variable :

$$F_a = \int_{-\infty}^{a} \frac{1}{\sqrt{(2\pi)}} \exp\left(-\frac{t^2}{2}\right) dt \tag{2.11}$$

Various researchers have proposed the values of *i* based on field and laboratory observations. From the data in Tables 2.2a and 2.2b, there is a wide range of limits for the values of *i* and ε. The empirical approach is easy to use but has its uncertainty due to the variability of different ground conditions, and the necessity to assume values of i and ε, which may be highly variable. Furthermore, tunnel construction sequences, as well as the effects of different machines, were not considered. It is also not readily applicable to highly stratified soil conditions. Finally, lateral deformation is often not captured under the framework of the empirical approach [e.g. Attewell (1977), Lee & Rowe (1992a, 1992b), Mair (1996)]. In spite of this, this framework remains the standard approach to find settlement computation in the industry.

2.3.2 Analytical research

Several researchers, as shown in Table 2.1, have used analytical approach to explain the settlement and stresses distributions for underground openings. In general, closed-form elastic solutions provide a framework for the computation of the distribution of surface settlement. Their predicted maximum surface settlement matched well with the site-measured data in their respective cases. However, the settlement trough tends to be wider than that observed in the field (e.g. Loganathan and Poulos, 1998). Verruijt and Booker (1996) suggested that this discrepancy in curvature is due to the non-linear plastic effects occurring above the crown of the tunnel excavation, which are not well modelled by elastic models. The plastic zones above the tunnel axis tend to localise the settlement zone thus giving a narrower trough. Davis et al (1980) provided an insight to tunnel heading stability by deriving a lower bound solution for plane strain condition. They compared it with the upper bound solutions (Mair, 1979) and attributed the difference to the complex three-dimensional effects of tunnel headings.

2.3.3 Numerical research

Table 2.3 summarized the previous numerical studies which have been conducted on tunnelling. However, as this table shows, much of the previous studies tend to focus on the effects of tunnel geometry, depth and soil conditions on ground loss [e.g. Ghaboussi and Ranken (1977), Lee and Rowe (1990)] and lining stresses [e.g. Ghaboussi and Hansmire (1983), Sharour and Mroueh (1997)]. Much less work has been reported on the effects of construction sequence. From the literature review, most FE analyses were plane strain (2-D) and the tunnel boundary conditions range from unsupported i.e. lining not constructed [e.g. Ghaboussi and Ranken (1977), Lee & Rowe (1989), Gunn (1993)] to supported i.e. lining was constructed [e.g. Ghaboussi et al. (1983), Atzl & Mayr (1994), Komiya et al. (1999), Lee et al. (1992a, 1992b)]. However, the assumption of plane strain does not allow the progressive changes in tunnel support conditions associated with the removal of the soil from the tunnel face and the build-up of the lining to be modelled correctly. As noted earlier, in most tunnelling scenarios, the unsupported span of the tunnel is often fairly short and only occurs between the face and the lined portion. As such, the problem is really 3-D, not 2-D. For this reason, 2-D FE analysis is usually not directly applicable to making predictive assessments of surface settlement, unless it is applied together with an assumed ground loss percentage.

There has been little research work on the response of the tunnel face, in particular on the effects of over applied face pressure in relation to EPB machine. Yi et al (1993) reported that an intentionally induced small amount of heave for shallow tunnels could reduce the final surface settlements. However, Shirlaw (1994) reported that by creating large initial heave at or near the ground surface is not an appropriate means of reducing settlement and protecting buildings from damage due to tunnelling. Tunnel face support is needed to prevent any inward collapse of the soft ground surrounding the heading. Ghaboussi and Hansmire (1983) presented a simplified modelling on the shield's boundary conditions using beam element, but this was conducted using a 2-D plane strain analysis thus the tunnel heading was again not modelled.

One of the major problems faced by researchers in numerical studies is the difficulty in simulating the Gaussian settlement profile correctly [e.g. Lee and Rowe (1989), Gunn (1993), Dasari (1996)]. Lee and Rowe (1989a, 1989b) suggested that the use of anisotropic elastic properties significantly improve the prediction while Gunn (1993) highlighted the usage of isotropic non-linear elastic perfectly plastic "small-strain" stiffness models [e.g. Simpson (1979), Jardine et al (1986)]. However, even with these modifications to the soil properties, a wider settlement trough than that usually observed is still predicted in most of the published studies. Combining cross-anisotropy with small-strain non-linearity may improve the matching but these have not been tried to date.

Mair and Taylor (1996) commented that almost all technical papers submitted are all coupled with case analysis i.e. numerical or experimental findings supported by field results. In fact, these approaches dominated the literature review. Closed-form solution is rarely used as an analytical tool in predicting surface and lateral deformation due to complex site conditions and tunnel configurations.

In summary, the stress and displacement field around an advancing tunnel is 3-D in nature [e.g. Clough and Leca (1989), New and O'Reilly (1991), Mair and Taylor (1997)]. A 2-D analysis can represent many salient aspects of the problem. While some 3-D FEA's have been reported [e.g. Ghaboussi et al. (1983), Lee and Rowe (1991), Komiya et al. (1999)], they remain relatively scarce and are limited to fairly coarse mesh over very limited ground domain (e.g., Lee and Rowe (1991), Swoboda and Krisha (1999), Burd et al (2000)]. Furthermore, little work has been done on simulating the advance of the EPB shield. Clough and Leca (1989) identified a number of reasons hindering the successful development of FE analysis for analysis of complex problems. They have identified them as follows:

1. Many unknown parameters such as choice of constitutive model, tail void size, tunnel lining properties.
2. Multiple analyses due to changes of geology and alignment geometry along the length of the tunnel.
3. No constitutive soil model has been shown to be highly successful at simulating all aspects of soil behaviour important to tunnelling.

Despite the progress that had been made over the years in FE analyses, the above reasons remain largely valid. However, important issues such as the rate of tunnel shield advancing, construction sequences, tunnel heading stability and tunnel-liner as well as tunnel-tunnel interactions (a pair of parallel tunnels) cannot be studied clearly with a 2-D analysis.

2.4 Issues To Be Examined in this Study

The above shortcomings provide a motivation in moving towards a 3-D FE analysis. The issues that will be examined in this study are as follows:

1. Feasibility study on the use of 3-D FE analysis for solution of tunnelling problems without making any recourse to high-performance computing workstations or supercomputers, which would have placed the computational resources needed well beyond the means of most engineering organizations. The intention is to stay within the PC platform, by means of faster and more memory-efficient solution algorithms which can better exploit the hierarchical nature of most modern day computers. This leads to the development of a new suit of iterative Krylov subspace solution algorithms with robust and rapid convergence characteristics.
2. Using the developed solution algorithm, an in-depth study on the issue of tunnel heading with applied pressure on the tunnel face will then be conducted, using data from a tunnel project as a benchmark. This study will shed light on the mechanism of the tunnel heading in relation to its influences on the surface and sub-surface ground movement. The significance of the various factors on the final solution will also be studied. The effects of different constitutive models will also be investigated. This illustrates the feasibility of conducting detailed and realistic 3-D analyses on relatively modest computational platforms which are readily available.
3. A comparison is also made between the predictions of full 3-D analysis and those from "pseudo-3-D" analysis which are essentially 2-D analyses, which allow for lining insertion when the tunnel walls have only been partially unloaded. This is the approach used by the "3-D" analysis in commercial softwares such as PLAXIS V.7 (1998).

Table 2.1 Summary of Analytical research

Reference	Description of Study	Soil conditions	Construction sequence	Findings
Burns and Richard (1964)	Assumed ground mass was unstressed. The single tunnel was excavated and lining was placed followed by ambience stresses being applied. Results were analysed on two cases namely non-full and full slippage contact with liner.	Elastic Soil Properties were used and Ko was set to 1.	Not appropriate	Modelling sequence was not exact because the ground mass was assumed weightless thus in-situ stress field was neglected. Overall, displacements were excessive.
Davies et al. (1980)	Investigate tunnel parameters that influence tunnel stability. 3 different shapes of shallow underground openings were considered. They were namely plane strain unlined circular tunnel, plane strain heading and circular tunnel heading. The lower bound and upper bound stability solutions were compared. The lower bound solutions were obtained using the limit theorems of plasticity.	Soil was idealised as an elastic perfectly plastic material and undrained property C_u was assumed constant with depth. Parameters influencing stability include depth and diameter of tunnel, overburden stresses, soil unit weight etc.	Simulate open face shield with possible instability to the tunnel face. Compressed air was used to maintain tunnel stability.	Stability ratio, N, shows variation from Broms and Bennermark (1967) stability criterion ($N < 6$). Under plane-strain circular tunnel heading and different ratios of C/D and $\gamma D/C_u$., lower bounds of N varies from 0 to 12. In the case of circular tunnel heading, the experimental collapse loads lies in the upper and lower bound solutions. C = Cover depth, D = tunnel diameter, γ = soil unit weight.
Sagaseta (1987)	Analytical study on ground deformation due to imposed ground loss on the tunnel geometry. Method of analysis using a point sink and extending to a line in the soil mass to represent ground loss. Eliminate the stresses and obtaining the strains using only the incompressibility condition. Basic solutions were obtained by considering a differential extracted volume and then integrated over the line.	Elastic isotropic undrained soil properties.	Tunnel was excavated and ground loss was estimated using empirical correlation or observation. Ground losses in tunnels were modelled as an equivalent point sink.	Provide a solution on the near surface ground settlement. Calculated movements for far field tends to overestimate the measured ones. At the tunnel boundary, the vertical displacements were well fit but the horizontal displacements show consistently higher values. Not applicable to drained case because of strain incompatibility to the closed form model.
Verruijt and Booker (1996)	Analytical solution for surface settlement due to deformation of tunnel in an elastic half-space. Two types of deformation mechanisms of the tunnel are considered. They are namely uniform radial displacement ground loss and ovalization of tunnel. Gives solution for different values of poisson's ratio.	Drained and undrained elastic soil properties. Relative displacements of the tunnel surface were expressed in terms of ground loss percentage and ovalization factor.	Procedure is equivalent to excavation of tunnel and placing of liner in a single step.	Serves as a reference to numerical computations. Introduced the effect of ovalization of tunnel (Muir Wood,1975) and strain components are derived from differentiation of displacements.
Loganathan and Poulos (1998)	Modified Verruijt and Booker's (1996) solution for case of non-uniformed radial displacement of tunnel wall.	Undrained elastic soil properties. Ground loss expressed as percentage.	Same as Verruijt and Booker (1996)	The maximum settlement fits well with field observations. Predicted troughs are wider than field observations.

Table 2.2a Values of i for settlement trough

Reference	Value of I	Remarks
Peck (1969) (Field Observations)	$\frac{i}{r} = \left(\frac{Y}{2r}\right)^n$	For Clay n = 0.8 ~ 1.0
Attewell et al (1974)	$\frac{i}{r} = \alpha\left(\frac{Y}{2r}\right)^n$	α = 1 n = 1
Atkinson & Potts (1977) (Field Observations and Model tests)	$i = 0.25(Y + r)$ $i = 0.25(1.5Y + 0.5r)$	For loose sand For Dense sand and overconsolidated clay
Clough and Schmidt (1981)	$\frac{i}{r} = \alpha\left(\frac{Y}{2r}\right)^n$	α = 1 n = 0.8
O'Reilly & New (1982) (Field Observations – UK tunnels)	$i = (0.43Y + 1.1)$ $i = (0.28Y - 0.1)$	For cohesive soils For granular soils
Rankin (1988) (Field Observations and Centrifuge Tests)	$i = 0.5Y$	

Table 2.2b Values of i for subsurface trough

Researchers	Value of I	Remarks
Mair et al. (1993) Field observations	$i_z = K(Y_o - Y)$	$K = \left(\frac{0.175 + 0.325\left(1 - \frac{Y}{Y_o}\right)}{\left(1 - \frac{Y}{Y_o}\right)}\right)$
Atkinson and Potts (1977)	$\frac{S_Y}{S_{\max}} = 1.0 - \alpha\left(\frac{Y - r}{2r}\right)$	α = 0.57 (dense sand) α = 0.4 (loose sand) α = 0.13 (overconsolidated clay)

Y_0 = depth of ground tunnel axis below ground level

Y = depth of subsurface settlement trough below ground surface

S_{max} = maximum settlement

S_Y = settlement at depth Y

Table 2.3 Summary on Numerical research

Reference	Description of Study	Soil and Boundary Conditions	Construction Sequence	Findings
Ghaboussi and Ranken (1977)	Study two parallel tunnels with various parametric studies on tunnel depth, sequence of construction, support condition, pillar width.	Plane strain case. Linear elastic and elasto-plastic soil properties were used. Ko used is 0.5	A full face excavation with two extreme conditions with regards to placement of liners. Case I was excavation and place lining within the same step while Case II was excavation in a single step and placement of liner in the subsequent step.	Established the assumptions on lined and unlined cases clearly. Studies indicated that interaction between two parallel tunnels influences tunnel displacements and liner forces. These interaction effects decrease as the pillar width was increased. When pillar width to tunnel diameter ratio is more than two, the tunnels behave independently of each other.
Ghaboussi and Hansmire (1983)	Simulate sewer tunnel crossing over subways and investigate the influence of sewer construction on the subway tunnel liner forces.	Plane strain case. Linear elastic soil properties. In short term, simulate forward jacking of shield at the edge of tunnel shield. Simulate shield and liner using beam element.	Analyses were done on two different cross sections. In Case I, the sewer tunnel appears as a circle and full face excavation were done in one step. In Case II, the subways appears as circles and the sewer tunnel is modelled with shield advancing.	Shield jacking, simulated as a pre-stressed beam element, was a prominent factor in the transmission of thrust to shear stress outside the shield. When stresses in the 2D case were compared with a simplified 3D-analysis, the tunnel bending moment and crown displacement were conservative by a factor of 2 and 5 respectively.
Lee and Rowe (1990)	Simulate 3D-ground deformation in soft ground. Used a 11 noded element type to reduce the mesh size and computing time. Establish procedures for defining the total gap parameter, which were based on amount of over excavation, workmanship, and the physical gap (i.e. total ground loss).	Mohr-Coulomb constitutive soil model was used. Soil parameters used were based on results determined by stress-path dependent triaxial tests.	Full release of axial stress to simulate face loss. Soil around tunnel boundary is allowed to deform freely. Once soil reaches a pre-defined shield loss and total ground loss, lining elements are activated. Assuming full contact between soil and liner.	Stresses ahead of the tunnel face were not as significant as compared to those behind the tunnel headings. The distance requiring the ground displacement to reach plane strain condition will depend on the amount of plasticity occur around the tunnel opening.
Sharour et al. (1997)	A non-linear 3D finite element analysis on a set of hypothetical closely spaced tunnels. Used a well-preconditioned conjugate gradient solver.	Mohr-Coulomb model	Excavation of soil and placing of liner in a single step with no support pressure on tunnel face.	Results of the second tunnel induced a higher axial force and bending moment in the first tunnel.

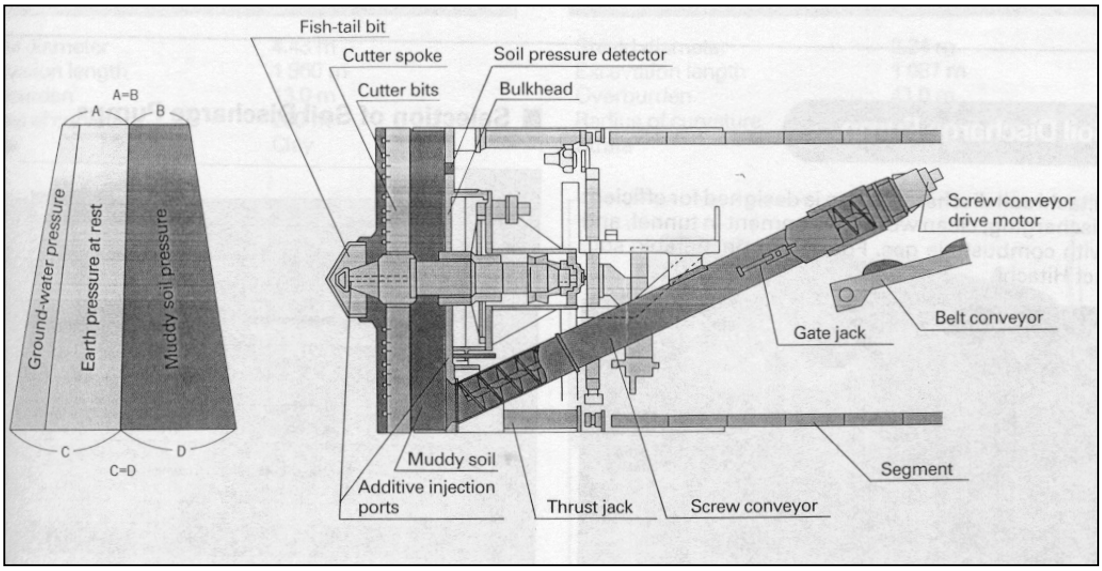

Figure 2.1 A schematic drawing of the typical EPB machine (after Howden, 1996)

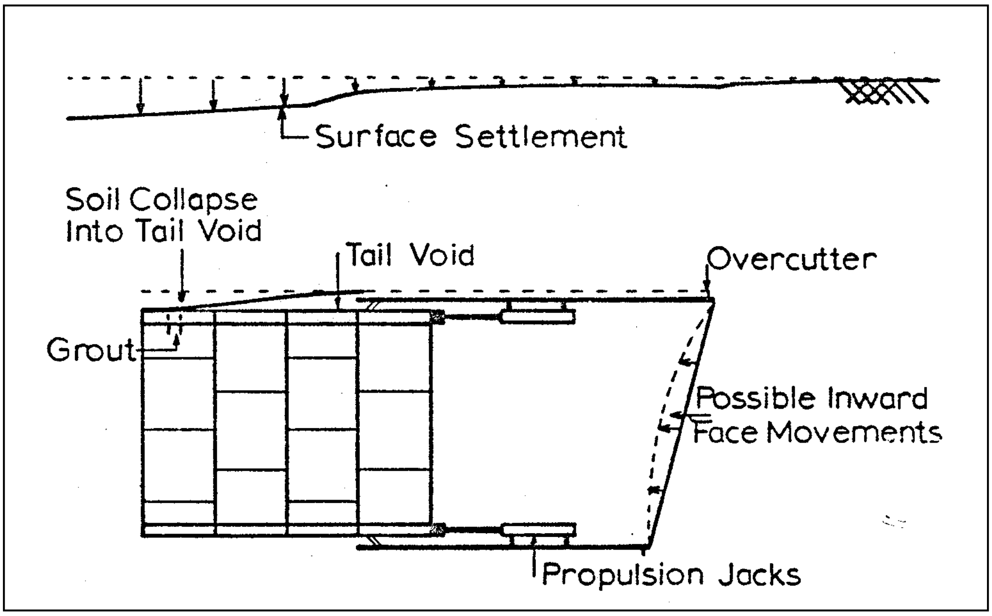

Figure 2.2 Various Components of ground loss (after Nelson, 1985)

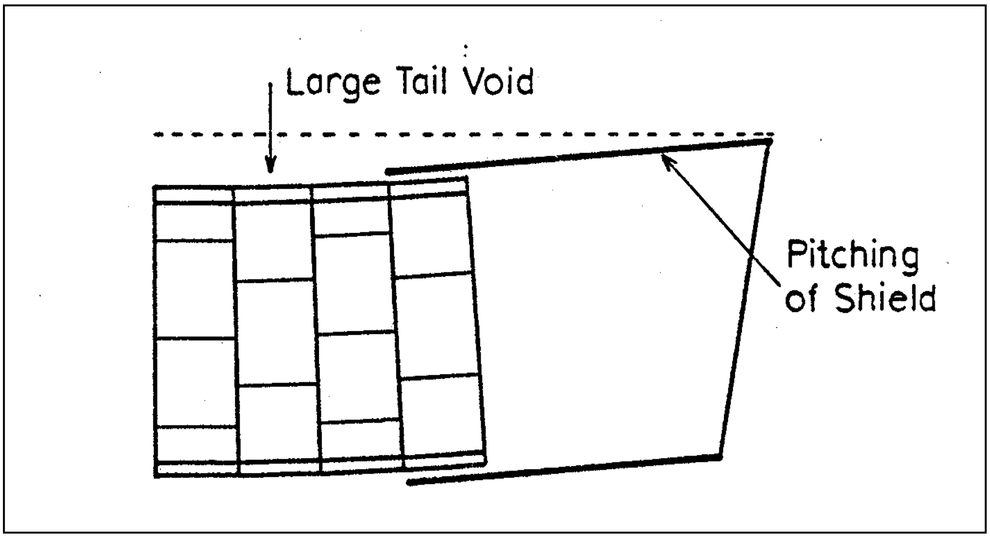

Figure 2.3 Pitching of shield causing additional shield and tail loss (after Nelson, 1985)

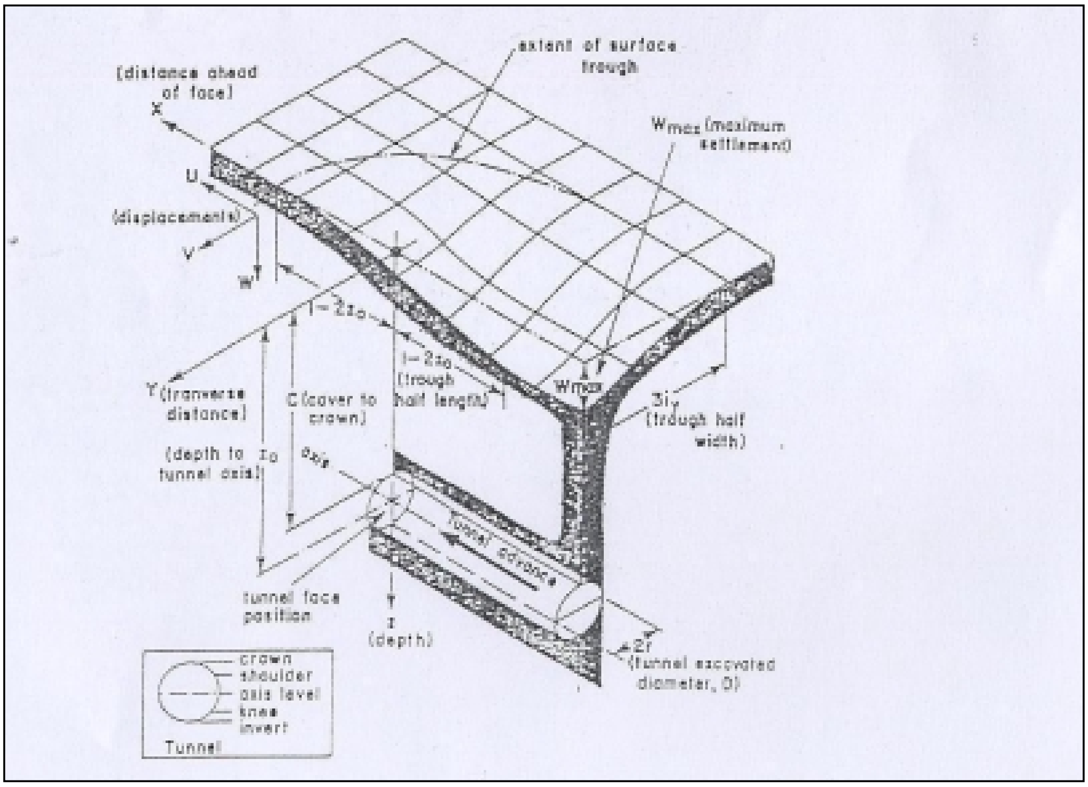

Figure 2.4 Green field effect due to tunnelling (after Yeates, 1985)

3 Performance of Jacobi Preconditioning in Krylov Subspace solution of finite element equations

3.1 Introduction

Finite element analysis (FEA) often leads to a set of linear algebraic equation of the form

$$Ax = b \tag{3.1}$$

where $A \in \Re^{ndf \times ndf}$, $x \in \Re^{ndf}$ and $b \in \Re^{ndf}$.

The matrix A has dimensions *ndf*-by-*ndf*, where *ndf* denotes the number of degrees-of-freedom. $\Re^{ndf \times ndf}$ denotes vector space of real *ndf*-by-*ndf* matrices and $\Re^{ndf}$ denotes the vector space of real *ndf*-vectors.

Many methods are available to solve Equation (3.1) but the most widely used algorithms are refined variants of the Gaussian elimination approach. These include the bandwidth solver (Zienkiewicz, 1989), Frontal solver (e.g. Irons, 1970; Britto and Gunn, 1987) and the multi-frontal solver implemented in the software ABAQUS (Hibbitt et al, 1997). If A is dense then the best solver is one that factorises A and solves the equation by back-substitution. Such solvers are very efficient for small and medium sized problems where the matrix is still fairly dense and the time spent on factoring is roughly equivalent to the time spent on solving the system iteratively.

For 3-D problems involving large and sparse matrices, even just storing the frontal or semi-bandwidth can require a large amount of memory. Factoring is not economical due to large amount of computer memory needed for storing the zero elements. Even when the user uses a banded storage solver, the solution is often solved out of core for large system of equation, due to limited computer memory space. In addition, in hierarchical computer systems that have multi-level clock rates, such algorithms with their indirect addressing, tends to lead to a rather low cache data re-use rate, thereby causing a drop in CPU efficiency.

To reduce computer memory usage, a method is needed which avoids the assembly of the global stiffness matrix. One such technique implemented in this project is the Element-by-Element (EBE) strategy. This is used in tandem with Krylov subspace iterative solvers namely Preconditioned Conjugate Gradient (PCG) method [e.g. Shewchuk (1994), Wang (1996), Smith (2000)] or Quasi-Minimal Residual method [e.g. Freund and Natchigal, (1991), (1994a), (1994b)].

In this chapter, the properties of a stiffness matrix arising from geotechnical finite element analysis will be discussed. This will help to decide the appropriate iterative solvers among the many available in the literatures. The formulation and implementation of two Krylov subspace iterative solvers are then presented. The algorithms are incorporated into in-house finite element software called CRISP (Britto & Gunn 1990); thereafter, the finite element code is termed NUSCRISP to differentiate it from the original CRISP which uses a frontal solution algorithm.

A 3-D test problem involving a two-layered ground subjected to uniform vertical pressure over a part of the ground surface is first used as a benchmark problem for these iterative algorithms. The convergence behaviour of drained, undrained and consolidation problems is then examined for a number of cases covering a range of condition number. Detailed spectral and eigenvector analyses will be conducted to furnish a comprehensive and rigorous basis to explain the performance of the Jacobi preconditioner on a representative range of drained, undrained and consolidation problems commonly encountered in practice.

Concluding this chapter, the solvers' timings were compared with those of the Frontal method (Irons, 1970) implemented in CRISP (Britto and Gunn, 1987) for various idealized problems. This serves to elucidate the economical performances of such iterative solvers for large 3-D problems. The benchmarking of these solvers was done on desktop featuring an Advanced Micro Devices (AMD) 1.4GHz processor and 1.0 Gigabytes of RAM (random access memory).

3.2 Stiffness Matrix and its relation with Iterative Methods

Finite element codes which solve Equation (3.1) using Gaussian elimination approaches usually have clear and consistent convergence characteristics which are not problem dependent [e.g Irons (1970), Britto & Gunn (1987)]. If the problem involved has a condition number which is less than the limit set by the precision of the code and computer, the time needed to obtain the solution is almost a constant. On the other hand, if the condition number exceeds the allowable limit, then the problem is usually perceived to be a singular problem by the code and solution will normally not be completed. This is not the case with iterative methods, which converges gradually towards the correct answer. Many iterative methods have convergence characteristics, which varies substantially with condition number. Thus, when dealing with the implementation of iterative solvers in finite element codes, a basic understanding in the formulation of the stiffness matrix and its properties is essential in deciding a suitable iterative solver and thus its true solution. The following sections introduce the basic forms and properties of the *A* matrix (see Equation 3.1) for different geotechnical problems and discusses their implications on the selection of appropriate iterative algorithms. Detailed geotechnical finite element formulations are presented in many published documents [e.g. Smith & Griffiths (1997), Britto & Gunn (1987)].

3.2.1 Drained and Undrained Problems

In geotechnical engineering, its more common to relate the stress-strain relationships using effective bulk modulus (*K'*) and shear modulus (*G'*). As described by Britto & Gunn (1987), the element stiffness matrix K_e can be represented by

$$A_e = \int_V B^T D\, B\, dV \quad \in \Re^{m\,x\,m} \quad B \in \Re^{n\,x\,m},\ D \in \Re^{m\,x\,n} \tag{3.2}$$

where *B* denotes the matrix of shape function derivatives for displacement, *D* is the elastic modulus matrix or stress-strain matrix. The matrix A_e has dimensions *m*-by-*m*, where *m* denotes the number of degrees-of-freedom for each element. $\Re^{m \times m}$ denotes vector space of real *m*-by-*m* matrices. The subscript “e” refers to an individual element and the summation of the individual element leads to the global stiffness matrix *A* commonly found in any linear algebra system (see Equation (3.1)).

The elastic modulus matrix D_e is represented by Equation (3.3):

$$D_e = \begin{bmatrix} K' + \frac{K_w}{n} + \frac{4}{3}G' & K' + \frac{K_w}{n} - \frac{4}{3}G' & K' + \frac{K_w}{n} - \frac{4}{3}G' & 0 & 0 & 0 \\ K' + \frac{K_w}{n} - \frac{4}{3}G' & K' + \frac{K_w}{n} + \frac{4}{3}G' & K' + \frac{K_w}{n} + \frac{4}{3}G' & 0 & 0 & 0 \\ K' + \frac{K_w}{n} - \frac{4}{3}G' & K' + \frac{K_w}{n} - \frac{4}{3}G' & K' + \frac{K_w}{n} - \frac{4}{3}G' & 0 & 0 & 0 \\ 0 & 0 & 0 & G' & 0 & 0 \\ 0 & 0 & 0 & 0 & G' & 0 \\ 0 & 0 & 0 & 0 & 0 & G' \end{bmatrix} \qquad (3.3)$$

where K_w is the bulk modulus of water and n is the porosity of the soil structure and it is governed by the constitutive relationship given in Equation (3.4):

$$\sigma' = D_e \varepsilon \text{ where } \sigma' = \begin{bmatrix} \sigma'_x \\ \sigma'_y \\ \sigma'_z \\ \tau'_{xy} \\ \tau'_{yz} \\ \tau'_{zx} \end{bmatrix} \in \Re^n \text{ and } \varepsilon' = \begin{bmatrix} \varepsilon_x \\ \varepsilon_y \\ \varepsilon_z \\ \gamma_{xy} \\ \gamma_{yz} \\ \gamma_{zx} \end{bmatrix} \in \Re^n \qquad (3.4)$$

Equation (3.4) is the approach used in SageCrisp (1997) and Plaxis (1998). The general structure of matrix D_e is applicable to drained and undrained elements. For drained formulation, $\frac{K_w}{n}$ is set to zero while for undrained elements $\frac{K_w}{n}$ is often given a much higher value than K'; usually about 1,000 times the K' value.

3.2.2 Consolidation Matrix

Geotechnical problems involving consolidation or dissipation of pore water pressure are typically solved based on the formulation by Biot (1941) e.g. Sage Crisp (1997), Plaxis (1998), ABAQUS (1997). This formulation can be illustrated by treating the soil skeleton as a porous elastic solid and the transient flow of fluid is coupled to the solid by the conditions of compressibility and of continuity. The finite element discretisation of Biot's equation has been discussed in many published documents e.g. Griffiths & Smith (1997) and Britto & Gunn (1987) and can be represented by Equation (3.1) in which the matrix A_e, as well as the vectors x and b are given by

$$A_e = \begin{bmatrix} K_e & L \\ L^{\mathrm{T}} & -C \end{bmatrix} \in \Re^{n\times n} \qquad K_e = K_e{}^{\mathrm{T}} \in \Re^{m\times m}, L \in \Re^{m\times(n-m)}, C = C^{\mathrm{T}} \in \Re^{(n-m)\times(n-m)} \tag{3.5}$$

$$x = \begin{Bmatrix} \Delta u \\ \Delta p \end{Bmatrix} \in \Re^{n} \qquad \Delta u \in \Re^{m}, \Delta p \in \Re^{n-m} \tag{3.6}$$

$$b = \begin{Bmatrix} \Delta f \\ Cp_t \end{Bmatrix} \in \Re^{n} \qquad \Delta f \in \Re^{m}, \mathrm{p_t} \in \Re^{n-m} \tag{3.7}$$

In Equation (3.5), K_e is the effective stress stiffness matrix, L is the link matrix, C is the flow matrix, and $\Re^{n\times n}$ denotes vector space of all n-by-n matrices. In Equation (3.6), Δu denotes the displacement increment, Δp denotes the excess pore water pressure increment; and $\Re^{n}$ denotes the vector space of real n-vectors. In Equation (3.7), Δf denotes the nodal load increment and p_{t} denotes the nodal pore water pressure at the current time step.

The sub-matrices K, L and C in Equation 3.5 can be represented by (e.g. Smith & Griffiths, 1997; Britto & Gunn, 1987)

$$K_e = \int_{\mathrm{V}} B^{\mathrm{T}} D_e B \,\mathrm{dV} \tag{3.8}$$

$$L = \int_V B^T m \overline{N} \, dV \tag{3.9}$$

$$C = \frac{\Delta t}{\gamma_w} \int_V E^T k E \, dV \tag{3.10}$$

where B denotes the shape function derivatives for displacement; D_e denotes the effective stress-strain matrix; m is a matrix equivalent of the Kronecker delta and is given by $[1]$ for 1-D analyses, $[1 \quad 1 \quad 0]^T$ for 2-D analyses, and $[1 \quad 1 \quad 1 \quad 0 \quad 0 \quad 0]^T$ for 3-D analyses; $\overline{N}$ denotes the shape function for excess pore water pressure; k denotes the permeability matrix; Δt denotes the time step; and E denotes the shape function derivatives for excess pore water pressure. By summing the contribution of each element A_e, the global matrix A in Equation (3.1) is formed.

3.2.3 Matrix Properties and Classification of Finite Element Matrix

A square matrix A is *positive definite* [e.g. Saad (1996), Shewchuk (1994)] if

$$x^T A\, x > 0 \tag{3.11}$$

for all nonzero column vector x.

The matrix A_e resulting from drained and undrained geotechnical problems can be shown to be positive definite (Chan, 2002). In contrast to drained and undrained problems, consolidation problems based on Biot's (1941) formulation generally lead to indefinite A matrices. An indefinite matrix is one for which $x^T A\, x > 0$ for some non-zero vectors x and $x^T A\, x < 0$ for some non-zero vectors x.

The convergence characteristic of a set of linear algebraic equation such as Equation 3.1 is closely related to its condition number. If A is symmetric and positive definite, then the computed condition number $\kappa(A)$ is equivalent to

$$\kappa(A) = \frac{\lambda_{\max}}{\lambda_{\min}} \tag{3.12}$$

where λ_{max} and λ_{min} refers to the maximum and minimum eigenvalues respectively (Shewchuk 1994). In general, the larger the condition number, the more likely is the failure to converge. However, the convergence characteristic of a matrix may be exhibited in different ways for different types of solution algorithms. For Gaussian elimination methods, the time needed to obtain the solution vector x tends to remain almost constant provided the condition number is below a certain limit, but the round-off errors will increase in magnitude. If the condition number exceeds the limit, the round-off errors overpower the computation and the matrix A is then often perceived by the solution algorithm as a singular matrix and no solution is possible (e.g. Britto & Gunn, 1987).

For iterative methods, the accuracy of the solution is normally prescribed by means of a tolerance within which the solution is deemed acceptable and iteration ceases. However, the time needed to obtain the solution will usually increase with the condition number (e.g. Shewchuk 1994; Barrett et al. 1994). However, this is only a general guideline and it will be shown later that the type of problem also has a major effect.

3.3 Previous research on Jacobi Preconditioning

Iterative methods for solving general, large sparse linear systems have been gaining popularity in many areas of scientific computing. According to Shewchuk (1994) and Saad (1996), one can take advantage of global matrix sparsity to design special direct methods that can be quite economical. Recent development (Barrett et al. 1994) shows that the combination of preconditioning and Krylov subspace iterations could provide efficient and simple "general purpose" procedures that could compare with direct solvers. Iterative methods were often designed with special purpose in mind and their efficiencies were often relied on problem dependent parameters. Research into the design of iterative methods for solving nonsymmetric and symmetric linear systems is an active area of research and new methods are still emerging. Nachtigal et al. (1992) showed that, for any of a group of iterative methods, there is a class of problems for which a given method is the winner and another one is the loser. In view of this, Barett et al. (1994) have stressed that selecting the "best" method for a given class of problem is largely a matter of trial and error.

As mentioned earlier, drained and undrained problems give rise to positive definite A-matrices. For such matrices, the conjugate gradient (CG) method is a widely used iterative method which has been shown to be highly memory- and time-efficient [e.g. Papadrakakis (1993), Mitchell & Reddy (1998), Wang (1996), Lim et al. (1998)].

The CG method was first presented by Hestenes and Stiefel (1952) but its usefulness was not fully appreciated until the 1970's. Its true potential was not realised until the vector processors made it possible to solve extremely large problems which could not be solved in other ways given limited computer memory. Figure 3.1 shows the pseudo-code of a typical CG algorithm.

Fox and Stanton (1968) and Fried (1969) pointed out that the assembly of the stiffness matrix is not essential in CG methods and that the matrix-vector operations can be performed at the element level. This opened the way for Element-by-element (EBE) implementation of CG methods, which can drastically reduce memory requirements in large 3-D finite element analyses. In this approach, the global stiffness matrix is not explicitly assembled.

The rate at which the iterative method converges depends greatly on the spectrum of the coefficient matrix. Hence iterative methods usually involved a second matrix that transforms the coefficient matrix into one with a more favourable spectrum. The transformation matrix is called a Preconditioner. Preconditioning is often used as an aid in iterative methods to speed up the convergence rate. For example, Axelsson (1972) suggested a preconditioned CG (PCG) by a scaled symmetric successive overrelaxation (SSOR) operator. This form of algorithm has a relaxation parameter to control the ellipticity of sparse system. A simple and inexpensive preconditioner is the Jacobi Preconditioner (e.g. Smith 2000, Saad 1996), which is a collection of the diagonal terms in the stiffness matrix. The EBE-PCG pseudocode is shown in Figure 3.2. Hereafter, it is designated as EPCG.

However, this may not necessarily give the highest convergence rate and many more sophisticated pre-conditioners such as incomplete cholesky preconditioners (Ajiz and Jennings, 1984), polynomial preconditioner (Johnson, 1983) or mutligrids (Bulgakov,

1995) preconditioner have been proposed. The flaw is that these approaches require the construction of global preconditioners, which impose heavy demands on storage capacity. As such they do not fully exploit the advantages of EBE strategies.

The simplest, and perhaps most commonly used, EBE preconditioner is probably the Jacobi preconditioner. In spite of its simplicity and low storage requirement, the Jacobi preconditioner can improve convergence rates of conjugate gradient iterations significantly (Smith and Wong, 1989). Moreover the Jacobi preconditioner can be applied to the individual element matrices before CG iterations. This allows the preconditioning process to be removed from PCG iterations, with resulting savings in operation counts per iteration. More complex EBE-based preconditioners have also been developed from approximate Cholesky factorisation (Winget and Huges, 1985) and LU splitting techniques (Nour-Omid and Parlett, 1985). Other preconditioners of similar form include the Crout and Gauss-Seidel EBE preconditioner (Papadrakakis, 1993). Smith and Wong (1889) and Dayle et al. (1997) showed that the reduction in the number of iterations through use of a product or polynomial-form preconditioner does not always translate into greatly reduced total CPU time since the time per iteration is substantially increased. Mitchell & Reddy (1998) developed a recursively-defined preconditioner based on successive p-refinement, which can be implemented with EBE strategies. However, substantial working storage may still be needed for hierachical vector spaces and the lowest-p order global matrix, even for 3-D problems with highly regular domains. For realistic 3-D geotechnical analyses, the storage demand is likely to be increased even further by the presence of complex geometries, multiple material zones and irreguar soil stratifications. As a result, the prospect of this approach being implemented in general 3-D codes for geotechnical analyses on

PC-type computing platform remains relatively remote at present. For these reasons, the Jacobi preconditioner remains widely used in EBE strategies [e.g. Wang (1996), Smith (1997), Lim et al. (1998)].

The performance of Jacobi preconditioning in geotechnical analysis remains unclear to date. For instance, Wang (1996) noted a marked increase in the number of iterations when PCG, with Jacobi preconditioning, is applied to nearly incompressible problems. However, the reasons for this have not been fully clarified. In this study, the performance of the Jacobi preconditioner in drained, undrained and consolidation problems is examined. A fundamental understanding of this issue is of practical and theoretical significance as it is a necessary first step towards a more systematic development of efficient preconditioners for common geotechnical problems. Moreover, if the convergence behaviour of Krylov subspace methods can be correlated to simple matrix properties, then the effect of any proposed preconditioners can be predicted by assessing its impact on the relevant matrix properties without having to conduct time-consuming trials.

As mentioned earlier, consolidation problems give rise to indefinite A-matrices. For such matrices, convergence cannot be guaranteed with CG methods [e.g. Paige & Saunders (1975), Golub and Van Loan (1989), Barett et al. (1994), Smith (2000)]. This is because the vector sequences in the CG method correspond to a factorisation of a tridiagonal matrix similar to the coefficient matrix and for each CG iteration corresponds to a LU factorisation of the tridiagonal form. As such, a situation of zero or near zero pivot may cause a breakdown for an indefinite system when PCG is used.

Krylov subspace methods such as Minimal Residual (MINRES) or Symmetric LQ (SYMMLQ) presented by Paige & Saunders (1975) can achieve iterative solutions of indefinite systems. These methods avoid the LU factorisation mentioned above and do not suffer breakdown. The pseudocodes for these methods are presented in Figures 3.3 and 3.4.

In MINRES method based on Lanczos process for symmetric matrices, the coefficient matrix of the preconditioned system needs to be symmetric and this has implied that the preconditioner needs to be symmetric positive definite. This restriction is rather unnatural when the coefficient matrix itself is highly indefinite [e.g. Freund and Nachtigal (1994), Vorst (2002)]. It is self evident that the construction of effective preconditioner for MINRES is largely an open problem. In addition, Saad and Vorst (2000) have highlighted that the usage of 3-term recurrence making MINRES very vulnerable to rounding off errors. Sleijpen & Vorst (1996) have shown that rounding errors due to the 3-term recurrence are propagated to the approximate solution with a factor proportional to the square of the condition number of A.

In SYMMLQ, Paige and Saunder (1975) employed a LQ decomposition of the tridiagonal matrix T and minimise the norm of the error instead of minimising the norm of the residual for MINRES method. By doing this, the advantage of SYMMLQ method over MINRES lies in regular short recurrences, minimal overhead and economy storage. However, the disadvantage of SYMMLQ is that it may converge a good deal slower than MINRES for ill-conditioned systems (Vorst, 2002).

Freund and Nachtigal (1994a, 1994b) proposed a Quasi-Minimal Residual (QMR) method for solving symmetric indefinite systems, the pseudo-code incorporating EBE format, is shown in Figure 3.5; hereafter designated as EQMR. QMR has the advantage over MINRES or its variants because it can be combined with indefinite preconditioner, which is readily available within the system matrix and is thus more practical. Table 3.1 shows the computational and storage cost for the methods discussed. As shown, the differences in the computational aspects are rather marginal. The additional storage vectors required by QMR are relatively cheap and the memory requirements are limited and modest when compared with direct solutions such as bandwidth (Zienkiewicz, 1989) or Frontal solver [e.g. Irons (1970), Britto and Gunn (1987)]. Freund and Nachtigal (1994b) presented that the QMR method as compared to MINRES converges in considerably less iteration; twice as fast. For these reasons mentioned above, the QMR remains a more robust method to solve symmetric but indefinite system. Owing to its relatively recent development, there is little or no literature on the use of the QMR method on geotechnical problems. To the best of the author's knowledge, this is one of the first studies to introduce and systematically evaluate the performance of the Jacobi-preconditioned QMR method for drained, undrained and consolidation problems.

3.4 Problem Configuration

3.4.1 Problem description

Figure 3.6 shows the quadrant-symmetric problem that is analysed. It consists of a uniformly distributed loading on part of the surface of a 3-D mesh comprising two soil layers. The top layer has a thickness of 2 m, while bottom layer has a thickness of 10 m. Both materials were assumed to be elastic and loading was applied in one increment. The sides of the mesh were constrained to move only in-plane while the bottom of the mesh was fixed. For consolidation analyses, the pressure at the ground surface was fixed at atmospheric pressure. All other surfaces of the mesh are impermeable.

3.4.2 Finite element model

For the drained and undrained analyses, 20-noded brick elements (Britto & Gunn, 1987), with 60 displacement degrees-of-freedom per element, were used. For consolidation analyses, each 20-noded brick element was supplemented with an additional 8 degrees-of-freedom for excess pore water pressure. The total number of elements used was 48. The total number of degrees-of-freedom, N_d, was 1005 for drained and undrained analyses, and 1105 for consolidation analyses. This problem was selected, as it is large enough to enable the convergence characteristics to be determined and yet small enough for the spectral properties of the global matrix to be evaluated.

Tables 3.2 to 3.4 show the combination of soil properties used in each of the analyses in this study. As can be seen, the properties that were varied are the following:

- The effective Young's moduli E_1' and E_2' of the upper and lower soil layers, respectively, for all analyses. The subscripts 1 and 2 denote the upper and lower soil layers, respectively.

- The ratio of the bulk modulus of water k_w to that of the soil skeleton k_s', for undrained analyses. For analyses in which the E_1' and E_2' are different, the bulk moduli of water k_w was varied so that the $\frac{k_{w1}}{k_{s1}'} = \frac{k_{w2}}{k_{s2}'}$, in which k_{s1}' and k_{s2}' are the effective bulk moduli of the upper and lower soil layers, respectively.

- The coefficients of permeability k_1 and k_2 of the upper and lower soil layers, respectively, for consolidation analyses.

3.4.3 Convergence Characteristics

Several parameters have been used to track the convergence behaviour of iterates, and Arioli et al. (2000) has shown that the observed convergence behaviour depends in part on which parameter is used to track convergence. For this reason, the effect of convergence parameter on perceived convergence behaviour is first examined, as a precursor to an examination of convergence characteristics. One possible parameter is the relative energy error norm $R_E^{(n)}$ e.g. Mitchell (1998), Shewchuk (1994), Arioli et al. (2000), Johnson (1987), defined as

$$R_E^{(n)} = \frac{\left\langle \left(x - x^{(n)}\right), A\left(x - x^{(n)}\right) \right\rangle^{1/2}}{\left\langle \left(x - x^{(0)}\right), A\left(x - x^{(0)}\right) \right\rangle^{1/2}} \tag{3.13}$$

where $\langle \cdot, \cdot \rangle$ denotes the inner product, x is the exact solution vector, $x^{(n)}$ is the approximate solution vector after n iterations and $x^{(0)}$ is the initial guess.It can be shown that e.g. Mitchell et al. (1998), Johnson (1987)

$$R_E^{(n)} \leq 2\left(\frac{\sqrt{\kappa(A)}-1}{\sqrt{\kappa(A)}+1}\right)^n \tag{3.13}$$

where $\kappa(A)$ is the condition number of the matrix A and is given by e.g. MATLAB (1999)

$$\kappa(A)=\|A\|_2\|A^{-1}\|_2=\frac{\sigma_{max}}{\sigma_{min}} \tag{3.14}$$

where $\|\cdot\|_2$ denotes the matrix 2-norm and $\sigma_{\max}$, $\sigma_{\min}$ are the maximum and minimum singular values. If A is symmetric and positive definite, then the computed $\kappa(A)$ is equivalent to

$$\kappa(A)=\frac{\lambda_{\max}}{\lambda_{\min}} \tag{3.15}$$

where λ_{max} and λ_{min} refers to the maximum and minimum eigenvalues respectively e.g. Anderson et al. (1995).

In this study, $\kappa(A)$ is evaluated by firstly assembling A and then exporting the latter into MATLAB (1999) for condition number computation. To compute $\kappa(A)$ for the preconditioned matrix, preconditioning is applied globally to A. The preconditioned global matrix A^* is then exported to MATLAB. The EPCG algorithm implies a left-and-right preconditioning (Shewchuk, 1994), that is, if M is a diagonal matrix with diagonal entries equal to the corresponding diagonal entries in A, then M^{-1} is the Jacobi preconditioner of A, and A^* for EPCG is given by

$$A_{PCG}^* = E^{-1}AE^{-\mathrm{T}} \tag{3.16}$$

where $EE^{\mathrm{T}} = M$. In the EQMR algorithm, right preconditioning was used as it does not modify the residual vector, $b - Ax$ (Freund et al. ,1994). This implies that

$$A^{*}_{QMR} = AM^{-1} \tag{3.17}$$

The condition number of the preconditioned matrix for both EPCG and EQMR will just be denoted by $\kappa(A^{*})$ hereafter. The parameter $R_E^{(n)}$ is assured to decrease monotonically with iterations. The rate of convergence is also lower-bounded by Equation (4.3). It is, however, impractical to use because the solution x is not known a priori. In this study, $R_E^{(n)}$ is determined post-analysis based on exact solutions evaluated using a frontal solver, to serve as the "theoretical" benchmark for comparison with practical and alternative convergence parameters.

One commonly used practical parameter e.g. Wang (1996), Smith (1997) is the relative "improvement" norm $R_i^{(n)}$, defined as

$$R_i^{(n)} = \frac{\overset{max}{\scriptstyle j}\left|x_j^{(n+1)} - x_j^{(n)}\right|}{\overset{max}{\scriptstyle j}\left|x_j^{(n)}\right|} \tag{3.18}$$

where $\overset{max}{\scriptstyle j}\left|\cdot\right|$ denotes the maximum absolute value term over index-j. Another parameter routinely used in numerical analysis e.g. Arioli et al. (2000), Johnson (1987) is the relative residual norm $R_r^{(n)}$, defined by

$$R_r^{(n)} = \frac{\left\|b - Ax^{(n)}\right\|}{\left\|b - Ax^{(0)}\right\|} \tag{3.19}$$

If x is the displacement vector, then $R_r^{(n)}$ is, in effect, a relative measure of the out-of - balance force remaining after n iterations.

Figures 3.7 to 3.11 show the variations of these convergence parameters, for A^*, against the number of iterations, n. In these figures, n has been normalised by N_d since the latter is also theoretically the maximum number of iterations required for convergence. The computations were made in double precision. The number of iterations is quite sensitive to the precision of variables used in computation. However, the trend in iteration numbers across different cases remains essentially the same when higher precision was used.

As expected, $R_E^{(n)}$ decreases monotonically with iterations. This is similar to the results of Arioli et al. (2000). However, comparison of DR6, UD4 and CONSO3 shows that the rate of convergence is not uniquely related to $\kappa(A^*)$. The practical norms mirror the trends of $R_E^{(n)}$ quite closely, with the exception of ill-conditioned cases such as UD4 and CONSO3. For CONSO3, $R_i^{(n)}$ resulted in pre-mature termination after oscillating below $R_E^{(n)}$. $R_r^{(n)}$ undergoes even larger oscillations in UD4 but the key difference is that the oscillations are above $R_E^{(n)}$. Hence, it at most prolongs the iterations unnecessarily, which is more acceptable than pre-mature termination. For this reason, $R_r^{(n)}$ is used for the rest of this study as the convergence criterion.

In this study, the number of iterations needed to achieve “convergence”, N_c, is taken to be the number of iterations needed for $R_r^{(n)}$ to fall below 1×10^{-6}. Although N_c

depends on the norm used in the convergence criterion, Figures 3.7 to 3.11 indicate that the choice of $R_r^{(n)}$ to determine N_c is reliable for most cases. For an extreme case such as UD4, N_c is only about 10% to 20% higher than that required by the "theoretical" norm. Figure 3.12 shows the variation of N_c/N_d versus $\kappa(A^*)$ for all the cases studied. As can be seen, although N_c/N_d, increases with the condition number, the rates of increase for drained, undrained and consolidation analyses are distinctly different.

For the drained cases, N_c/N_d increases gradually from about 10% to about 30% for the drained cases analysed. Both the EPCG and EQMR algorithms require roughly the same number of iterations for the same condition number. However, each EQMR iteration involves slightly more operations than each EPCG iteration; hence, EPCG appears to be faster for this class of problems. For the undrained problems, the points are banded differently from those of the drained cases, with N_c/N_d increasing much more rapidly with $\kappa(A^*)$ than the drained problems. For consolidation problems, the points fall largely into a third band between that of the drained and undrained analyses, Figure 3.12b. Although using $R_r^{(n)}$ slightly over-estimates N_c for undrained and consolidation problems, it is insufficient to account for the differences in Figure 3.12. The above results may be explained by the fact that the convergence characteristic of the PCG algorithm, and perhaps that of the QMR algorithm, depend not only on λ_{max} and λ_{min}, but also on the spread of the eigenvalues [e.g. Shewchuk (1994), Meurant (1999)], with tightly clustered eigenvalues enabling faster convergence than widely scattered eigenvalues. In view of this, it is plausible that the different performance of the Jacobi preconditioner on drained, undrained and consolidation problems may be explained in terms of its effect on the eigenvalue distribution for these problems. This aspect will be examined in the next section.

3.5 Spectral Analysis

3.5.1 Effect of boundary conditions

Figure 3.13a shows the cumulative eigenvalue distribution of drained cases DR1 and DR6 before preconditioning. In each case, there is a cluster of eigenvalues concentrated at 10^{10}; furthermore, the sizes of the clusters are the same in both cases. These large eigenvalues can be attributed to the applied fixities. In CRISP, fixed boundary conditions are applied by adding a large penalty number to the diagonal entry of the global matrix A, corresponding to the fixed degree-of-freedom (Britto & Gunn, 1987). As proven in Appendix A, if a matrix has a very large diagonal term, it will also have a corresponding eigenvalue with a value nearly equal to this diagonal term.

In order to examine the effect of Jacobi preconditioning on the large eigenvalues corresponding to the fixed degrees-of-freedom, the preconditioner was applied in two steps. In the first step, only fixed degrees-of-freedom were preconditioned using the Jacobi approach. This "partial Jacobi" preconditioning reduces the large diagonal terms of these degrees-of-freedom to unity. The remaining degrees-of-freedom were then preconditioned in a second step. By so doing, the eigenvalue distribution can be determined after each step.

As shown in Figure 3.13a, after "partial Jacobi" preconditioning, the cluster of very high eigenvalues at $\sim 10^{10}$ transforms into a cluster with eigenvalue of ~ 1, whereas the other eigenvalues remain unaffected. As shown in Appendix A, if the entire row and column of a fixed degree-of-freedom is scaled, as is done for symmetric Jacobi preconditioning, the dominance of the diagonal term is unaffected and the eigenvalue is also scaled by the same factor. Furthermore, the eigenvector associated with such an eigenvalue is highly localised to the "fixed" degrees-of-freedom, with very little participation from the other degrees-of-freedom. In summary, the effect of the Jacobi preconditioner on the fixed degrees-of-freedom is the same regardless of the nature of the problem analysed. The ability to transform fixity-induced high eigenvalues to 1 translates into a reduction in iteration number for all three classes of problems under partial preconditioning, as shown in Table 3.5.

As shown in Table 3.5, the effect of Jacobi preconditioning on the "free" degrees-of-freedom is dependent on the type of problem analysed. Case DR6 converges rapidly when its "free" degrees-of-freedom are scaled. UD4 is very resistant to improvement, while standard application of Jacobi preconditioning is counter-productive for CONSO3. The reasons underlying these behaviours are investigated next.

3.6 Drained problems

As shown in Figure 3.13a, the eigenvalues corresponding to the "free" degrees-of-freedom exhibit a spread that depends on the problem. For a well-conditioned problem (e.g. DR1) the spread is relatively small while for an ill-conditioned problem (e.g. DR6) the spread is relatively large. Furthermore, as shown in Figure 3.13b, increasing E_1' increases the higher eigenvalues more than the lower eigenvalues. On the other hand, decreasing E_1', as in DR7, leads to a larger decrease in the lower eigenvalues. This suggests that the eigenvalue spread in the four drained cases examined may be due to differences in stiffness of the two material zones. However, this is by no means conclusive since eigenvalue distribution does not imply a one-to-one correlation of eigenvalues (and eigenvectors) of the different cases.

The difference between a well-conditioned problem (e.g. DR1) and an ill-conditioned problem (e.g. DR6) is also reflected in the structure of the global stiffness matrix. Figures 3.14a and 3.14b show two blocks marked I and II, which contain the stiffness coefficients of some "free" degrees-of-freedom from within material zones I and II, respectively, of the global matrix A for DR1 and DR6. As shown in Figure 3.14a, for DR1, the magnitude of the terms in both blocks are similar. On the other hand, as shown in Figure 3.14b, for DR6, the magnitude of the terms in portion I are generally larger than those in portion II by approximately the order of the ratio E_1'/E_2', as expected. This suggests that the larger spread of the eigenvalues in DR6, compared to DR1, is related to the large difference in moduli of the two material zones. This hypothesis can be easily tested by preconditioning the global stiffness matrix of DR6 by a diagonal preconditioner M^{-1^*} such that

$$m_{ii}^{-1*} = E_2'/E_1' \tag{3.20}$$

for all "free" degrees-of-freedom that are at or within material zone I, and

$$m_{ii}^{*} = 1 \tag{3.21}$$

for all other "free" degrees-of-freedom. This has the effect of scaling down the magnitude of the terms in block I to the magnitude of those in block “II”. As shown in Figure 3.15, the spread of the "free" eigenvalues is now much closer to that of DR1, thereby verifying the hypothesis. Thus, increasing E_I' has the effect of raising the higher eigenvalues (with smaller increase to the lower eigenvalues) through an increase in the magnitude of a block of terms in the global stiffness matrix. The above observation suggests that the higher eigenvalues have a higher participation from the "free" degrees-of-freedom within the stiffer material zone than the lower eigenvalues. That this is indeed so is shown in Figures 3.16 and 3.17, which present selected eigenvectors from DR6 and DR12.

As shown in Figure 3.18, preconditioning has the effects of centering the cluster closer to unity and compressing the distribution. The latter allows Krylov subspace algorithms to converge with less iterations. Furthermore, after preconditioning, the difference between the eigenvalue distributions of cases DR1 and DR6 is substantially reduced; the residual difference in $\kappa(A^*)$ between the two cases being due largely to differences in the last few eigenvalues at the low end of the distribution. As shown in Table 3.2, the relatively small difference in N_c between DR1 and DR6 does not reflect the large difference in $\kappa(A^*)$ between them, and indicates that the few outlying eigenvalues at the lower end of the distribution does not significantly increase N_c. This supports the notion that the eigenvalue distribution has a significant influence on N_c. Since $\kappa(A^*)$ only takes into account λ_{max} and λ_{min}, it is unable to fully represent this distribution. This would explain why different cases with very similar values of $\kappa(A^*)$ can have very different N_c values.

The effect of the Jacobi preconditioner is also reflected on the structure of the global matrix A^* as well as the eigenvector set. Comparison of Figures 3.19 and 3.14b shows the magnitudes of the terms in blocks I and II are not only reduced but the magnitude of terms in block I now has a similar order as those in block II. This is not surprising, since the Jacobi preconditioner normalises the coefficients of each degree-of-freedom with respect to the diagonal term, and thereby eliminates the large differences between the magnitudes of the terms in the two blocks. In other words, the preconditioned matrix A^* resembles one with a uniform, and much lower, modulus. This explains why the eigenvalue distributions of DR1 and DR6 after Jacobi preconditioning are similar.

It should be mentioned that the eigenvalues and eigenvectors of a problem depends, not only upon the differences in material stiffness, but also the boundary conditions and geometry; the fact that the eigenvalue distributions of DR6 and DR12 are different is evidence of this. This study involves only one geometry and boundary condition set, and ill-condition was introduced by large differences in moduli. Other causes of ill-conditioning may well exist to which the above discussion cannot be applied. Furthermore, only selected portions of the global stiffness matrix and eigenvectors are examined. Thus, the influence of other factors cannot be entirely precluded. Nonetheless, the parameters examined consistently suggests that large differences in material stiffness is indeed the cause of the observed ill-conditioning in the problems studied and may often be a cause of ill-conditioning in other problems with different material zones having large differences in moduli. In such cases, Jacobi preconditioning accelerates convergence by transforming the matrix approximately to one of a uniform material and thereby compressing the eigenvalue spread.

3.7 Undrained problems

In CRISP, finite element equations for undrained problems are generated by adding the stiffness of the pore water phase to that of the soil skeleton (Britto & Gunn, 1987).

The stiffness of the pore water phase is proportional to the bulk modulus of water k_w, thus the global stiffness matrix A becomes

$$A = K_s' + k_w K_1 \tag{3.22}$$

in which K_s' represents the stiffness matrix of the soil skeleton, K_1 represents the constraints arising from incompressibility and k_w is effectively a large "penalty number" (Zienkiewicz, 1999). The same result is obtainable by setting Poisson's ratio, ν, close to 0.5. For a uniform soil skeleton with given effective Poisson's ratio ν', the stiffness of the soil skeleton is directly proportional to the effective bulk modulus k_s', so that Equation (3.22) can be expressed as

$$A = k_s' K_2 + k_w K_1 \tag{3.23}$$

Table 3.3 shows the parameters of the undrained analyses conducted. Case UD4 will be examined in greater detail since $\kappa(A^*)$ for UD4 and DR6 are approximately equal. As shown in Figure 3.20a, the magnitude of the terms in blocks I and II for UD4 does not differ greatly, in contrast to DR6. This is due to the fact that there is only one material zone in UD4, and suggests that the causes of ill-conditioning in the two cases are different.

Table 3.3 shows that, for a given combination of E_1' and E_2', the condition number increases as the ratio k_w/k_s' increases. Furthermore, comparison of the unconditioned eigenvalue distributions of UD1, UD3 and UD4 in Figure 3.21 shows that if k_w is increased while k_s' is kept constant, the lower end of the eigenvalue distribution is not altered but the higher eigenvalues are right-shifted, thereby increasing the spread of the distribution and thus $\kappa(A)$. On the other hand, comparison of the unconditioned eigenvalue distribution of UD4 and UD5 shows that increasing k_s' while keeping the ratio k_w/k_s' constant right-shifts the entire eigenvalue spectrum without affecting the eigenvalue spread. This suggests that ill-conditioning in these few problems is caused by large k_w/k_s' ratio. Figure 3.22 shows selected eigenvectors from the unconditioned stiffness matrix of UD4. As can be seen, convective shear flow patterns are evident in the eigenvectors corresponding to the low eigenvalues. On the other hand, the eigenvectors corresponding to the higher eigenvalues show little evidence of any shear flow pattern; instead the deformation mode appears to be characterized by zones of dilatation and compression. The total bulk modulus of the soil increases as k_s' and/or k_w increases, whereas the shear modulus only increases with k_s'. Thus, if k_w is increased while k_s' is kept constant, the consequent increase in the total bulk modulus of the soil raises the high-end eigenvalues corresponding to compression/dilatation modes. However, as the shear modulus G does not change, low-end eigenvalues corresponding to shear modes are largely unaffected. In short, this type of ill-conditioning arises because the separation between compression-dominated eigenvalues and shear-dominated eigenvalues is increased when k_w/k_s' is increased.

Figure 3.21 also shows the cumulative distribution of the eigenvalues of UD1, UD3 and UD4 after preconditioning, with the "fixed" eigenvalues removed for clearer comparison of the "free" eigenvalues. In contrast to the drained problems, the spread of the eigenvalues in the undrained problem is not significantly reduced by preconditioning, although there is a similar shift in the eigenvalue distribution towards unity. Furthermore, after preconditioning, the spread of the eigenvalues in UD4 is evidently much larger than that of DR6, even though $\kappa(A^*)$ for the two cases are similar. Thus, the different convergence behaviour of the two problems having similar $\kappa(A^*)$ can be explained by the difference in spectral distribution.

Comparison of Figures 3.20a and 3.20b shows that the main effect of Jacobi preconditioning is to scale down all the terms in the two blocks by roughly the same order of magnitude. In other words, the effect of Jacobi preconditioning is approximately akin to pre-multiplying the matrix A by a scalar. This effect is similar to that which can be achieved by reducing the Young's modulus of the material while keeping its Poisson's ratio constant. This accounts for the almost rigid-body translation of the eigenvalue distribution, with relatively little change to the shape. Furthermore, as shown in Figure 3.23, shear flow and compression/dilatation modes still dominate the low and high eigenvalues, respectively. In other words, Jacobi preconditioning has a much less significant effect on the eigenvalue distribution and eigenmodes of UD4 than it has in the case of DR6. By reducing the Young's modulus while keeping the Poisson's ratio constant, Jacobi preconditioning does not alter the ratio of shear modulus to bulk modulus. Thus, although preconditioning causes the high eigenvalues to be lowered by a decrease in bulk modulus, the low eigenvalues associated with the shear flow modes are similarly decreased by the reduction in shear modulus, and the resulting eigenvalue spread is not significantly reduced.

3.8 Consolidation Problems

In CRISP, the consolidation problem is solved using Biot's consolidation equation (Biot, 1941), which leads to Equation (3.1), with

$$A = \begin{bmatrix} S' & L \\ L^{\mathrm{T}} & -C \end{bmatrix} \in \Re^{ndf \times ndf}$$

where $S' = S'^{\mathrm{T}} \in \Re^{mdf \times mdf}$, $L \in \Re^{mdf \times (mdf - ndf)}$, $C = C^{\mathrm{T}} \in \Re^{(ndf-mdf)\times(ndf-mdf)}$ (3.24)

$$x = \begin{bmatrix} \Delta u \\ \Delta p \end{bmatrix} \in \Re^{ndf} \qquad \Delta u \in \Re^{mdf}, \Delta p \in \Re^{(ndf-mdf)} \tag{3.25}$$

and $b = \begin{bmatrix} \Delta f \\ Cp_t \end{bmatrix} \in \Re^{ndf} \qquad \Delta f \in \Re^{mdf}, p_t \in \Re^{(ndf-mdf)}$ (3.26)

In Equation (3.24), S' is the effective stiffness matrix, L is the link matrix and C is the flow matrix, respectively. A is symmetric but indefinite, with *mdf* positive eigenvalues and (*ndf-mdf)* negative eigenvalues. In Equation (3.25), Δu denotes the displacement increments whilst Δp denotes the excess pore pressure increments. In Equation (3.26), Δf denotes the nodal load increments and p_t denotes the excess pore pressure at the current time step.

Table 3.4 shows the consolidation problems studied and their parameters. Since the unconditioned global matrix A is symmetric but indefinite, the eigenvalues are real, but not necessarily positive, quantities. On the other hand, the right-preconditioned matrix A^*_{QMR} is unsymmetrical and its eigenvalues are complex quantities. To enable direct comparison with drained and undrained problems, the cumulative distribution of the moduli of the eigenvalues for the unconditioned and preconditioned matrices is shown in Figure 3.24. As can be seen, $\kappa(A)$ increases as the permeability of the soil decreases and as the effective Young's modulus increases. Comparison of CONSO1 and CONSO3 as well as CONSO4 and CONSO6 also shows that a change in the permeability has the largest effect on the low end of the eigenvalue distribution, while the high end of the distribution is hardly affected.

Table 3.6 shows the maximum displacement and pore pressure magnitudes, $|u|_{max}$ and $|p|_{max}$, of selected eigenvectors for CONSO3 before preconditioning. The magnitudes of the displacement and excess pore pressure components have been scaled so that the L_2-norm of the eigenvector is unity. As can be seen, the ratio $|u|_{max}/|p|_{max}$ for the three lowest eigenvalues is well below unity, signifying relatively strong pore pressure participation. In contrast, the three highest eigenvalues have relatively strong displacement participation. This is consistent with the effect of permeability seen in Figure 3.24, and suggests that, in the unconditioned matrix, the lowest and highest eigenvalues are closely linked to excess pore pressure and displacement degrees-of-freedom, respectively.

Figure 3.25 shows the matrix structures of *A* for CONSO3. In this figure, block I relates to the pore pressure degrees-of-freedom whereas block II relates to the displacement degrees-of-freedom. As can be seen, the terms in block I are much smaller in magnitude than those in block II. This is consistent with the expressions of *S'* and *C* (Britto & Gunn, 1987), which also imply that the magnitudes of the terms in blocks I and II vary directly with the permeability and effective Young's modulus, respectively. Thus, a problem with low permeability and high stiffness will see large differences between the magnitudes of the terms in the two blocks. This matrix structure is similar to that of DR6; and suggests that eigenvalues with strong participation from pore pressure degrees-of-freedom are likely to be low whereas those with strong participation from displacement degrees-of-freedom are likely to be high. As shown in Table 3.6, this is indeed the case.

As shown in Figure 3.24, preconditioning of CONSO3 produces a compressed lower end that is similar to CONSO1 but the upper end is now over-scaled. The fact that the two cases have the same effective Young's modulus and different permeability suggests that the over-scaled top-end eigenvalues are closely related to excess pore pressure degrees-of-freedom, while the compressed bottom-end eigenvalues are closely related to displacement degrees-of-freedom. This is supported by Table 3.7, which shows that the ratio $|u|_{max}/|p|_{max}$ for the three lowest eigenvalues is now much greater than the corresponding ratio of the three highest eigenvalues.

This notion is also supported by the eigenvalue distribution in CONSO9, in which about 1/3 of the domain has high permeability and the other 2/3 has a very low permeability of 10^{-12} m/s. As Figure 3.26 shows, the number of eigenvalues within over-scaled top band of CONSO9 is roughly 2/3 of that for CONSO3. However, the over-scale factor is now higher than that of CONSO3 owing to the lower permeability of the nearly impermeable zone. In other words, Jacobi preconditioning tends to over-scale the excess-pore-pressure-dominated eigenvalues in a consolidation problem where ill-conditioning arises as a result of the low permeability of the domain. Since over-scaling expands the eigenvalue distribution, it also retards the convergence process. This problem has been noted by Chan et al. (2001), who attributed the ill-conditioning induced with low permeability to the large magnitude of the terms in the upper link matrix *L*, relative to those in the stiffness sub-matrix *S'*, after preconditioning. However, Chan et al.'s (2001) explanation fails to explain why

CONSO6 does not suffer from over-scaling. In this respect, Chan et al.'s (2001) framework only offers a partial explanation, which applies to problems involving low permeability and low stiffness. The use of eigenvalue distribution offers a more general framework for assessing convergence characteristics.

3.9 Application

The findings above suggest new possibilities for fine-tuning of the diagonal preconditioner. For example, Chan et al. (2001) suggested a modified Jacobi preconditioner, which scales down the terms in the columns corresponding to the pore pressure degrees-of-freedom by comparing the diagonal and off-diagonal terms in the element stiffness matrix. The discussion above indicates that a rationale to the modified Jacobi preconditioner can also be found in terms of its effect on the eigenvalue distribution. Figure 3.27 shows an eigenvalue distribution which was achieved by under-scaling the excess pore pressure degrees-of-freedom of CONSO3 100000 times, that is by applying under-scaled preconditioning factors m_{pij}^{-1} such that

$$m_{pij}^{-1} = \frac{1}{100000} m_{ij}^{-1}$$

$$\text{for i = j = an excess pore pressure degree - of - freedom number} \qquad (3.27)$$

As Figure 3.27 and Table 3.8 show, the amount of over-scaling and N_c are both markedly reduced. Alternatively, the displacement degrees-of-freedom may also be over-scaled so as to achieve an increase in their magnitudes, thereby right-shifting the displacement-dominated eigenvalues (Figure 3.27). Physically, it is equivalent to raising the effective stiffness of the soil skeleton by a uniform factor and is consistent with the fact that a problem involving a stiff soil skeleton with low permeability, such as CONSO6, shows no over-scaling. As shown in Table 3.8, N_c is again markedly reduced. The effectiveness of simple scaling techniques such as these suggests that an undrained problem may be more efficiently solved, using Krylov-subspace iterative methods, as a nearly-impermeable consolidation problem than as a nearly-incompressible problem.

3.10 Performance of EPCG and EQMR Solver in Larger Problems

In this section, a series of benchmark tests were conducted to assess the performance of the EBE-PCG (EPCG) and EBE-QMR (EQMR) algorithms on large finite element domains. Figure 3.28 and Figure 3.29 show the finite element mesh of a single lined-tunnel and a twin lined tunnel mesh respectively. As can be seen, both these problems involve considerably more elements and degrees-of-freedom than the problems discussed earlier.

3.10.1 Test Conditions

The sample problem size ranges from 3120 to 9920 3-D-elements. Each element has 68 degrees-of-freedom for consolidation analysis and 60 degrees-of-freedom for drained and undrained analysis. In the first mesh (see Figure 3.28), a symmetrical half block of soil is used to simulate a single tunnel construction while in the second mesh (see Figure 3.29), a full block of soil is used to simulate the staggered lined tunnel construction. For both meshes, the side boundaries are laterally restrained (i.e. on rollers) and the base of the mesh is fixed. For finite element analysis of consolidation domain which has pore-pressure boundary, all lateral and top-sides (i.e. ground level) are assumed to be free-draining with hydrostatic conditions except for the axis of symmetry in the single tunnel problem, which is impermeable. The physical properties and the test configurations of the two meshes are tabulated in Table 3.9.

The simulation of the tunnelling process is carried out by removing the tunnel's soil element at a single step and in the next step; followed by an installation of concrete lining. This is equivalent to the simulation of tunnelling in 2-D analyses, and is done only for this problem as the objective here is to assess the ability of EPCG/EQMR for solving large finite element domains. In the single tunnel mesh, the excavation of soil and installation of lining is done completely in the Z-direction of the mesh. As for the twin tunnel mesh, the simulation exercise was carried out only for the first tunnel through the mesh in Z-direction. The soil is to be a Mohr Coulomb model with the soil parameters shown in Table 3.10 while the lining properties are reflected in Table 3.11. The water table is assumed to be located 10 m below ground level.

3.10.2 Results of Benchmark Tests

The test results were summarised and shown in Figure 3.30. As can be seen, the frontal solver is faster for the undrained and low permeability consolidation problems of the single tunnel mesh. In all other cases, EPCG or EQMR is faster. Owing to limitation of memory, the Frontal method is able to solve in-core only for the single tunnel mesh which has 3120 elements. The frontal solution timings for the twin tunnel mesh of 9960 elements were estimated based on the method recommended by Britto and Gunn (1990). They suggested the timing for the frontal solver could be reasonably computed by multiplying a timing factor with the product of the square of the maximum frontwidth and the total degrees of freedom. Using the direct method (i.e.

Frontal method) of solving single tunnel mesh, the timing factor was determined with a constant of 9.48E-09 second per entry.

The average timing using various solvers is shown in Figure 3.31. As noted, the relative efficiency of EPCG and EQMR is dependent on mesh size and the type of domain analysis (i.e. Drained, Undrained or Consolidation). Larger 3-D problems such as the twin tunnel mesh, EPCG or EQMR is more efficient compared to the frontal solver. For each problem size, the Drained (D) cases will always outperform the Consolidation (C) followed by the Undrained (UD) cases. In the analysis, UD cases are the slowest to converge and to reach the ideal solutions. This is the same trend as observed in the smaller problem studied earlier.

Traditionally, large 3-D finite element problems are analysed using the supercomputers which may not be readily available to many practicing engineers. This investigation shows that, if the EPCG and the EQMR algorithms can be implemented within an FE code, relatively large 3-D problems can be realistically solved on a desktop PC, which is widely available and may look attractive enough for the practicing industry to have a second look. The discussion above shows that, for drained and consolidation problems, the speedup in turnround time achievable by using an iterative solver can be quite significant.

For the undrained (UD) problems, the processing timings are much longer. This is similar to Wang's (1990) observation when he modelled the finite element domain with a poisson's ratio $\upsilon = 0.4999$. However, as noted earlier, the undrained problem can also be solved faster by treating it as a nearly impermeable problem rather than a nearly incompressible problem.

3.11 Summary

The foregoing discussion shows that the trend and rate of convergence are dependent not only on the condition number but also on the type of analysis. The convergence behaviour of drained problems afflicted by “material ill-conditioning” arising from large stiffness ratios between the different material zones is readily improved by Jacobi preconditioning. This is explainable by the fact that the stiff and soft material zones occupy different spatial sub-domain and are thereby linked to different degrees-of-freedom. By normalising the stiffness coefficients for the degrees-of-freedom by their respective diagonal entries, Jacobi preconditioning, in effect, homogenises the various sub-domains.

For undrained problems modelled using a nearly incompressible pore fluid, Jacobi preconditioning appears to be much less effective. The number of iterations needed is far higher than the drained problems, even though the condition number, after preconditioning, may be similar. This is because the material ill-conditioning of an undrained problem arises from the large stiffness ratios between compression/dilatation and shear flow eigenmodes. Jacobi preconditioning changes the eigenvalues for these modes by approximately the same ratio, thus causing little or no compression to the eigenvalue distribution.

For consolidation problems, some eigenvalues are displacement dominated whereas others are excess pore pressure dominated. The Jacobi preconditioner compresses the displacement-dominated eigenvalues in a similar manner to the drained cases. However, the pore pressure eigenvalues appear to be over-scaled.

A series of large geotechnical finite element domains were tested and overall for 3-D problems involving large degrees-of-freedom and elements, the EPCG/EQMR solver developed offers simplicity in terms of timing and resources over the Frontal method.

Table 3.1 Computational cost for solving indefinite matrix system

	Matrix-Vector	Scalar Product	SAXPY	Storage vectors
MINRES	1	2	7	6
SYMMLQ	1	2	7	5
QMR	1	2	8	16

* SAXPY computes a constant times a vector plus a vector (LINPACK, 1984)

Table 3.2 Physical properties for drained cases

Case number	Material properties			PCG		QMR	
	$E_1^{\prime}$ (MPa)	$E_2^{\prime}$ (MPa)	$E_1^{\prime}/E_2^{\prime}$	$\kappa(A^*)$	N_c	$\kappa(A^*)$	N_c
DR1	10	10	1	4.445E+02	104	5.618E+02	101
DR2	100	10	10	2.385E+03	150	3.583E+03	145
DR3	300	10	30	6.606E+03	163	1.053E+04	159
DR4	1000	10	100	2.123E+04	173	3.494E+04	168
DR5	3000	10	300	6.290E+04	179	1.047E+05	174
DR6	10000	10	1000	2.087E+05	186	3.492E+05	181
DR7	1	10	0.1	2.600E+02	94	3.967E+02	90
DR8	10	100	0.1	2.600E+02	94	3.967E+02	90
DR9	10	300	0.0333333	2.480E+02	95	3.941E+02	89
DR10	10	1000	0.01	2.438E+02	95	3.938E+02	89
DR11	10	3000	0.0033333	2.426E+02	92	3.938E+02	89
DR12	10	10000	0.001	2.422E+02	92	3.938E+02	89
DR13	100000	10	10000	2.083E+06	196	3.493E+06	192
DR14	1.00E+06	10	100000	2.083E+07	209	3.493E+07	206
DR15	1.00E+07	10	1000000	2.083E+08	218	3.493E+08	217

Table 3.3 Physical properties for undrained cases

Case number	Material properties				PCG		QMR	
	$E_1^{\prime}$ (MPa)	$E_2^{\prime}$ (MPa)	$E_1^{\prime}/E_2^{\prime}$	$k_w/k_s^{\prime}$	$\kappa(A^*)$	N_c	$\kappa(A^*)$	N_c
UD1	10	10	1	1	4.161E+02	121	5.488E+02	116
UD2	10	10	1	10	1.244E+03	262	2.108E+03	251
UD3	10	10	1	100	1.089E+04	770	2.247E+04	773
UD4	10	10	1	1000	1.042E+05	1527	2.400E+05	1459
UD5	100	100	1	1000	1.042E+05	1635	2.400E+05	1617
UD6	1000	10	100	100	1.620E+05	1027	3.677E+05	1035
UD7	10000	10	1000	100	2.270E+05	1253	5.164E+05	1227
UD8	100	10	10	1000	5.243E+05	2502	1.166E+06	2136
UD9	1000	10	100	1000	1.473E+06	2554	3.502E+06	2504
UD10	10000	10	1000	1000	2.004E+06	2791	4.767E+06	2589
UD11	10	100	0.1	100	7.878E+03	557	2.396E+04	558
UD12	10	1000	0.01	100	8.124E+03	523	2.679E+04	502
UD13	10	10000	0.001	100	8.152E+03	733	2.715E+04	589
UD14	10	100	0.1	1000	7.263E+04	1175	2.586E+05	1171
UD15	10	1000	0.01	1000	7.479E+04	1304	2.905E+05	1262
UD16	10	10000	0.001	1000	7.506E+04	1309	2.946E+05	1306

Table 3.4 Physical properties for consolidation cases

Case number	Material properties						QMR	
	$E_1^{\prime}$ (MPa)	$E_2^{\prime}$ (MPa)	$E_1^{\prime}/E_2^{\prime}$	k_1 (m/s)	k_2 (m/s)	Δt (sec)	$\kappa(A^*)$	N_c
CONSO1	10	10	1	1.157E-03	1.157E-03	1.	3.261E+03	130
CONSO2	10	10	1	1.157E-06	1.157E-06	1.	1.993E+07	1105
CONSO3	10	10	1	1.157E-09	1.157E-09	1.	2.193E+10	2781
CONSO4	1.0E+06	1.0E+06	1	1.157E-03	1.157E-03	1.	1.094E+05	102
CONSO5	1.0E+06	1.0E+06	1	1.157E-06	1.157E-06	1.	8.082E+10	103
CONSO6	1.0E+06	1.0E+06	1	1.157E-09	1.157E-09	1.	3.786E+14	250
CONSO7	10	10	1	1.157E-03	1.157E-06	1.	1.881E+07	1067
CONSO8	10	10	1	1.157E-03	1.157E-09	1.	2.060E+10	2636
CONSO9	10	10	1	1.157E-03	1.157E-12	1.	2.060E+13	5084
CONSO10	1.0E+06	1.0E+01	100000	1.157E-03	1.157E-06	1.	1.909E+11	2157
CONSO11	1.0E+06	1.0E+01	100000	1.157E-03	1.157E-09	1.	1.909E+14	5898
CONSO12	1.0E+06	1.0E+01	100000	1.157E-03	1.157E-12	1.	1.910E+17	11493

Table 3.5 Comparison of iterations for various types of matrices

Case number	Unconditioned (penalty number = 1×10^{17})	Preconditioned only fixed DOFs to 1	Preconditioned all DOFs to 1
DR6 (using EPCG)	3687	1668	186
UD4 (using EPCG)	4829	2398	1527
CONSO3 (using EQMR)	3579	1668	2781

Tolerance = 1×10^{-6}, DOFs = degrees-of-freedom

Table 3.6 Maximum magnitudes of nodal displacement and excess pore pressure for the unconditioned matrix in CONSO3

Order of eigenvalue	$\lvert\lambda\rvert$	Max. displacement magnitude $\lvert u\rvert_{max}$ (m)	Max. excess pore pressure magnitude $\lvert p\rvert_{max}$ (kPa)	$\frac{\lvert u\rvert_{max}}{\lvert p\rvert_{max}}$ (m/kPa)
Lowest	2.97×10^{-3}	5.29×10^{-2}	6.32×10^{-1}	8.36×10^{-2}
2nd lowest	7.52×10^{-3}	3.62×10^{-2}	5.95×10^{-1}	6.08×10^{-2}
3rd lowest	8.85×10^{-3}	2.74×10^{-2}	4.04×10^{-1}	2.74×10^{-2}
3rd highest	6.05×10^{2}	3.80×10^{-1}	8.64×10^{-3}	4.40×10^{1}
2nd highest	8.71×10^{2}	3.49×10^{-1}	3.27×10^{-3}	1.07×10^{2}
Highest	8.74×10^{2}	3.49×10^{-1}	4.24×10^{-3}	8.23×10^{1}

Table 3.7 Maximum magnitudes of nodal displacement and excess pore pressure for the preconditioned matrix in CONSO3

Order of eigenvalue	$\lvert\lambda\rvert$	Max. displacement magnitude $\lvert u\rvert_{max}$ (m)	Max. excess pore pressure magnitude $\lvert p\rvert_{max}$ (kPa)	$\frac{\lvert u\rvert_{max}}{\lvert p\rvert_{max}}$ (m/kPa)
Lowest	2.01×10^{-2}	1.50×10^{-1}	2.05×10^{-9}	7.32×10^{7}
2nd lowest	2.13×10^{-2}	3.48×10^{-1}	2.33×10^{-9}	1.49×10^{8}
3rd lowest	3.11×10^{-2}	2.39×10^{-1}	9.09×10^{-10}	2.63×10^{8}
3rd highest	1.65×10^{3}	2.31×10^{-1}	3.08×10^{-5}	7.50×10^{3}
2nd highest	1.94×10^{3}	1.98×10^{-1}	2.81×10^{-5}	7.03×10^{3}
Highest	1.97×10^{3}	1.92×10^{-1}	3.41×10^{-5}	5.64×10^{3}

Table 3.8 Condition number for CONSO3 corresponding to the Jacobi preconditioned, under-scaled and over-scaled matrix.

	N_c	$\kappa(A^*)$
Normal Jacobi Preconditioning	2781	2.19E+10
Jacobi Preconditioning with under-scaled excess pore pressure degree-of-freedom	291	2.19E+05
Jacobi Preconditioning with over-scaled displacement degree-of-freedom	297	2.19E+05

Table 3.9 Physical Properties of Different Meshes

	NEL	NDF (Drained/Undrained element)	NDF (Consolidation element)	MAX. Frontwidth (Drained/Undrained/ Consolidation
Single Tunnel	3120	40005/40005	43533	1650/1650/1916
Twin Tunnel	9920	115131	115131	7461/7461/8445

Table 3.10 Typical Soil Parameters (Mohr Coulomb constitutive soil model)

Types of Domain	E' (kN/m^3)	ν	c' (kN/m^3)	ϕ	γ_{unit} (kN/m^3)	k_x & k_y (m/s)	Time /increment (sec)
Undrained	27	0.3	5	30	20/10	NA	NA
Drained	27	0.3	5	30	20/10	NA	NA
Consolidation Case I	27	0.3	5	30	20/10	1.0E-3	1.73E4
Consolidation Case II	27	0.3	5	30	20/10	1.0E-9	0.2

Table 3.11 Typical Concrete Parameters (Isotropic Elastic model)

Concrete Properties	E' (kN/m^3)	ν	G (kN/m^3)	γ_{conc} (kN/m^3)	k_x & k_y (m/s)
Concrete in Drained/Undrained Case	28E3	0.25	11.2E3	24	NA
Concrete in Consolidation Case I	28E3	0.25	11.2E3	24	1.0E-3
Concrete in Consolidation Case II	28E3	0.25	11.2E3	24	1.0E-9

```
Compute $r^{(0)} = b - Ax^{(0)}$ for some initial guess $x^{(0)}$
$p^{(1)} = r^{(0)}$
For $i = 1, 2, \ldots$
        if $i = 1$
                $\rho_0 = r^{(0)T} r$
                $\rho_1 = \rho_0$
        else
                $\beta_{i-1} = \frac{\rho_{i-1}}{\rho_{i-2}}$
                $p^{(i)} = r^{(i-1)} + \beta_{i-1} p^{(i-1)}$
        endif
    $q^{(i)} = Ap^{(i)}$
    $\alpha_i = \frac{\rho_{i-1}}{p^{(i)T} q^{(i)}}$
    $x^{(i)} = x^{(i-1)} + \alpha_i p^{(i)}$
    $r^{(i)} = r^{(i-1)} - \alpha_i q^{(i)}$
    Check convergence, continue if necessary
end
```

Figure 3.1 Pseudocode for the CG (modified after Shewchuk,1994)

```
Compute $r^{(0)} = b - \sum_{e=1}^{nel} A_e x^{(0)}$ for some initial guess $x^{(0)}$
For $i = 1, 2, .......$
    $Mz^{(i-1)} = r^{(i-1)}$
    $\rho_{i-1} = r^{(i-1)} z^{(i-1)}$
        if $i = 1$
            $p^{(1)} = z^{(0)}$
        else
            $\beta_{i-1} = \rho_{i-1} / \rho_{i-2}$
            $p^{(i)} = z^{(i-1)} + \beta_{i-1} p^{(i-1)}$
        endif
    $q^{(i)} = \sum_{e=1}^{nel} A_e p^{(i)}$
    $\alpha_i = \rho_{i-1} / p^{(i)T} q^{(i)}$
    $x^{(i)} = x^{(i-1)} + \alpha_i p^{(i)}$
    $r^{(i)} = r^{(i-1)} - \alpha_i q^{(i)}$
    Check convergence; continue if necessary
end

NOTE : M is the preconditioner; nel is the total number of elements
```

Figure 3.2 Pseudocode for the EBE-PCG (modified after Barett et al.,1994)

```
Compute $\upsilon_1 = b - Ax^0$ for some initial guess $x^0$
$\beta_1 = \|\upsilon_1\|_2; \eta = \beta_1;$
$\gamma_1 = \gamma_0 = 1; \sigma_1 = \sigma_0 = 0;$
$\upsilon_0 = 0; \omega_{-1} = 0;$
for $i = 1,2,......$

The Lanczos recurrence :
    $\upsilon_i = \frac{1}{\beta_i}\upsilon_i; \alpha_i = \upsilon_i^T A\upsilon_i;$
    $\upsilon_{i+1} = A\upsilon_i - \alpha_i\upsilon_i - \beta_i\upsilon_{i-1}$
    $\beta_{i+1} = \|\upsilon_{1+1}\|_2$

QR part :
old Givens rotations on new column of T :
    $\delta = \gamma_i\alpha_i - \gamma_{i-1}\sigma_i\beta_i; \rho_1 = \sqrt{\delta^2 + \beta_{i+1}^2}$
    $\rho_2 = \sigma_i\alpha_i + \gamma_{i-1}\gamma_i\beta_i; \rho_3 = \sigma_{i-1}\beta_i$

New Givens rotations for subdiagonal element :
    $\gamma_{i+1} = \frac{\delta}{\rho_1}; \sigma_{i+1} = \frac{\beta_{i+1}}{\rho_1}$

Update of solution (with $W_i = V_i R_{i,i}^{-1}$ )
    $\omega_i = (\upsilon_i - \rho_3\omega_{i-2} - \rho_2\omega_{i-1}) / \rho_1$
    $x^i = x^{i-1} + \gamma_{i+1}\eta w_i$
    $\|r^i\|_2 = \|\sigma_{i+1}\|\|r^{i-1}\|_2$
    check convergence; continue if necessary
    $\eta = -\sigma_{i+1}\eta$
```

Figure 3.3 Pseudocode for MINRES (after Vorst, 2002)

```
$c_1 = -1; s_1 = 0; s_0 = 0; \varsigma_0 = -1; \varsigma_{-1} = -0;$
$\hat{x}^0 = x^0; \widetilde{\omega}^0 = 0; q^0 = 0; \widetilde{q} = b - Ax^0$ for some initial guess $x^0$;
$\beta_0 = \|\widetilde{q}\|_2; q^1 = \frac{\widetilde{q}}{\beta_0};$

for i = 1,2,....
    $\widetilde{q} = Aq^i - \beta_{i-1}q^{i-1};$
    $\alpha_i = \widetilde{q}^T q^i;$
    $\widetilde{q} = \widetilde{q} - \alpha_i q^i;$
    $\beta_i = \|\widetilde{q}\|_2;$
    $\widetilde{\gamma}_i = -c_i\alpha_i - c_{i-1}s_i\beta_{i-1}; \gamma_i = \sqrt{\widetilde{\gamma}_i^2 + \beta_i^2};$
    $\delta_{i-1} = s_i\alpha_i - c_i c_{i-1}\beta_{i-1}; \varepsilon_{i-2} = s_{i-1}\beta_{i-1};$
    $c_{i+1} = \frac{\widetilde{\gamma}_i}{\gamma_i}; s_{i+1} = \frac{\beta_i}{\gamma_i};$
    $\widetilde{\omega}^i = s_i\widetilde{\omega}^{i-1} - c_i q^i;$
    $\varsigma_i = \frac{-(\varepsilon_{i-2}\varsigma_{i-2} + \delta_{i-1}\varsigma_{i-1})}{\gamma_i};$
    $q^{i+1} = \frac{\widetilde{q}}{\beta_i}; \hat{x}^i = \hat{x}^i + \varsigma_i(c_{i+1}\widetilde{\omega}^i + s_{k+1}q^{i+1});$
    $x^{i+1} = \hat{x}^i + \frac{\varsigma_i\widetilde{\omega}^i}{c_{i+1}}$
    check convergence, continue if necessary.
```

Figure 3.4 Pseudocode for SYMMLQ (after Vorst, 2002)

```
Compute $r^{(0)} = b - \sum_{e=1}^{nel} A_e x^{(0)}$ for some initial guess $x^{(0)}$
$M = M_1 M_2$; $\tilde{\upsilon}^{(1)} = r^{(0)}$; Solve $M_1 y = \tilde{\upsilon}^{(1)}$; $\rho_1 = \|y\|_2$
Choose $\tilde{\omega}^{(1)}$, for example $\tilde{\omega}^{(1)} = r^{(0)}$
Solve $M_2^T z = \tilde{\omega}^{(1)}$; $\xi_1 = \|z\|_2$; $\gamma_0 = 1$; $\eta_0 = -1$
For $i = 1, 2, .......$
  if $\rho_i = 0$ or $\xi_i = 0$ method fails
  $\upsilon^{(i)} = \tilde{\upsilon}^{(i)} / \rho_i$; $y = y / \rho_i$; $\omega^{(i)} = \tilde{\omega}^{(i)} / \xi_i$; $z = z / \xi_i$
  $\delta_i = z^T y$; if $\delta_i = 0$ method fails
  solve $M_2 \tilde{y} = y$; solve $M_1^T \tilde{z} = z$
    if $i = 1$
      $p^{(1)} = \tilde{y}$; $q^{(1)} = \tilde{z}$
    else
      $p^{(i)} = \tilde{y} - (\xi_i \delta_i / \varepsilon_{i-1}) p^{(i-1)}$; $q^{(i)} = \tilde{z} - (\rho_i \delta_i / \varepsilon_{i-1}) q^{(i-1)}$
    endif
  $\tilde{p} = \sum_{e=1}^{nel} A_e p^{(i)}$
  $\varepsilon_i = q^{(i)T} \tilde{p}$; if $\varepsilon_i = 0$ method fails; $\beta_i = \varepsilon_i / \delta_i$; if $\beta_i = 0$ method fails
  $\tilde{\upsilon}^{(i+1)} = \tilde{p} - \beta_i \upsilon^{(i)}$
  solve $M_1 y = \tilde{\upsilon}^{(i+1)}$
  $\rho_{i+1} = \|y\|_2$
  $\tilde{\omega}^{(i+1)} = \sum_{e=1}^{nel} A_e^T q^{(i)} - \beta_i \omega^{(i)}$
  solve $M_2^T z = \tilde{\omega}^{(i+1)}$
  $\xi_{i+1} = \|z\|_2$
  $\theta_i = \rho_{i+1} / (\gamma_{i-1} |\beta_i|)$; $\gamma_i = 1 / \sqrt{1 + \theta_i^2}$; if $\gamma_i = 0$ method fails
  $\eta_i = -\eta_{i-1} \rho_i \gamma_i^2 / (\beta_i \gamma_{i-1}^2)$
    if $i = 1$
      $d^{(1)} = \eta_1 p^{(1)}$; $s^{(1)} = \eta_1 \tilde{p}$
    else
      $d^{(i)} = \eta_1 p^{(i)} + (\theta_{i-1} \gamma_i)^2 d^{(i-1)}$; $s^{(i)} = \eta_1 \tilde{p}^{(i)} + (\theta_{i-1} \gamma_i)^2 s^{(i-1)}$
    endif
  $x^{(i)} = x^{(i-1)} + d^{(i)}$; $r^{(i)} = r^{(i-1)} + s^{(i)}$
check convergence; continue if necessary
end
```

Figure 3.5 Pseudocode for EBE-symmetric QMR (modified after Barett et al.,1994)

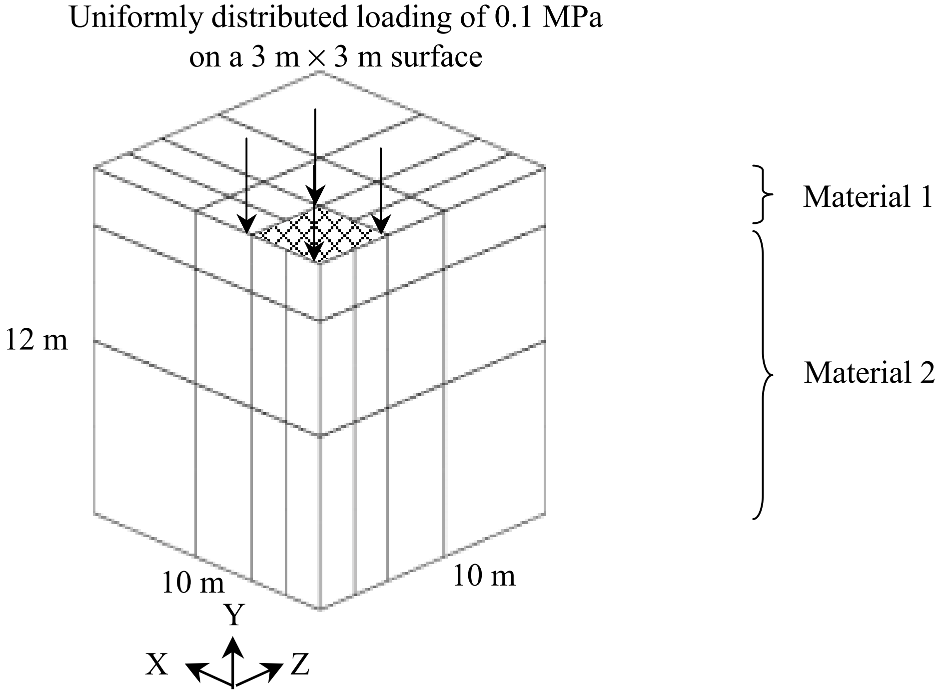

Figure 3.6 Typical 3D FE mesh (quadrant symmetric).

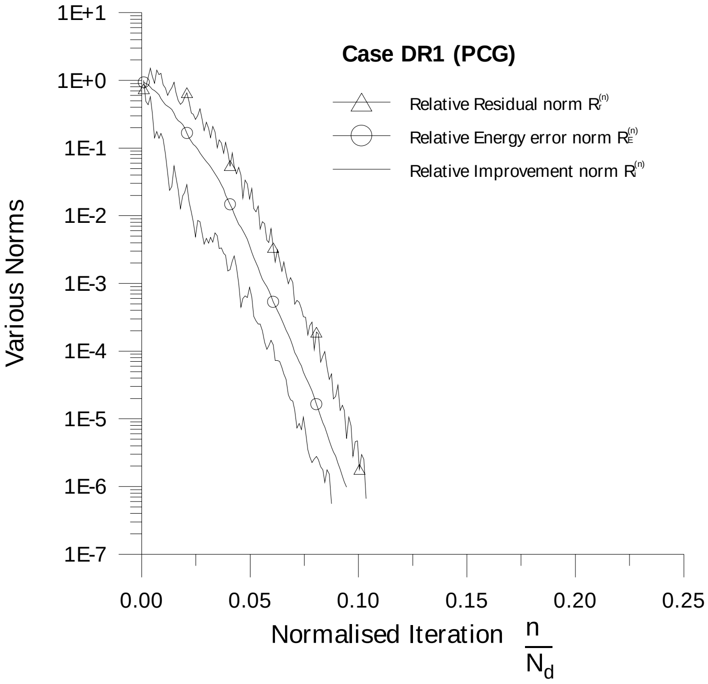

Figure 3.7a Behaviour of various norms using EPCG (Case DR1, κ(A*) = 4.445×10^2)

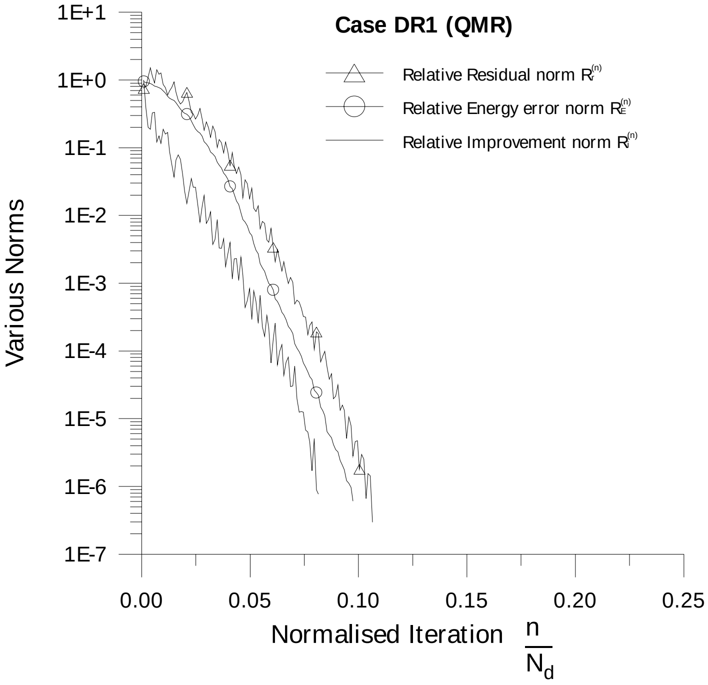

Figure 3.7b Behaviour of various norms using EQMR (Case DR1, κ(A*) = 5.618×10^2)

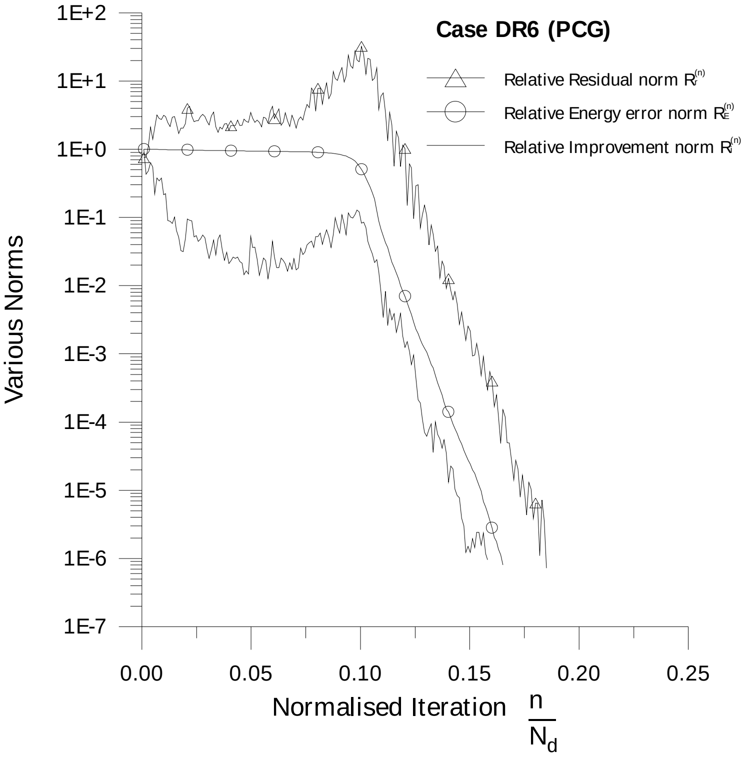

Figure 3.8a Behaviour of various norms using EPCG (Case DR6, κ(A^*) = 2.087×10^5).

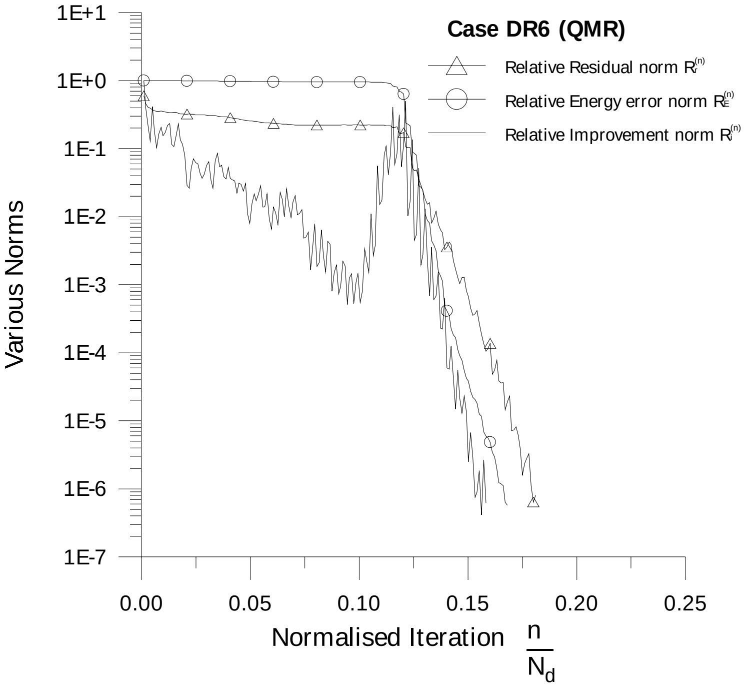

Figure 3.8b Behaviour of various norms using EQMR (Case DR6, κ(A^*) = 3.492×10^5)

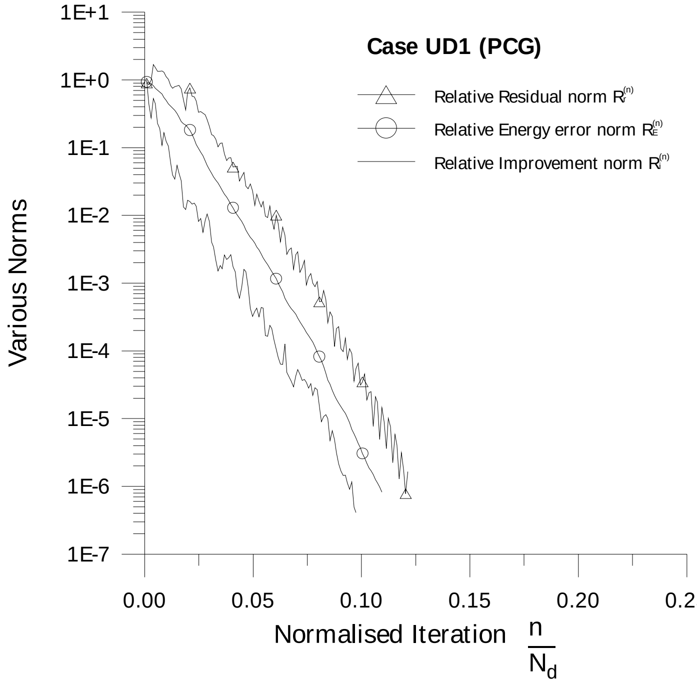

Figure 3.9a Behaviour of various norms using EPCG (Case UD1, $\kappa(A^*) = 4.161\times10^2$).

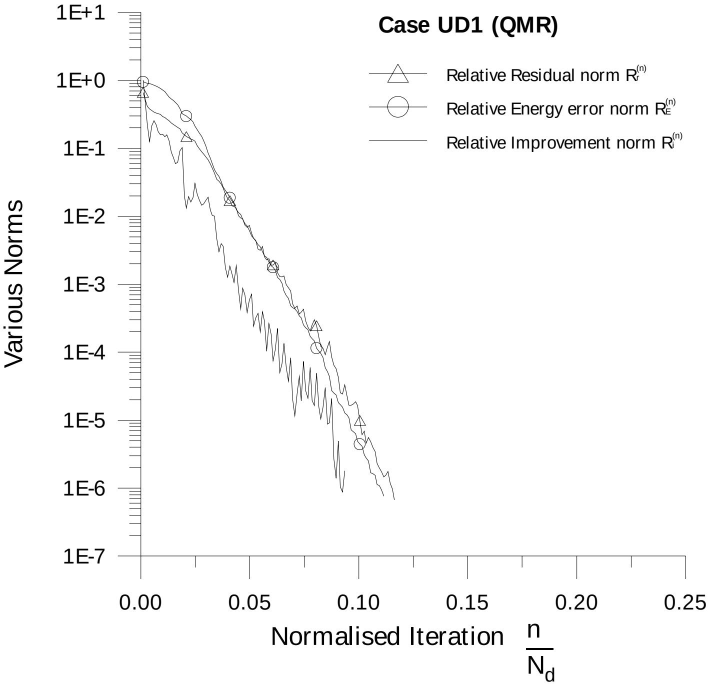

Figure 3.9b Behaviour of various norms using EQMR (Case UD1, $\kappa(A^*) = 5.488\times10^2$)

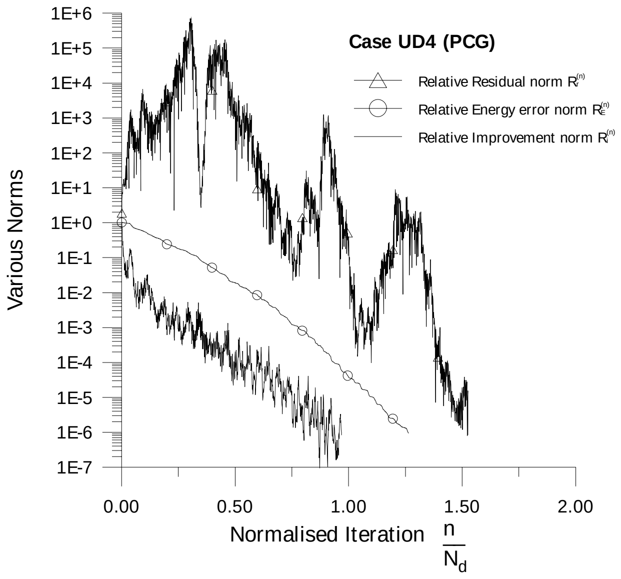

Figure 3.10a Behaviour of various norms using EPCG (Case UD4, $\kappa(A^*) = 1.042\times10^5$)

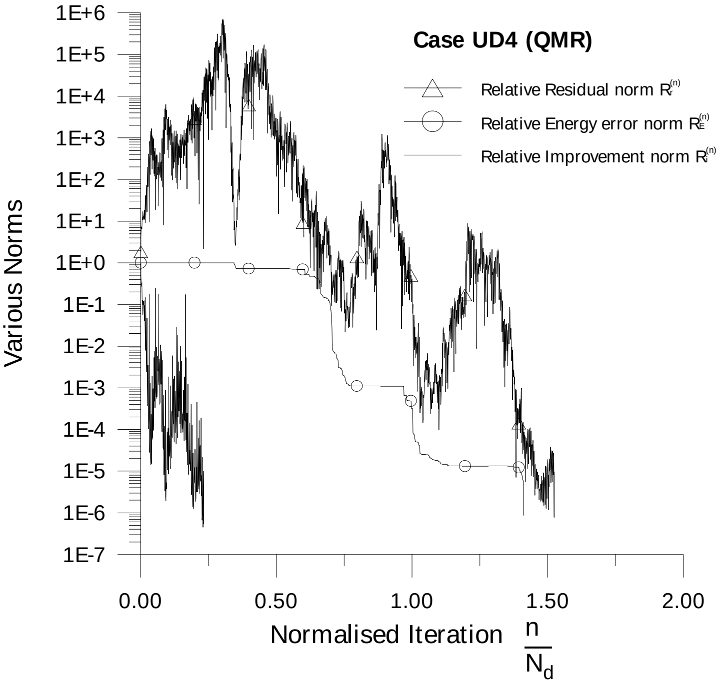

Figure 3.10b Behaviour of various norms using EQMR (Case UD4, $\kappa(A^*) = 2.400\times10^5$)

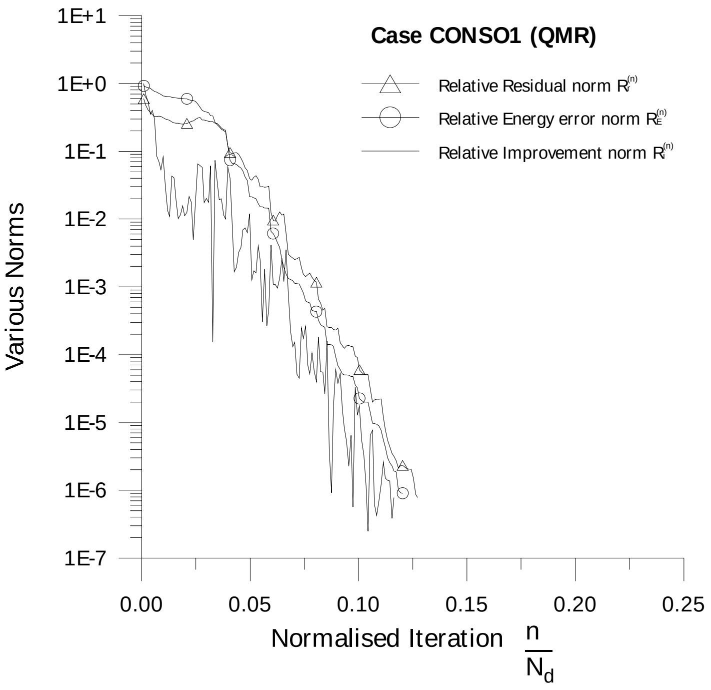

Figure 3.11a Behaviour of various norms using EQMR (Case CONSO1, $\kappa(A^*) = 3.261\times10^3$)

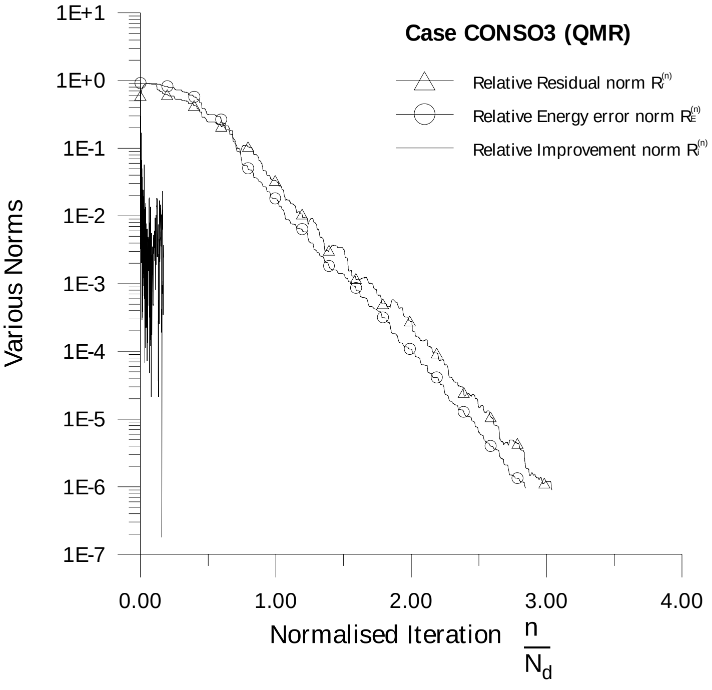

Figure 3.11b Behaviour of various norms using EQMR (Case CONSO3, $\kappa(A^*) = 2.193\times10^{10}$)

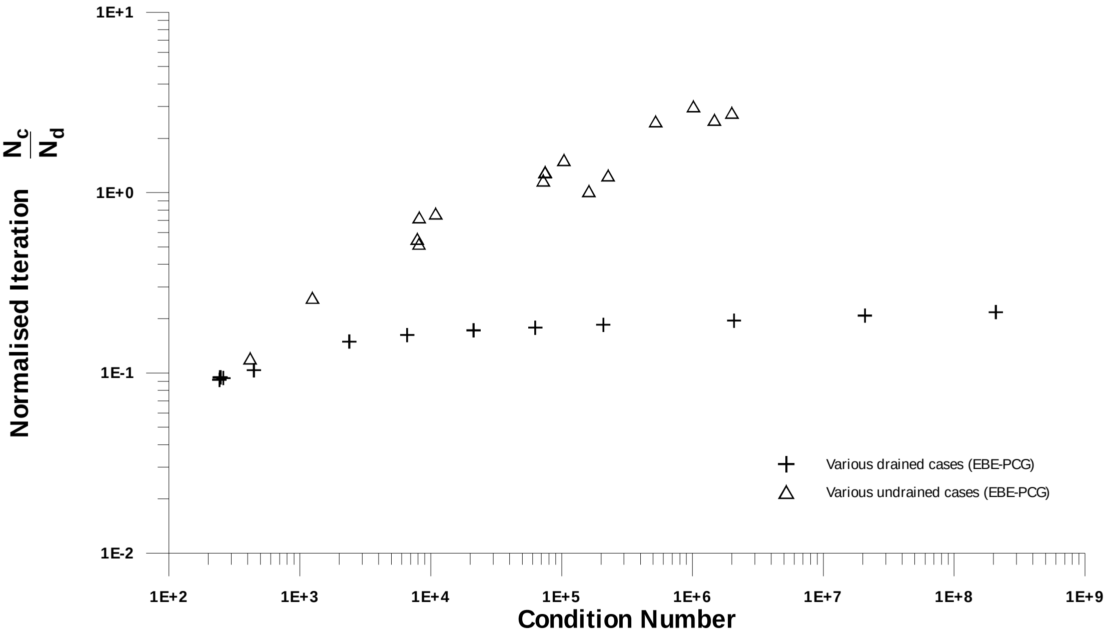

Figure 3.12a Variation of iteration number with condition number for EPCG algorithm on drained and undrained problems

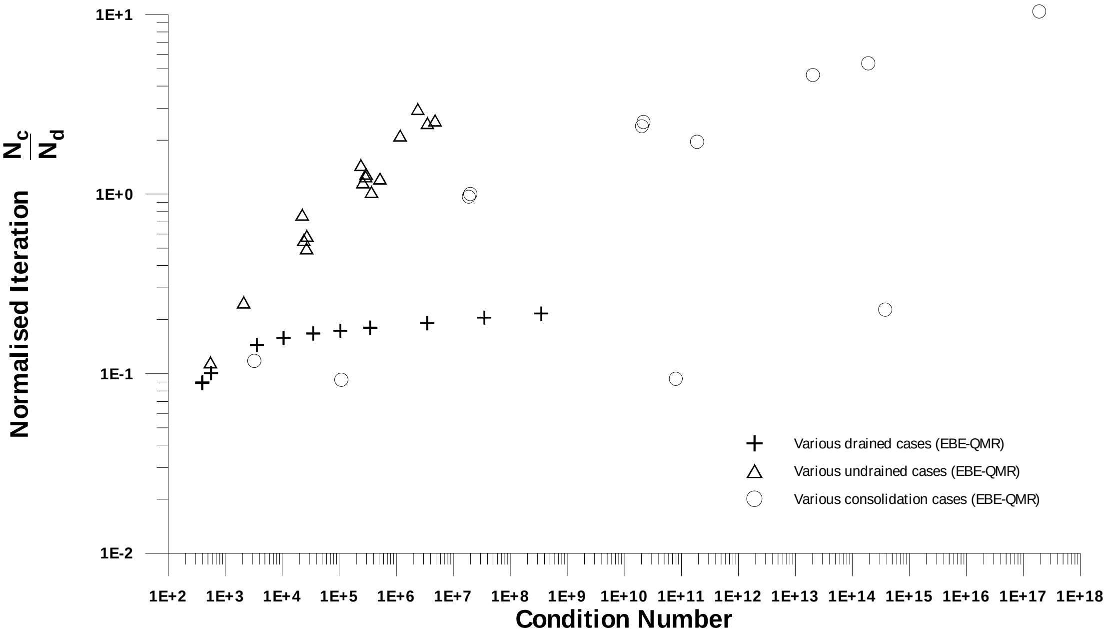

Figure 3.12b Variation of iteration number with condition number for EQMR algorithm on drained, undrained and consolidation problems

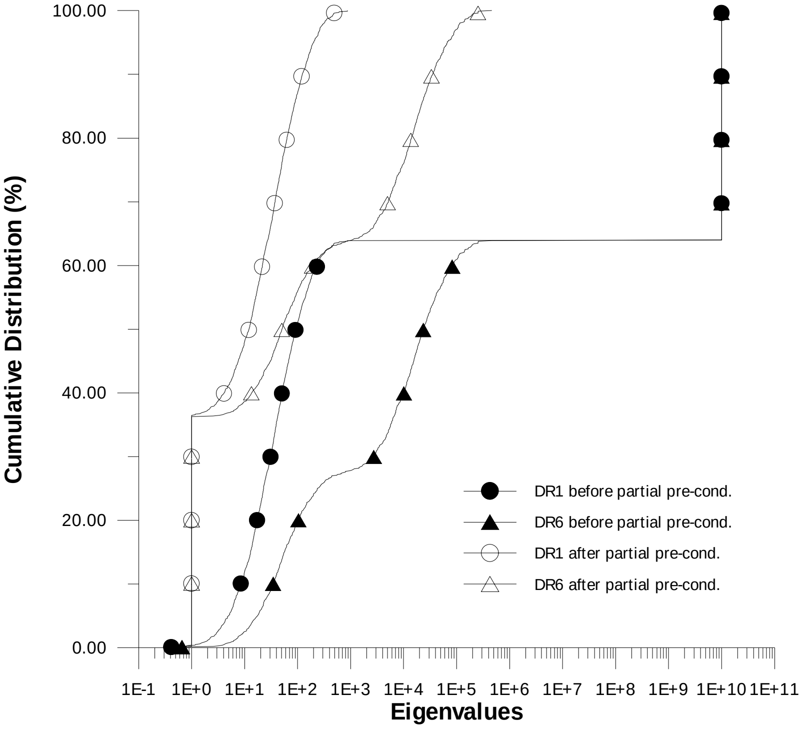

Figure 3.13a Cumulative distribution of eigenvalues in problems DR1 and DR6 before and after "partial Jacobi" preconditioning

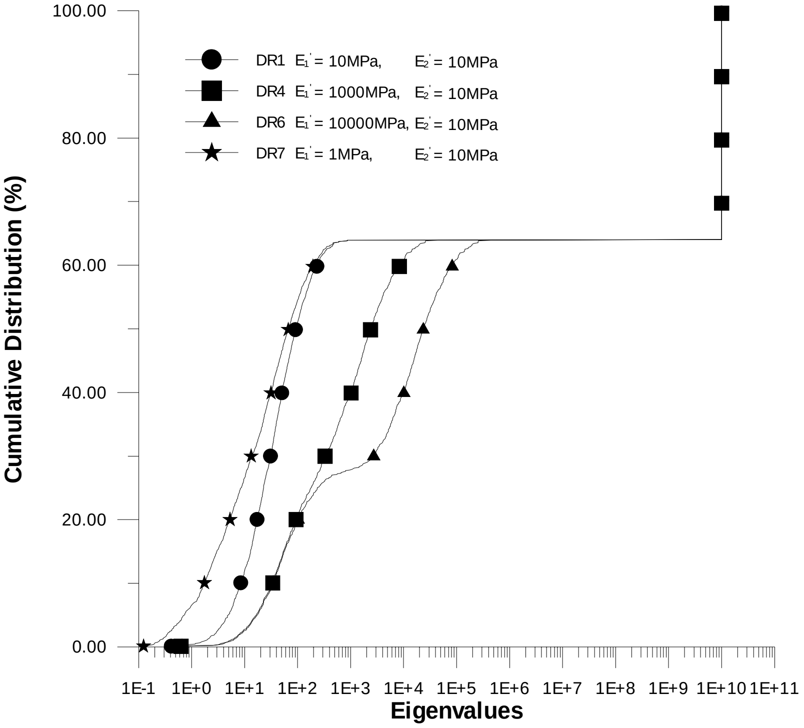

Figure 3.13b Cumulative distribution of eigenvalues in problems DR1, DR4, DR6 and DR7 before "partial Jacobi" preconditioning

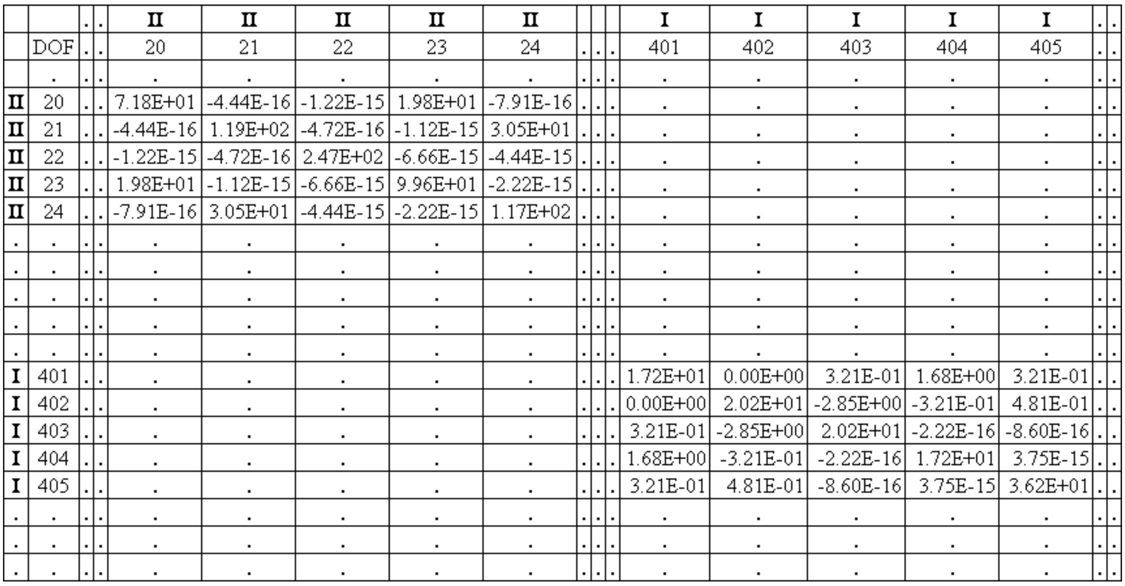

		.	.	II	II	II	II	II				I	I	I	I	I	.	.
	DOF	.	.	20	21	22	23	24	.	.	.	401	402	403	404	405	.	.
	.	.	.	.	.	.	.	.	.	.	.	.	.	.	.	.	.	.
II	20	.	.	7.18E+01	-4.44E-16	-1.22E-15	1.98E+01	-7.91E-16	.	.	.	.	.	.	.	.	.	.
II	21	.	.	-4.44E-16	1.19E+02	-4.72E-16	-1.12E-15	3.05E+01	.	.	.	.	.	.	.	.	.	.
II	22	.	.	-1.22E-15	-4.72E-16	2.47E+02	-6.66E-15	-4.44E-15	.	.	.	.	.	.	.	.	.	.
II	23	.	.	1.98E+01	-1.12E-15	-6.66E-15	9.96E+01	-2.22E-15	.	.	.	.	.	.	.	.	.	.
II	24	.	.	-7.91E-16	3.05E+01	-4.44E-15	-2.22E-15	1.17E+02	.	.	.	.	.	.	.	.	.	.
.	.	.	.	.	.	.	.	.	.	.	.	.	.	.	.	.	.	.
.	.	.	.	.	.	.	.	.	.	.	.	.	.	.	.	.	.	.
.	.	.	.	.	.	.	.	.	.	.	.	.	.	.	.	.	.	.
.	.	.	.	.	.	.	.	.	.	.	.	.	.	.	.	.	.	.
.	.	.	.	.	.	.	.	.	.	.	.	.	.	.	.	.	.	.
I	401	.	.	.	.	.	.	.	.	.	.	1.72E+01	0.00E+00	3.21E-01	1.68E+00	3.21E-01	.	.
I	402	.	.	.	.	.	.	.	.	.	.	0.00E+00	2.02E+01	-2.85E+00	-3.21E-01	4.81E-01	.	.
I	403	.	.	.	.	.	.	.	.	.	.	3.21E-01	-2.85E+00	2.02E+01	-2.22E-16	-8.60E-16	.	.
I	404	.	.	.	.	.	.	.	.	.	.	1.68E+00	-3.21E-01	-2.22E-16	1.72E+01	3.75E-15	.	.
I	405	.	.	.	.	.	.	.	.	.	.	3.21E-01	4.81E-01	-8.60E-16	3.75E-15	3.62E+01	.	.
.	.	.	.	.	.	.	.	.	.	.	.	.	.	.	.	.	.	.
.	.	.	.	.	.	.	.	.	.	.	.	.	.	.	.	.	.	.
.	.	.	.	.	.	.	.	.	.	.	.	.	.	.	.	.	.	.

Figure 3.14a Parts of the unconditioned global stiffness matrix from DR1

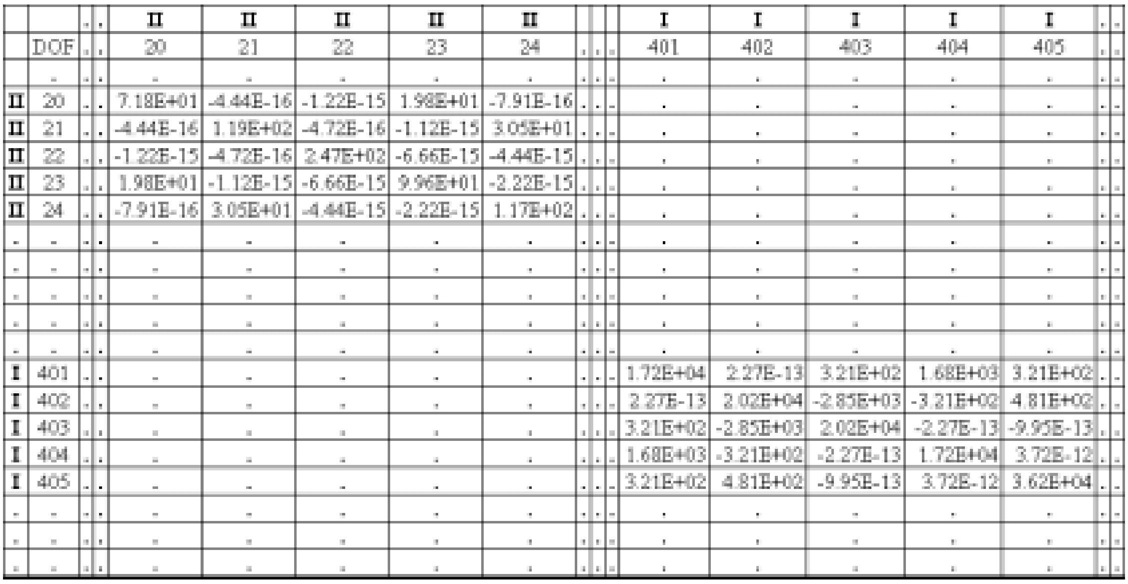

		.	.	II	II	II	II	II				I	I	I	I	I	.	.
	DOF	.	.	20	21	22	23	24	.	.	.	401	402	403	404	405	.	.
	.	.	.	.	.	.	.	.	.	.	.	.	.	.	.	.	.	.
II	20	.	.	7.18E+01	-4.44E-16	-1.22E-15	1.98E+01	-7.91E-16	.	.	.	.	.	.	.	.	.	.
II	21	.	.	-4.44E-16	1.19E+02	-4.72E-16	-1.12E-15	3.05E+01	.	.	.	.	.	.	.	.	.	.
II	22	.	.	-1.22E-15	-4.72E-16	2.47E+02	-6.66E-15	-4.44E-15	.	.	.	.	.	.	.	.	.	.
II	23	.	.	1.98E+01	-1.12E-15	-6.66E-15	9.96E+01	-2.22E-15	.	.	.	.	.	.	.	.	.	.
II	24	.	.	-7.91E-16	3.05E+01	-4.44E-15	-2.22E-15	1.17E+02	.	.	.	.	.	.	.	.	.	.
.	.	.	.	.	.	.	.	.	.	.	.	.	.	.	.	.	.	.
.	.	.	.	.	.	.	.	.	.	.	.	.	.	.	.	.	.	.
.	.	.	.	.	.	.	.	.	.	.	.	.	.	.	.	.	.	.
.	.	.	.	.	.	.	.	.	.	.	.	.	.	.	.	.	.	.
.	.	.	.	.	.	.	.	.	.	.	.	.	.	.	.	.	.	.
I	401	.	.	.	.	.	.	.	.	.	.	1.72E+04	2.27E-13	3.21E+02	1.68E+03	3.21E+02	.	.
I	402	.	.	.	.	.	.	.	.	.	.	2.27E-13	2.02E+04	-2.85E+03	-3.21E+02	4.81E+02	.	.
I	403	.	.	.	.	.	.	.	.	.	.	3.21E+02	-2.85E+03	2.02E+04	-2.27E-13	-9.95E-13	.	.
I	404	.	.	.	.	.	.	.	.	.	.	1.68E+03	-3.21E+02	-2.27E-13	1.72E+04	3.72E-12	.	.
I	405	.	.	.	.	.	.	.	.	.	.	3.21E+02	4.81E+02	-9.95E-13	3.72E-12	3.62E+04	.	.
.	.	.	.	.	.	.	.	.	.	.	.	.	.	.	.	.	.	.
.	.	.	.	.	.	.	.	.	.	.	.	.	.	.	.	.	.	.
.	.	.	.	.	.	.	.	.	.	.	.	.	.	.	.	.	.	.

Figure 3.14b Parts of the unconditioned global stiffness matrix from DR6

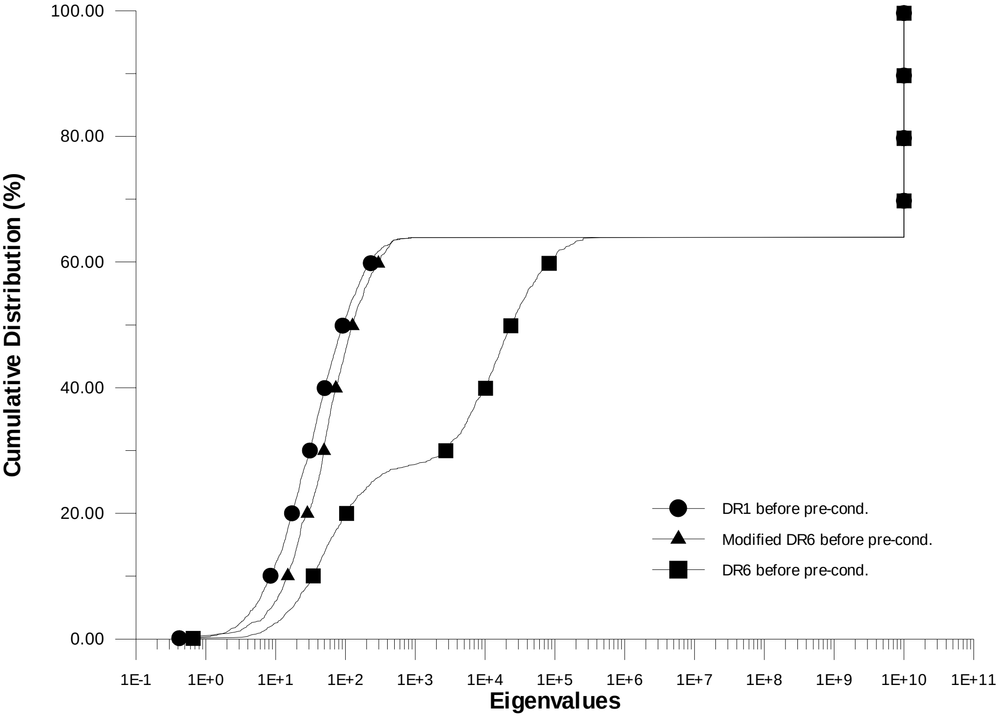

Figure 3.15 Cumulative distribution of eigenvalues in problems DR1, modified DR6 and DR6 before and after “full Jacobi” preconditioning

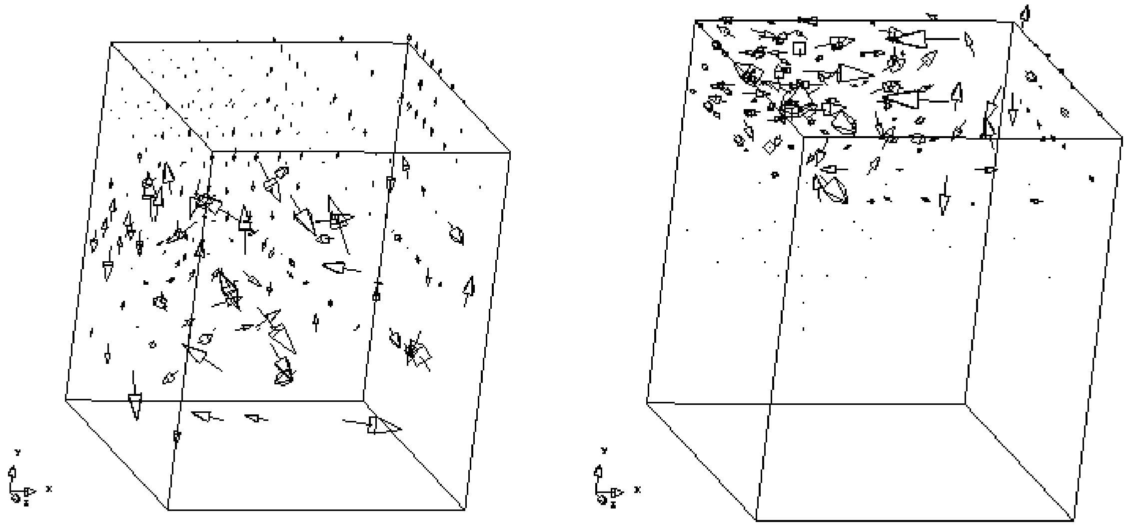

(a) (b)

Figure 3.16 Eigenvectors corresponding to (a) the 20-percentile eigenvalue and (b) the 80-percentile eigenvalue, of DR6 before conditioning

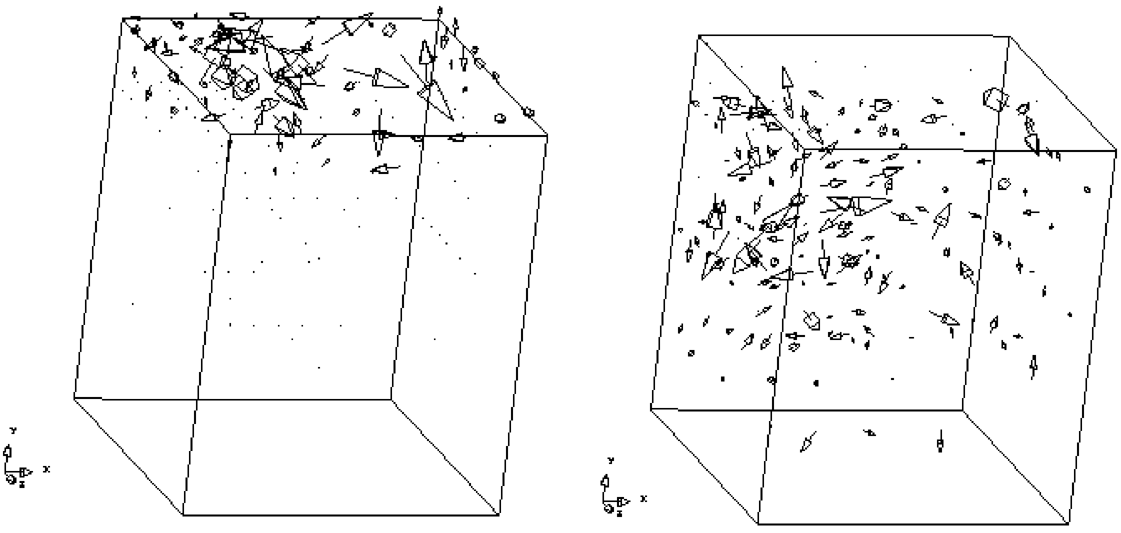

(a) (b)

Figure 3.17 Eigenvectors corresponding to (a) the 20-percentile eigenvalue and (b) the 80-percentile eigenvalue, of DR12 before conditioning

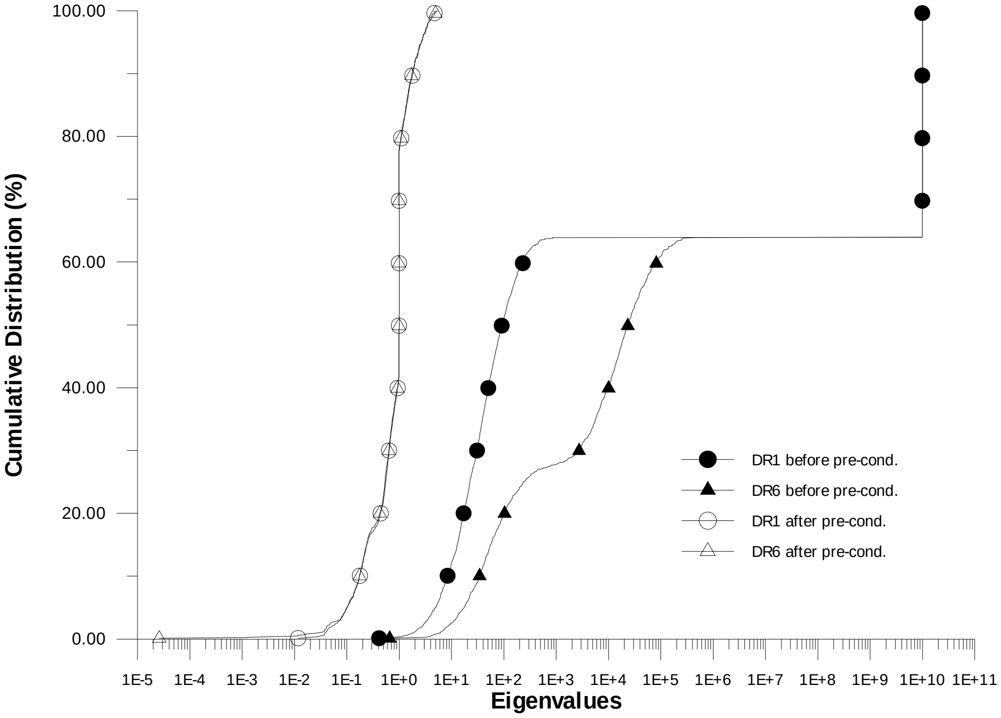

Figure 3.18 Cumulative distribution of eigenvalues in problems DR1 and DR6 before and after "full Jacobi" preconditioning

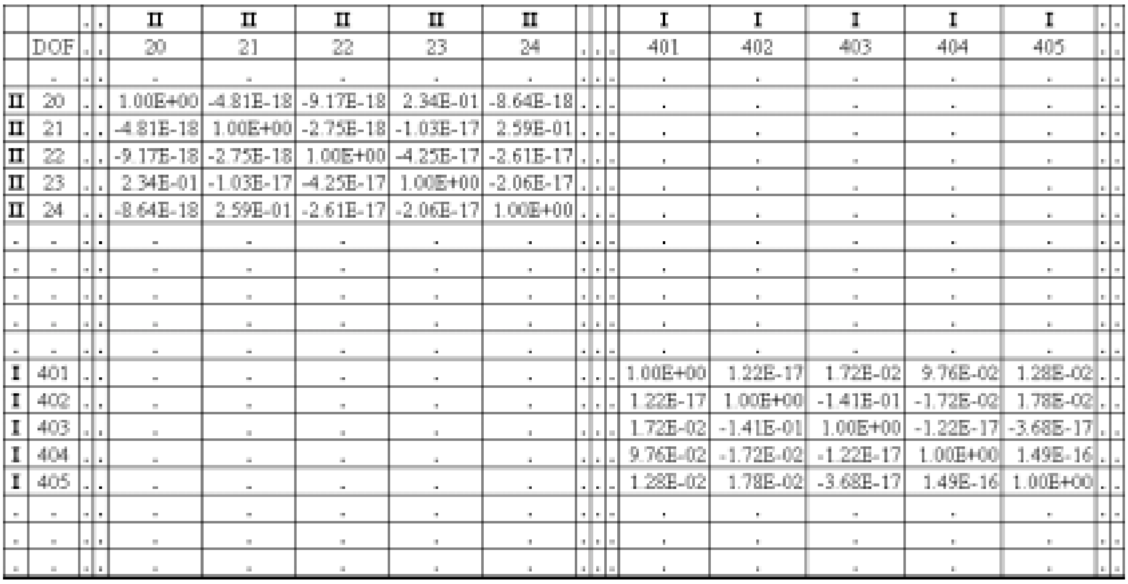

		.	.	II	II	II	II	II				I	I	I	I	I	.	.
	DOF	.	.	20	21	22	23	24	.	.	.	401	402	403	404	405	.	.
	.	.	.	.	.	.	.	.	.	.	.	.	.	.	.	.	.	.
II	20	.	.	1.00E+00	-4.81E-18	-9.17E-18	2.34E-01	-8.64E-18	.	.	.	.	.	.	.	.	.	.
II	21	.	.	-4.81E-18	1.00E+00	-2.75E-18	-1.03E-17	2.59E-01	.	.	.	.	.	.	.	.	.	.
II	22	.	.	-9.17E-18	-2.75E-18	1.00E+00	-4.25E-17	-2.61E-17	.	.	.	.	.	.	.	.	.	.
II	23	.	.	2.34E-01	-1.03E-17	-4.25E-17	1.00E+00	-2.06E-17	.	.	.	.	.	.	.	.	.	.
II	24	.	.	-8.64E-18	2.59E-01	-2.61E-17	-2.06E-17	1.00E+00	.	.	.	.	.	.	.	.	.	.
.	.	.	.	.	.	.	.	.	.	.	.	.	.	.	.	.	.	.
.	.	.	.	.	.	.	.	.	.	.	.	.	.	.	.	.	.	.
.	.	.	.	.	.	.	.	.	.	.	.	.	.	.	.	.	.	.
.	.	.	.	.	.	.	.	.	.	.	.	.	.	.	.	.	.	.
.	.	.	.	.	.	.	.	.	.	.	.	.	.	.	.	.	.	.
I	401	.	.	.	.	.	.	.	.	.	.	1.00E+00	1.22E-17	1.72E-02	9.76E-02	1.28E-02	.	.
I	402	.	.	.	.	.	.	.	.	.	.	1.22E-17	1.00E+00	-1.41E-01	-1.72E-02	1.78E-02	.	.
I	403	.	.	.	.	.	.	.	.	.	.	1.72E-02	-1.41E-01	1.00E+00	-1.22E-17	-3.68E-17	.	.
I	404	.	.	.	.	.	.	.	.	.	.	9.76E-02	-1.72E-02	-1.22E-17	1.00E+00	1.49E-16	.	.
I	405	.	.	.	.	.	.	.	.	.	.	1.28E-02	1.78E-02	-3.68E-17	1.49E-16	1.00E+00	.	.
.	.	.	.	.	.	.	.	.	.	.	.	.	.	.	.	.	.	.
.	.	.	.	.	.	.	.	.	.	.	.	.	.	.	.	.	.	.
.	.	.	.	.	.	.	.	.	.	.	.	.	.	.	.	.	.	.

Figure 3.19 Parts of the preconditioned global stiffness matrix from DR6

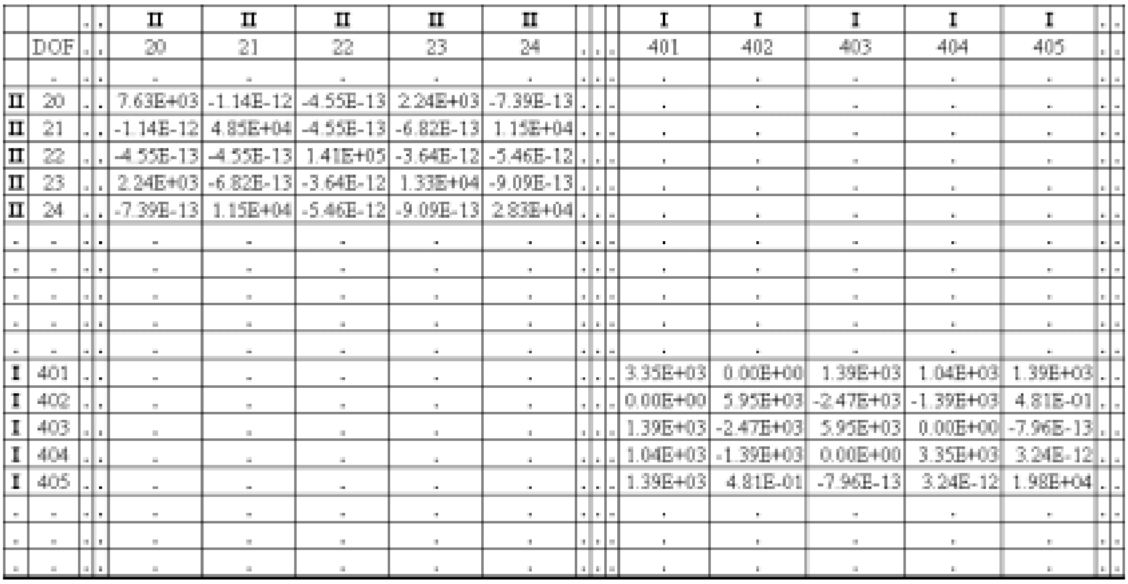

		.	.	II	II	II	II	II				I	I	I	I	I	.	.
	DOF	.	.	20	21	22	23	24	.	.	.	401	402	403	404	405	.	.
	.	.	.	.	.	.	.	.	.	.	.	.	.	.	.	.	.	.
II	20	.	.	7.63E+03	-1.14E-12	-4.55E-13	2.24E+03	-7.39E-13	.	.	.	.	.	.	.	.	.	.
II	21	.	.	-1.14E-12	4.85E+04	-4.55E-13	-6.82E-13	1.15E+04	.	.	.	.	.	.	.	.	.	.
II	22	.	.	-4.55E-13	-4.55E-13	1.41E+05	-3.64E-12	-5.46E-12	.	.	.	.	.	.	.	.	.	.
II	23	.	.	2.24E+03	-6.82E-13	-3.64E-12	1.33E+04	-9.09E-13	.	.	.	.	.	.	.	.	.	.
II	24	.	.	-7.39E-13	1.15E+04	-5.46E-12	-9.09E-13	2.83E+04	.	.	.	.	.	.	.	.	.	.
.	.	.	.	.	.	.	.	.	.	.	.	.	.	.	.	.	.	.
.	.	.	.	.	.	.	.	.	.	.	.	.	.	.	.	.	.	.
.	.	.	.	.	.	.	.	.	.	.	.	.	.	.	.	.	.	.
.	.	.	.	.	.	.	.	.	.	.	.	.	.	.	.	.	.	.
.	.	.	.	.	.	.	.	.	.	.	.	.	.	.	.	.	.	.
I	401	.	.	.	.	.	.	.	.	.	.	3.35E+03	0.00E+00	1.39E+03	1.04E+03	1.39E+03	.	.
I	402	.	.	.	.	.	.	.	.	.	.	0.00E+00	5.95E+03	-2.47E+03	-1.39E+03	4.81E-01	.	.
I	403	.	.	.	.	.	.	.	.	.	.	1.39E+03	-2.47E+03	5.95E+03	0.00E+00	-7.96E-13	.	.
I	404	.	.	.	.	.	.	.	.	.	.	1.04E+03	-1.39E+03	0.00E+00	3.35E+03	3.24E-12	.	.
I	405	.	.	.	.	.	.	.	.	.	.	1.39E+03	4.81E-01	-7.96E-13	3.24E-12	1.98E+04	.	.
.	.	.	.	.	.	.	.	.	.	.	.	.	.	.	.	.	.	.
.	.	.	.	.	.	.	.	.	.	.	.	.	.	.	.	.	.	.
.	.	.	.	.	.	.	.	.	.	.	.	.	.	.	.	.	.	.

Figure 3.20a Parts of the unconditioned global stiffness matrix from UD4

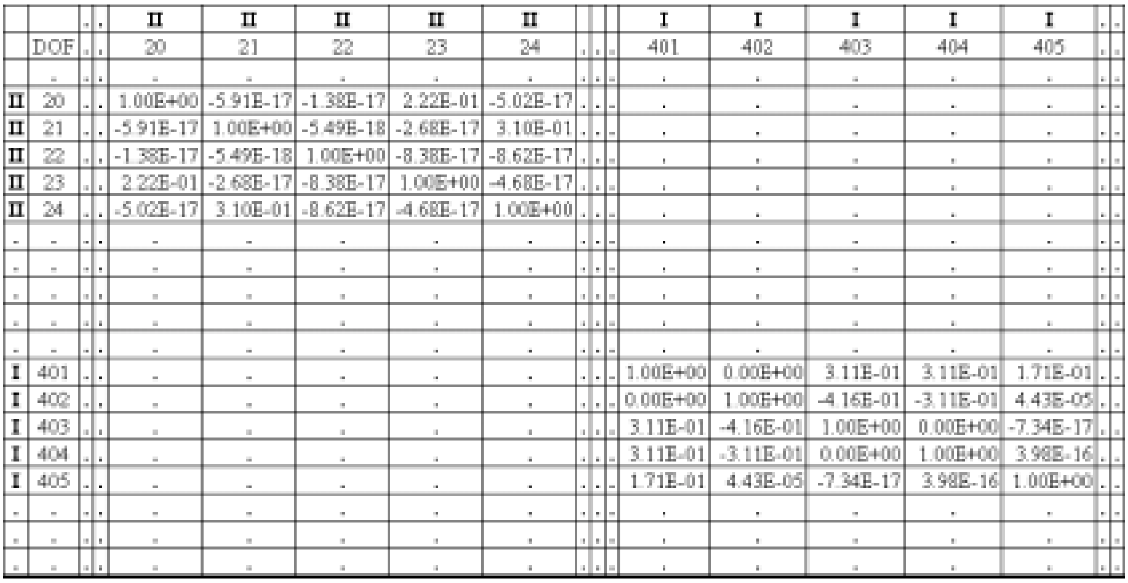

		.	.	II	II	II	II	II				I	I	I	I	I	.	.
	DOF	.	.	20	21	22	23	24	.	.	.	401	402	403	404	405	.	.
	.	.	.	.	.	.	.	.	.	.	.	.	.	.	.	.	.	.
II	20	.	.	1.00E+00	-5.91E-17	-1.38E-17	2.22E-01	-5.02E-17	.	.	.	.	.	.	.	.	.	.
II	21	.	.	-5.91E-17	1.00E+00	-5.49E-18	-2.68E-17	3.10E-01	.	.	.	.	.	.	.	.	.	.
II	22	.	.	-1.38E-17	-5.49E-18	1.00E+00	-8.38E-17	-8.62E-17	.	.	.	.	.	.	.	.	.	.
II	23	.	.	2.22E-01	-2.68E-17	-8.38E-17	1.00E+00	-4.68E-17	.	.	.	.	.	.	.	.	.	.
II	24	.	.	-5.02E-17	3.10E-01	-8.62E-17	-4.68E-17	1.00E+00	.	.	.	.	.	.	.	.	.	.
.	.	.	.	.	.	.	.	.	.	.	.	.	.	.	.	.	.	.
.	.	.	.	.	.	.	.	.	.	.	.	.	.	.	.	.	.	.
.	.	.	.	.	.	.	.	.	.	.	.	.	.	.	.	.	.	.
.	.	.	.	.	.	.	.	.	.	.	.	.	.	.	.	.	.	.
.	.	.	.	.	.	.	.	.	.	.	.	.	.	.	.	.	.	.
I	401	.	.	.	.	.	.	.	.	.	.	1.00E+00	0.00E+00	3.11E-01	3.11E-01	1.71E-01	.	.
I	402	.	.	.	.	.	.	.	.	.	.	0.00E+00	1.00E+00	-4.16E-01	-3.11E-01	4.43E-05	.	.
I	403	.	.	.	.	.	.	.	.	.	.	3.11E-01	-4.16E-01	1.00E+00	0.00E+00	-7.34E-17	.	.
I	404	.	.	.	.	.	.	.	.	.	.	3.11E-01	-3.11E-01	0.00E+00	1.00E+00	3.98E-16	.	.
I	405	.	.	.	.	.	.	.	.	.	.	1.71E-01	4.43E-05	-7.34E-17	3.98E-16	1.00E+00	.	.
.	.	.	.	.	.	.	.	.	.	.	.	.	.	.	.	.	.	.
.	.	.	.	.	.	.	.	.	.	.	.	.	.	.	.	.	.	.
.	.	.	.	.	.	.	.	.	.	.	.	.	.	.	.	.	.	.

Figure 3.20b Parts of the preconditioned global stiffness matrix from UD4

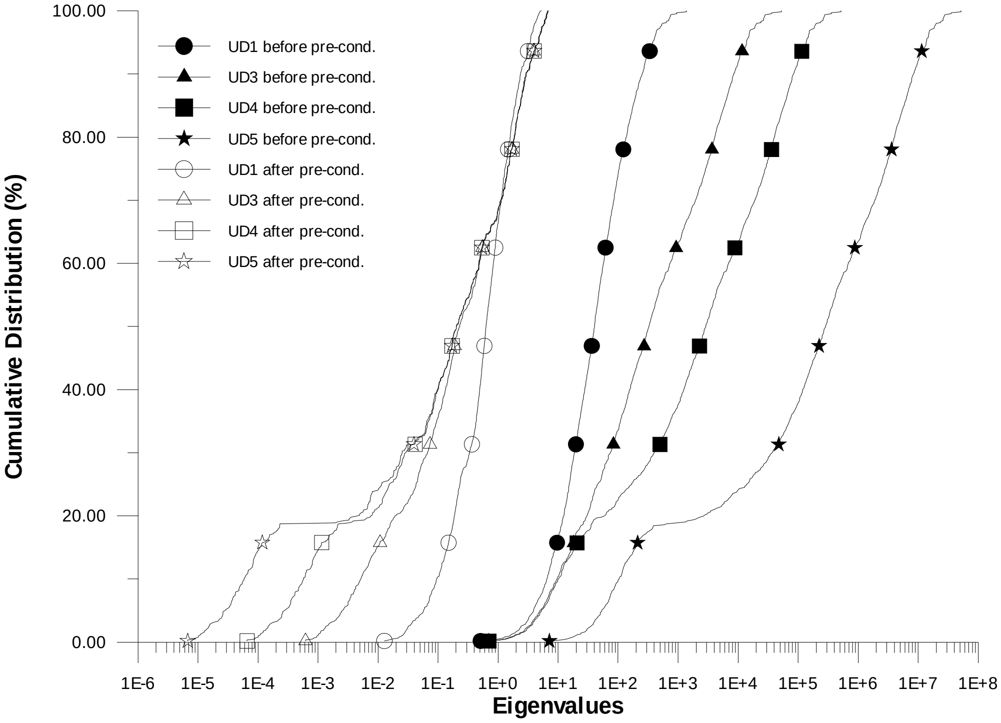

Figure 3.21 Eigenvalue distribution of some undrained problems before and after Jacobi preconditioning

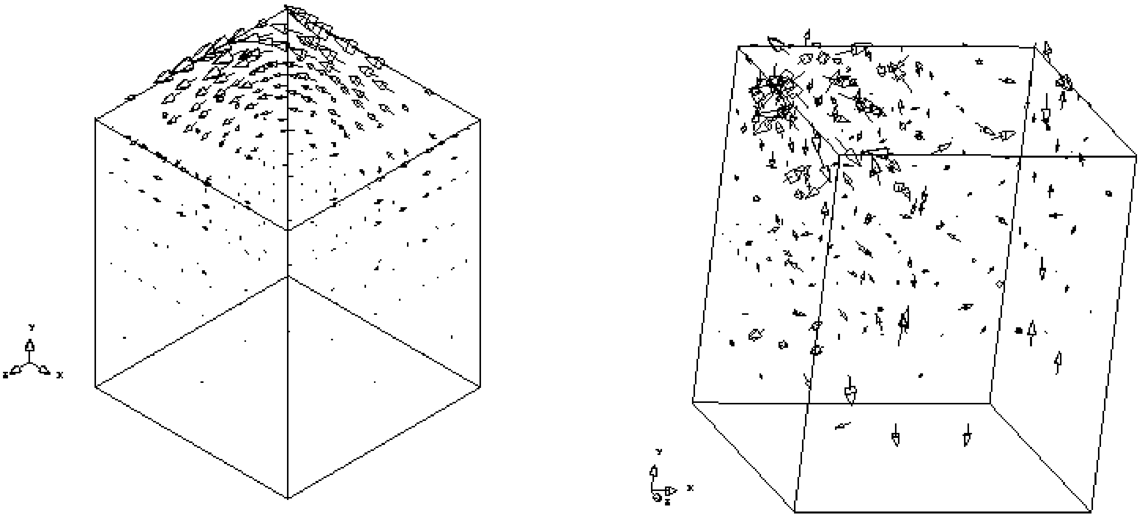

(a) (b)

Figure 3.22 Eigenvectors corresponding to (a) the 3rd smallest eigenvalue and (b) the 80-percentile eigenvalue, of UD4 before preconditioning

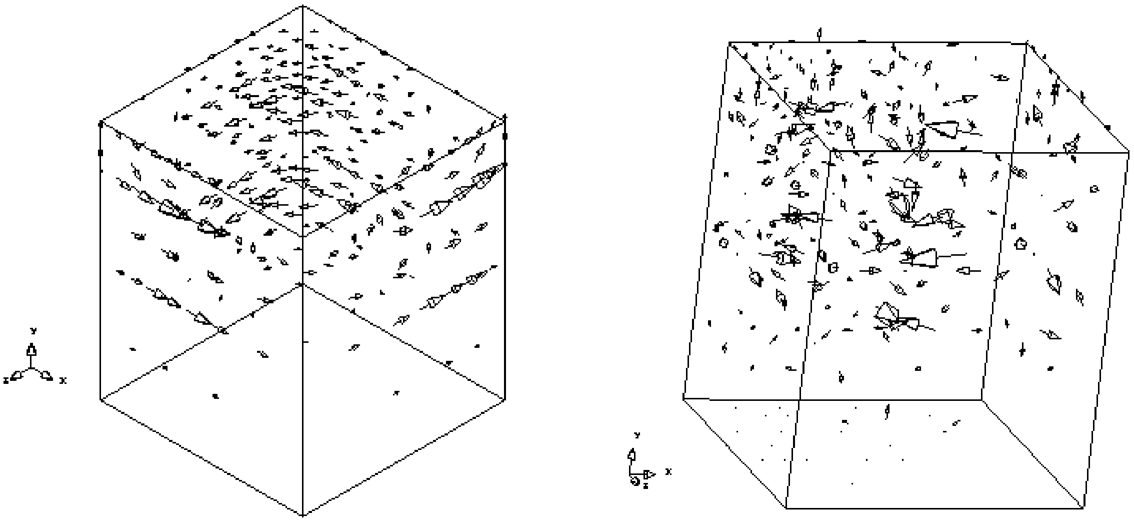

(a) (b)

Figure 3.23 Eigenvectors corresponding to (a) the 3rd smallest eigenvalue and (b) the 80-percentile eigenvalue, of UD4 after preconditioning

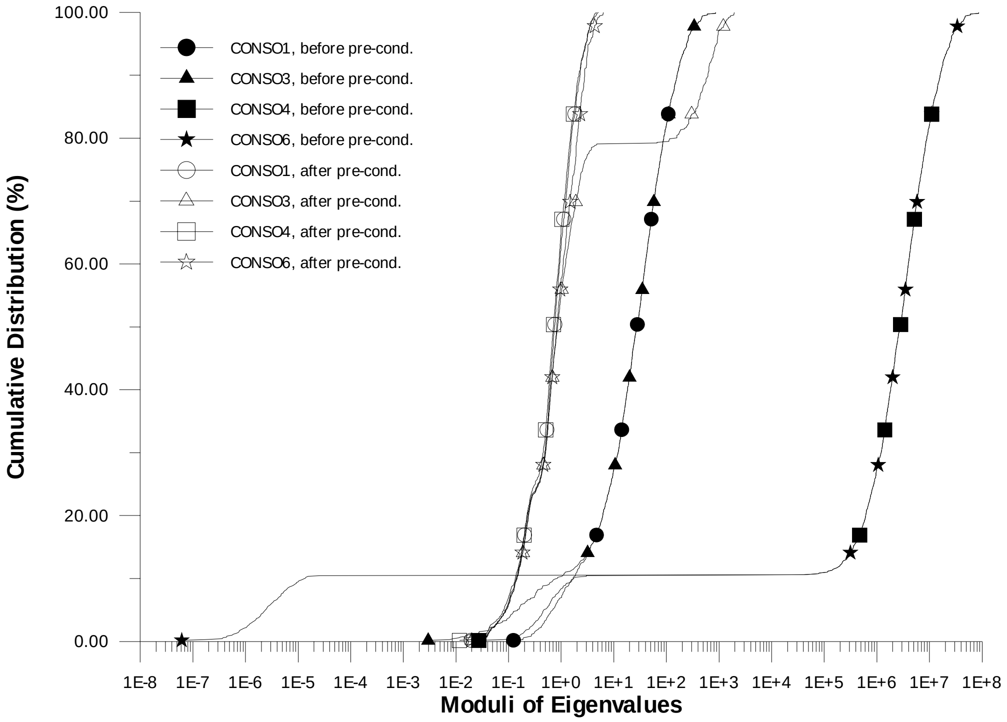

Figure 3.24 Cumulative distribution of eigenvalue moduli for some consolidation cases before and after preconditioning

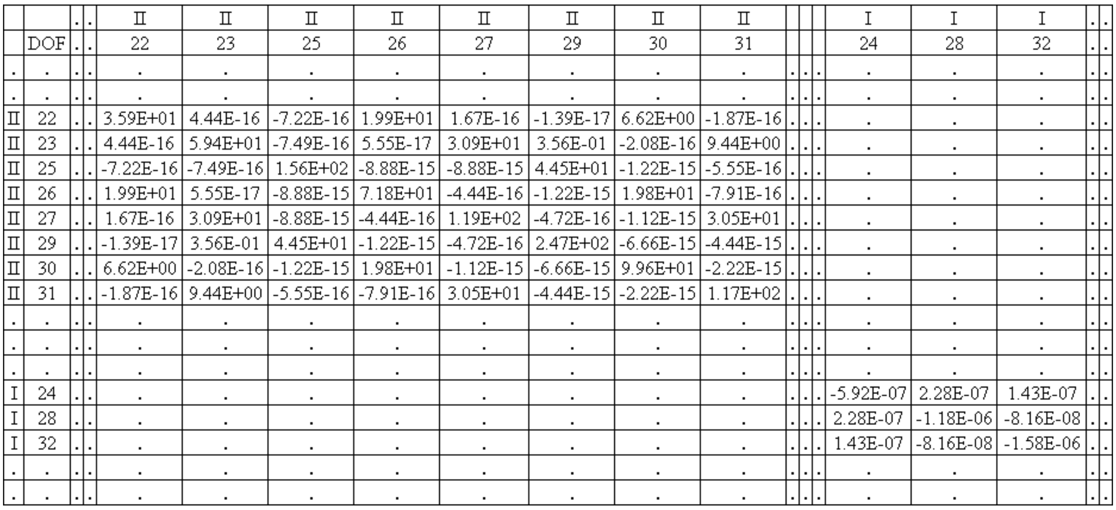

		.	.	II	II	II	II	II	II	II	II				I	I	I	.	.
	DOF	.	.	22	23	25	26	27	29	30	31				24	28	32	.	.
.	.	.	.	.	.	.	.	.	.	.	.	.	.	.	.	.	.	.	.
.	.	.	.	.	.	.	.	.	.	.	.	.	.	.	.	.	.	.	.
II	22	.	.	3.59E+01	4.44E-16	-7.22E-16	1.99E+01	1.67E-16	-1.39E-17	6.62E+00	-1.87E-16	.	.	.	.	.	.	.	.
II	23	.	.	4.44E-16	5.94E+01	-7.49E-16	5.55E-17	3.09E+01	3.56E-01	-2.08E-16	9.44E+00	.	.	.	.	.	.	.	.
II	25	.	.	-7.22E-16	-7.49E-16	1.56E+02	-8.88E-15	-8.88E-15	4.45E+01	-1.22E-15	-5.55E-16	.	.	.	.	.	.	.	.
II	26	.	.	1.99E+01	5.55E-17	-8.88E-15	7.18E+01	-4.44E-16	-1.22E-15	1.98E+01	-7.91E-16	.	.	.	.	.	.	.	.
II	27	.	.	1.67E-16	3.09E+01	-8.88E-15	-4.44E-16	1.19E+02	-4.72E-16	-1.12E-15	3.05E+01	.	.	.	.	.	.	.	.
II	29	.	.	-1.39E-17	3.56E-01	4.45E+01	-1.22E-15	-4.72E-16	2.47E+02	-6.66E-15	-4.44E-15	.	.	.	.	.	.	.	.
II	30	.	.	6.62E+00	-2.08E-16	-1.22E-15	1.98E+01	-1.12E-15	-6.66E-15	9.96E+01	-2.22E-15	.	.	.	.	.	.	.	.
II	31	.	.	-1.87E-16	9.44E+00	-5.55E-16	-7.91E-16	3.05E+01	-4.44E-15	-2.22E-15	1.17E+02	.	.	.	.	.	.	.	.
.	.	.	.	.	.	.	.	.	.	.	.	.	.	.	.	.	.	.	.
.	.	.	.	.	.	.	.	.	.	.	.	.	.	.	.	.	.	.	.
.	.	.	.	.	.	.	.	.	.	.	.	.	.	.	.	.	.	.	.
I	24	.	.	.	.	.	.	.	.	.	.	.	.	.	-5.92E-07	2.28E-07	1.43E-07	.	.
I	28	.	.	.	.	.	.	.	.	.	.	.	.	.	2.28E-07	-1.18E-06	-8.16E-08	.	.
I	32	.	.	.	.	.	.	.	.	.	.	.	.	.	1.43E-07	-8.16E-08	-1.58E-06	.	.
.	.	.	.	.	.	.	.	.	.	.	.	.	.	.	.	.	.	.	.
.	.	.	.	.	.	.	.	.	.	.	.	.	.	.	.	.	.	.	.

Figure 3.25 Parts of the unconditioned global stiffness matrix from CONSO3

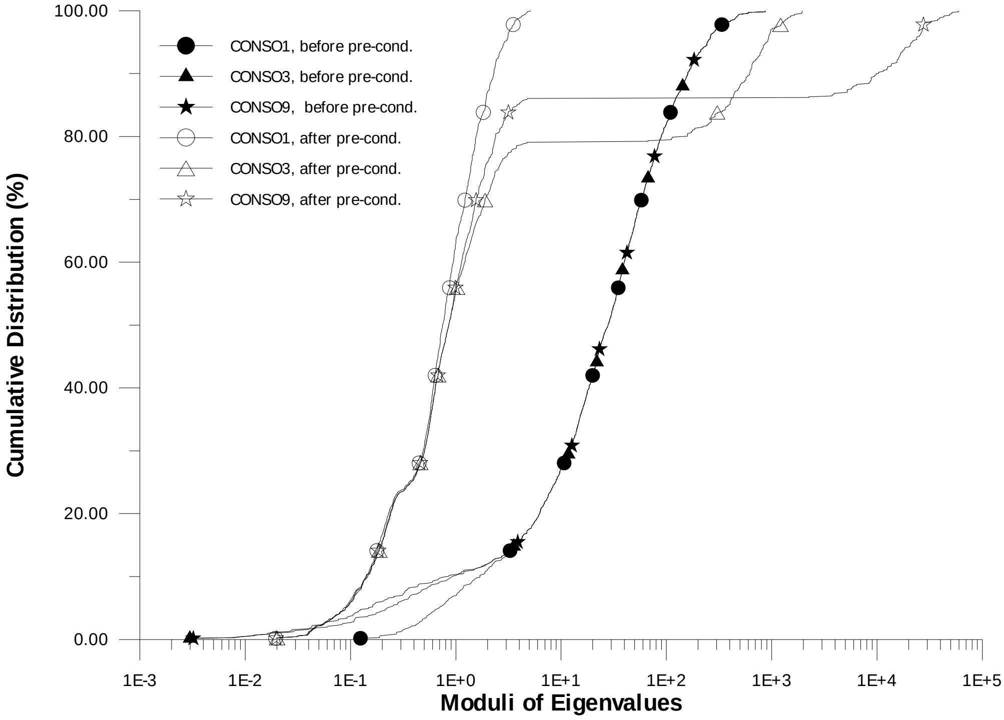

Figure 3.26 Cumulative distribution of eigenvalue moduli for some consolidation cases before and after preconditioning.

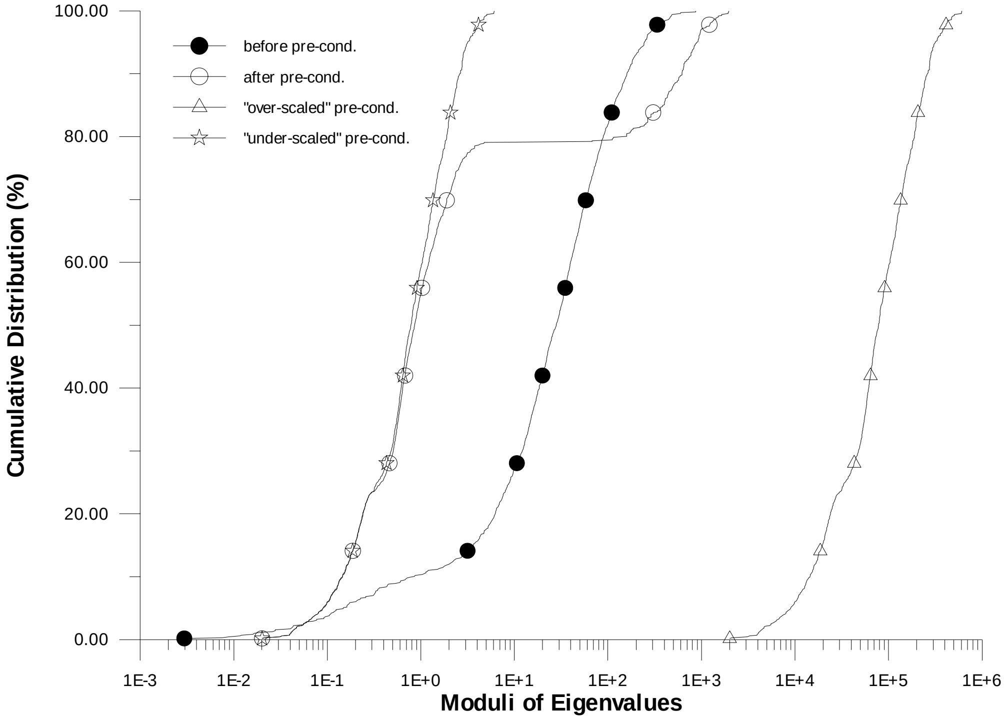

Figure 3.27 Eigenvalue distribution of CONSO3 before and after different variants of diagonal preconditioning

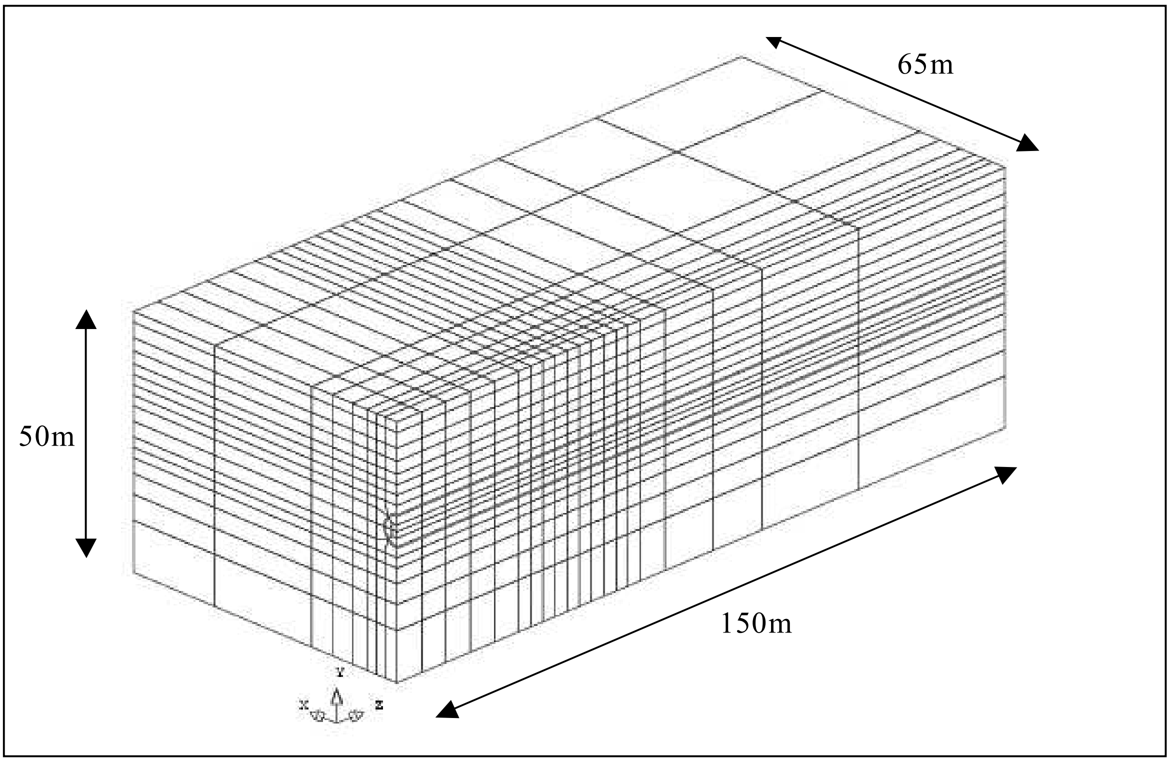

Figure 3.28a Single Tunnel Mesh (3120 3-D elements)

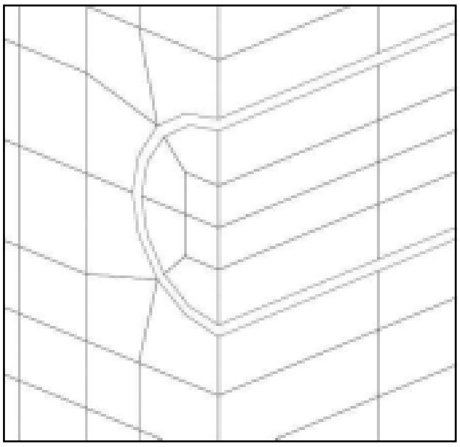

Figure 3.28b Tunnel geometry closed-up

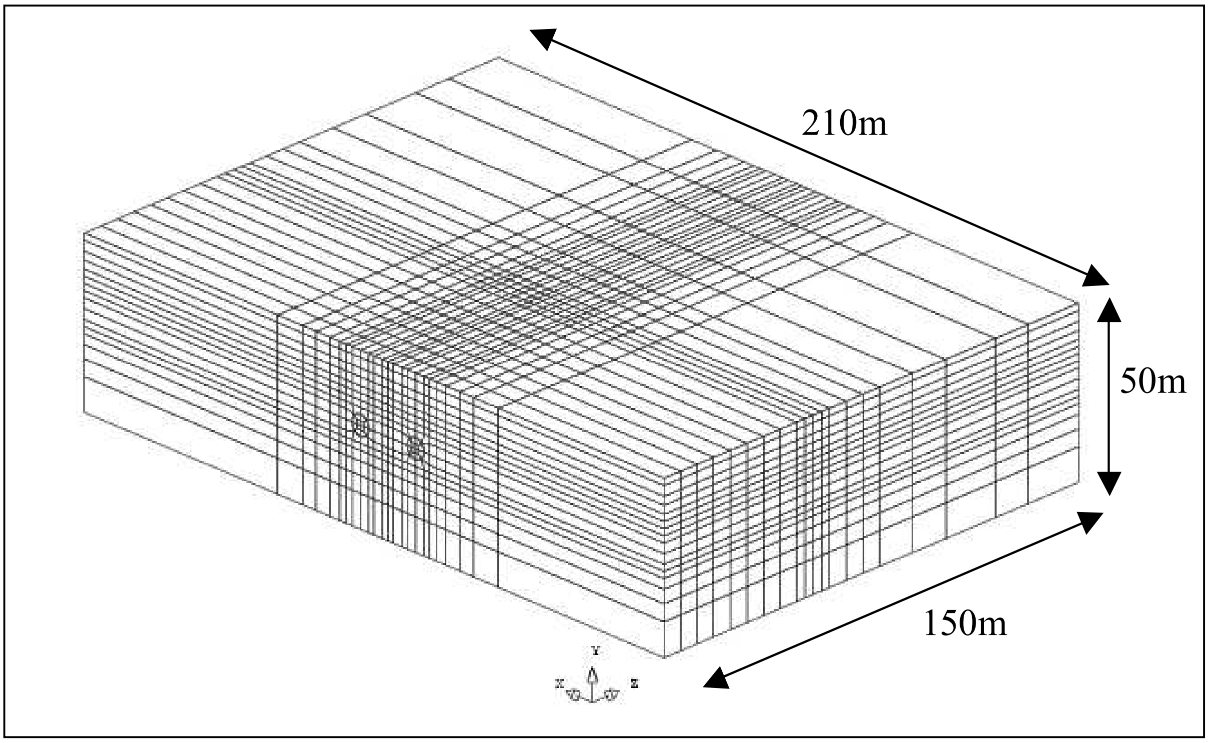

Figure 3.29a Twin-Tunnel Mesh (9920 3-D elements)

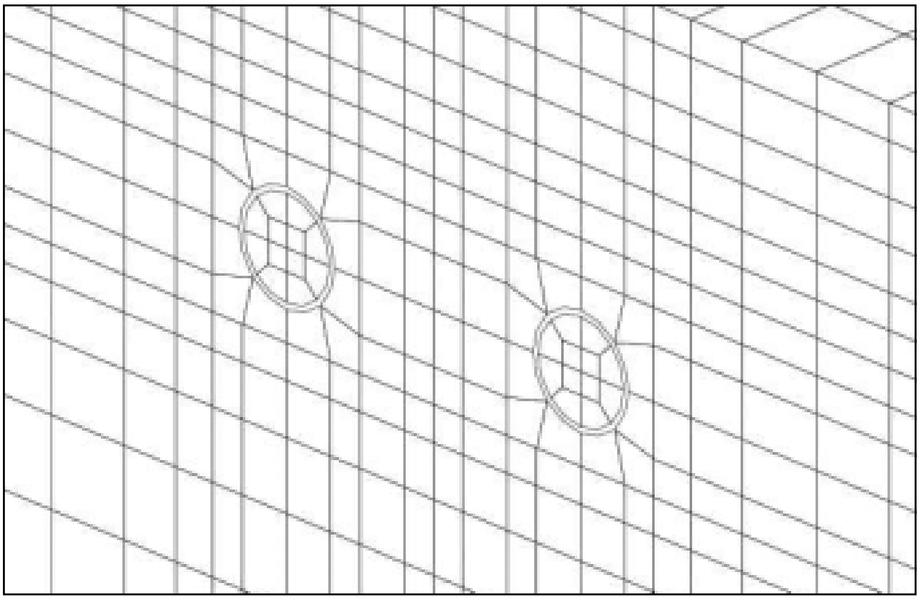

Figure 3.29b Twin-Tunnel geometry closed-up

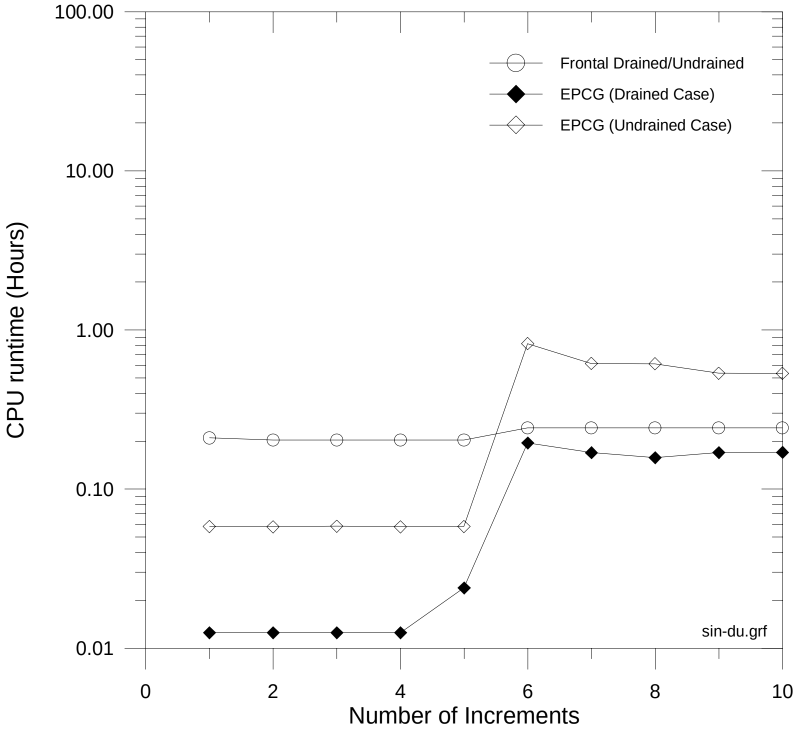

Figure 3.30a CPU runtime for single tunnel drained and undrained cases

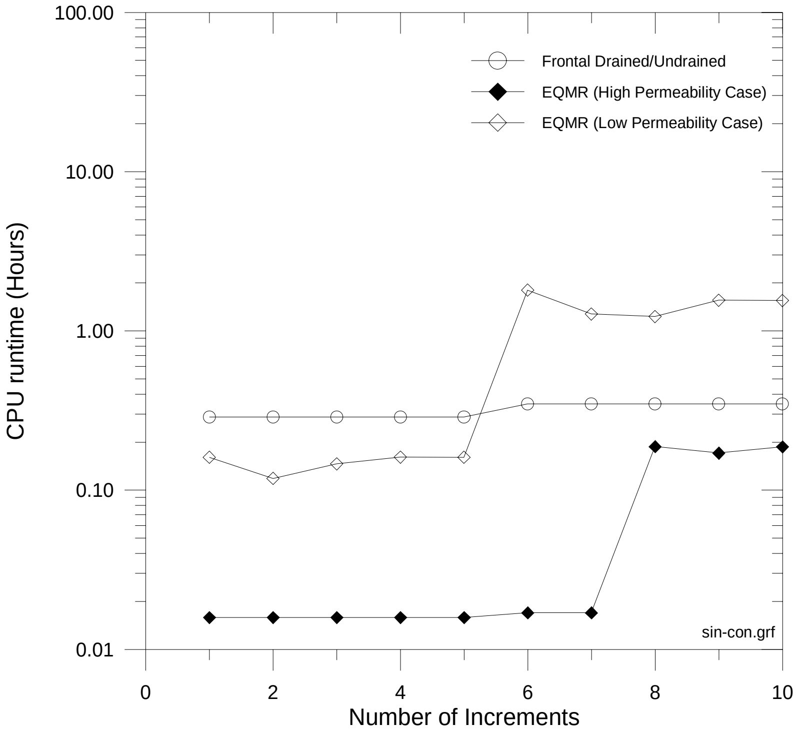

Figure 3.30b CPU runtime for single tunnel consolidation cases

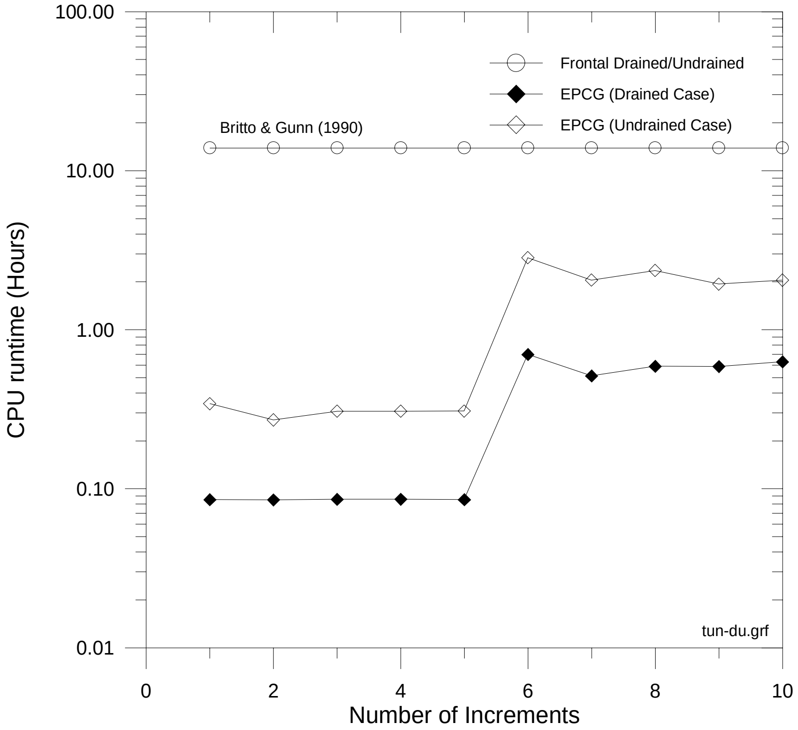

Figure 3.30c CPU runtime for twin tunnel drained and undrained cases

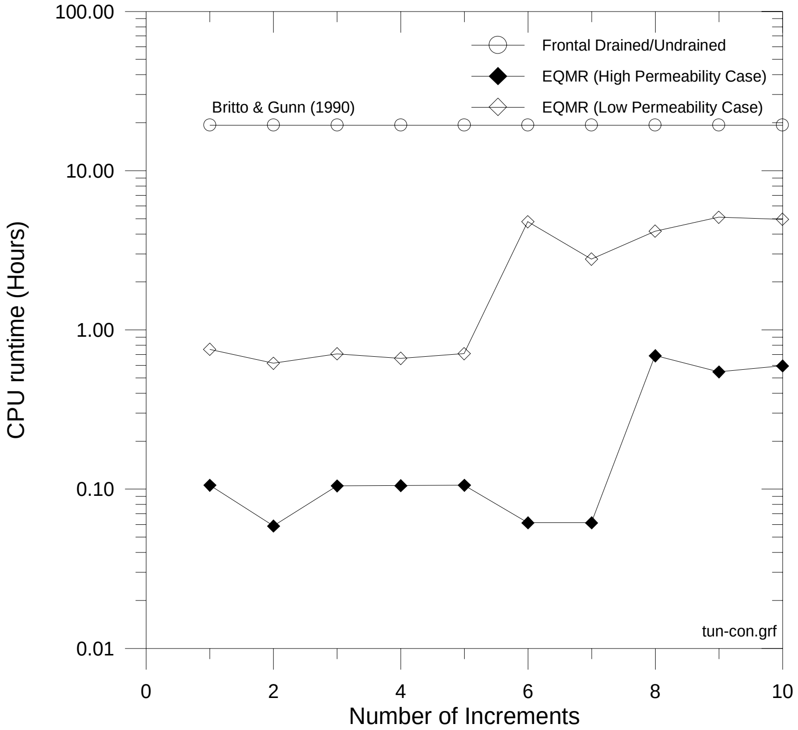

Figure 3.30d CPU runtime for twin tunnel consolidation cases

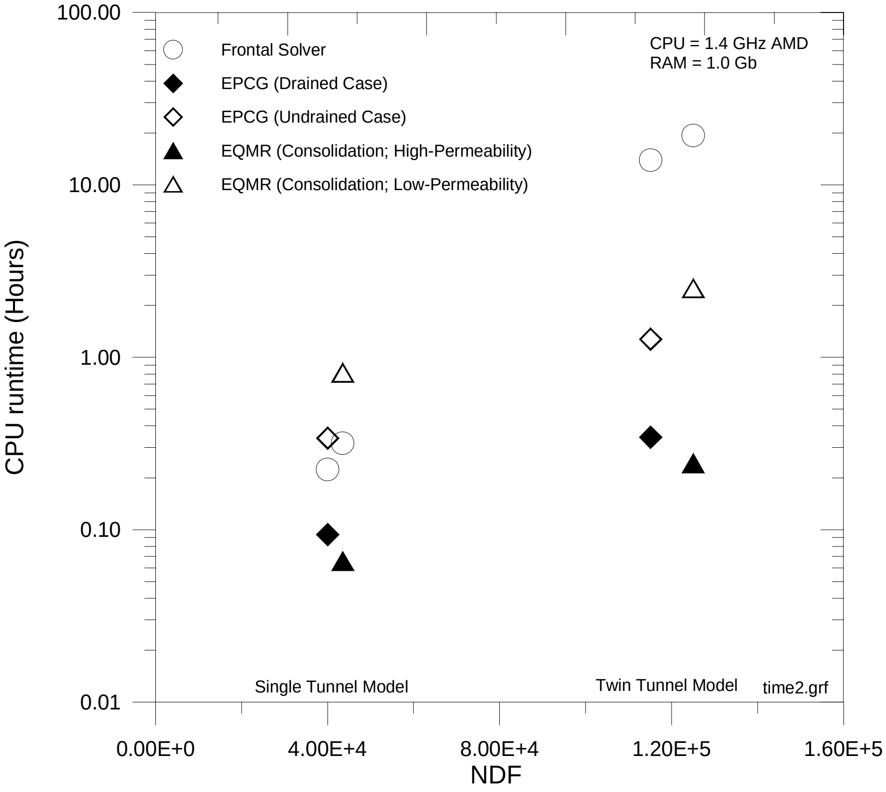

Figure 3.31 Average timings using various solvers

4 A Case study of EPB Tunnelling

4.1 General Information of C704

The tunnelling project studied herein is the North East line (NEL) tunnel, contract C704 segment. The North East line (NEL) is part of the Singapore Mass Rapid Transit system and has a total underground route length of 20 km. Figure 4.1 shows the layout of the NEL tunnels in Singapore. The NEL project consists of the construction of about 20 km of tunnels and 16 stations, connecting the World Trade Centre at the southern part of the Singapore island to Punggol at the northeast part of the island. The construction of the tunnels and stations started in 1997 and took 5 years to complete. The civil engineering works were divided into 12 packages and C704 was one of them. C704 is separated into two sections with a total route length of 2.5 km and two cut-and-cover stations, namely Woodleigh and Serangoon stations. From Woodleigh to Serangoon stations, the twin-bored tunnels are 1 km in length while from Serangoon to Kovan stations; the twin-bored tunnels are 1.5 km long. Kovan station was part of the works of C703. The C704 tunnels were completed in October 2000 using two LOVAT RME257SE Earth Pressure Balance (EPB) machines. The contract also includes the construction of approximately 1.7 km of dual-lane viaduct. In addition, two dual carriageway underpass structures are located at Boundary/Upper Paya Lebar roads and Bartley/Braddell roads. Due to the cohesive nature of residual soils, this tunnel was constructed using EPB shields rather than conventional slurry shields. C704 will be used as a case study to validate the finite element procedures and codes.

4.2 Geological Information

A total of seventy-seven (77) numbers of boreholes were sunk along the tunnel route segments. Forty four boreholes were sunk between Woodleigh and Serangoon stations and thirty-three (33) boreholes were sunk between Serangoon to Kovan stations. As shown in Figure 4.2, the C704 tunnels passed through two major geological formations, namely the Bukit Timah Granite (Woodleigh to Serangoon) and the Old Alluvium (Serangoon to Kovan) formations. Since this study uses data from the Woodleigh-Serangoon segment, the discussion below will focus mainly on the geological and geotechnical information of the Bukit Timah Granite formation. In particular, soil data from the first 300–metre segment starting from Serangoon station and going towards Woodleigh station direction will be interpreted in detail. This is to complement the comprehensive range of soil instrumentation and results available at this segment.

As defined by PWD (1976), the Bukit Timah Granite formation refers to an entire suite of igneous rocks, principally granite, adamellite and granodiorite. Dames and Moore (1983) classified the Bukit Timah formation into four sub-layers taking into account of the degree of weathering. The physical descriptions and its sub layer properties are summarised in Table 4.1 and Table 4.2 respectively.

As shown in Figure 4.3, the top few metres of soil is almost invariably man-made fill material, the mechanical properties of which are highly variable and indeterminate. Below this, down to the tunnel springline depth of approximately 21 m ~ 25 m, completely weathered granitic saprolites, designated by the code G4, are commonly encountered. As shown in Figure 4.3, the tunnel profile lies almost entirely in the RSG4-b residual soil.

4.3 Geotechnical Properties of G4 soils

This section summarizes the soil properties along the tunnel alignment and discusses the basis for selection of soil parameters in the later stage of this study. The soil data were compiled primarily from three sources viz. in-situ and laboratory tests conducted from the soil samples extracted from the boreholes in Figure 4.3 and previously published material on G4 soils e.g. Dames & Moore (1983), Wang (2003), Poh et al. (1985), Leong et al. (2003). The soil properties that will be discussed in the following sections include the strength, permeability and compressibility.

4.3.1 Basic Properties

Figure 4.4 shows the variation in bulk unit weight, moisture content, Atterberg limits and percentage of fine grain with depth.

The average natural water content (w) is about 30 % and is generally on the lower range of the plasticity index PI (Liquid limit (LL)– Plastic limit (PL)). Figure 4.5 shows the liquidity index $LI = \frac{w - PL}{PI}$, which ranges from –0.2 to +0.4; with the majority of the samples lying in the positive region. Furthermore, as Figure 4.5 shows, there appears to be a decreasing trend of liquidity index as the depth increases. This implies that the G4 soil at this location is likely to behave like a plastic material when sheared. Using Skempton and Northey's (1953) data from a range of different soil types, Wood (1983) showed that the undrained shear strength of the soil at its plastic limit is likely to lie between 170 kPa and 220 kPa. Wood (1983) also proposed a semi-empirical relationship for estimating the undrained shear strength C_u of a soil given its liquidity index *LI*, which is given by

$$C_u = 170\ e^{-4.6LI}\ (\text{kPa}) \qquad (4.1)$$

Using LI = 0.4 and -0.2 return C_u values of 27kPa and 427kPa. However, since Skempton and Northey's (1953) data lie largely between the plastic and liquid limits, Wood's (1983) relationship may not give reasonable values for water contents which are below the plastic limit. Thus, the C_u value of 427 kPa may not be realistic. However, what we can conclude thus far is that, since most of the samples have *LI* lying between 0 and 0.4, the range of undrained shear strength is likely to lie largely between 27 kPa and 170 kPa and increases with depth. This is consistent with the measured undrained shear strength data shown in Figure 4.7.

As shown in Figure 4.6, the soil can be described as a clay of intermediate to high plasticity. This indicates that the proportion of clay-sized particles is likely to be high enough to dominate the soil behaviour. On the other hand, the range of particle size distribution shown in Figure 4.8, shows a preponderance of silt-sized particles, with silt-sized particles making up between 40 % and 75 % of all particles, by mass. On the other hand, clay-sized particles only make up between 10 % and 36 % of all particles, by mass. The apparent inconsistency in the trends of these two measurements is also evident in Dames & Moore's (1983) data and is readily explained by the fact that only about 20 % to 30 % of the particles needs to be clay for the soil to behave in a clay-like manner (Holtz and Kovacs, 1981).

4.3.2 Strength Parameters

Drained and undrained strength parameters were obtained from triaxial compression tests that were carried out in C704 tunnel route and Serangoon station. The laboratory tests, which were conducted in accordance with British Standards Code of Practice BS 1377 (1999), were Unconsolidated Undrained Triaxial Compression Tests (UU), Consolidated Undrained Triaxial Compression Tests (CU), Consolidated Drained Triaxial Compression Tests (CD) and Direct Shear Tests (DS).

The variation of soil strength against depth is shown in Figure 4.7. As mentioned earlier, the soil type G4 can generally be categorized into four separate sub-layers, the strength and SPT blow counts of which are presented in Table 4.2. As shown in Figure 4.7, the undrained shear strength and SPT blow counts shows an increasing trend with depth, corresponding to the reducing degree of weathering. However, both parameters also show significant scatter about the trend, which is similar to that obtained by Dames and Moore (1983). This suggests that the pattern and degree of weathering, and thus the soil properties vary substantially from one borehole to another. As Figure 4.7 shows, the undrained shear of the soil at the depth where the tunnel is to be driven ranges from 75 kPa to 150 kPa. This is a wide range of variation and probably explains the variability in the measured ground response to tunnel.

As observed in Figure 4.7, it shows a general trend for strength to increase with depth through the weathering profile. However, the wide distribution of data points does not allow a linear profiling of the strength against depth. Dames and Moore (1983) recommended that due to the changes in topography, natural erosion in different levels of the weathering profile, the proposed design profiles are based on mean strength less the standard deviation. This approach was similarly adopted and reflected in Table 4.3.

The effective stress parameters have been estimated from DS, CD and CU tests. The test results against depth are shown in Figure 4.7. As can be seen, the trends of changes in c'(effective cohesion) and ϕ' (internal friction angle) are even less evident than that for C_u . The c' values appear to show an initially increasing trend with depth down to about 15 m. Beyond that, no significant changes can be observed. The shallow-depth ϕ' values appear to fall into two clusters, with one cluster having a ϕ' of about 32° and the other having ϕ' of less than 10°. Since soil minerals rarely have ϕ' less than 10°, this cluster of lower ϕ' values must be treated with suspicion.

4.3.3 Compressibility

The compressibility of the soil type G4 can be determined by using the following parameters Compression Index (C_c) and Recompression/Swelling Index (C_r). Figure 4.9 shows the variation of compressibility, initial void ratio (e_o) and Overconsolidation ratio (OCR) of soil type G4 against depth. The values are summarised in Table 4.3.

Wang (2003) have suggested empirical relations of the indices and OCR with depth for G4 soil as follow:

$C_c = -0.0024N + 0.2774$

$C_r = -0.0007N + 0.0514$ and

$e_o = -0.0115N + 1.0667$ where N is the SPT blow counts

$OCR = 5.238H^{-0.4717}$ where H is the depth of the soil.

Wang's (2003) empirical relationships were superimposed into the C704 data and as shown in Figure 4.9, the empirical relationships matches the field data reasonably well. Since not much C_c and C_r tests were being conducted for the third layer (CW-G4a). These empirical relations were used to compile the values as shown in Table 4.3.

4.3.4 Permeability

Permeability was measured using the "Falling Head In-Situ Permeability" tests. As shown in Figure 4.10, the permeability (k) results are plotted against depth with values ranging from $6x10^{-8}$ m/s to $2x10^{-6}$ m/s. The average values are summarised in Table 4.3. Limited field permeability tests were conducted for the third (weathered rock) layer (CW-GS4a). Wang (2003) reported some tests data collected using the same tests (permeability) at Serangoon Station site, which lie in the range from $1x10^{-8}$ m/s to $1x10^{-7}$ m/s. This set of results is consistent with the findings of Dames & Moore (1983).

4.3.5 Coefficient of Earth Pressure at Rest (K_o)

Pressuremeter Tests were used to estimate the coefficient of earth pressure at rest (K_o). This is done using the corrected pressure at rest (P_o), assuming it equals the in-situ effective horizontal load. The results were compiled in Figure 4.11 and summarised in Table 4.3. Typical K_o ranges from 0.5 to 2.0. This is generally consistent with Dames & Moore's (1983) data, which showed K_0 ranging between 1.0 and 2.0.

4.3.6 Depth of Groundwater Table

Water standpipes are installed at various locations to study the natural ground water table of C704 project site. The summary of groundwater measurements in standpipes were given in Figure 4.12 and the lowest ground water level is about 5 m below ground surface.

4.3.7 Summary of Geotechnical Soil Investigations

The data presented above show a high degree of variability, which suggests that ground conditions are likely to vary significantly from one point to another. In the interpretation of the instrumented data on ground response to tunnelling, this point needs to be borne in mind. Table 4.3 highlighted the values of the parameters which will be used as baseline data for finite modelling purposes.

4.4 Geotechnical Instrumentation of tunnel route

The length of tunnel from Serangoon to Woodleigh station is about 1 km. Several sections were monitored during the tunnelling process. This study is focusing mainly on data collected from the first 300 m. Figure 4.13 shows the location of the monitored sector. This sector is further divided into five monitored sections namely L1 to L5. From sections L1 to L5, the average tunnel depth varies from 18 m to 21 m These sections were selected for this study as their conditions are near to “green-field” conditions, in that there are no buildings and foundations around the sections. It should be noted that the monitored area covers only about half of each section, this is because on the other half, ground conditions deviate significantly from “green-field”.

In C704 project, a 2-way vehicular viaduct was also constructed that runs parallel to the tunnel alignment. The cross sectional layout of the two tunnels is shown in Figure 4.14. As this figure shows, the viaduct is supported by the piers, which in turn are supported by pile groups of four 1.2 m diameter piles, spaced at 3.6 m centre-to-centre. The piles for the viaduct were constructed before the tunnels were bored to prevent loading on tunnel lining. This is important due to the proximity of the piles from the tunnel linings. In selecting the five monitored sections, one of the considerations applied was that they should not coincide with the locations of the piles.

Instruments, which have been installed along the tunnel route, were described by Coutts & Wang (2000). In the sector studied (see Figure 4.13), the monitoring instruments including the monitoring frequencies are tabulated in Table 4.4.

The South-Bound (SB) tunnel route was driven first followed by the North-Bound (NB) route. On average, the two tunnelling shield machines are about 300 m apart. The rate of tunnel advancement, based on three shifts a day and each shift of 8 hours, was about 4 m/day. On some occasions where machine was overheated or stopped for maintenance, the advancement rate would drop to as low as 1 m/day. The highest construction rate recorded at this segment was about 18 m/day.

4.5 C704 Ground Response

This section summarizes the surface and sub-surface ground response along the tunnel alignment and discusses the various instruments measurements with reference to the tunnel heading.

4.5.1 Surface ground movement: Trough width & Trough length

As shown in Table 4.5, the maximum settlement varies from about 5 mm to 20 mm. The average maximum settlement is about 12 mm. The large variation in maximum settlement is a reasonable reflection of the ground, which is highly variable. The normalised settlement troughs for the South Bound tunnel are shown in Figure 4.15a. The troughs represent the shape after the South Bound tunnel has already passed the monitored section for about 50 m i.e. ~ 8 D where D is the diameter of the tunnel. At this stage of tunnelling, the North Bound tunnel is still at its "launching" stage and tunnelling works have not begun. Thus, the presented settlement data in Figure 4.15a show the final settlement after the passage of one tunnel. Peck (1969), using data from a variety of tunnelling projects, postulated that the settlement profile of the ground surface across the tunnel cross-section can be approximated by a Gaussian distribution curve of the form

$$\delta = \delta_{\max} \exp\left(\frac{-x^2}{2i^2}\right) \tag{4.2}$$

in which x is the distance from the centreline.

O'Reilly and New (1983) suggested that the point of inflexion of the Gaussian distribution curve can be expressed as

$$i = kY_0 \tag{4.3}$$

where Y_0 is the depth from the ground surface to the springline level. As shown in Figure 4.15a, the normalized settlement curves are reasonably well-described by using

k = 0.5. This observation is consistent with data collected from Shirlaw (2001). CIRIA (1996) presented case history data for tunnels with depth greater than 20 m and back-fitted value of k ranging from 0.4 for stiff soil type to 0.6 for soft silty clays. They have highlighted the value $k = 0.5$ appears to be the best fit value for all cases studied.

The development of the settlement trough as the tunnel face approaches the monitored section is shown in Figure 4.16. In this figure, the distance between the tunnel heading and monitored is considered to be positive when the monitored section is in front of the tunnel face, and negative when the reverse occurs. For instance, settlement curve B with distance of +20 m refers to the settlement curve when the monitored section was 20 m ahead of the tunnel heading.

As shown in Figure 4.16a to d, settlement magnitudes are not uniform within the monitored site. In Figure 4.16a and c, about 40% to 50% of the final settlement has occurred when the tunnel heading reaches the monitored section. Furthermore, comparison of Figures 4.16a – d shows that up to the point when the tunnel heading reaches the monitored section, the maximum settlement of all four sections is in reasonably close agreement. In the case of L1 and L4, significant additional settlement occurs after the tunnel heading had passed the monitored section. This contrasts sharply with L2 and L5 which suffered little or no additional settlement (and indeed some small amount of heave) after the tunnel has passed through. For this reason, the differences in settlement between L1, L2, L4 and L5 is likely to be due to the differences in the tail void losses, rather than losses which occur in front of the tunnel face.

Attewell and Woodman (1982) have observed from field studies that the 3-D surface settlement follows a normal probability curve (see Equation 4.2) form for the transverse profile i.e. trough width while the longitudinal profile along the tunnel axis, also commonly known as trough length, follows a cumulative probability format shown below:

$$F_a = \int_{-\infty}^{a} \frac{1}{\sqrt{(2\pi)}} \exp\left(-\frac{t^2}{2} \right) dt \tag{4.4}$$

where t is a standardised normal random variable

Figure 4.17 shows the normalized bow wave along the tunnel longitudinal axis as compared to the empirical relationship (Equation 4.4).

The settlement data indicated that the first sign of vertical settlement was observed when the tunnel heading approaches within a distance of 8 D of the monitored section, which is about 2 to 3 times of the trough width point of inflexion. This is consistent with most literature reported [e.g CIRIA (1996), Hurell (1986)]. Settlement is normally stabilized when the tunnel face went ahead for about 30 m (~ -5 D) to 50 m (~ -8 D), which is again 2 to 3 times of the trough width point of inflexion. As Figure 4.17 shows, in some cases, heaving occurred just ahead or behind the tunnel heading.

4.5.2 Subsurface ground movement: Inclinometer & Extensometer

Subsurface measurements were taken via 2 inclinometers and 3 numbers of magnetic extensometer. The measured readings for the inclinometers were shown in Figure

4.18. The inclinometers measure both longitudinal and lateral movement i.e. parallel to the driving axis and perpendicular to the driving axis respectively.

Figure 4.18a shows the lateral (perpendicular to tunnel axis) movement of inclinometer I5101 when the South Bound tunnel advances through. The other inclinometer i.e. I5102 did not record any lateral movement owing to a damaged axis. As this figure shows, tunnelling-induced movement was recorded by I5101 when the tunnel heading was about 8 D away from the monitored section (see the curve marked "1" in Figure 4.18a). As the tunnel heading approaches the monitored section, the I5101 shows a movement away from the tunnel, this is attributable to the compression of the soil around the tunnel face. As the tunnel passes through the monitored section, the ground moves back towards the tunnel centreline, finally stabilizing at –8 D standoff at a slightly larger lateral movement than that recorded initially at +8 D. In general, the movements are relatively small, being no more than about 3mm in either direction. As shown in Figure 4.18c, inclinometer I5102 shows a longitudinal movement away from the tunnel face, followed by movement towards the tunnel face. It is likely that this longitudinal movement is heavily dependent upon the face pressure which is used at a point.

Three sets of Magnetic Extensometer were used to monitor the vertical subsurface ground movements. These were all found in section L3 of the monitored site. Figure 4.19 shows the cross sectional view of the instrumented location. As can be seen, there are three lines of extensometers. For lines MX5102 and MX5101, readings were taken at a depth of about 1 m below the ground surface. Line MX51011 has three measurement depths for subsurface vertical settlement.

As shown in Figure 4.20a, the settlement trend of lines MX5101 and MX5102 reflects the development of the bow wave i.e trough length as the tunnel passes through the monitored section L3. Line MX51011 is not greatly affected by the driving of the south bound tunnel (Figure 4.20b). This is to be expected since this line of extensometers is relatively far away from the south bound tunnel. It is, however, much more significantly affected by the north bound tunnel which is much nearer (Figure 4.20c). In this figure, all three extensometers show heaving as the tunnel facing approaches, followed by settlement, ending up with a slight net settlement. This clearly differs from the bow wave development at the ground surface, and indicates that around the tunnel level, soil movement is likely to be much more affected by the buoyancy effect arising from removal of dead weight during tunnelling.

4.5.3 Ground Water response

Figure 4.14 shows the typical location for the pneumatic piezometers and standpipes. As this figure shows, groundwater standpipes were located within sections L1, L4 and L5. Two-tip pneumatic piezometers were used at this site. For section L1, the two-tip pneumatic instruments are located near to the springline and invert level i.e. less than 0.5 D away from tunnel excavated boundary while for section L4 and section L5; they are placed at depths approximately equivalent to 1 D above the crown and springline levels of the tunnel respectively.

Figure 4.21 shows the measured pore pressure variations as the tunnels advances through. The general trend is that when the tunnel is approaching, due to excavation, the pore water pressure drops. As the tunnel crosses the instruments, the pore pressure magnitude variations are not consistent across the monitored sections.

For L1 section as shown in Figure 4.21a, both pneumatic markers are showing consistent trend of losing pore water pressure as the tunnels approaching the pneumatic tips. As the tunnels advance through, the negative pore water pressures were equilibrated by the restoration of ground water level as such pore water pressure measured shows that it is moving back to its baseline level.

For L4 section as shown in Figure 4.21b, the pneumatic tips are generally decreasing due to excavation as the tunnels are approaching the instruments. However, when the EPB passes through the section, the pneumatic tip at the springline level is losing pore water pressure much faster than at the crown level.

For L5 section as shown in Figure 4.21c, when the southbound tunnel was approaching the pneumatic tips, both show signs of losing pore water pressure. Similarly, as the southbound tunnel advances through, the pore water pressure for both tips drops down and subsequently restoring to its baseline level.

From the above observations, when the tunnel approaches the sections, the removal of soil created a loss of total stress at the excavated surface and thus generating negative pore suction. Subsequently during the installation of the lining, the regeneration of an impermeable boundary leads to a recharging of water to its baseline level. If the groundwater seeps along the excavated surface i.e. permeable boundary then the general pore pressure variation would show a sharp decline in the water level as observed in Figure 4.21b’s springline level. It is interesting to note that under true field conditions, drainage conditions vary around the excavated tunnel boundary.

4.6 Summary of Field Results

This chapter serves as a benchmark as to how the ground behaves when an EPB tunnelling machine performs in a stiff residual soil. The results obtained from the field measurements have highlighted the following issues:

- When the tunnel machine advances far away from the monitored section, single tunnel ground surface settlement can be predicted accurately using the conventional empirical method (Gaussian method).
- Subsurface movement near the tunnel axis are affected by the performance of the tunnelling construction sequences.
- A well-supported face can reduce initial ground loss before the tunnel passes through the monitored section. A badly supported tunnel face with either too high or too low face pressure will affect the range of settlement.
- Ground water response is closely linked to the drainage conditions at the excavated boundary.

Table 4.1 Physical Description of the Granite Formation

Grade	Description
G1	Fresh to slightly weathered rock or Granite with stiffness range between strong to very strong granite or rock and a weathering grade between II and I.
G2	Moderately to highly weathered Granite and a weathering grade between II and IV. The weathering of the Bukit Timah Granite appears to pass very rapidly from weathering grade III to IV and tends to be indistinct and relatively thin transition zone. The stiffness range can be from weak to moderately strong rock and generally highly fractured.
G3	"Bouldery" soil to boulders exceeding 400mm in average dimension surrounded by completely weathered residual rocks and soils with a weathering grade between III and IV.
G4	Completely weathered rock or residual soil with a weathering grade between V and VI. In general, the soil is present, either to ground level or underlying some fills. It consist of clayey silt or sandy silt with stiffness range between firm and hard and of a medium dense to very dense silty sand, depending on depth. There are also deposits of firm to very stiff silty clay in variable extent and dimensions. Some quartz gravels were found locally.

Table 4.2 Sub-layers of G4

Depth (m) Below Ground Level	Thickness used in FEM Mesh (m)	Name of Sub-layer	Physical Description	SPT N Blows
2 ~ 15	7.5	RS-G4a	Residual soil consisting of Clayey Silt and Silty Clay.	2 ~ 20
15 ~ 30	32.5	RS-G4b	Residual soil consisting of Clayey Silt and Silty Clay.	10 ~ 60
35 ~ 50	10	CW-G4a	Completely weathered Granite consisting of Clayey Silt and Silty Clay.	20 ~ 100
50 ~ 60	Not simulated	CW-G4b	Completely weathered Granite consisting of Clayey Silt and Silty Clay.	30 ~ 100

Table 4.3 Typical G4 soil parameters found in C704

Sub-layer	RS-G4a	RS-G4b	CW-G4a
Thickness (m)	0 ~ 7.5	7.5 ~ 40	40 ~ 50
SPT N Values	11	31	50
C_u (kPa)	73 ± 26	80 ± 29	150 ± 26
c' (kPa)	19.8	19.6	20
ϕ'	19.2	24.2	30.5
C_c	0.26	0.24	0.16
C_r	0.041	0.054	0.0164
OCR	3	2	1.0
e_o	0.99	0.82	0.49
k (m/s)	$2.16\text{x}10^{-7}$	$1.46\text{x}10^{-6}$	$1\text{x}10^{-8}$ ~$1\text{x}10^{-7}$
K_0	0.86	0.65	0.51

Table 4.4 Monitoring Frequencies for Field Instruments.

Instrument	Quantities	Location of instruments	Location of tunnel face relative to instrumentation cross section	Monitoring Frequency
Settlement Markers	44	At L1 to L5	D_L > 50m	Two initial readings
Magnetic Extensometer	2	At L3	30m > D_L > 5m	Once per two days*
Inclinometer	8	At L1, L2, L4 and L5.	D_L < 5m	Once a day*
Pneumatic Piezometer	6	At L1, L4 and L5	D_L < 10m	Once a day

Where $D_L > 0$, the tunnel face is approaching the instruments &

$D_L < 0$, the tunnel face is away from the instruments.

* = Magnetic extensometer above each tunnel to be monitored at least three times.

** = Magnetic extensometer above each tunnel to be monitored once per two days until the distance is longer than 20m.

Table 4.5 Maximum Settlement due to single driven south bound tunnel.

Sections	L1	L2*	L3*	L4	L5
Maximum Settlement (mm)	17.2	7.5	8.5	13	7.5

* denotes maximum settlement found along the trough width

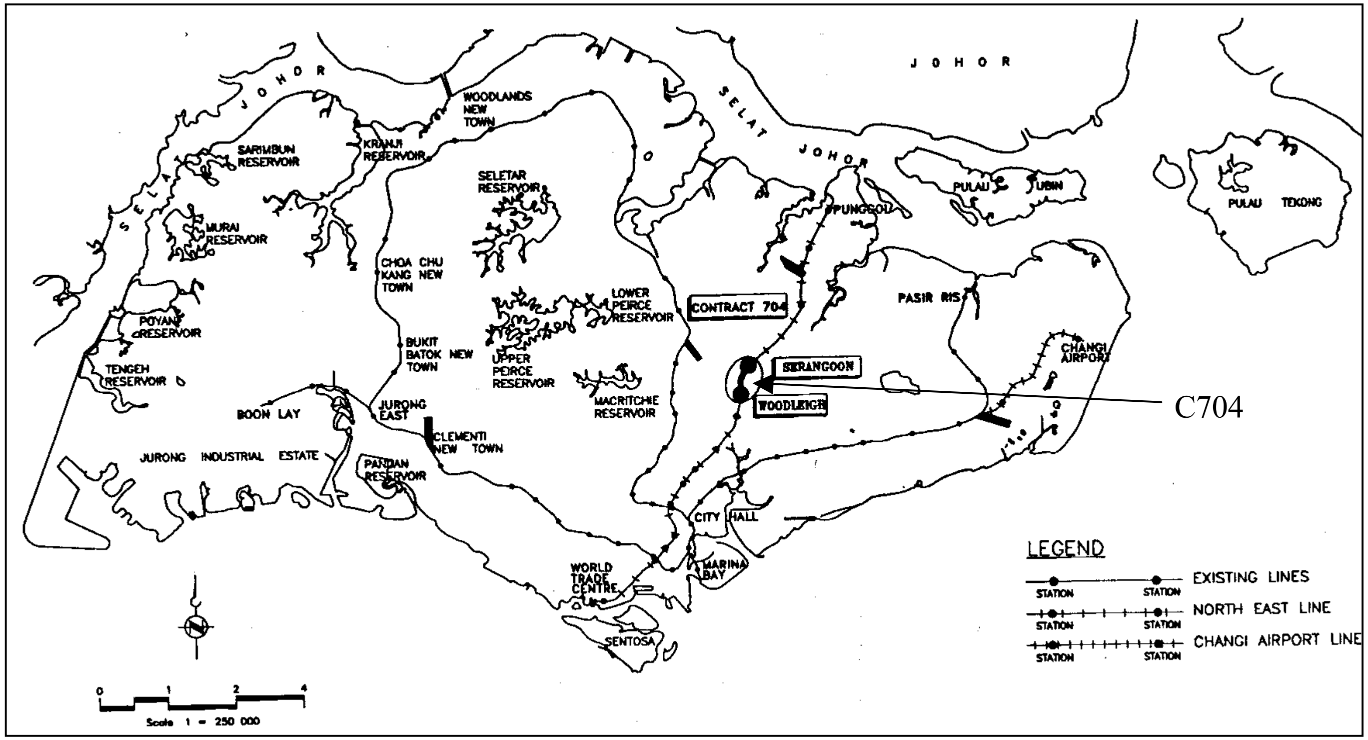

Figure 4.1 Locations of C704, North East Line in Singapore

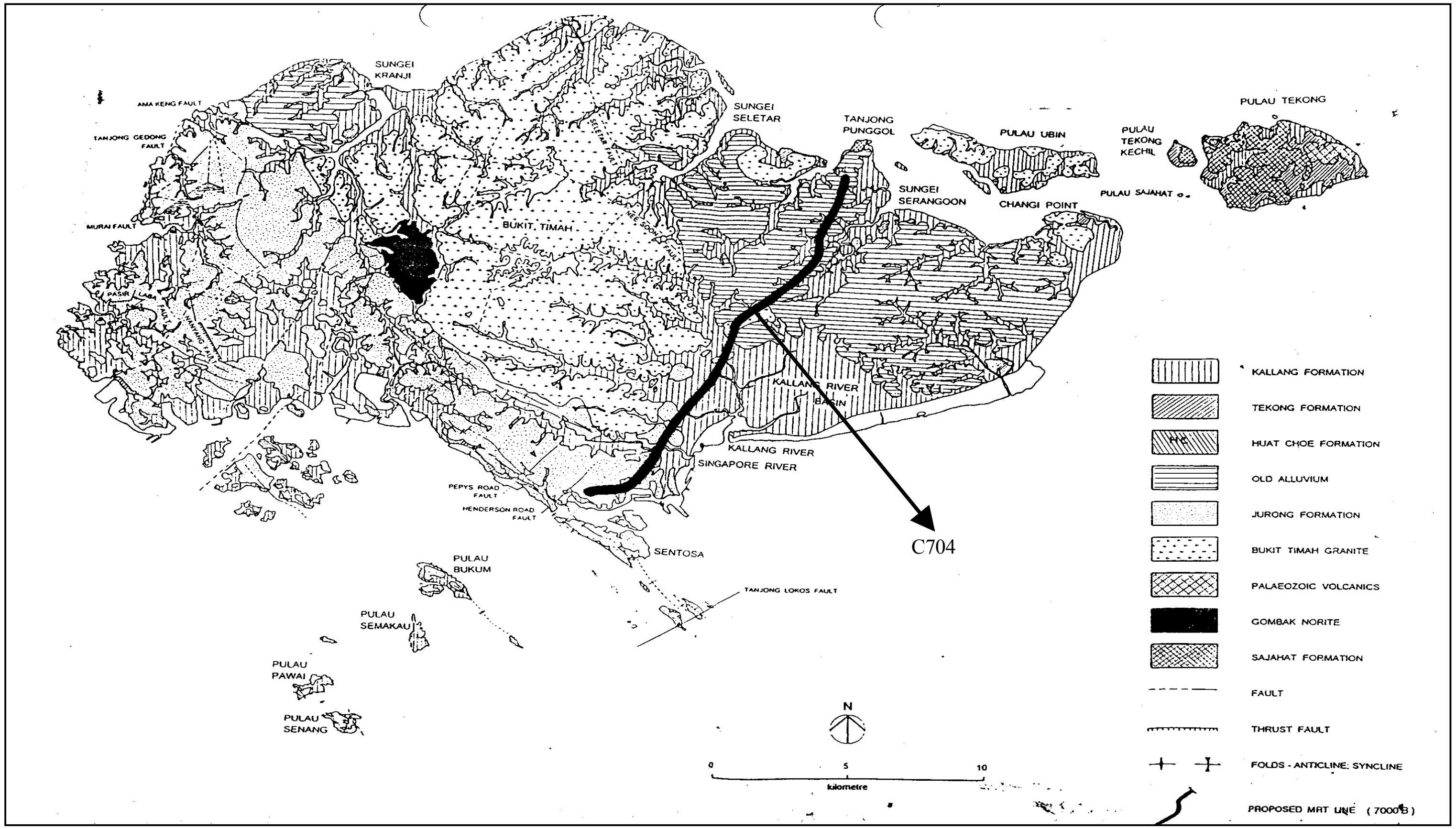

Figure 4.2 Geological Map of Singapore Island (PWD, 1976)

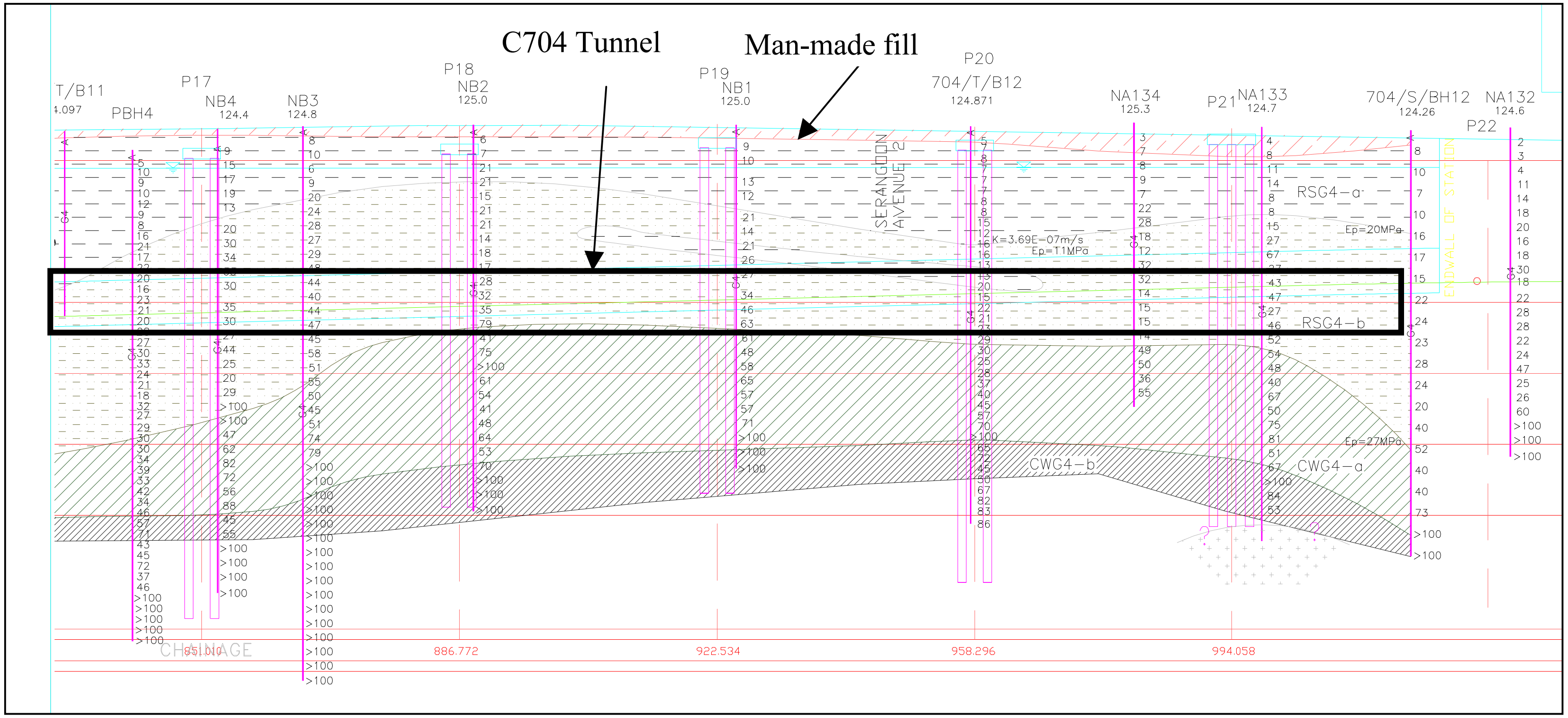

Figure 4.3 Subsurface soil profile of C704 project

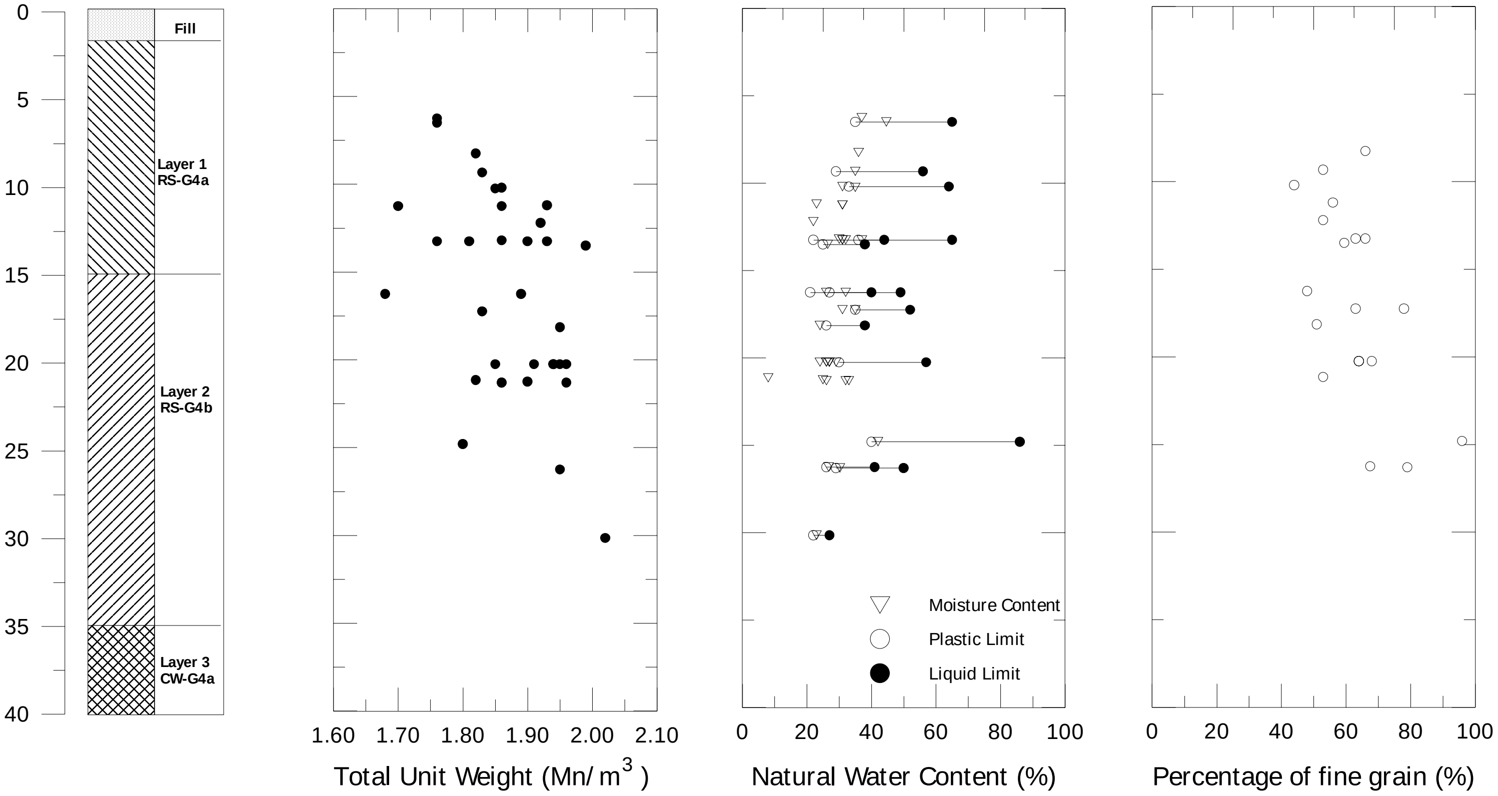

Figure 4.4 Variation of physical properties against depth at C704 tunnel route (Serangoon to Woodleigh)

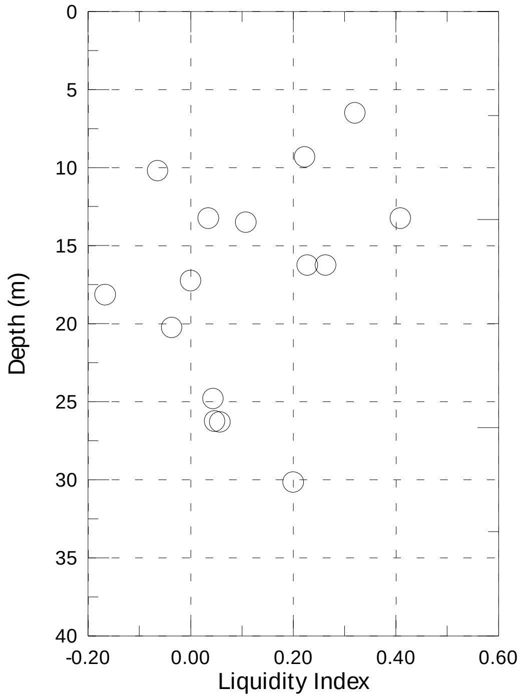

Figure 4.5 Liquidity Index of G4 soil

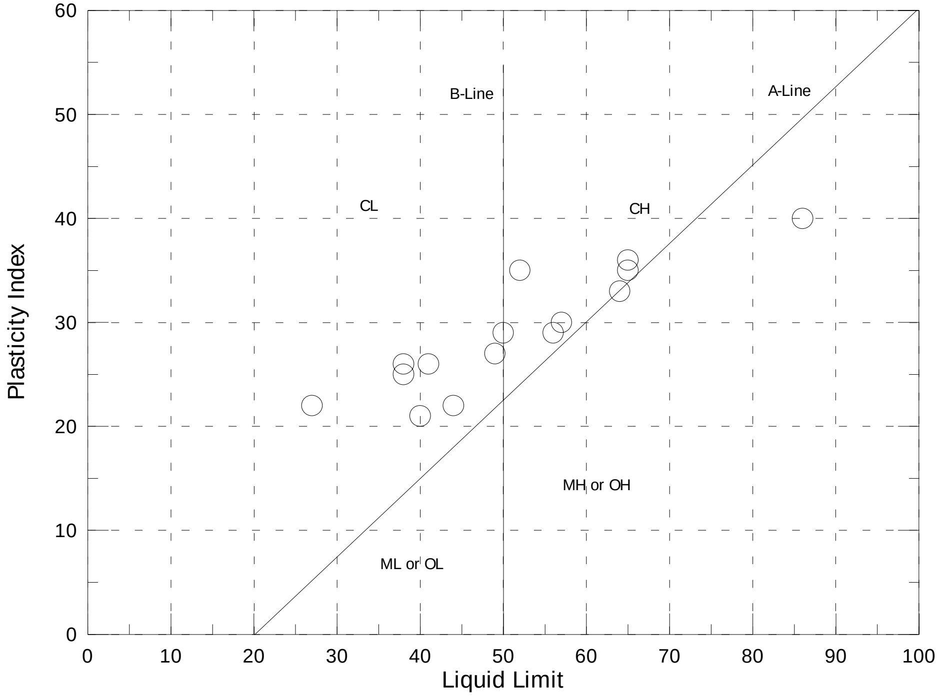

Figure 4.6 Atterberg Limits – Soil Type G4.

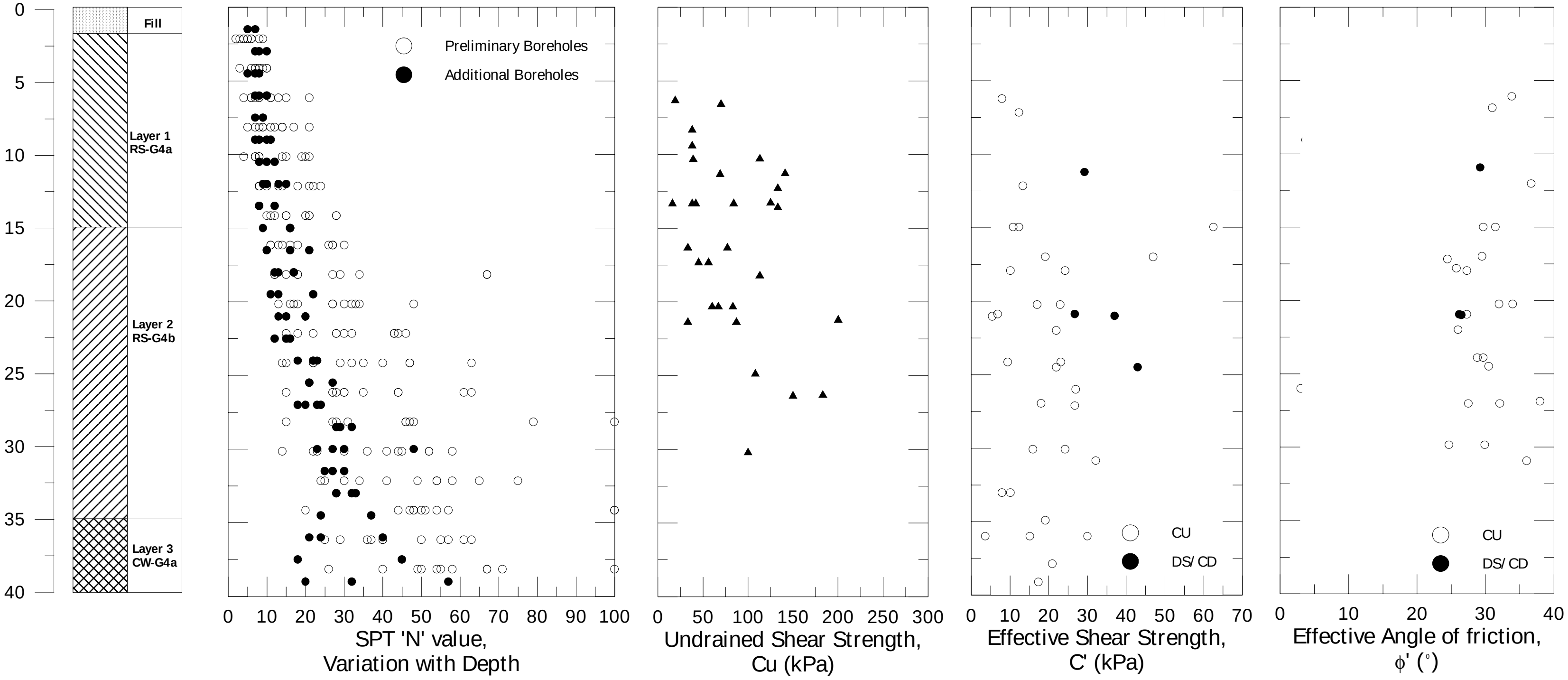

Figure 4.7 Variation of Drained and Undrained strength parameters against Depth at C704 for soil type G4

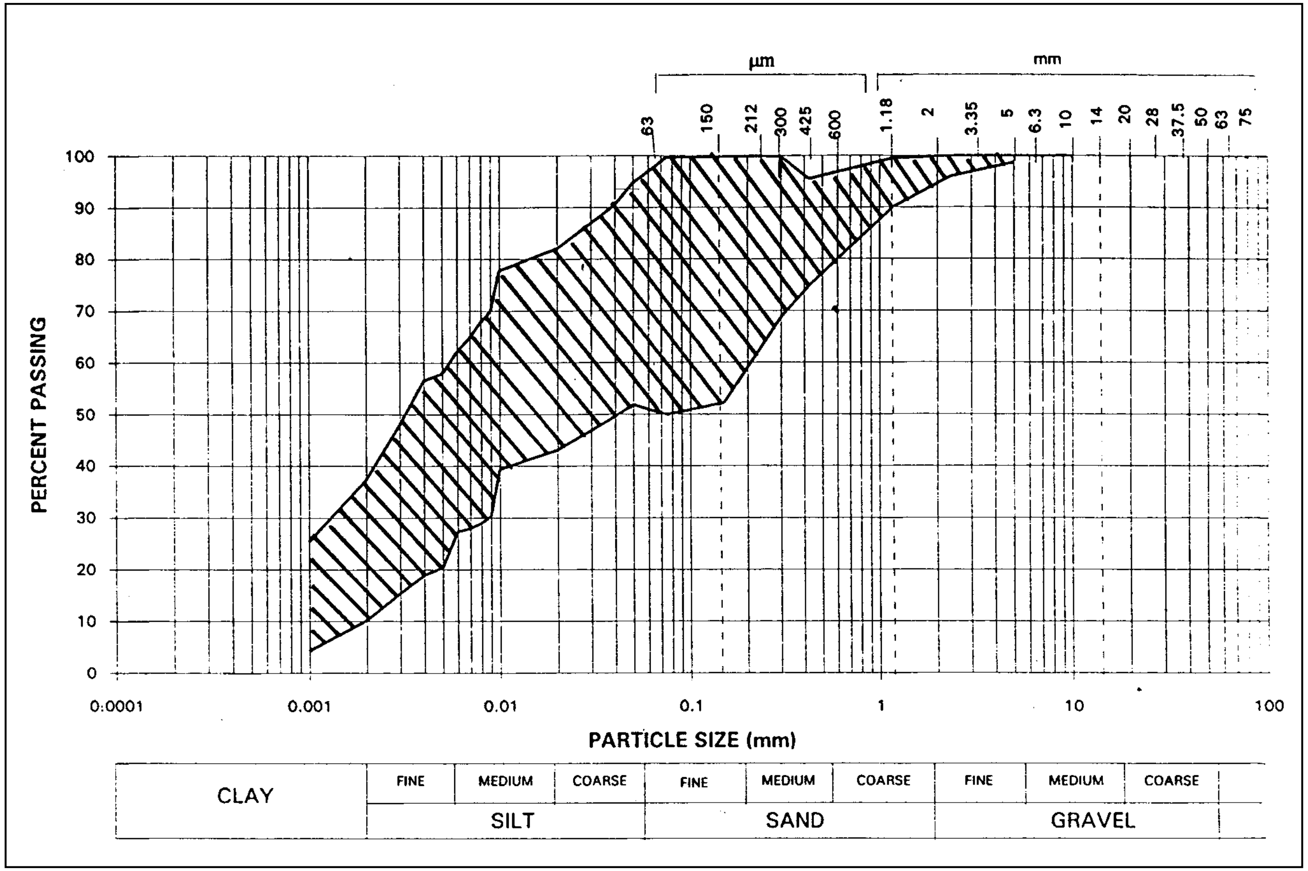

Figure 4.8 Typical grain size distributions for G4 soil at C704 tunnel route (Serangoon to Woodleigh)

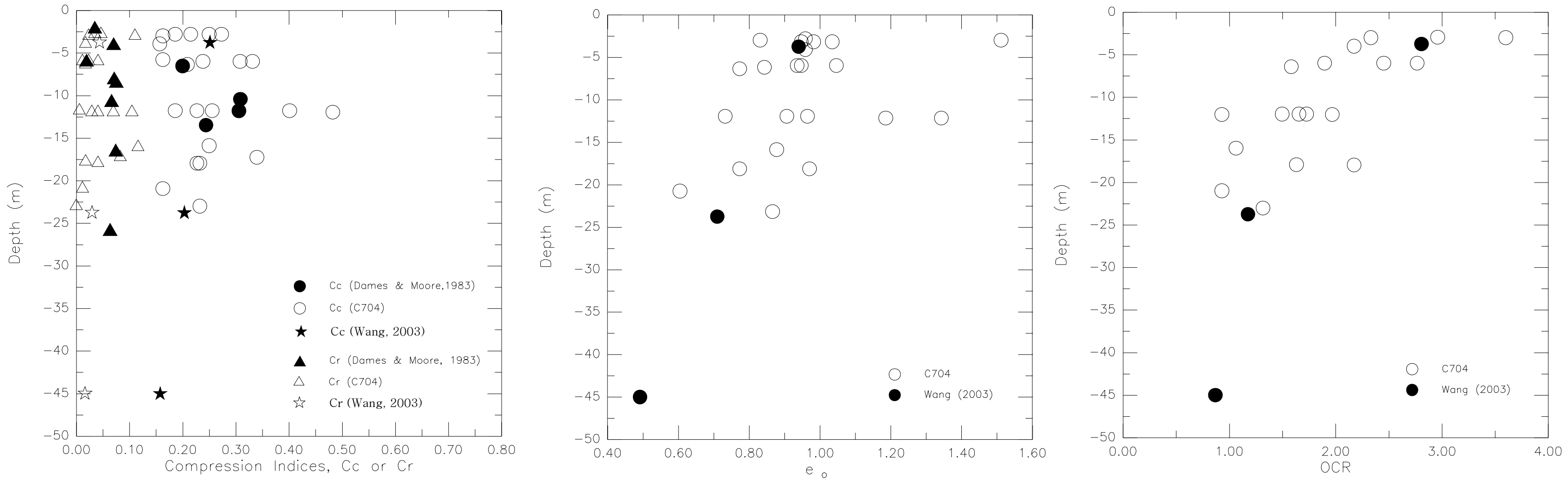

Figure 4.9 Variation of Compression parameters against depth.

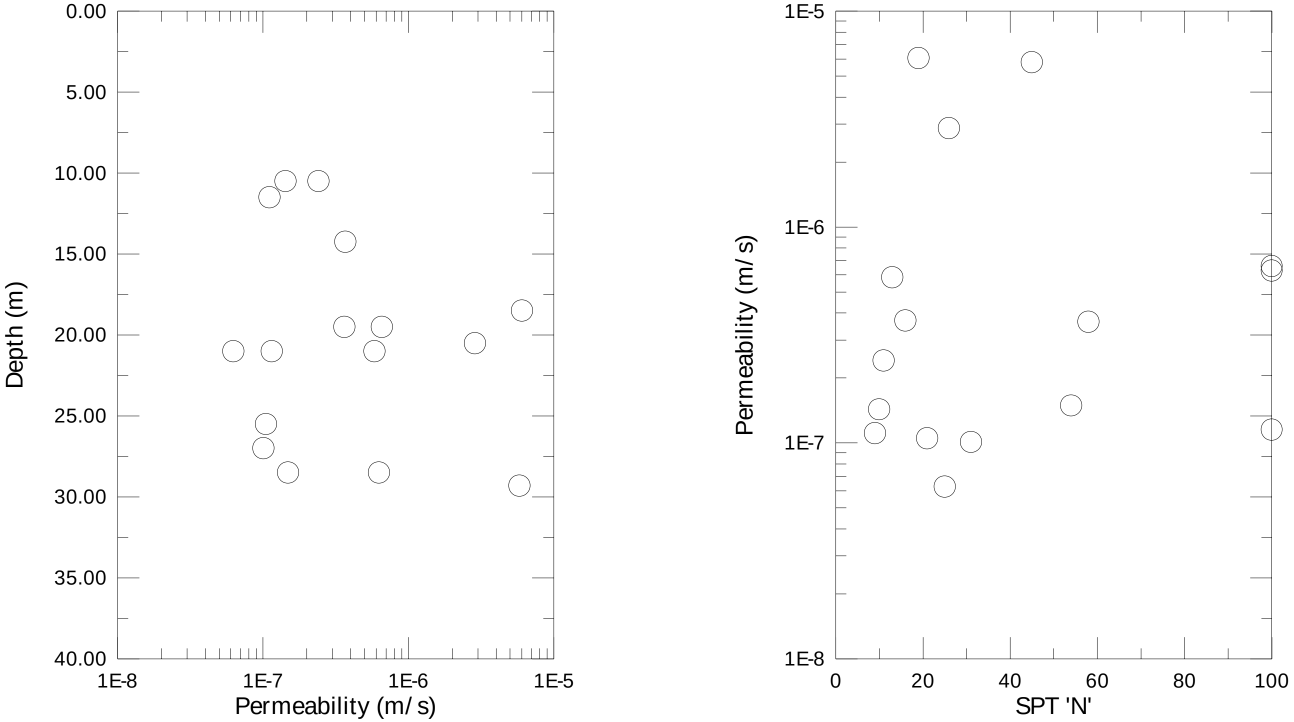

Figure 4.10 Variation of (i) Permeability against depth (ii) Permeability against SPT ‘N’.

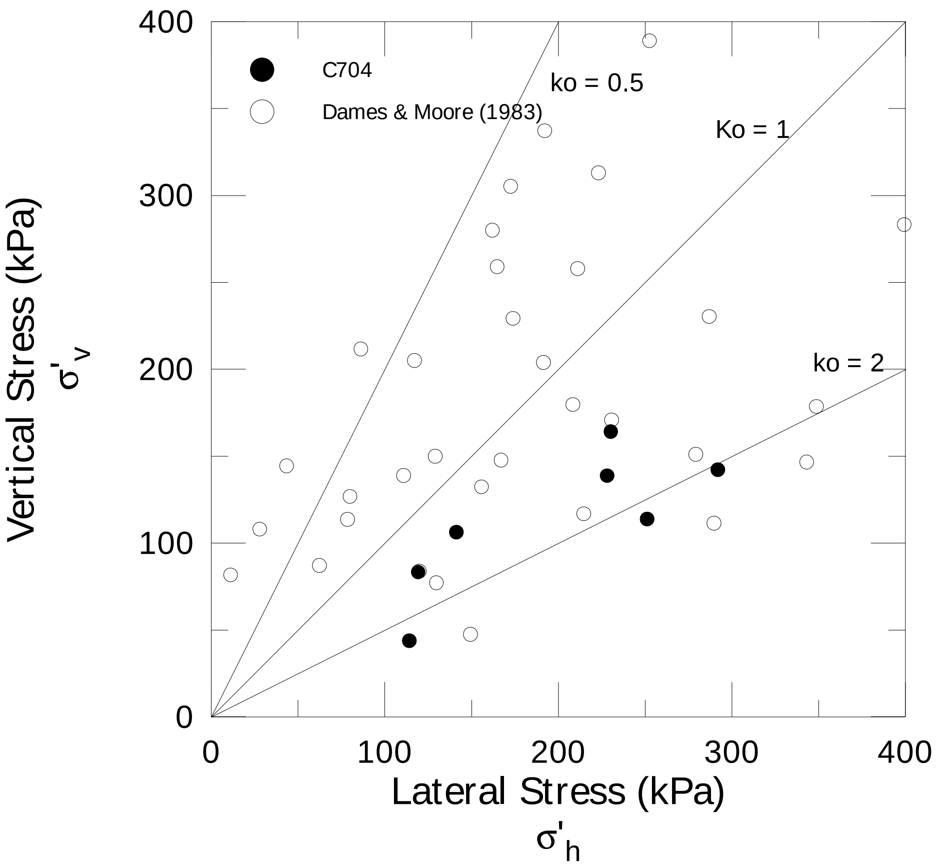

Figure 4.11 Horizontal effective stress from pressuremeter results (from Dames & Moore (1983) and C704 of soil type G4.

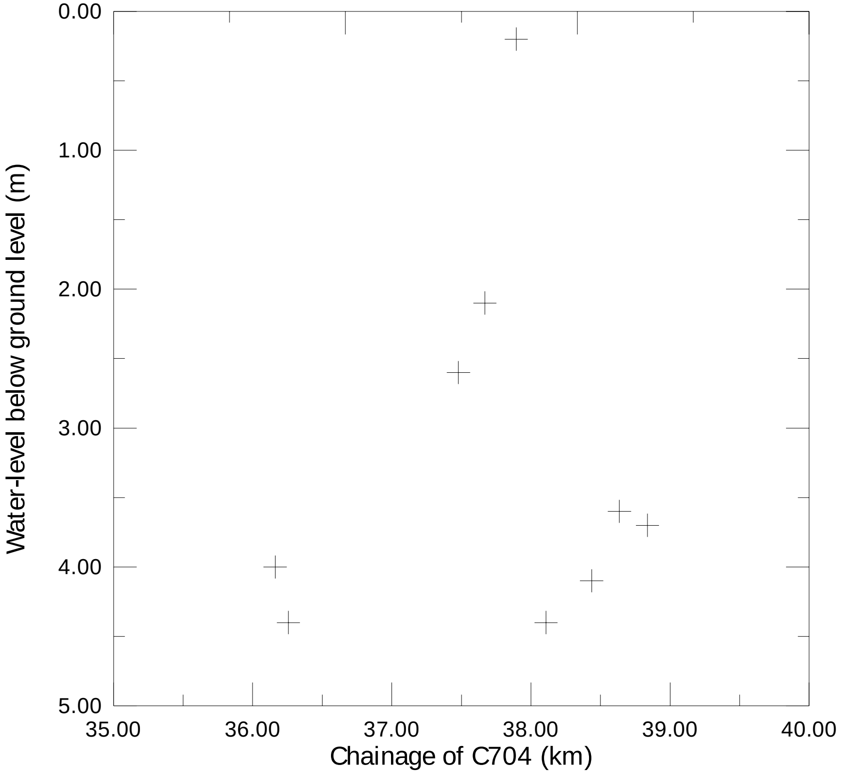

Figure 4.12 Ground-water level in standpipes.

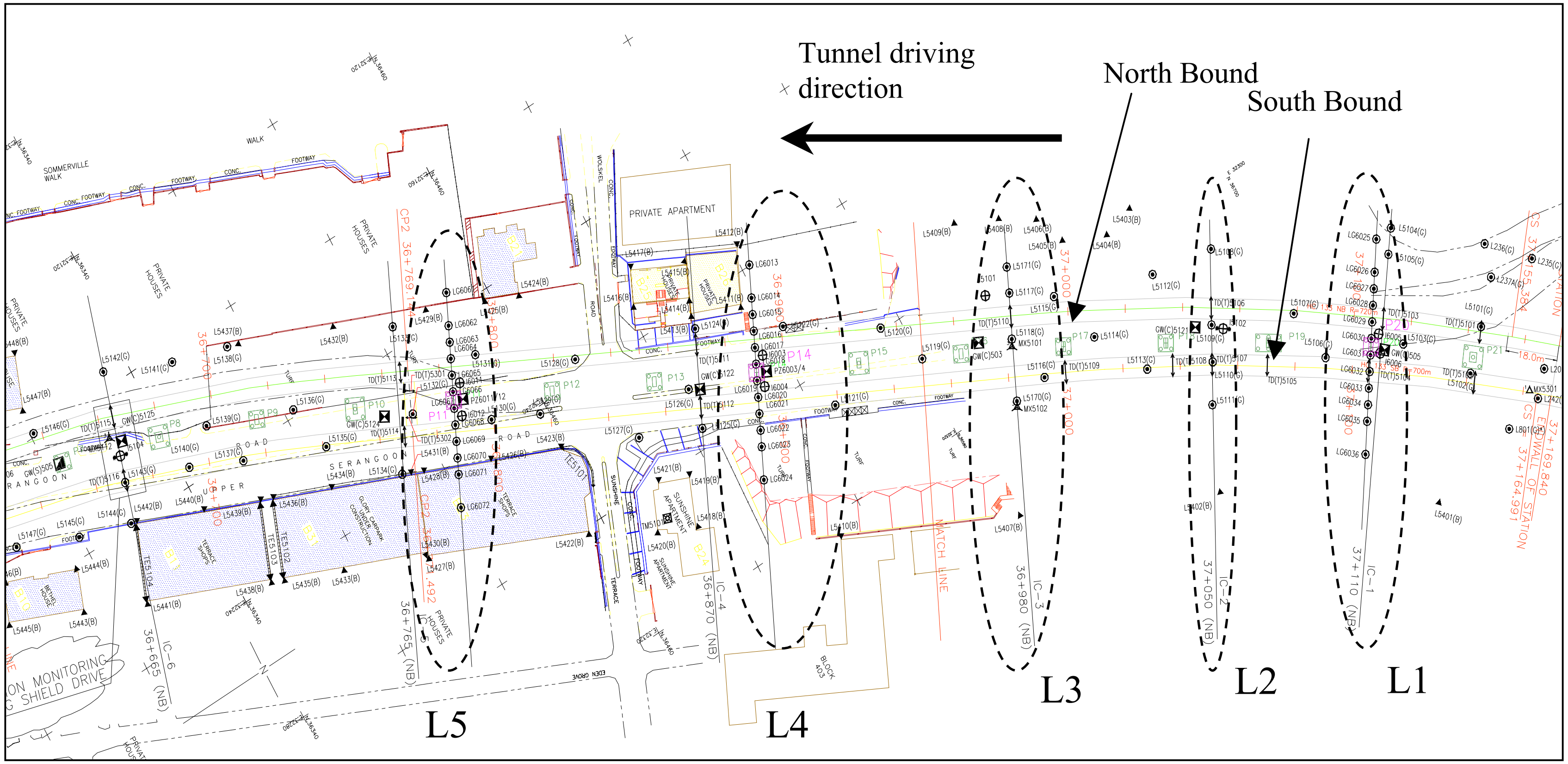

Figure 4.13 Monitoring sector in C704

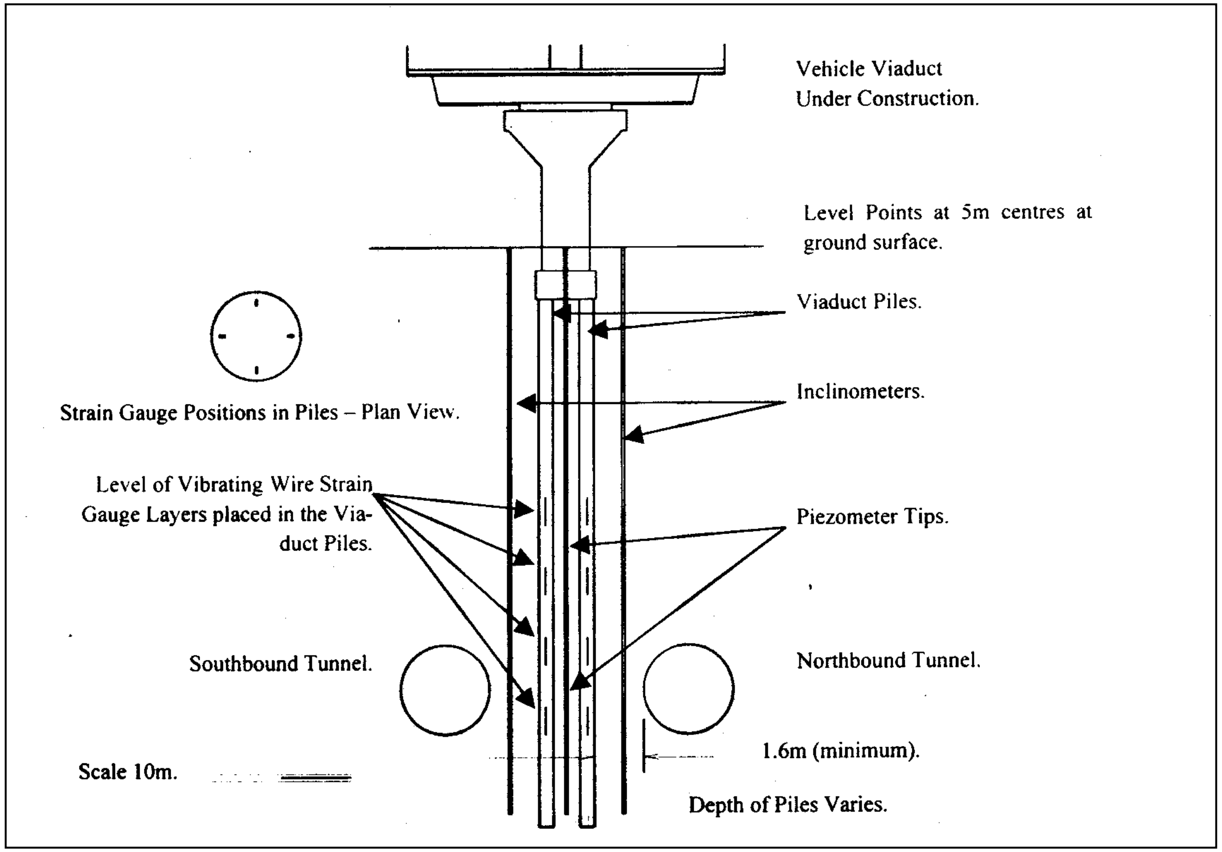

Figure 4.14 Layout of instruments in pile-group in C704.

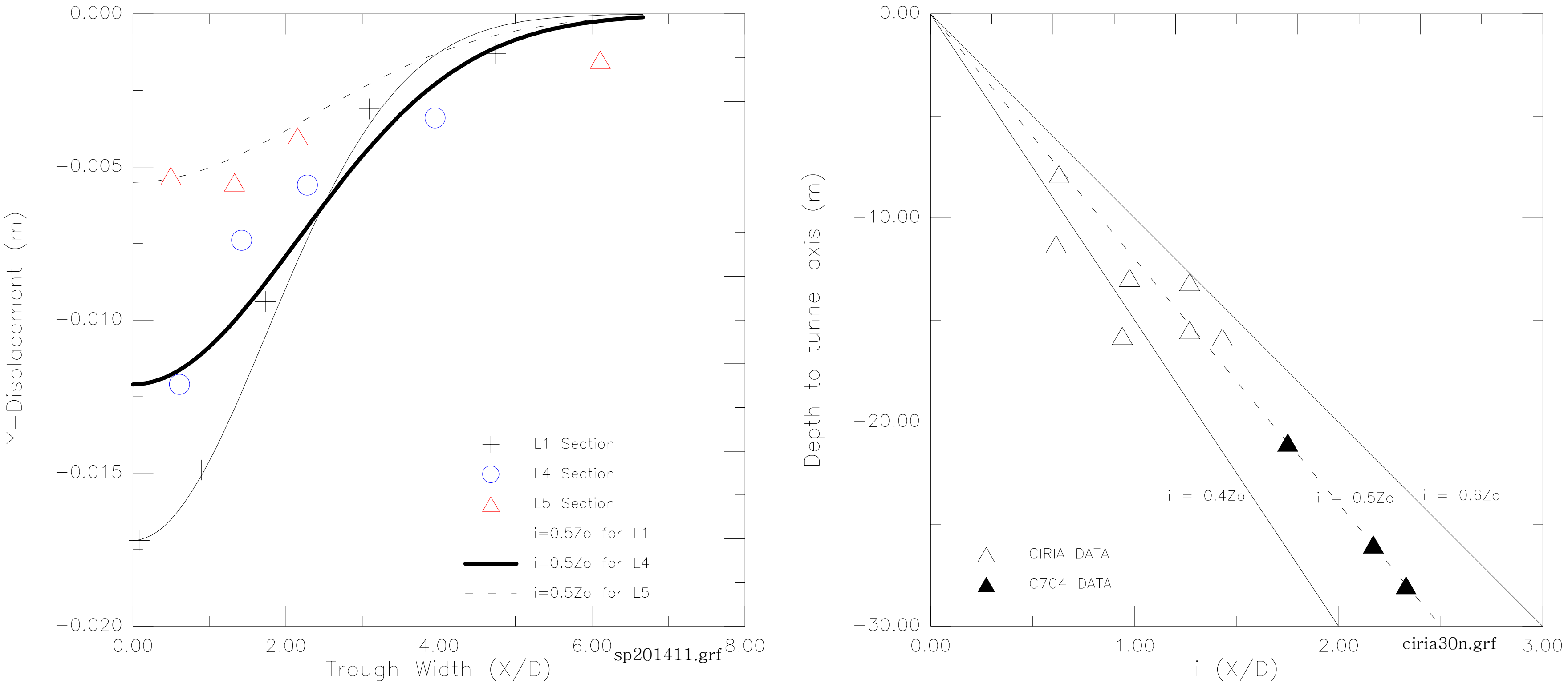

Figure 4.15a

Figure 4.15b

Figure 4.15 Settlement width characteristics of C704: (a) normalised settlement behaviour with i= 0.5k_o b) Comparison with other field data as reported in CIRIA, Project Report 30.

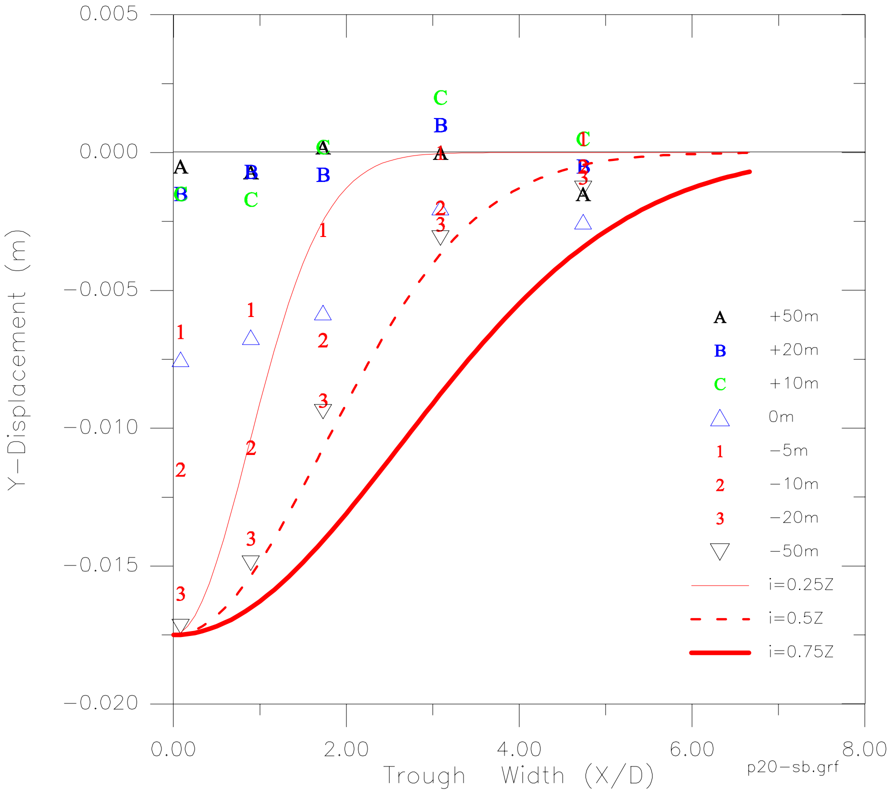

Figure 4.16a Section L1 trough width

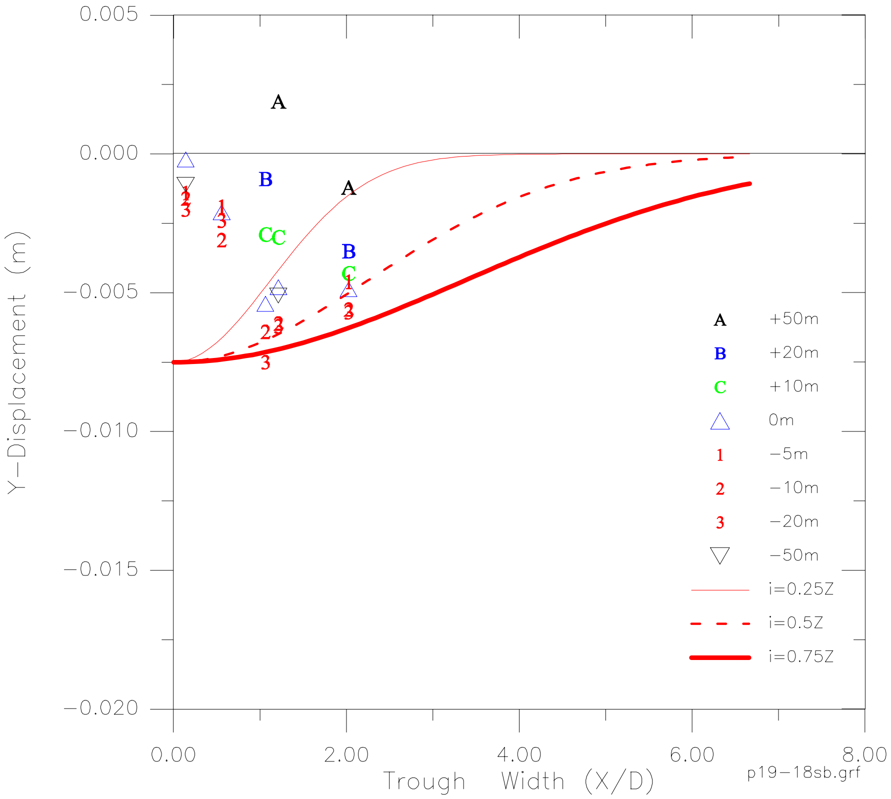

Figure 4.16b Section L2 trough width

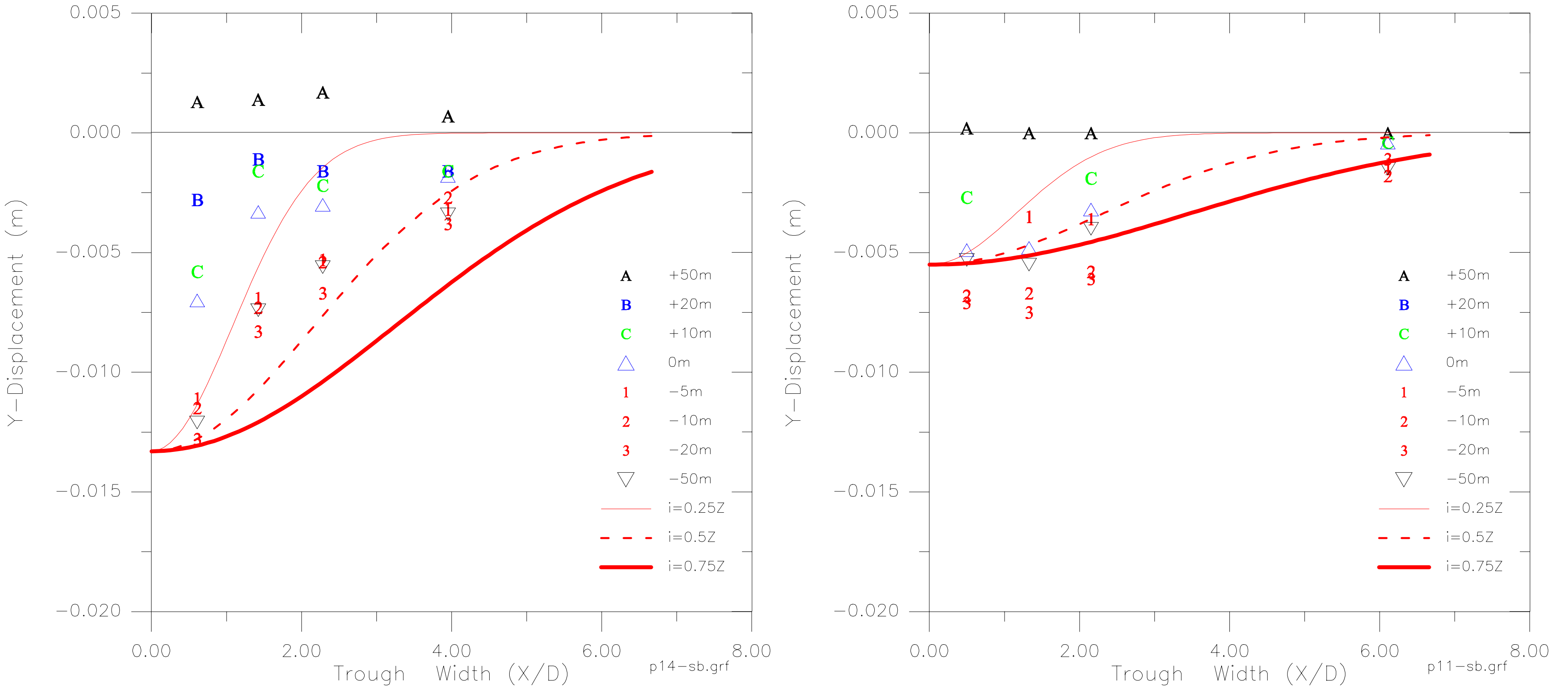

Figure 4.16c Section L4 trough width

Figure 4.16d Section L5 trough width

Figure 4.16 Settlement behaviour of the monitored "green-field" condition.

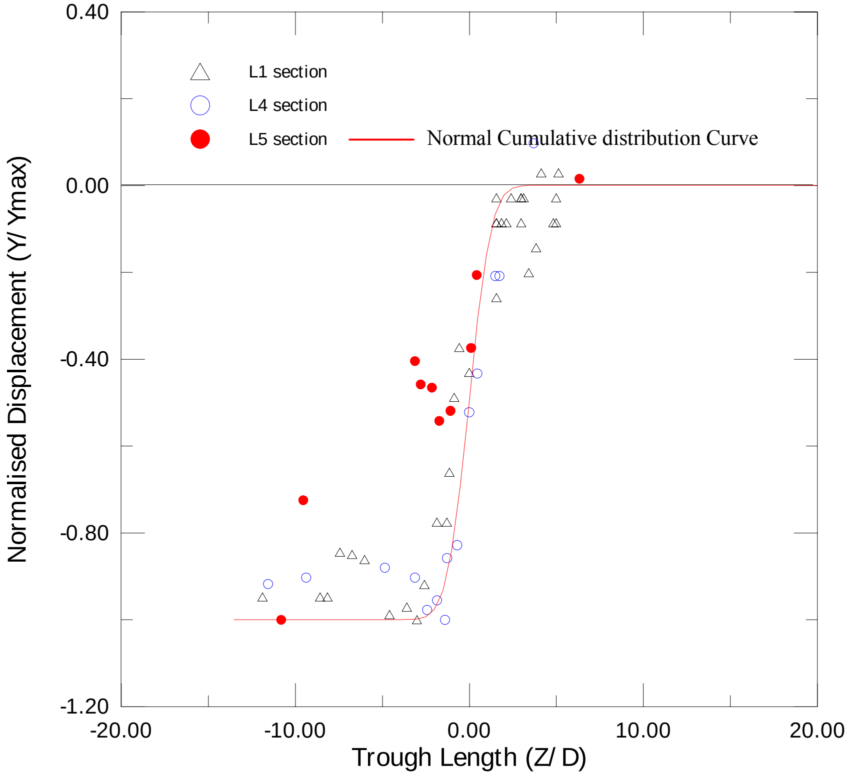

Figure 4.17 Comparison of normalised field data with normal cumulative distribution curve.

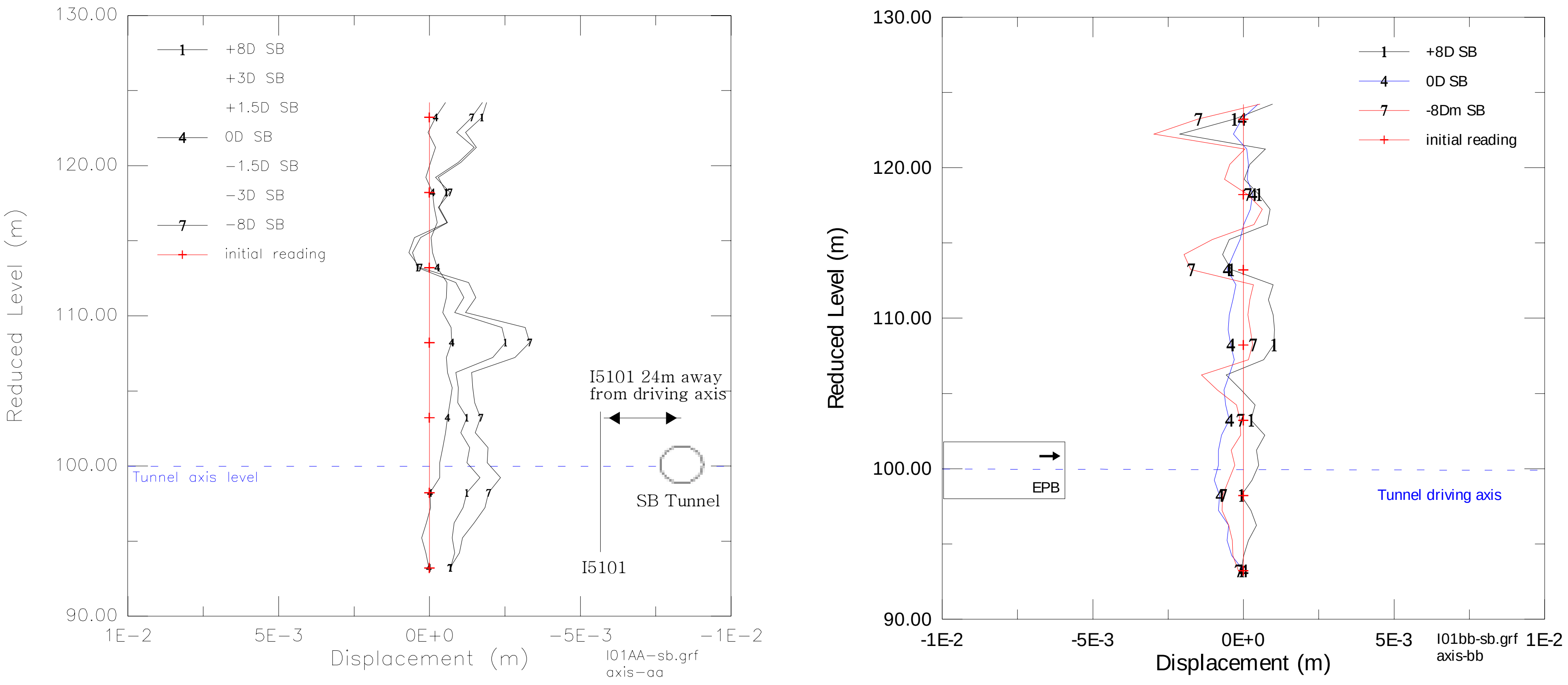

Fig 4.18a Lateral Response

Fig 4.18b Longitudinal Response

Figure 4.18 (a) Lateral and (b) longitudinal subsurface movements before and after southbound tunnelling (inclinometer I5101).

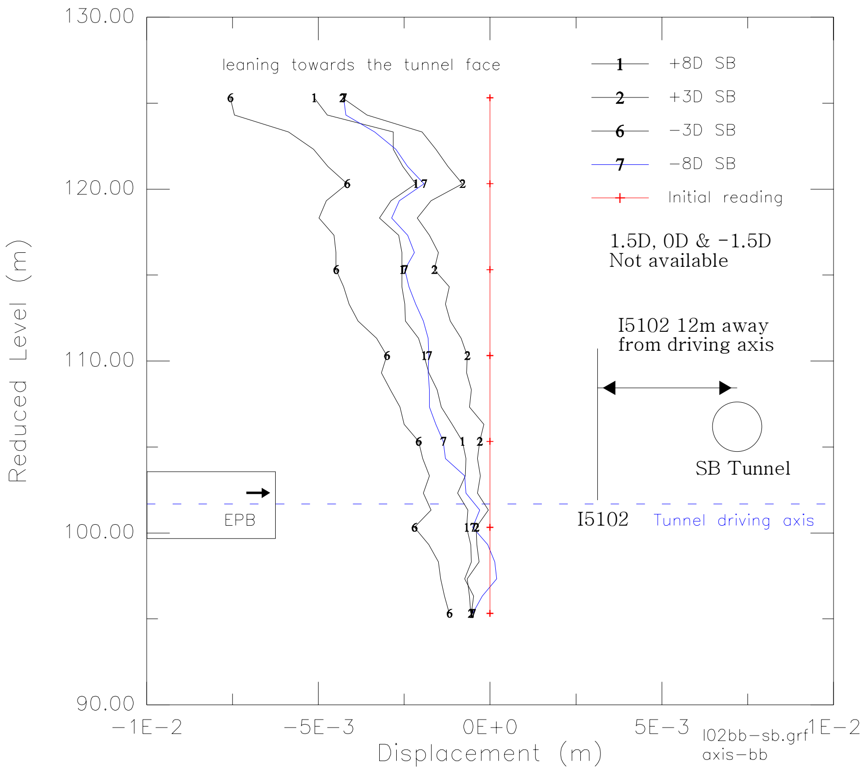

Fig 4.18c Longitudinal Response

Figure 4.18c Longitudinal subsurface movements before and after southbound tunnelling (inclinometer I5102)

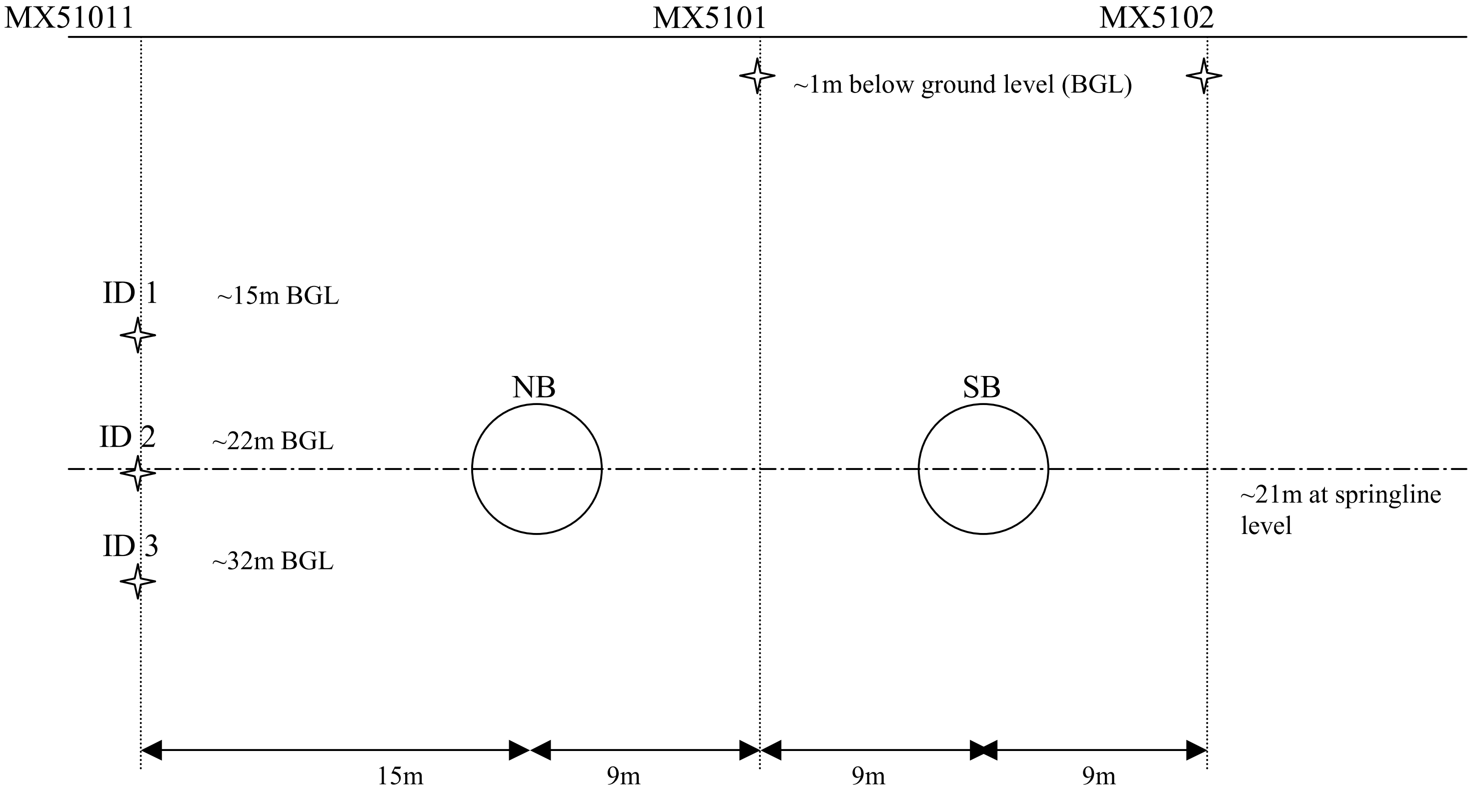

Figure 4.19 Cross sectional view of the magnetic extensometer locations (not to scale) in section L3.

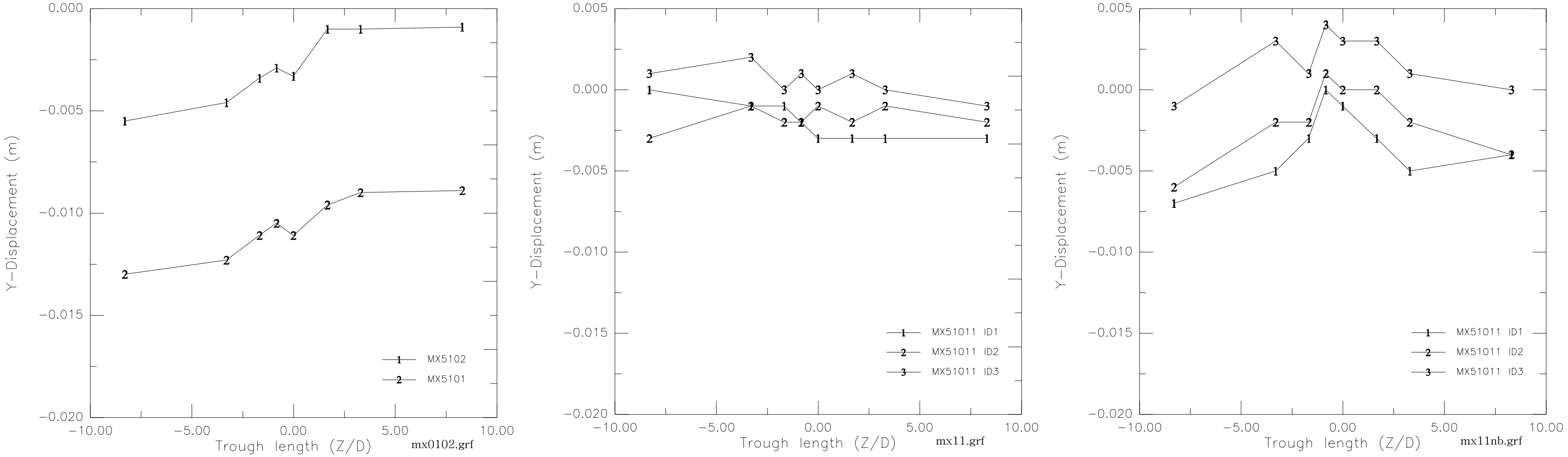

Figure 4.20a

Figure 4.20b

Figure 4.20c

Figure 4.20 Subsurface vertical movement a) MX5102 & MX5101, b) MX51011 (SB) and c) MX51011 (NB)

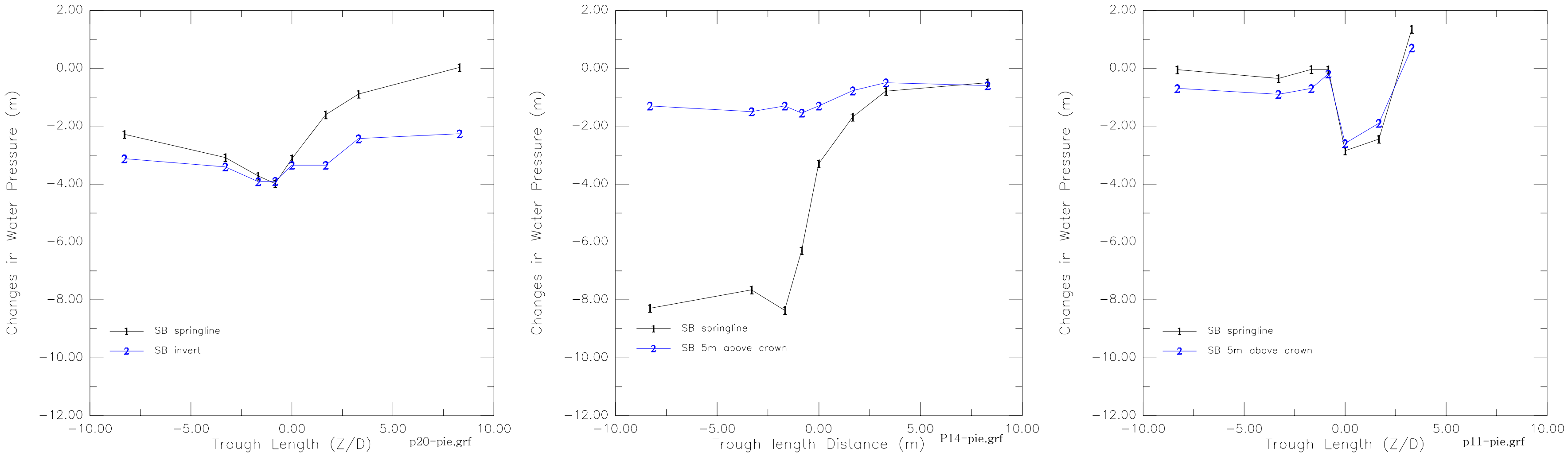

Fig. 4.21a

Fig 4.21b

Fig 4.21c

Figure 4.21 Measured pore water pressure response in section a) L1, b) L4, and c) L5 during tunnelling.

5 Finite Element Study of C704 EPB Tunnelling

5.1 Introduction

Prediction of ground settlement due to tunnelling could be based on analytical, empirical or the numerical methods. However, as more tunnelling projects are located in an urbanised area congested with important infrastructure facilities such as gas pipes, power grids or even with existing foundations, numerical methods such as Finite Element Modelling (FEM) gives much more flexibility to design engineers in predicting the ground settlement pattern. Tunnelling at the heading is essentially a three dimensional (3-D) problem, although two dimensional (2-D) FEM gives a good indication on the magnitude of the settlement, it will not be able to give a true assessment of the relationship between trough length, trough width and its related differential settlement. It is this issue that motivates the use of 3-D FEM simulation to study ground movement due to tunnelling.

In this chapter, a back-analysis of C704 EPB tunnelling project will be carried out to verify the simulation of the EPB tunnelling construction sequence. In addition, various sensitivity studies involving Modified Cam Clay (MCC) model, a small strain Cam Clay model (HCC), an anisotropy elastic model (MCEA) and a hybrid model (HMCEA) comprising of HCC and MCEA will be conducted to assess the performance of these models in back-predicting the field measurements. All the FE analyses were done on a PC with AMD 1.4 GHz chipset with 1.0 GB random access memory.

In the final section, 3-D and 2-D FEM using conventional soil models were analysed for various soil stiffnesses to determine the 3-D and 2-D relationship of ground loss.

5.2 Problem Definition and Finite Element Mesh of an EPB Excavation

In C704, the springline of the tunnel varies from a depth of 18 m to 21 m below the ground surface. In the finite element modelling, for ease of geometrical modelling, the springline depth was modelled 21 m from ground surface. This is a reasonable assumption because the chainages from L1 to L5 is about 400 m and the tunnel invert level has a gradual slope of 1:130.

The tunnel extrados diameter was 6 m and the EPB shield was 9 m in length. As Figure 5.1 shows, taking advantage of symmetry, only half of the tunnel and ground domain was modelled. The finite element mesh extended laterally for a distance of approximately 10 times the diameter, D, from the centre of the tunnel. This is to ensure that the lateral boundaries have no significant effects on the results (Oteo, 1982). Lin et al. (2001) suggested that the longitudinal boundary is not significant if the distance between the boundary and the tunnel is larger than 8 D, both ahead and behind the tunnel face. As shown in Figure 5.1, in this study, the longitudinal boundary is set at 20 D i.e. approximately 120 m for both ahead and behind the tunnel face at the monitored section. The finite element mesh used in this analysis consisted of 3120 20-noded brick elements.

The soil domain was modelled using 20-noded linear strain brick (LSB) elements with pore pressure degrees of freedom at the vertices. The vertical sides of the mesh were laterally restrained against transverse movement whilst the base is completely fixed.

Following pre-construction standpipe readings, the in-situ groundwater table is assumed to lie at a depth of 5 m below the ground surface. The ground surface is also assumed to be a drainage boundary, so that the pore pressure at the ground surface is fixed at atmospheric pressure throughout the analysis. The vertical plane of symmetry, base as well as the initiating and terminating faces of the mesh were assumed to be impermeable, so as to allow any tunnel drawdown effects to be manifested. The vertical side of the mesh, which runs parallel to the tunnel axis and opposite of the vertical plane of symmetry is assumed to be a hydrostatic drainage (i.e. recharge) boundary throughout the analysis.

The ground domain was sub-divided into three soil layers, the parameters and in-situ conditions of which are shown in Table 5.1. The soil in the three layers were modelled using the modified Cam Clay model (Roscoe and Burland 1968), a hyperbolic Cam Clay model (Nasim 1999) and an anisotropic elastic model.

Conventional laboratory tests e.g. Dames and Moore (1983) showed that the granitic saprolites found in Singapore generally behave in a manner that is akin to an over-consolidated soil with over-consolidation ratio (OCR) of about 3. This includes its tendency to dilate in consolidated undrained tests conducted under in-situ effective stress levels. The moderately high OCR of 3 indicate that while compression and shear yielding are possible, it is also rather unlikely apart from isolated regions of stress concentration around the tunnel heading. For this reason, it is quite possible that the ground behaviour is dictated by elastic rather large-scale plastic behaviour. To assess this, the elastic behaviour of the ground was also separately modelled using a Cam Clay model which follows a hyperbolic shear stress-strain law in the elastic regime (Nasim 1999) as well as an anisotropic elastic model. These models will be discussed further in the sensitivity study shown below.

The concrete tunnel liner was assumed to be impervious, as the concrete lining has permeability that is typically at least two orders of magnitude lower than that of the surrounding soil (Fitzpatrick 1980). The concrete lining properties used are shown in Table 5.2. Poulos and Loganathan (1998) suggested that the weight of the liner is a significant percentage of that of the excavated soil and therefore must be included into the analysis. Other researchers, e.g. Lee & Rowe (1990, 1992a) and Sagaseta (1987), had shown that the excavated tunnel boundary deforms to an elliptical shape with the least movement at the invert level. This is consistent with the notion that the self-weight of the liner and tunnel boring machine has a significant effect. In this study, the weight of the liner and EPB machine (see Table 5.3 for EPB technical specifications) was modelled through 3-D brick elements having full shield weight or liner weight and thus act as a pressure loading on the invert of the tunnel.

The liner is assumed to be continuous in the analysis. In practice, the liner used consisted of pre-cast segments. This may have a lower stiffness than a continuous liner. To assess the significance of liner stiffness on ground response, sensitivity studies will be conducted below to determine the effects of the stiffness of liner.

5.3 Construction Sequences

As shown in Figure 5.2, the tunnel excavation and liner installation consists of three repeated steps. The first step involves excavation of the tunnel face which takes place concurrently with the extension of the thrust rams (piston jacks) against the tunnel lining. The piston jacks were then retracted (Figure 5.2b), followed by the construction of the segmental lining by a rotary erector (Figure 5.2c). This cycle of activities is then repeated, with the piston jacks being extended against the new lining and the shield advancing again. In the ideal scenario, once the liner is grouted, no further ground movement should occur. However, ground movement occur over the span of the TBM machine, which typically has a diameter slightly smaller than that of the cut cavity.

To facilitate finite element modelling, a simplified sequence was simulated as shown in Figure 5.3. As shown in this figure, at any stage of tunnelling, the space which is to be occupied by the tunnel can be sub-divided into three region. The first comprised the original soil domain which is ahead of the tunnel face and yet to be excavated. The second consisted of the space occupied by the TBM machine. To enable ground movement into the cut cavity, the excavated soil is replaced by "shield machine elements" which have properties shown in Table 5.4. To avoid numerical ill-conditioning, the EPB shield's Young Modulus is reduced 10 times however, as noted by Britto & Gunn (1990), the soil-structure interaction would not be greatly affected when the stiffness ratio between the structure and the soil are more than 100 times.

The external compressible shield elements allow the surrounding soil to move inwards and partially take up the gap between the machine and the cut cavity. These shield machine elements are necessitated by the lack of gap elements in CRISP. Finally, the shield machine elements are followed by a span of tunnel liner elements which consisted of an elastic layer of brick elements surrounded by another layer of more compressible "grout" elements. The purpose of this grout layer is to allow stress relieve due to the occurrences of the shield and tail voids and at the same time allowing compatibility with the rest of the finite element domain. It is evident that the properties of the shield, liner and grout elements are not readily measured or defined since they are likely to be highly dependent upon operating parameters and workmanship. For this reason, a series of sensitivity studies will be conducted to assess the significance of the properties of these regions on the computed results, as well as to back-calibrate the parameters of these regions.

The advancement of the tunnel and liner are simulated in the analysis using the following stages:

- The soil elements ahead of the EPB shield were removed and face pressure was applied. In C704, the applied face pressure due to EPB advancing was about 100 kPa to 200 kPa (Shirlaw, 2001). In this study, a face pressure of 100 kPa was adopted in the analysis. Parametric study on the sensitivity of the face pressure will be shown later. At the excavated boundary, pore pressure was fixed at atmospheric pressure.
- The excavated soil elements were replaced by the EPB shield elements (see Figure 5.3a). A rate of advance of 4 m/day was adopted, this being typical of the rate of advance in this segment of tunnel.
- The finite element mesh for the relevant shield elements was upfront discretised into two annular layers. During the shield simulations, the two annular layers had similar elastic properties. However, during tunnel liner installation, the inner annular layer was simulated by replacing the relevant shield elements by concrete liner elements (Figure 5.3b). The presence of tail

voids occupied by injected cement grout was simulated by replacing the most outer layer of shield elements by a layer of compressible elastic elements.

5.3.1 Parametric Studies

This section discusses a series of sensitivity studies conducted to examine the sensitivity of the computed results to excavation step sizes, face pressure, pore pressure boundary and weight of tunnel liner and EPB machine. The studies were all conducted using the FE mesh, boundary conditions and soil parameters described in the previous sections.

5.3.2 Excavation Step Size

The EPB shield used in C704 was approximately 6 m in diameter and 9 m in length. In reality, the excavation is continuous, not step-wise, since earth is continuously being cut up and removed by the rotating cutter head. Thus, ideally, the excavation step size should be as small as possible in order to simulate the continuous excavation done by the EPB machine. However, a small excavation step will mean a large number of tunnel driving stages, which will, in turn, increase the computer time needed for the analysis. Lin et al. (2001) suggested that an excavation step size which is equal to or less than half the shield length is sufficient for simulation of tunnelling excavation. However in their simulation, the shield length i.e. the length between the tunnel face and the tunnel liner was not considered in the simulation. In this study, the shield length was taken into account since the distance between the tunnel face and the start of the liner may have an effect on the ground response. For this reason, Lin et al.'s (2001) findings may not be directly applicable. In all of the analyses, a face pressure of 100 kPa was adopted, together with full liner stiffness and EPB machine weight of 650 tonnes, these values being typical of those used on the site.

Figure 5.4 shows the excavation sequence which was simulated by adopting excavation step sizes Z_{excav} of 3 m, 4.5 m and 9 m. The length L_{shield} of the shield machine used in this project is 9 m. Thus, the simulated step sizes correspond to $\frac{Z_{excav}}{L_{shield}}$ ratios of $\frac{1}{3}$, $\frac{1}{2}$ and 1. In the discussion below, the step ratio $\frac{Z_{excav}}{L_{shield}}$ will be denoted by R_{sr}

The longitudinal and lateral ground settlement profiles computed using these three different excavation step ratios are shown in Figures 5.5 and 5.6. As Figure 5.5 shows, quite discernible differences are evident between the longitudinal settlement profile computed using R_{sr} of 1 and those computed using R_{sr} of 1/2 and 1/3. This suggests that reasonable good convergence is likely to be achieved by using $R_{sr} \leq 1/3$. As Figures 5.5 and 5.6 show, the field data are well-fitted by the widely-used normal distribution curve across the tunnel section and the cumulative normal distribution along the tunnel axis (e.g. Peck 1969, Attewell & Woodman 1982). All three sets of numerical predictions show varying degree of discrepancy with the field data. However, as will be shown later, this is at least partly attributable to the constitutive model used. It is, nonetheless, reassuring to note that, of the three sets, the longitudinal settlement profile for the smallest R_{sr} of 1/3 also yields the closest agreement with the field data, indicating that the smaller the excavation step ratio, the closer is the approach to reality, as should be the case, between $\frac{Z}{D} = -3$ and $\frac{Z}{D} = -12$, the field data and numerical results show longitudinal settlement rebound of varying magnitudes. As will be shown later, this settlement rebound may be attributed to the re-establishment of the groundwater table above the tunnel after the latter has been lined and grouted. Once again, the settlement rebound predicted using R_{sr} of 1/2 and 1/3 show a closer agreement with the field data than that predicted using $R_{sr} = 1$.

As shown in Fig. 5.27, the excavation step ratio R_{sr} has much less influence on the cross-sectional settlement profile. The best normal distribution fit to the field data is obtained using a standard deviation of $i = 0.5Y_o$, which is consistent with the observations made by Shirlaw (2001).

Thus, this parametric study not only shows that using $R_{sr} = \frac{1}{3}$ gives the closest fit (of the three values tested) to the field data, but also indicates a definite convergence of results between R_{sr} of 1/2 and 1/3. This suggests that using a step ratio of less than a third is unlikely to achieve further significant improvement in the results. Hereafter, the step ratio R_{sr} of $\frac{1}{3}$ will be used in all the subsequent analyses.

5.3.3 Effects of pore-pressure fixity

In the numerical simulation, the excavated tunnel face and side over the unlined length of the tunnel was assumed to be a flow boundary where the pore pressure was maintained at atmospheric pressure. This pore pressure fixity condition was released as the lining elements were inserted to simulate the sealing of the lined portion. This assumption is reasonable as EPB machines usually inflict some degree of overcutting, which is defined as the difference between the cross-sectional area of the tunnel cut by the machine and that of the tailskin shield. In C704, the overcutting is about 0.5 % of the face area (Shirlaw, 2001). This is approximately equivalent to an all-round 75-mm gap between the excavated tunnel and the tailskin shield. In this project, grouting was only conducted at the tailend of the shield and was mainly used to fill up the overcut and tailvoid gaps. Furthermore, the stiff to very stiff residual soil is stable (see Equation 2.1) with a N_{broms} factor of only about 2.5. Thus, the excavated tunnel is unlikely to have collapsed inwards significantly. There is therefore ample time and space for the excavated boundary to be exposed to normal atmospheric pressure. For this reason, it is not unreasonable to fix the pore pressure along the unlined segment.

To determine the effects of pore pressure fixity on the ground response, a case with no pore pressure fixity was simulated and compared with the baseline case. In both cases, the pore pressure fixity at the face remains the same and the only difference lies in the presence or otherwise of pore pressure fixity at the unlined tunnel periphery. As shown in Figure 5.7, removing the pore pressure fixity leads to much reduced settlement and a virtual absence of rebound at the lower end of the trough length. In terms of transverse direction, minor deviations was observed (See Figure 5.8).

Moreover, as Figure 5.9 shows, the drawdown effect arising from the pore pressure fixity is also evident from the sharp drop in pore pressure at a point located 2 m above the crown of the tunnel. On the other hand, removing the pore pressure fixity leads to an initially small drop in pore pressure due to lateral relief of earth pressure ahead of the tunnel, followed by a slight increase due to the influence of the face pressure at very near field. Thereafter, the pore pressure continues to drop till the installation of liner leads to another increase in the pore pressure.

5.3.4 Effects of TBM weight

Figure 5.10 shows the effect of including the TBM weight into the computation. As can be seen, for $-0.5 < \frac{S}{S_{\max}} < 0.0$, the normalised results for both cases analysed does not show much deviations. Some discrepancies are present further behind the tunnel face; the results computed without considering TBM weight deviating away from the cumulative normal distribution curve. However, the differences remain fairly small indicating that the weight of the TBM machine does not have an influence over the shape of the settlement profile in the longitudinal direction. In the transverse direction, the differences are even smaller, with both cases showing essentially similar settlement profiles, Figure 5.11. In the subsequent analyses, the TBM weight will be included.

5.3.5 Effects of Face pressure

In this sensitivity, results were computed for 3 different face pressures, namely 10 kPa, 100 kPa and 500 kPa. The total overburden pressure at the springline of the tunnel is about 400 kPa. In the following discussion, the normalised face pressure F_p will be used, this being defined as

$$F_p = \frac{Face\ \mathrm{Pr}essure}{Total\ Overburden\ \mathrm{Pr}essure} \qquad (5.5)$$

As shown in Figure 5.12, for $F_p = 1.25$, heaving of the ground ahead of the tunnel face is computed, the maximum heave being at about 4 D ahead of the tunnel face. The effect of face pressure is also greatest ahead of the tunnel, where a higher face pressure inhibits settlement. On the other hand, the face pressure appears to have insignificant effect on the settlement profile behind the TBM.

As Figure 5.13 shows, the effect of face pressure is even more significant when viewed in terms of actual settlement. As this figure shows, using a higher face pressure leads to larger heave ahead of the tunnel and larger settlement behind the TBM. This is readily attributable to the fact that using a higher face pressure inhibits the movement of soil ahead of the tunnel face towards the rear of the TBM. This is also evident from the stress paths shown Figure 5.14. As shown in this figure, using a higher face pressure not only increases the compressive stresses prior to arrival of the tunnel heading but also increases the deviator stress and reduces the compressive stress after the tunnel heading has passed. Thus, while face pressure is useful for enhancing stability of the tunnel face, using a higher face pressure may actually aggravate the settlement of the ground surface. More importantly, it also aggravates the differential settlement, as seen from the maximum gradient of the longitudinal settlement profile. Compared to the longitudinal settlement profile, the influence of the face pressure on the cross-sectional settlement profile is much less, as shown in Figure 5.15. This is to be expected since the face pressure is only applied in the longitudinal direction.

5.3.6 Tail Voids and Lining Stiffness

Apart from face and shield losses, tail void losses also contribute to ground loss. Whereas face and shield losses are dependent upon the face pressure and overcutting of the shield, which can be measured, tail void losses are dependent upon the workmanship in the grouting of the tail void. For this reason, tail void losses can be quite variable. In this study, brick elements were also used to represent the grouted tail void between lining and soil, see Figure 5.1. The strength and stiffness of the grout is likely to variable and much lower than that of concrete. The latter is due to the fact that the grout is much leaner than normal concrete mortar and the fact that the grout has to start taking load almost immediately upon injection, without any curing period. Sharma (2000) reported the shotcrete-grout layer is variable in strength and the initial Young's modulus E, is 20 MPa. He has further observed that the strength of the grout gained over time has no significant impact on the final settlement, this being probably due to the fact that much of the load on the grout is transferred within a short time of grout injection.

In this project, the liner used consisted of pre-cast segments; however, in the FE analysis, the liner is assumed to be continuous. The presence of joints in the segmental casting will lower the flexural rigidity of the liner. For segmental linings, the U.S. Army Corps of Engineers (1997) suggested that, the 2nd moment of area I of the liner be reduced as follow:

$$I_{eff} = I_j + \left(\frac{4}{n}\right)^2 I \qquad (5.6)$$

where

I = 2nd moment of area of a continuous concrete lining with the same dimensions,

I_j = 2nd moment of area of each joint,

n = number of joints in the lining ring where $n > 4$

In C704, each liner was constructed from 5 segments and 1 key; thus giving $n = 6$. By taking $I_j = 0$, $I_{eff} = 0.44I$. In the analyses, the liner thickness simulated was the same as that used in the field, this being done in order not to degrade the aspect ratio of the already-thin liner elements. Because of this, the 2nd moment of area cannot be reduced. Instead, the reduction in the flexural rigidity (*EI*) was effected by reducing the Young's modulus to 0.44 times that of normal concrete.

The liner was modelled using a linear elastic material model. In this study, three combinations of liner modulus E_c and grout modulus E_g were examined, as shown below:

- Case I: E_c = 28 GPa and E_g =28 MPa;
- Case II: E_c = 28 GPa and E_g =28 GPa (this assumes that a high strength grout is achieved.)
- Case III: E_c = 11.2 GPa (0.4 times of the original concrete modulus) and E_g = 28 MPa.

The permeability of the liner and grout is assumed to be isotropic and has a value of $1\text{x}10^{-12}$ m/s. The liner and grout is assumed to have unit weight of 24 kN/m^3.

As shown in Figures 5.16 to 5.18, the longitudinal and transverse settlement profiles are not significantly affected by the three combinations of liner and grout moduli. This can be attributed to the fact that, in all the three cases, the liner is much stiffer than the soil around it. The grout modulus is much closer to that of the soil but the grout layer is likely to be effective only in transferring the radial earth pressure to the liner. Since the grout layer is very thin, it should also have a high radial stiffness. This finding is consistent with Sharma's (2000) findings on the effects of shotcrete stiffness in open cut NATM (New Austrian Tunnelling Method) tunnelling. The runtimes for the three cases are 6.25 hours, 10 hours and 5 hours, respectively. In the subsequent analysis, Case 3 grout and liner properties will be used.

5.4 Effects of Soil Models

As discussed earlier, in all the cases analysed so far, the longitudinal and transverse settlement profiles are significantly gentler than those measured in the field. This is likely to be at least partially attributable to the material model used for the soil. Lee & Rowe (1989a, 1989b) reported that using an elastic anisotropic model gave significantly better agreement between calculated and measured surface settlement within two diameters of the tunnel's centreline. However the width of the settlement trough was still overestimated by the finite element prediction. They attributed this discrepancy to the fact that the initial stiffness of the soil at low strain may be substantially higher than that obtained by conventional measurement.

Gunn (1992) and Dasari (1996) also reported non-linear small strain effects on tunnel problems in cohesive soils. As reported by them, the settlement trough width obtained using small strain soil model agrees much better with experimental data than that obtained using a linear elastic soil model. Notwithstanding this, however, the computed settlement trough is still much wider than that indicated by experimental results or empirical data, see Figure 5.19. Stallebrass and Taylor (1997) have further highlighted that the small strain stiffness is also highly dependent on the recent stress history. In their study, the range of initial shear modulus values can vary upto 6 times dependent on the pattern of the recent stress paths.

It should be mentioned that most studies relate to the width of the settlement trough in cross-section. Little or no studies have been conducted on the longitudinal settlement profile to date. In the discussion below, 3-D FE analyses will be used to study and compare the effects of elastic anisotropy and small strain non-linearity on the longitudinal and cross-sectional settlement profiles induced by tunnelling.

It should be mentioned that the soil models studies discussed herein were meant to determine the influence of elastic anisotropy and small strain non-linearity on tunnelling induced ground settlement in residual soils. The development of a soil model to simulate the residual soil behaviour is not the main emphasis in this study. As such, the elastic anisotropic model was largely implemented from formulation of Graham and Houlsby (1983), whilst the small strain non-linearity model was adopted from Nasim's (1999) hyperbolic Cam Clay (HCC) formulation.

5.4.1 Modified Cam Clay model with Elastic Anisotropy effects (MCEA)

The stress-strain matrix D_e for the elastic anisotropic model formulated by Graham and Houlsby (1983) and later summarised by Wood (1990) is given by:

$$D_e = \begin{bmatrix} \alpha^2(K' + \frac{K_w}{n} + \frac{4}{3}G') & \alpha(K' + \frac{K_w}{n} - \frac{4}{3}G') & \alpha^2(K' + \frac{K_w}{n} - \frac{4}{3}G') & 0 & 0 & 0 \\ \alpha(K' + \frac{K_w}{n} - \frac{4}{3}G') & K' + \frac{K_w}{n} + \frac{4}{3}G' & \alpha(K' + \frac{K_w}{n} + \frac{4}{3}G') & 0 & 0 & 0 \\ \alpha^2(K' + \frac{K_w}{n} - \frac{4}{3}G') & \alpha(K' + \frac{K_w}{n} - \frac{4}{3}G') & \alpha^2(K' + \frac{K_w}{n} - \frac{4}{3}G') & 0 & 0 & 0 \\ 0 & 0 & 0 & \alpha G' & 0 & 0 \\ 0 & 0 & 0 & 0 & \alpha G' & 0 \\ 0 & 0 & 0 & 0 & 0 & \alpha^2 G' \end{bmatrix} \quad (5.7)$$

where $\alpha^2 = \frac{E_h}{E_v}$, E_h being the horizontal elastic Young's modulus and E_v the vertical elastic Young's modulus. Equation 5.7 was implemented in CRISP to describe the elastic behaviour of the Modified Cam Clay, which is hereafter termed Modified Cam Clay with Elastic Anisotropy (MCEA).

Gibson (1974) showed that the theoretical bounds for α^2 ranges from 0 to 4 while Becker (1981) reported typical values ranging from 0.5 to 2.4 for different types of cohesive soils. Dames and Moore (1983) reported that, for the granitic residual soils of Singapore, $\frac{E_h}{C_u} = 150$ (taken from pressuremeter tests) whereas $\frac{E_v}{C_u} = 70 \sim 250$ (taken from cyclic Unconsolidated Undrained (UUR) tests). As shown in Table 5.5, UUR tests conducted on soil samples collected about 100 m away from the tunnelling monitored sector gives $\frac{E_v}{C_u} = 400 \sim 480$. Taking into consideration Dames & Moore's (1983) data and the C704 data, it seems likely that the typical value of α^2 varies from 0.31 to 2.14.

5.4.2 Hyperbolic Cam clay model (HCC)

It is now well-recognised that the shear modulus of soils decreases with increasing shear strain (e.g. Jardine et al. 1986; Shibuya 1995; Jamiolkowski et al. 1999). Variants of the Cam Clay model incorporating non-linear behaviour in the elastic regime have been developed by Dasari (1996) and Nasim (1999). In this study, Nasim's hyperbolic Cam-clay (HCC) model, which prescribes a decrease in *G* with deviatoric shear strain ε_s according to a hyperbolic function, is used. In the elastic regime, Nasim's (1999) HCC prescribes a deviator stress *q* which is related to the deviator strain ε_s via a hyperbolic function of the form:

$$q = \frac{(S_0 - S_\infty)\varepsilon_s}{\left(1 + \frac{(S_0 - S_\infty)\cdot|\varepsilon_s|}{q_f}\right)} + S_\infty \varepsilon_s \tag{5.8}$$

where

S_0 is the initial tangential stiffness of the q vs ε_s curve

S_∞ is the tangential stiffness at very large strain

ε_s is the shear strain

ε_∞ is the shear strain at yielding

q_f is the deviator stress at failure

Combining Equation 5.8 with

$$S = \frac{dq}{d\varepsilon_s} = 3G \tag{5.9}$$

leads to the relation

$$G = \frac{G_0 - G_\infty}{\left(1 + \frac{3(G_0 - G_\infty)\cdot|\varepsilon_s|}{q_f}\right)^2} + G_\infty \tag{5.10}$$

where

G_0 is the initial tangential stiffness

G_∞ is the tangential stiffness at very large strain

The initial shear modulus, G_0, is related to the current state of soil by the relation:

$$G_0 = Cp'^n \; OCR^m \tag{5.11}$$

where

C is a constant

n is the effective stress exponent

m is the OCR exponent

Hong (2002) have reported the usage of Nasim's HCC model in his study for strutted excavation at the Serangoon Station which was also constructed in the granitic residual soil and in the vicinity of the tunnel.

5.5 Hybrid HCC and MCEA model

The discussions of HCC and MCEA in previous sections have so far been restricted to tackle the shortcomings of a typical FEM tunnelling problem independently. A hybrid model comprising of HCC and MCEA features, seeks to address the ground response deficiency posed by each independent soil model.

The proposed hybrid soil model (HMCEA) was added to the finite element program, NUSCRISP, through a subroutine DSMCAM. The flow chart for the HMCEA model is shown in Figure 5.20. The proposed model HMCEA is to assign the soil stiffness when the soil is in the elastic regime (i) based on the small strain stiffness input as discussed previously to determine the Bulk Modulus (*K)*, (ii) depending on the input magnitude of $\alpha^2 = \frac{E_h}{E_v}$ which according to Equation (5.7) provides the coupling of the volumetric and shear behaviour inside the yield surface (Graham & Houlsby, 1983).

5.6 Effect of material model on FE prediction of tunnelling

In this section, the ground response predicted by the material models above will be compared using the measured settlement results as reference. In this comparative study, soil parameters were selected from the values indicated by the C704 soil investigation report and shown in Table 5.6. These values are also similar to Dames and Moore's (1983) recommended values for G4 soil. The Young's moduli of the concrete lining and grout layer were taken to be 11.2 GPa and 28 MPa respectively. However, parametric studies indicate that the results are not sensitive to the slight variations in the moduli of the concrete lining and grout layer; this is probably due to the fact that these two materials are much stiffer than the surrounding soil anyway. The face pressure was taken to be 160 kPa and the tunnel advancement rate was assumed to be 4 m/day, these values being approximately the average rate achieved for the segment being simulated. The finite element mesh used is shown in Figure 5.1.

The simulated excavation stages have been shown in Figure 5.3. The monitored cross-section, at which settlement profiles are compared with the field measurements, is the mid-plane of the ground domain, as shown in Figure 5.1. This section will be termed as FEM-L1 in subsequent discussion. The pre-excavation stage refers to the construction stage when EPB shield is moving towards the monitored section FEM-L1. The excavation stage refers to the excavation of the monitored section FEM-L1 while the post-excavation stage refers to the stage at which the EPB shield has passed and is moving away from the monitored section FEM-L1.

In any tunnelling project, there are two types of settlement namely short and long term settlement. Short-term ground settlement will occur due to ground loss formed by the face, body and tail of the shield. Long-term settlement normally arises from the drawdown and dissipation of excess pore pressure generated during the tunnelling process (CIRIA, 1996). This study focuses on the short-term settlement assuming that all settlement are completed within a few weeks of the tunnel face passing any point of reference on the surface. The field and computed data are presented in the order in which the construction occurred.

5.6.1 Comparison of results predicted with different soil models

Figure 5.21 shows the trough length results obtained from FEA and C704 field data. In terms of magnitude, both the MCC and MCEA appear to have overestimated the settlement magnitude while HCC and HMCEA appear to fit the data better. As shown in Figures 5.23 to 5.27, the MCC and MCEA modelling for the entire construction sequence consistently predict larger settlement. As mentioned earlier, the parameters for the MCC and MCEA models were deduced from the triaxial and consolidation test results reported in the soil investigation report. The parameters ignore the fact that, in the small-strain range, the stiffness of the soil can be far higher than that measured in conventional triaxial and oedometer tests. The variation in stiffness in the small strain range is accounted for by the HCC and HMCEA models but not the MCC and MCEA models. As a result, the effective stiffness modelled by the MCC and MCEA is too low to be representative of that of the soil.

Figure 5.22 shows the variation in the predicted longitudinal settlement profile by the HMCEA model. As can be seen, by adjusting the parameters of HMCEA model, various amounts of tail void settlement can be predicted.

Figure 5.28 shows the normalised longitudinal settlement profile computed by the various models. As can be seen, when the settlement is normalized by the maximum settlement, all the models show very similar profiles. However, some slight differences remain, with the HCC and HMCEA models predicting a slightly faster fall in the settlement ahead of the tunnel than the MCC and MCEA models. This can again be attributed to the ability of the HCC and HMCEA models to replicate the reduction in stiffness in the small strain range whereas the MCC and MCEA models cannot. This is also illustrated in Figure 5.29 which shows the deviatoric stress-strain responses are plotted out for HCC and MCC soil models. In HCC model, the shear strain is modelled after a hyperbolic relationship (Nasim, 1999) and it follows a drop faster at small strains and more slowly at large strains as compared to MCC model. This observation is consistent with tests conducted on triaxial samples done by Viaggiani (1992) and Dasari (1996). The sharp drop in strains is transformed to a greater distortion and thus a sharper settlement profile.

Figures 5.30 and 5.31 show the measured and computed response of two inclinometers which measured lateral movement of the ground during the construction process. As can be seen, much larger movements are once again predicted by the MCC and MCEA models than the HCC and HMCEA. This can again be attributed to the differences in the model of the small strain stiffness discussed earlier.

5.7 Comparison of 2-D and 3-D ground response

Apart from the research community, three-dimensional FE analysis is still not widely used for routine engineering analysis and design. This is due to the voluminous amount of data input typically required, even with a pre-processor, and the much longer computing time needed for the analysis. For this reason, 2-D FE analysis is still more widely used. The problems of analysing an advancing tunnel using 2-D FE analysis are well-known and have been discussed in an earlier chapter. In recent years, some commercial softwares [e.g. PLAXIS (1998), SAGE CRISP (1997)] have attempted to simulate tunnel advance by 2-D analysis, by partially unloading the tunnel walls, inserting the lining and then completing the unloading to simulate the removal of the soil elements. In this section, the viability of this “pseudo - 3-D” approach will be examined by comparing its results with those of an actual 3-D analysis.

5.7.1 Soil Types & Parameters

The comparative exercise is carried out for idealized versions of four different soil formations in Singapore, namely:

- Case I: Granitic saprolite formation, typified by a gradual increase in modulus with depth as shown in Table 5.7a. This is typically denoted as a G4 formation and will be designated as such in subsequent discussion.
- Case II: Weathered, heavily over-consolidated alluvium, characterised by a rather large Young’s modulus increasing progressively with depth, as shown in Table 5.7b. This is typically denoted as an OA formation and will be designated as such in subsequent discussion.
- Case III: Weathered sedimentary rock profile, characterized by rapidly increasing modulus with depth soil whereby elastic modulus varies rapidly with depth, as shown in Table 5.7c. This is typically denoted as an S3 formation and will be designated as such in subsequent discussion.
- Case IV: Soft soil typically resembling the normally to lightly-overconsolidated Singapore Marine Clay, characterised by low strength and

modulus as shown in Table 5.7d. This is typically denoted as an M formation and will be designated as such in subsequent discussion.

Table 5.8 summarises the different types of K_0 conditions i.e. coefficient of earth pressure at rest used for the numerical analyses. The soil model used in the first three cases is the Mohr Coulomb model since plastic compression is unlikely to feature strongly in these three materials. For Case IV, the modified Cam Clay model was used in order to model plastic hardening behaviour on the volumetric cap. Soil properties are taken primarily from Dames and Moore (1983). The permeability for all the soil types are deliberately set to very low value to simulate the virtually undrained conditions occurring during the excavation stage. The ground water table is assumed to be 5 m below ground level for the stiff soil in Case I to III whereas for Case IV, the water table is set to ground level, fully saturated. This also reflects the typical field scenarios for these four soil types. Figure 5.32 shows the graphical representation of the adopted soil data as against Dames and Moore (1983).

5.8 Finite Element Mesh and Modelling

The 3-D mesh adopted is the same one as shown in Figure 5.1. The first three cases are modelled similarly to the case study discussed earlier in this chapter. The modelling sequences such as the excavation step size, excavation sequences and the boundary conditions are also same as those described in Section 5.2 and 5.3. For Case IV, two minor variations are made to the modelling, viz.,

- the face pressure is set equal to the total overburden pressure in order to forestall face collapse in the very soft soil conditions, and

- the nodal co-ordinates are updated incrementally during the analysis to take account of the much larger ground deformation.

Two different softwares were used for the 2-D analysis, viz. Crisp (1990) and Plaxis (2000). The meshes used in these two software are shown in Figures 5.33a and 5.33b, respectively. In Crisp, the tunnel deformation can be controlled by controlling the earth pressure acting on the inner walls of the tunnel. Plaxis, on the other hand, uses a "pseudo – 3-D" method, which involves controlling the displacement of the nodes lining the inside wall of the tunnel. The Crisp mesh comprises of 280 4-noded linear strain quadrilaterals while Plaxis uses a total of 186 6-noded linear strain triangular elements. The sides of the 2-D meshes were laterally restrained while the bases of the meshes were fixed. The physical boundary conditions for the meshes were laterally extended to more than 9 diameters of the tunnel opening to cut-off the boundary effects.

5.9 3-D and 2-D ground surface response

Figure 5.34 compares the maximum deflection computed by the 3-D and 2-D analyses for the Case I soil parameters. This figure consists of three figures stacked together on a common x-axis that plots the maximum settlement of the trough at the monitored cross-section. The y-axis of the bottommost figure shows the distance between the tunnel and the monitored cross-section, that is $\frac{Z}{D}$, in the 3-D analysis. It can therefore be interpreted as the longitudinal settlement profile rotated 90° anti-clockwise.

The middle figure plots the maximum settlement computed by CRISP against a parameter known as the ground relaxation ratio. In the FE computation of CRISP, when the soil mass within the tunnel is removed from the FE domain, the equilibrating earth pressure that it applies to the surrounding ground is slowly relaxed to zero over a number of increments (in the form of nodal forces). Within each increment, the proportion of the equilibrating earth pressure that is relaxed at all the points is the same, although the absolute value of the pressure decrement may be different. The ground relaxation ratio is the fraction of the total equilibrating earth pressure that has been relaxed up to that point of time. A ground relaxation ratio of 0 refers to no relaxation of the earth pressure whereas a ground relaxation ratio of 1 refers to a state wherein the equilibrating earth pressure on the tunnel periphery has been fully relaxed to zero. As expected, the maximum settlement increases with the ground relaxation ratio but not necessarily in a linear fashion. In Figure 5.34, a kink is present in the curve at a ground relaxation of about 0.75; this corresponds to the onset of significant amount of yielding around the tunnel.

The top most figure plots the maximum settlement against the face area contraction, which is a parameter used by PLAXIS to simulate tunnel excavation. In PLAXIS, specifying the inward displacement of the nodes on the tunnel wall simulates tunnelling operation. This inward displacement causes a reduction in cross-sectional area of the tunnel. The percentage reduction in the tunnel cross-sectional area is termed as the face area contraction. In this study, all the nodes on the tunnel wall are prescribed to move inwards by the same amount, so that, in effect, the tunnel wall contracts uniformly all round.

As shown in Figure 5.34, Case I is sub-divided into two sub-cases, one with $K_0 = 1.0$ and the other with $K_0 = 0.8$. This represents the typical range of K_0 for granitic saprolites. As shown by the bottommost figure, when the tunnel heading arrives at the monitored section, the maximum settlement is about 15 mm. In the CRISP analysis, this maximum settlement is reached when the ground relaxation ratio is about 0.60. In the PLAXIS analysis, this maximum settlement is reached when the face area contraction reaches about 3.3%. By the time the tunnel has passed the monitored section by about 2.5 D, the ground relaxation ratio reaches about 85% and the face area contraction reaches about 4%. Thus, by equating the maximum settlement obtained from the analyses, the ground relaxation ratio or face area contraction corresponding to a given tunnel heading standoff can be found. We also note that the kink in the ground relaxation ratio curve occurs approximately at $\frac{Z}{D} = 0$, which would suggests onset of significant yielding upon arrival of the tunnel heading. This is intuitively reasonable and lends confidence to the results.

Figures 5.35 to 5.37 show the corresponding figures for Cases II to IV and Table 5.9 shows the ground relaxation ratio and face area contraction for various values of $\frac{Z}{D}$. As can be seen from Table 5.9, the stiffer is the soil around the tunnel, the higher is the ground relaxation ratio and the lower is the face area contraction for a given $\frac{Z}{D}$. In an extreme case such as Case IV, the ground relaxation ratio may still be at a relatively low value when the lining is installed. In other words, in soft ground conditions, a larger proportion of the in-situ earth pressure will ultimately have to be carried by the tunnel lining, compared to stiff ground conditions.

Figures 5.38 to 5.41 compare the cross-sectional settlement profiles for the four cases at various values of $\frac{Z}{D}$. In all cases, the 2-D settlement profiles are computed using CRISP (1990). As these figures show, for Cases I to III, prior to the arrival of the tunnel heading at the monitored section, the 2-D settlement trough is narrower than the 3-D settlement trough. For all cases, the 3-D settlement trough shows a heave at $\frac{Z}{D} = 3$, which is not reflected in the 2-D analysis. This is not surprising, since the heave is caused by the face pressure of the EPB machine, which could not be simulated in 2-D analysis. On the other hand, after the passage of the EPB machine, the 3-D analysis shows a narrower settlement trough than the 2-D analysis with much smaller far-field settlement, which can be attributed to stress transfer from the sections which still lie ahead of the tunnel. Thus, part of the large far-field settlement often seen in 2-D analysis can be explained by 3-D effects.

As shown in Figure 5.41, for the Case IV involving soft soil, the 3-D trough width is quite sensitive to the lateral earth pressure coefficient K_0, especially when the tunnel face standoff $\frac{Z}{D}$ is between -3 and +3. Comparison of Figure 5.41a and 5.41b shows that 3-D trough width increases as the K_0-value decreases. This “bulging” of the trough is due to the soil flow arising from the higher face pressure. Thus, in soft soil conditions, the face pressure and K_0-value may have a significant effect on the accuracy of the 2-D analysis in representing the 3-D behaviour of the tunnel heading.

5.10 Summary

In this chapter, finite element studies were conducted and back-analysed based on the measured soil parameters and field response of the C704 EPB tunnelling project. This chapter is divided into three sections namely the parametric studies on construction sequences, effects of various soil models on ground response and lastly the comparison of 3-D and 2-D ground response.

In the first section, parametric studies were conducted to determine the large amount of uncertainties arising from the effects of construction sequences. The numerical response is largely affected by these few parameters as follows:

- Choosing a finite excavation step length taking into account the length of the tunnel boring machine shield. A step length less than one-third of the shield length gives reasonable fit to the longitudinal ground response.
- Varying the amount of the face pressure gives a difference to the settlement magnitude. An over-pressurised excavated face leads to a higher settlement.
- Drainage boundary conditions at the excavated tunnel boundary are found to be much more complicating. By imposing pore pressure fixities during excavations of the tunnel peripheral boundary and releasing the pore pressure fixities upon installation of liners; it is shown to be able to model the recharging of the ground water and thus the trough length rebound when the tunnel boring machine is far away from the monitored face.
- Grout stiffnesses were found not to be influencing the residual soils ground response greatly due to the reason that the liner being stiffer than the grout and most of the radial earth pressure stress relief is transferred to the liner.

- Tunnel boring machine (TBM) weight was found not to be influencing the ground response greatly. This is largely due to overcutting by the TBM allowing radial soil pressure stress relief and thus the soil itself self stabilising independent of shield's weight.

In the second section of this chapter, among the various soil models used in the finite element analyses, the measured and computed magnitude lies very much in-between models using non-linear small strain models such as HCC and HMCEA. The results show that using the modified Cam Clay without small strain non-linearity and parameters from conventional triaxial and consolidation tests significantly over-estimates of the ground settlement. This is attributable to the fact that, with Earth Pressure Balance (EPB) control of the face, strain levels in the soil around the tunnel are kept relatively low. The conventionally obtained parameters are derrived under much larger strain conditions; thus they do not reflect the characteristics of the soil around the tunnel under field conditions.

Finally, 3-D and 2-D FEM comparative studies were conducted over a range of stiff and soft soils. A graphical approach depicting 2-D ground loss and face area contraction to the 3-D ground responses was crafted to isolate ground response for different stages of tunnelling excavations i.e. pre- and post- excavations. By equating the 3-D ground settlement to the 2-D ground relaxation ratio or face area contraction, corresponding to a given tunnel heading standoff, its related ground pressure on the liner and its face area contraction can be found respectively. In terms of trough width for stiff soils, before the arrival of the tunnel heading, the two-dimensionally computed settlement trough is often narrower than three-dimensionally computed trough. The reverse occurs after the tunnel heading has past the monitored section. In particular, much smaller far-field settlement is predicted by the three-dimensional analysis than the two-dimensional analysis; this being explainable by the stress-transfer effect of the soil in front of the tunnel heading. This is an often-encountered problem with two-dimensional analysis and the study shows that it is at least partially due to the three-dimensional effect of the tunnel heading. For soft soils, the three-dimensionally computed trough is generally narrower than the two-dimensionally computed trough as the tunnel face approaches and passes through the section. However, when the tunnel is near the monitored section (either ahead or behind), the three-dimensionally computed trough may be narrower or wider than the two-dimensionally computed trough, depending upon the in-situ K_0 value. This is due to the effect of face pressure, which is simulated in the three-dimensional analyses but not in the two-dimensional analyses.

Table 5.1 Typical Soil parameters used for finite element analysis

Thickness of sublayer (m)	Soil Model	κ	λ	e_{cs}	M	k_0	γ_{water} (kN/m^3)	γ_{soil} (kN/m^3)	$k_x = k_y$ (m/s)	OCR
Layer 1 14	Modified Cam Clay	0.026	0.13	2.0	1.2	1.5	10	18	$1x10^{-7}$	3
Layer 2 26	Modified Cam Clay	0.026	0.13	1.9	1.2	1.5	10	19	$1x10^{-7}$	2
Layer 3 10	Modified Cam Clay	0.026	0.13	1.9	1.2	1.5	10	20	$1x10^{-7}$	1

Table 5.2 Concrete lining properties

Young's modulus (Gpa), E_c	Shear modulus (Gpa), G_c	Poisson's ratio, υ	k_x (m/s)	k_y (m/s)
28	11.2	0.25	$1x10^{-12}$	$1x10^{-12}$

Table 5.3 Specification of the EPB shield used in C704

Items	tonne		Items	Dimensions
Cutter Head	58		Length of tailskin	~ 9m
Forward Shell and Motor Plate	122		Diameter of tailskin	~ 6m
Stationary Shell	125			
Tailskin	24			
Airlock	10			
Erector & Support	22			
Screw Conveyor	20			
Oil fill	7			
Transporter Beam	8			
Total	396			

Table5.4 Properties of EPB used in FEM

Type	Young's modulus (Gpa), E_s	Shear modulus (Gpa), G_s	Poisson's ratio, υ	k_x	k_y
Inner Shield (Internal Rim)	28	11.2	0.25	$1x10^{-12}$	$1x10^{-12}$
Outer shield to simulate the gap due to face overcut	2.8	1.2	0.25	$1x10^{-12}$	$1x10^{-12}$

Table 5.5 Summary of UUR results for Serangoon Station

Young's Modulus E_v (MPa)	Undrained Shear Strength C_u (kPa)	SPT N	$\frac{E_v}{N}$ (MPa/blow)	$\frac{E_v}{C_u}$
151.6	317	43	3.5	478
198.3	440	100	1.98	451
43.2	108	20	2.16	400
75.4	187	40	1.89	403

Table 5.6 Typical soil parameters for C704 FEA

Model	κ	λ	e_{cs}	M	υ	α	C	n	m	q_f (kPa)
MCC (Layer 1)	0.0267	0.113	1.8	0.73	0.3	1	---	---	---	---
MCC (Layer 2)	0.0350	0.104	1.9	0.94	0.3	1	---	---	---	---
MCC (Layer 3)	0.0110	0.0693	2.0	1.2	0.3	1	---	---	---	---
MCEA (Layer 1)	0.0267	0.113	1.8	0.73	0.3	1.3	---	---	---	---
MCEA (Layer 2)	0.0350	0.104	1.9	0.94	0.3	1.3	---	---	---	---
MCEA (Layer 3)	0.0110	0.0693	2.0	1.2	0.3	1.3	---	---	---	---
HCC (Layer 1)	0.0267	0.113	1.8	0.73	0.3	1	250	0.8	0.23	250
HCC (Layer 2)	0.0350	0.104	1.9	0.94	0.3	1	140	0.8	0.23	300
HCC (Layer 3)	0.0110	0.0693	2.0	1.2	0.3	1	140	0.8	0.23	300
HMCEA 1 (Layer 1)	0.0267	0.113	1.8	0.73	0.3	1.3	250	0.8	0.23	250
HMCEA 1 (Layer 2)	0.0350	0.104	1.9	0.94	0.3	1.3	140	0.8	0.23	300
HMCEA 1 (Layer 3)	0.0110	0.0693	2.0	1.2	0.3	1.3	140	0.8	0.23	300
HMCEA 2 (Layer 1)	0.0267	0.113	1.8	0.73	0.3	1.3	250	0.8	0.23	150
HMCEA 2 (Layer 2)	0.0350	0.104	1.9	0.94	0.3	1.3	140	0.8	0.23	200
HMCEA 2 (Layer 3)	0.0110	0.0693	2.0	1.2	0.3	1.3	140	0.8	0.23	300
HMCEA 3 (Layer 1)	0.0267	0.113	1.8	0.73	0.3	1.3	250	0.8	0.23	150
HMCEA 3 (Layer 2)	0.0350	0.104	1.9	0.94	0.3	1.3	140	0.8	0.23	300
HMCEA 3 (Layer 3)	0.0110	0.0693	2.0	1.2	0.3	1.3	140	0.8	0.23	400

Note: $G\infty$ = 1 kPa for HCC & HMCEA

Table 5.7a Summary of Case I soil properties (G4)

Case No.	Depth below ground level	E (MPa)	υ	c' (kPa)	ϕ'	γ (kN/m^3)	ΔE (kPa)	Δc (kPa)	k (m/s)
I	0 m ~ 7.5 m	1.5	0.33	30	30	18	1.43	0	$1\text{x}10^{-12}$
	7.5 m ~ 40 m	30.03	0.33	30	35	19	1.43	0	$1\text{x}10^{-12}$
	40 m ~ 50 m	64.35	0.33	30	38	20	1.43	0	$1\text{x}10^{-12}$

Table 5.7b Summary of Case II soil properties (OA)

Case No.	Depth below ground level	E (MPa)	υ	c' (kPa)	ϕ'	γ (kN/m^3)	ΔE (kPa)	Δc (kPa)	k (m/s)
II	0 m ~ 7.5 m	45	0.33	30	30	19	0	0	$1\text{x}10^{-12}$
	7.5 m ~ 40 m	65	0.33	30	35	20	0	0	$1\text{x}10^{-12}$
	40 m ~ 50 m	85	0.33	30	38	21	0	0	$1\text{x}10^{-12}$

Table 5.7c Summary of Case III soil properties (S3)

Case No.	Depth below ground level	E (MPa)	υ	c' (kPa)	ϕ'	γ (kN/m^3)	ΔE (kPa)	Δc (kPa)	k (m/s)
III	0 m ~ 7.5 m	10.98	0.33	30	30	19	11	0	$1\text{x}10^{-12}$
	7.5 m ~ 40 m	231	0.33	30	35	20	11	0	$1\text{x}10^{-12}$
	40 m ~ 50 m	495	0.33	30	38	21	11	0	$1\text{x}10^{-12}$

Table 5.7d Summary of Case IV soil properties (MC)

Case No.	Depth below ground level	κ	λ	e_{cs}	M	γ (kN/m^3)	OCR	k (m/s)
IV	0 m ~ 7.5 m	0.03	0.1	2	1.2	18	1.5	$1\text{x}10^{-12}$
	7.5 m ~ 40 m	0.06	0.3	2.5	0.9	16	1.3	$1\text{x}10^{-12}$
	40 m ~ 50 m	0.026	0.13	1.9	1.4	18	3	$1\text{x}10^{-12}$

Table 5.8 Type A and Type B K_0 conditions

Case No.	Type A K_0	Type B K_0
I, II & III (Layer 1)	1.0	0.8
I, II & III (Layer 2)	1.0	0.8
I, II & III (Layer 3)	1.0	0.8
IV (Layer 1)	0.8	0.618
IV (Layer 2)	0.8	0.646
IV (Layer 3)	1.2	1.2

Table 5.9 Ground relaxation ratio and the tunnel face position

$\frac{Z}{D}$	Ground relaxation Ratio (%)							
	Case I (G4)		Case II (OA)		Case III (S3)		Case IV (M)	
	Type A	Type B	Type A	Type B	Type A	Type B	Type A	Type B
20	0.000	0.000	0.000	0.000	0.000	0.000	0.000	0.000
10	0.000	0.000	0.000	0.167	0.000	0.000	0.000	0.000
5	0.000	0.000	0.290	0.253	0.333	0.333	0.000	0.000
3	4.000	3.833	6.167	5.733	7.000	6.333	0.000	0.000
1	28.667	30.500	36.667	39.000	39.000	40.000	5.500	6.500
0	57.000	60.000	72.333	72.833	73.333	72.000	20.833	16.500
1.5	84.167	83.333	91.000	91.333	91.667	91.167	31.500	23.500
-3	88.167	87.833	96.667	97.667	99.000	99.167	34.833	29.500
-4	87.500	87.333	96.667	98.000	100.000	100.000	34.667	30.500
-5	87.167	87.333	97.000	98.333	100.000	100.000	33.667	31.167

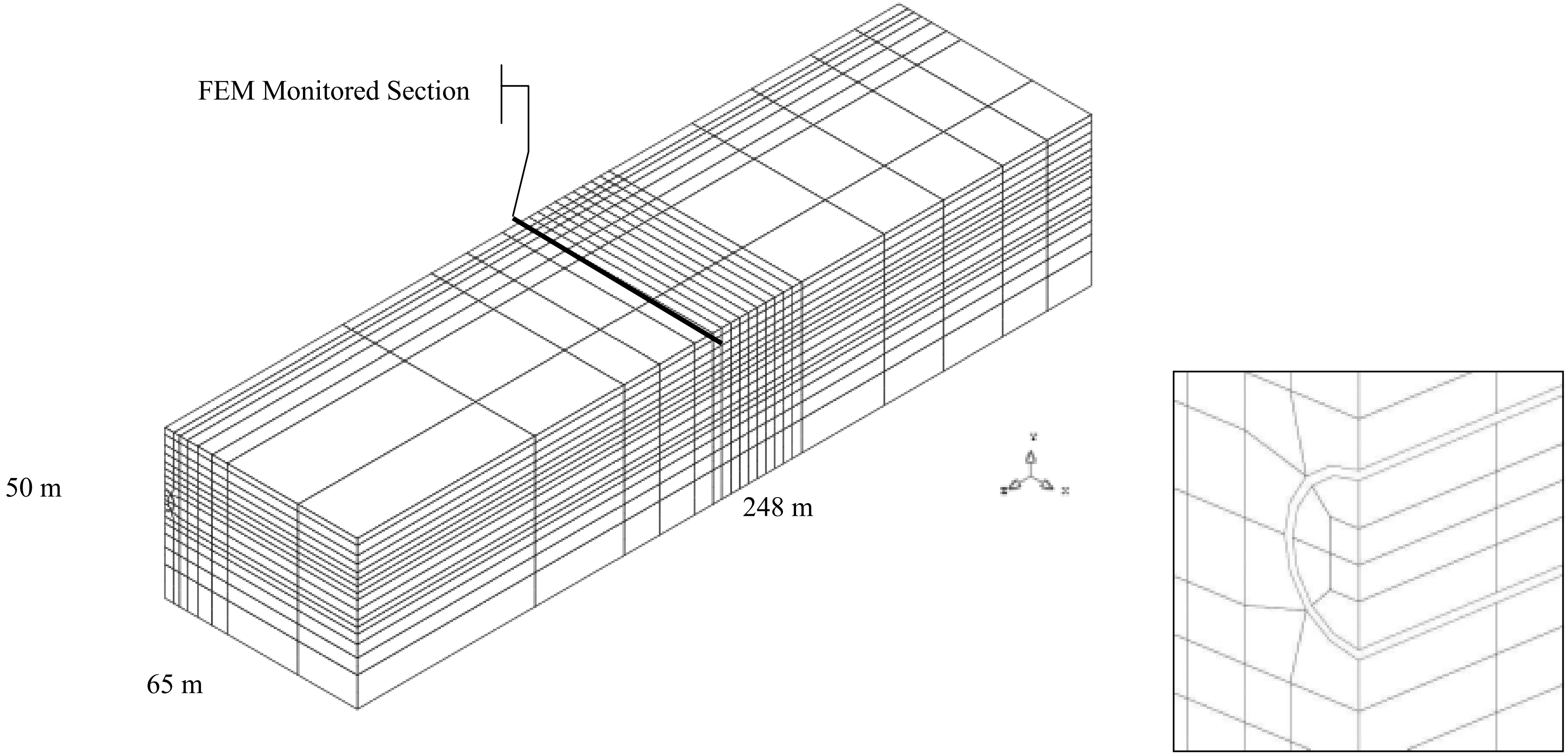

Figure 5.1a Finite element Mesh (3120 elements)

Figure 5.1b Close up of tunnel boundary

Figure 5.1 Typical finite element mesh

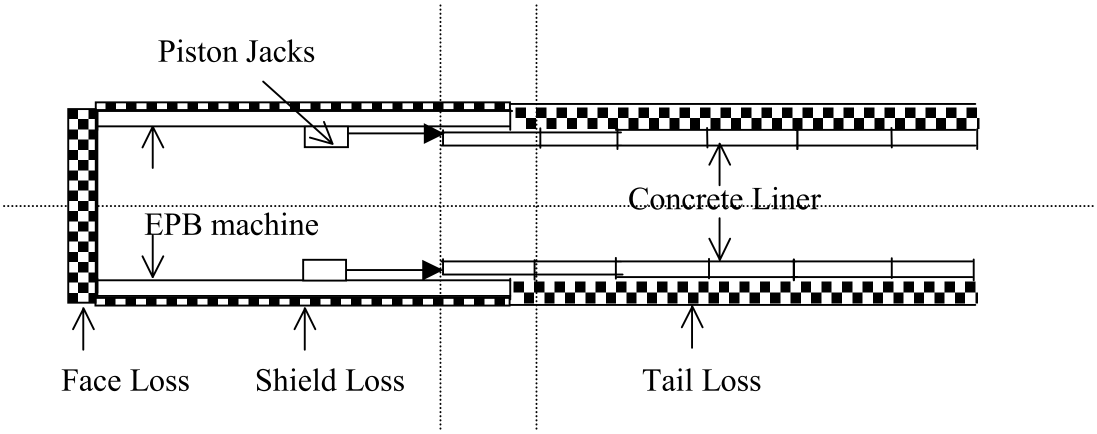

Figure 5.2a Tunnel excavation through jacking of piston ram

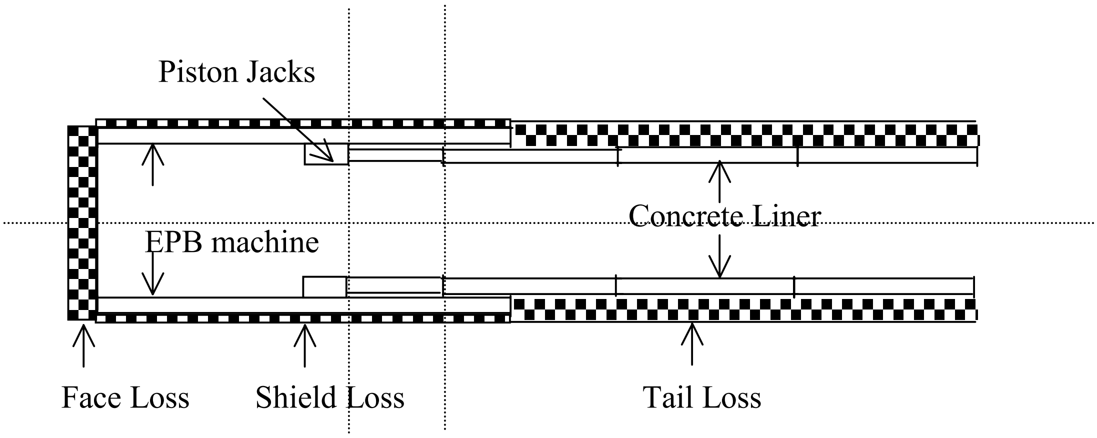

Figure 5.2b Retraction of piston ram and installation of concrete lining

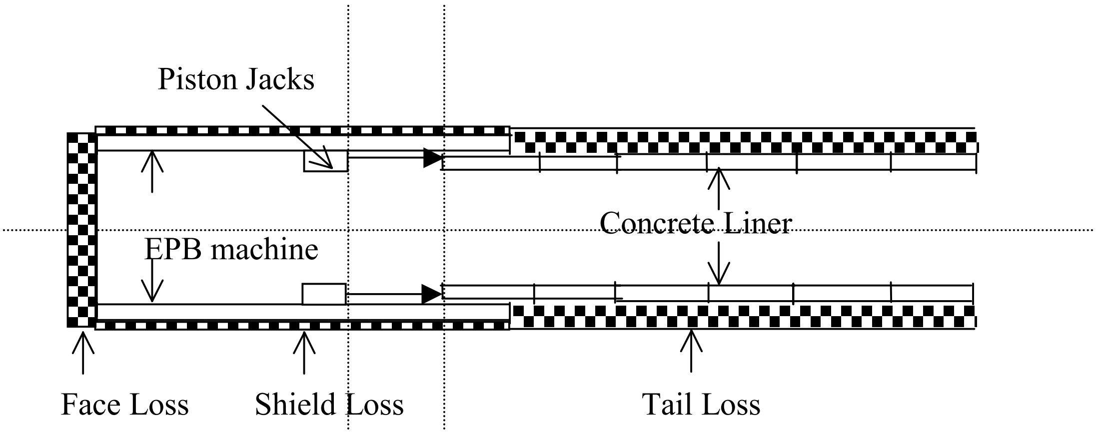

Figure 5.2c Shield advanced through jacking of piston ram

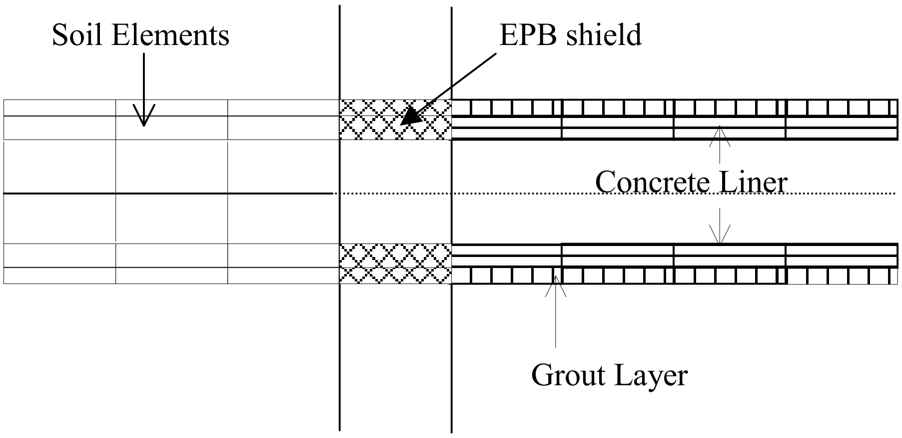

Figure 5.3a FE construction sequences for EPB modelling (Stage A)

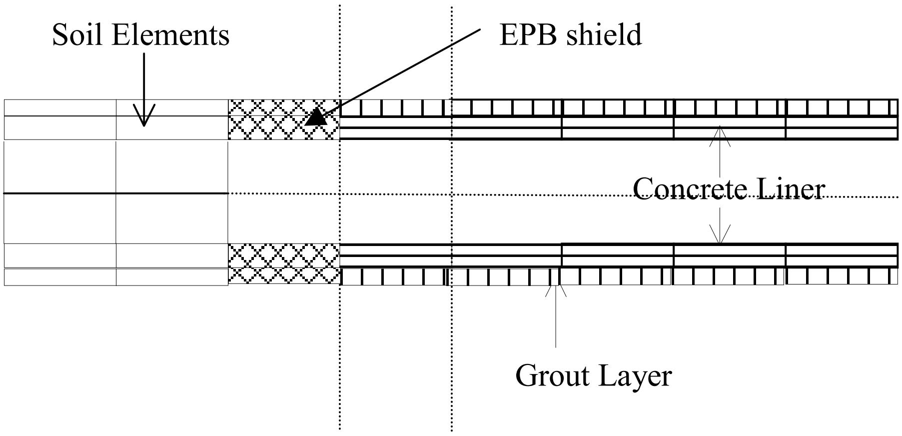

Figure 5.3b FE construction sequences for EPB modelling (Stage B)

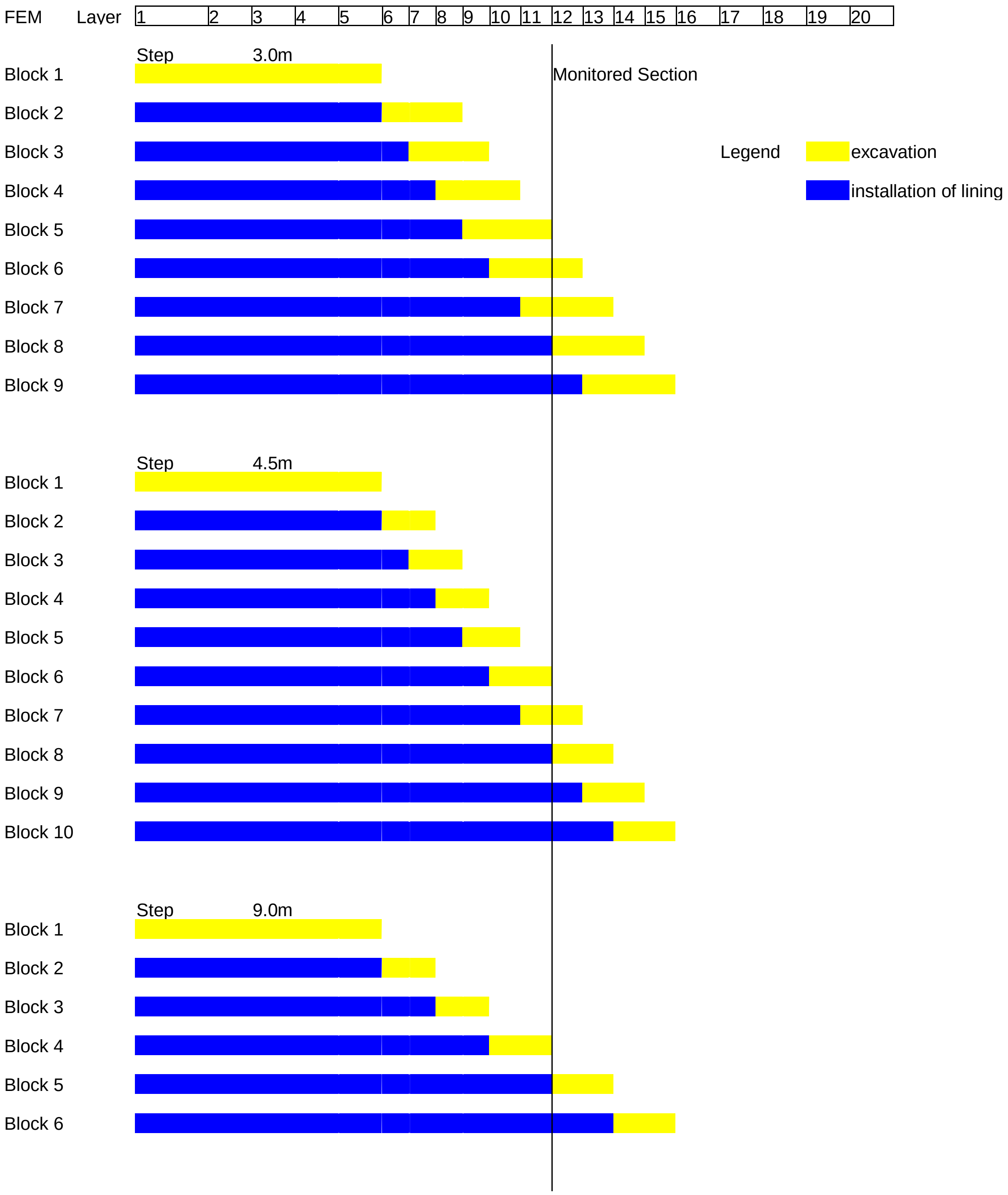

Figure 5.4 Excavation sequences for various excavation step sizes

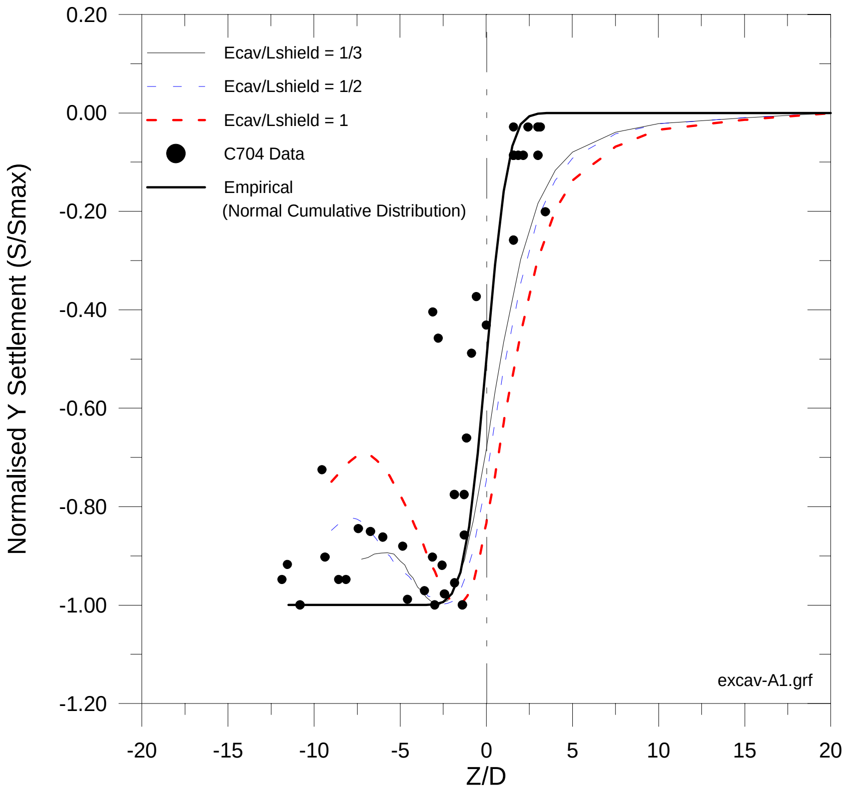

Figure 5.5 Trough length response due to different excavation step sizes

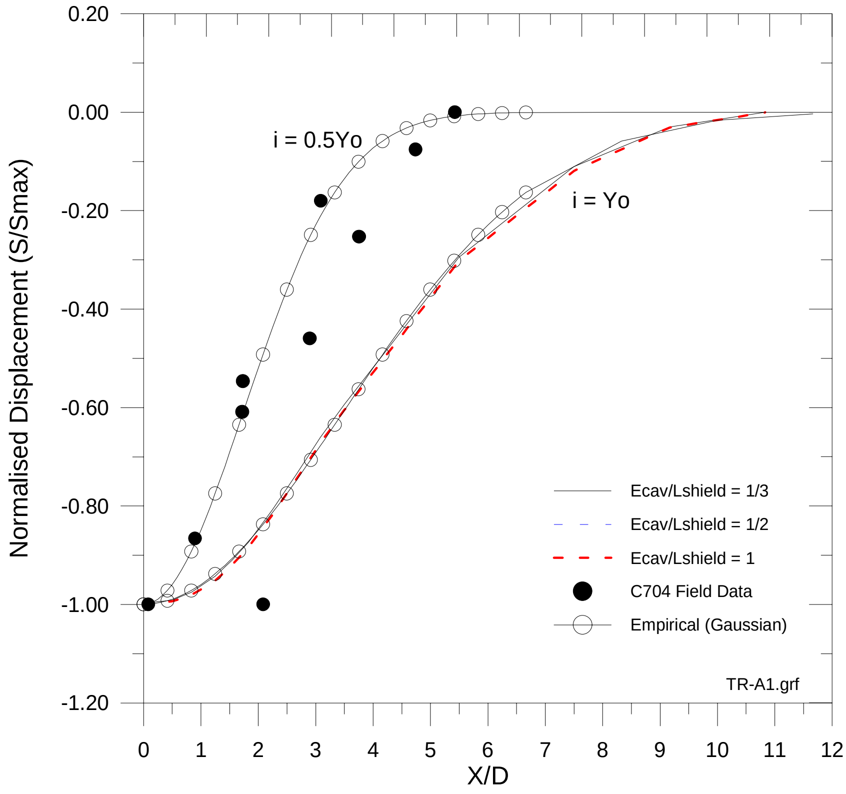

Figure 5.6 Trough width response due to different excavation step sizes

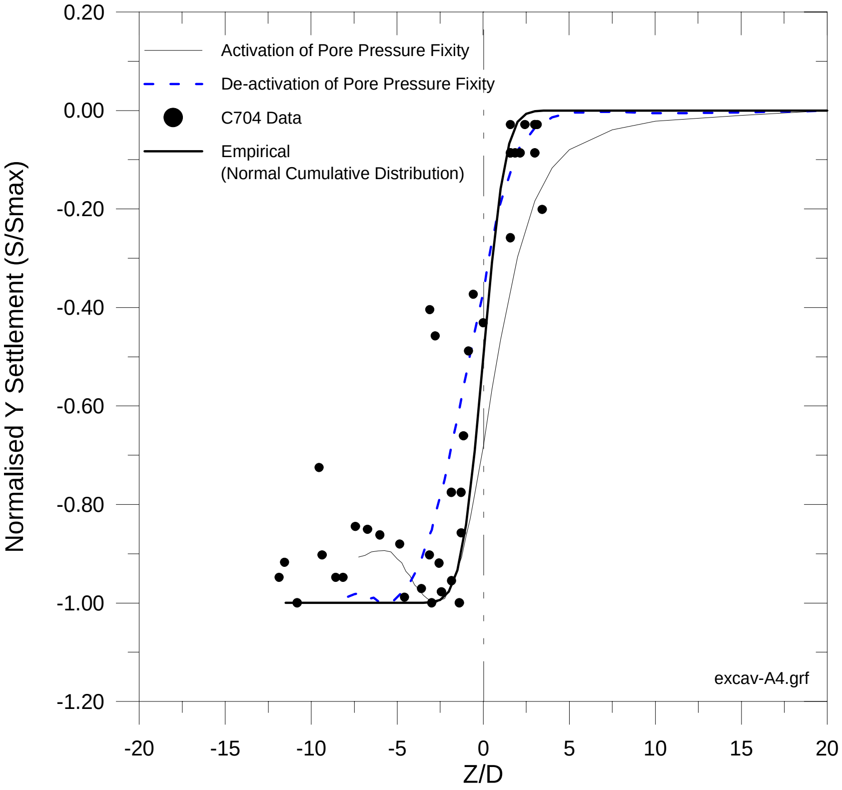

Figure 5.7 Trough length response due to pore pressure fixity

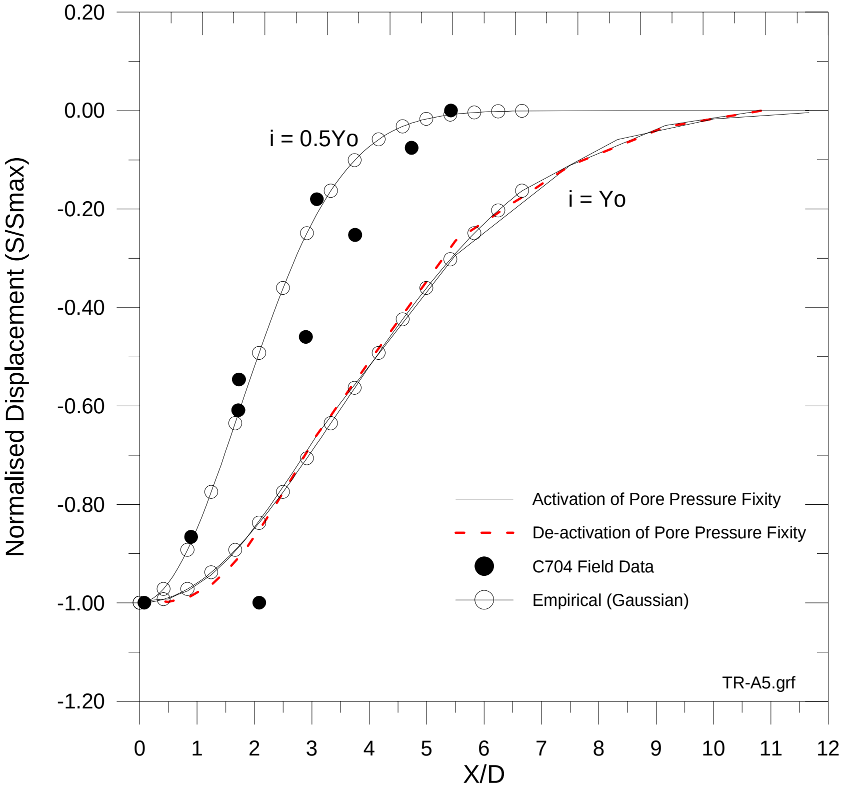

Figure 5.8 Trough width response due to pore pressure fixity

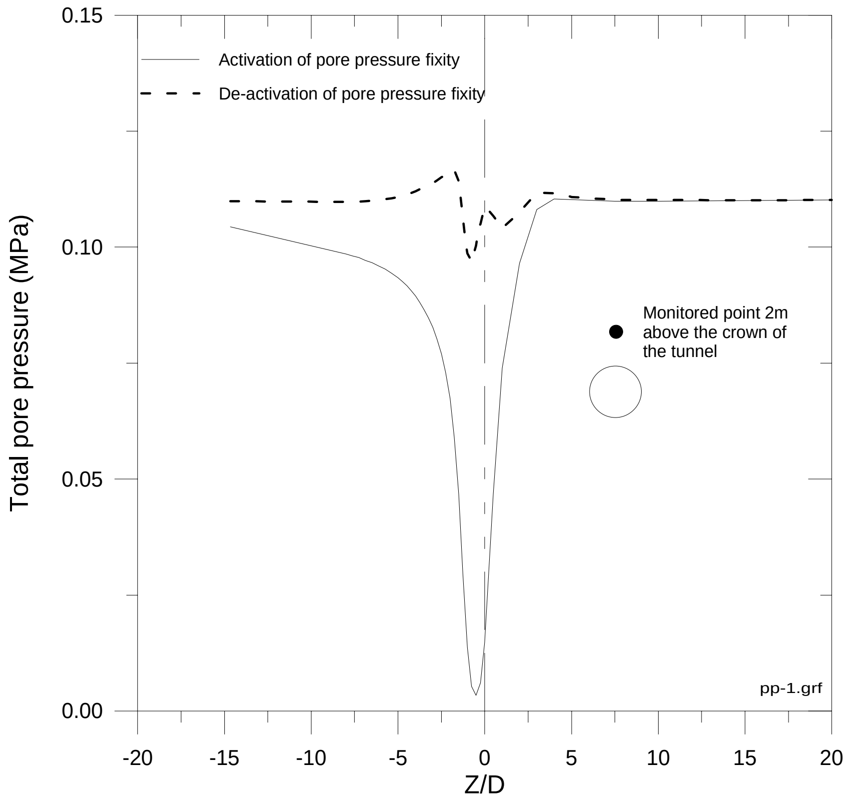

Figure 5.9 Total pore pressure variations due to pore pressure fixity

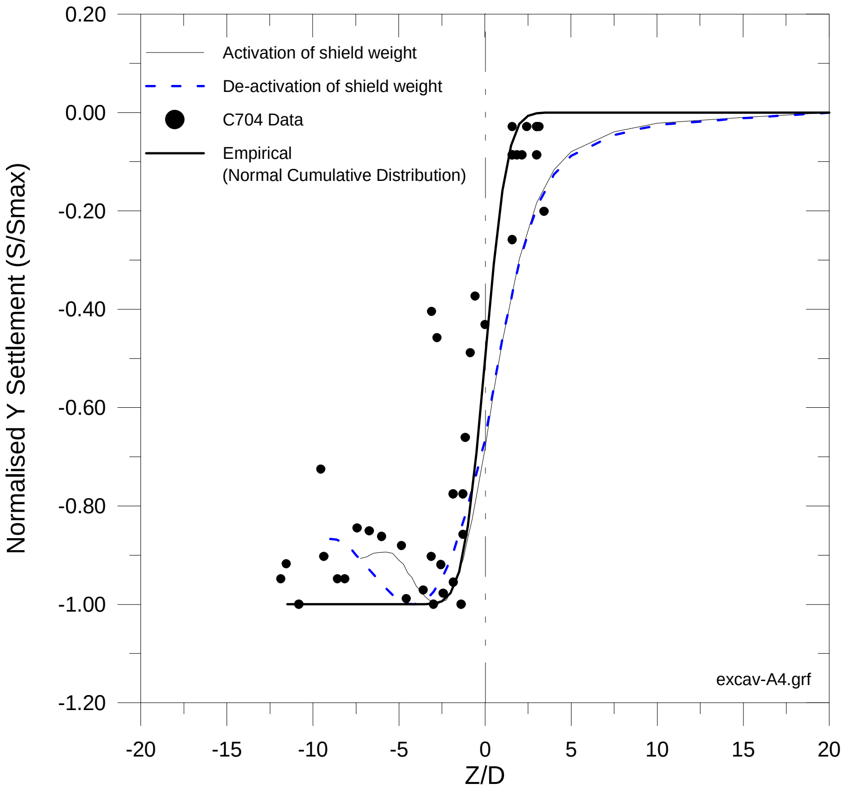

Figure 5.10 Trough length response due to EPB shield's weight

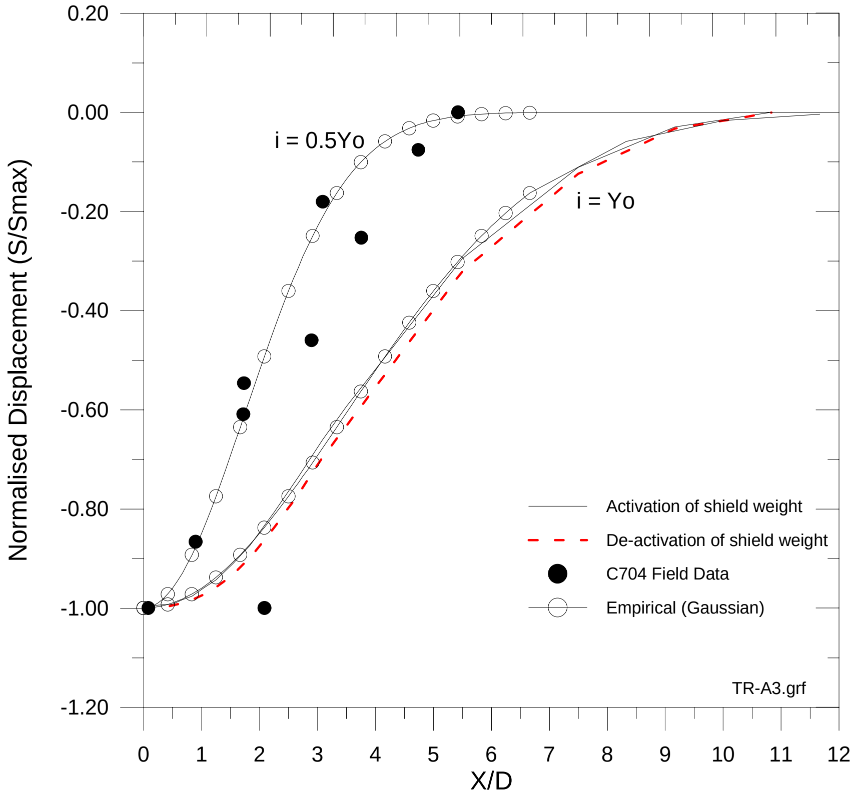

Figure 5.11 Trough width response due to EPB shield's weight

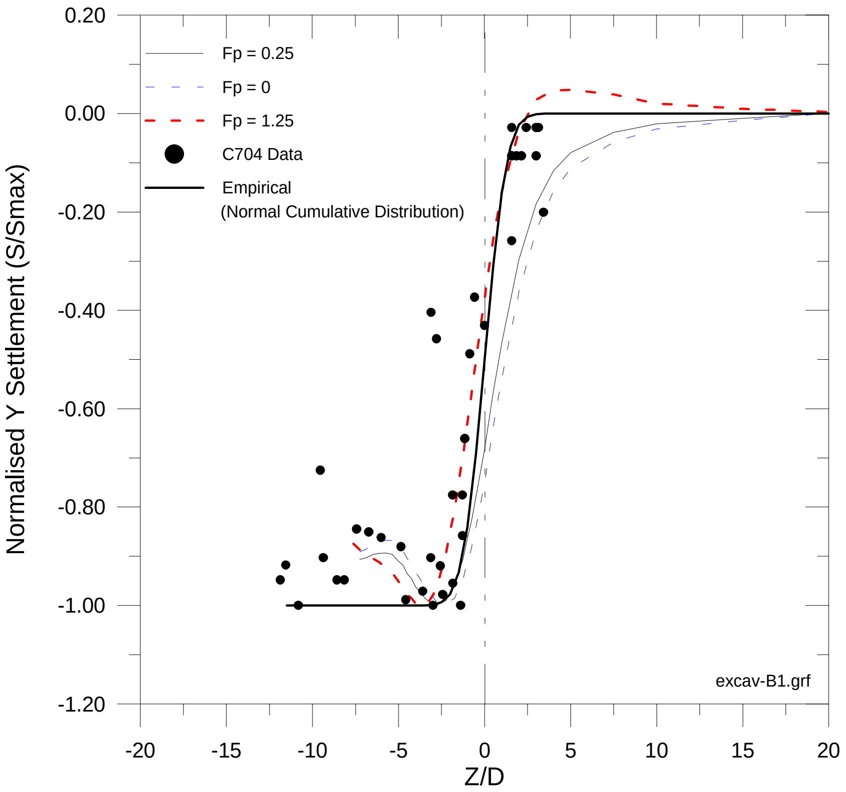

Figure 5.12 Trough length response due to different applied face pressure

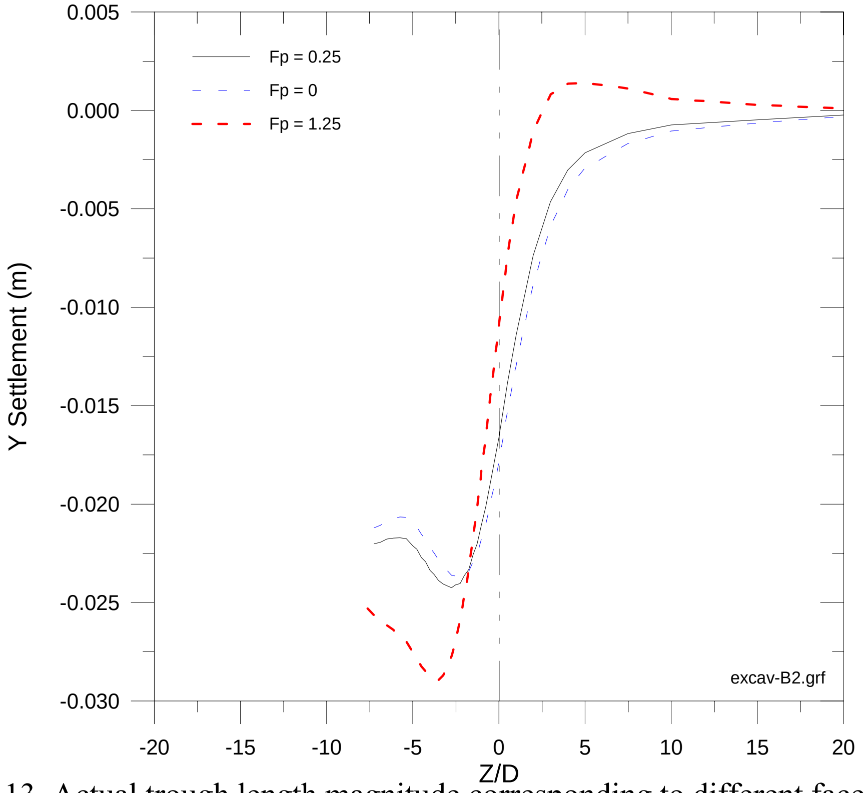

Figure 5.13 Actual trough length magnitude corresponding to different face pressure

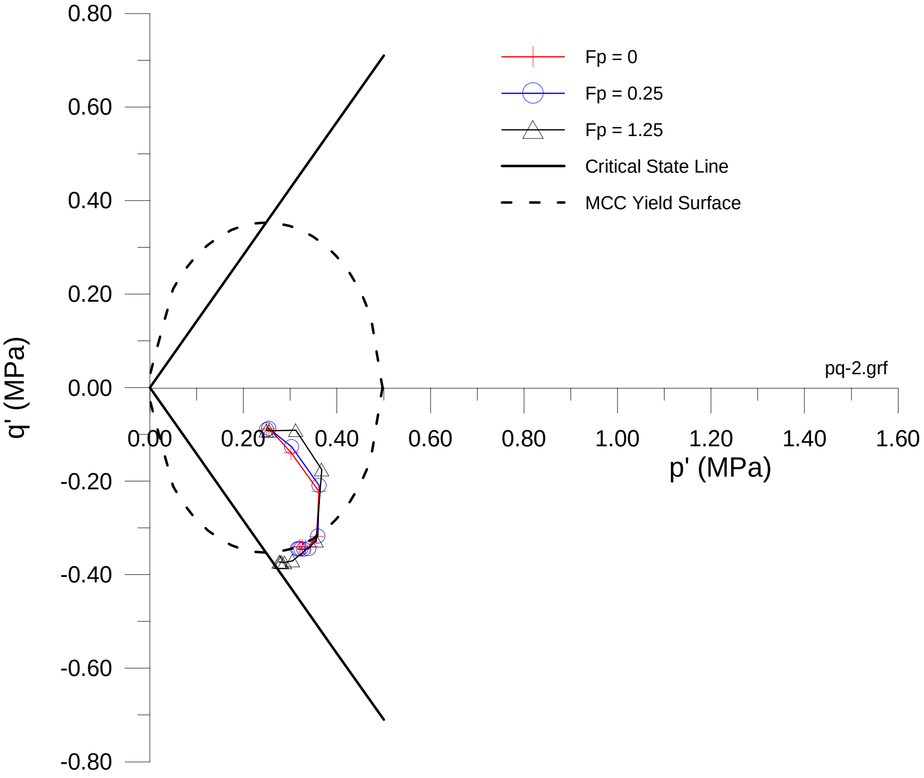

Figure 5.14 Stress paths near the crown of a tunnel for face pressure variations

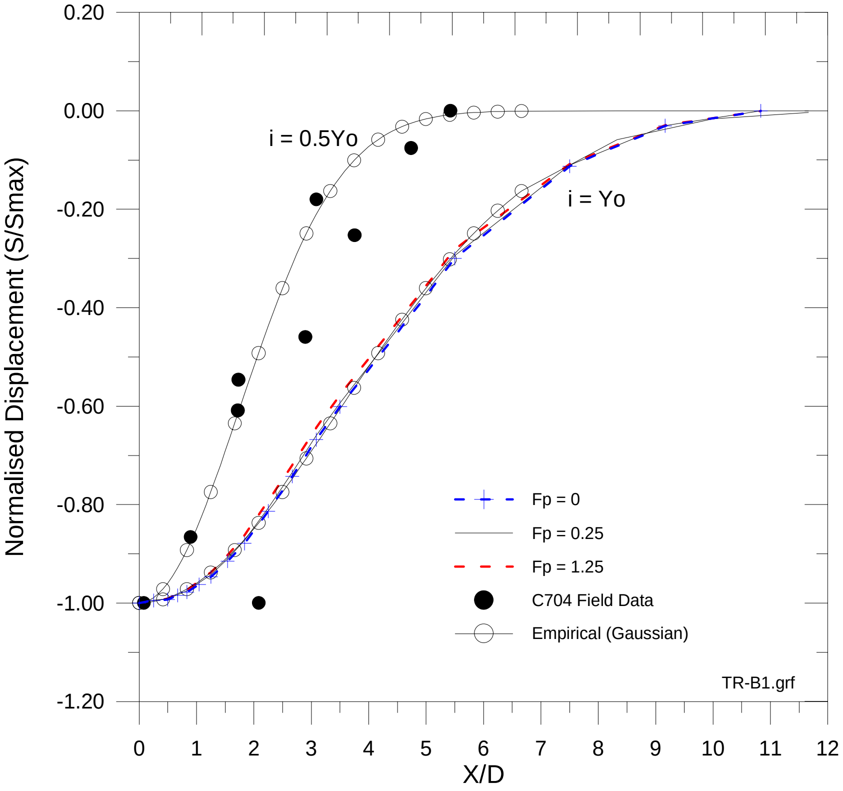

Figure 5.15 Trough width response due to face pressure variations

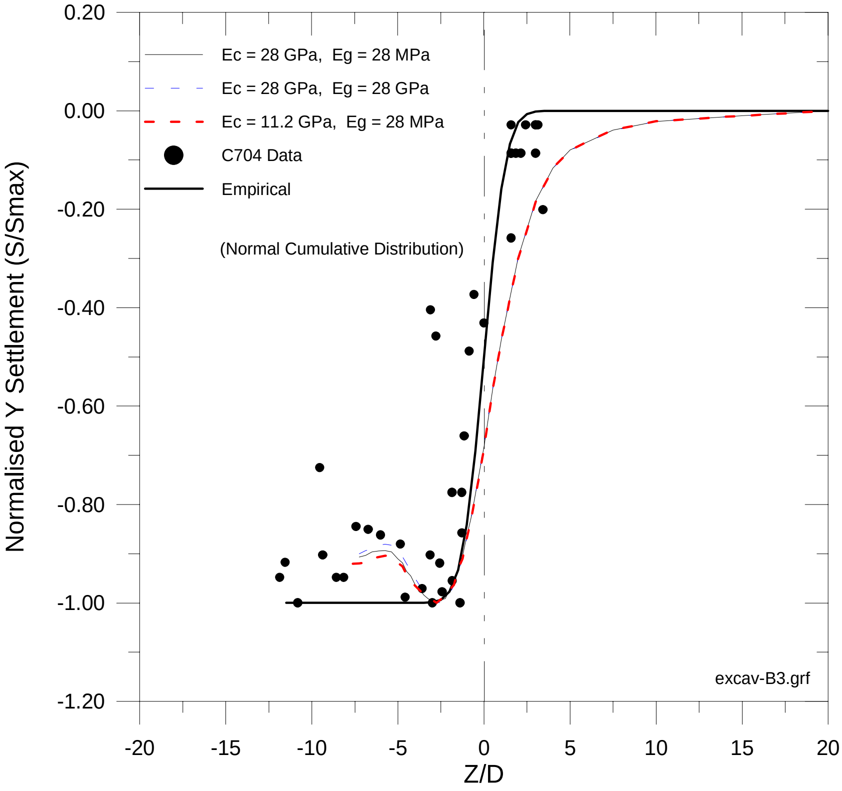

Figure 5.16 Trough length response of Concrete and Grout stiffness variations

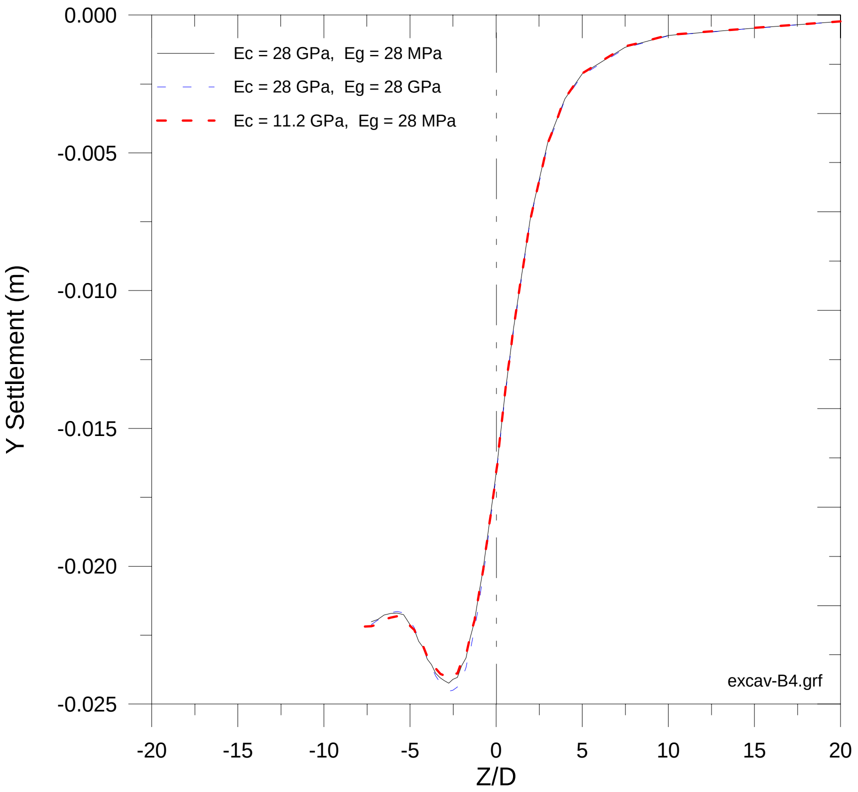

Figure 5.17 Trough length magnitude due to different liner stiffness combinations

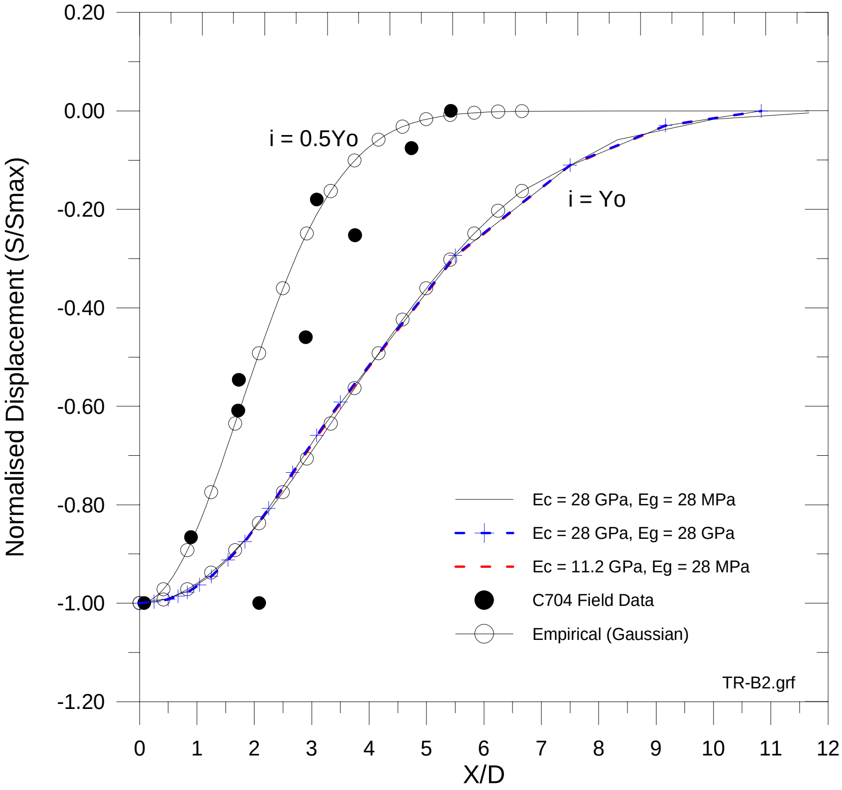

Figure 5.18 Trough width response due to different liner stiffness combinations

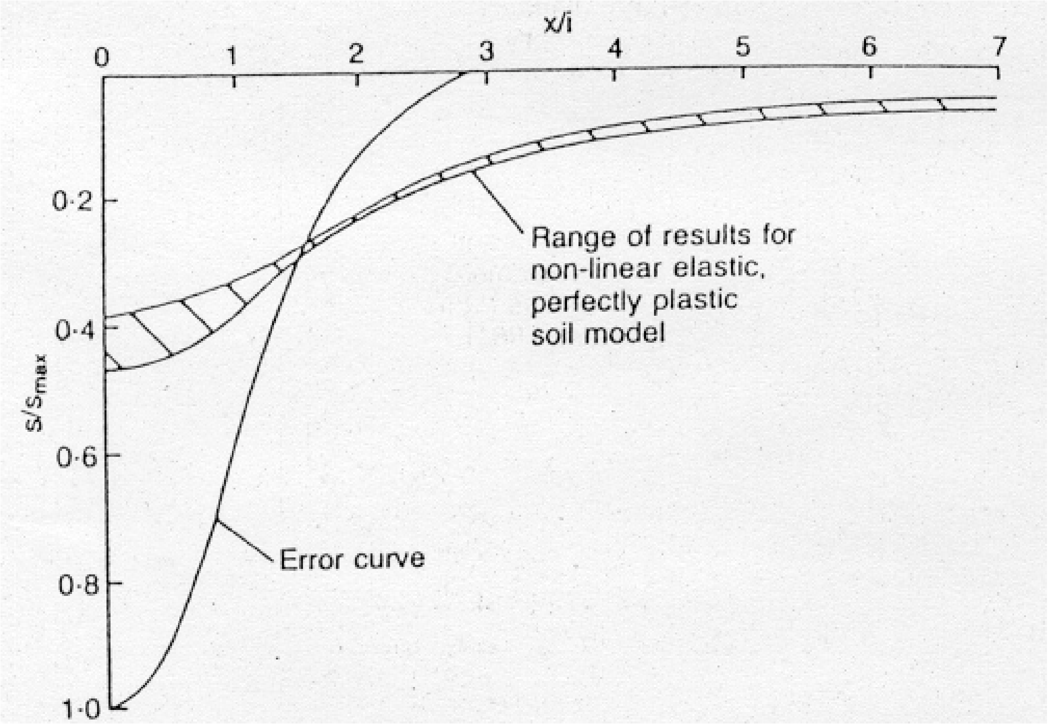

Figure 5.19a Typical computed trough width response (after Gunn,1992)

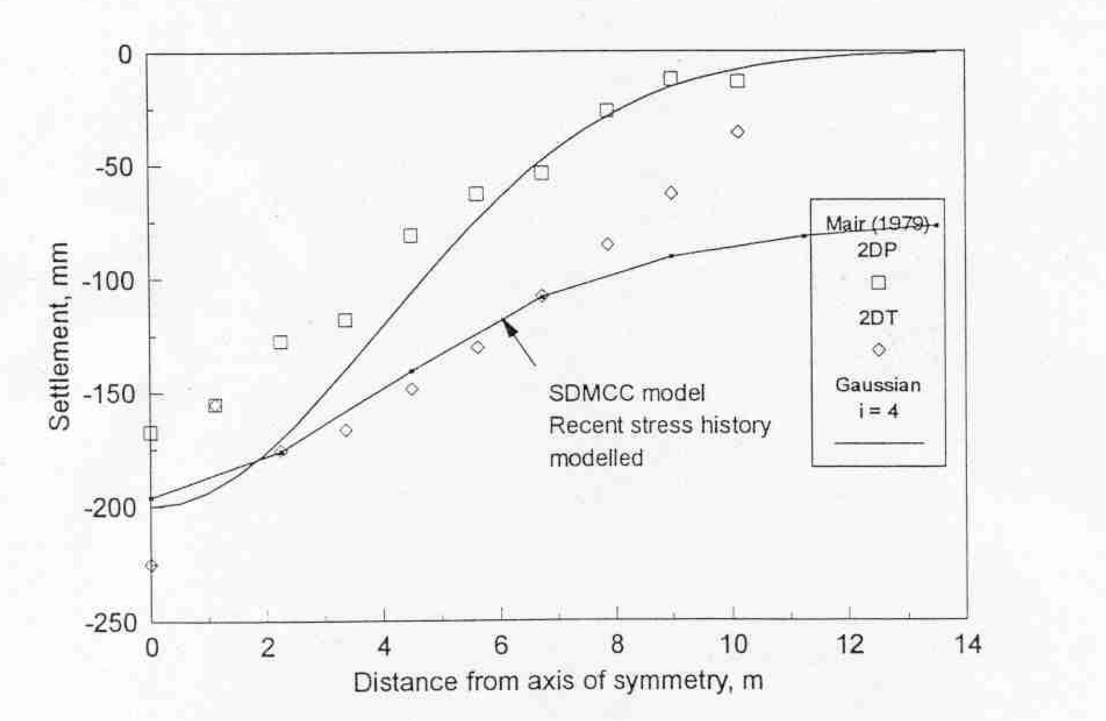

Figure 5.19b Typical computed trough width response (after Dasari,1996)

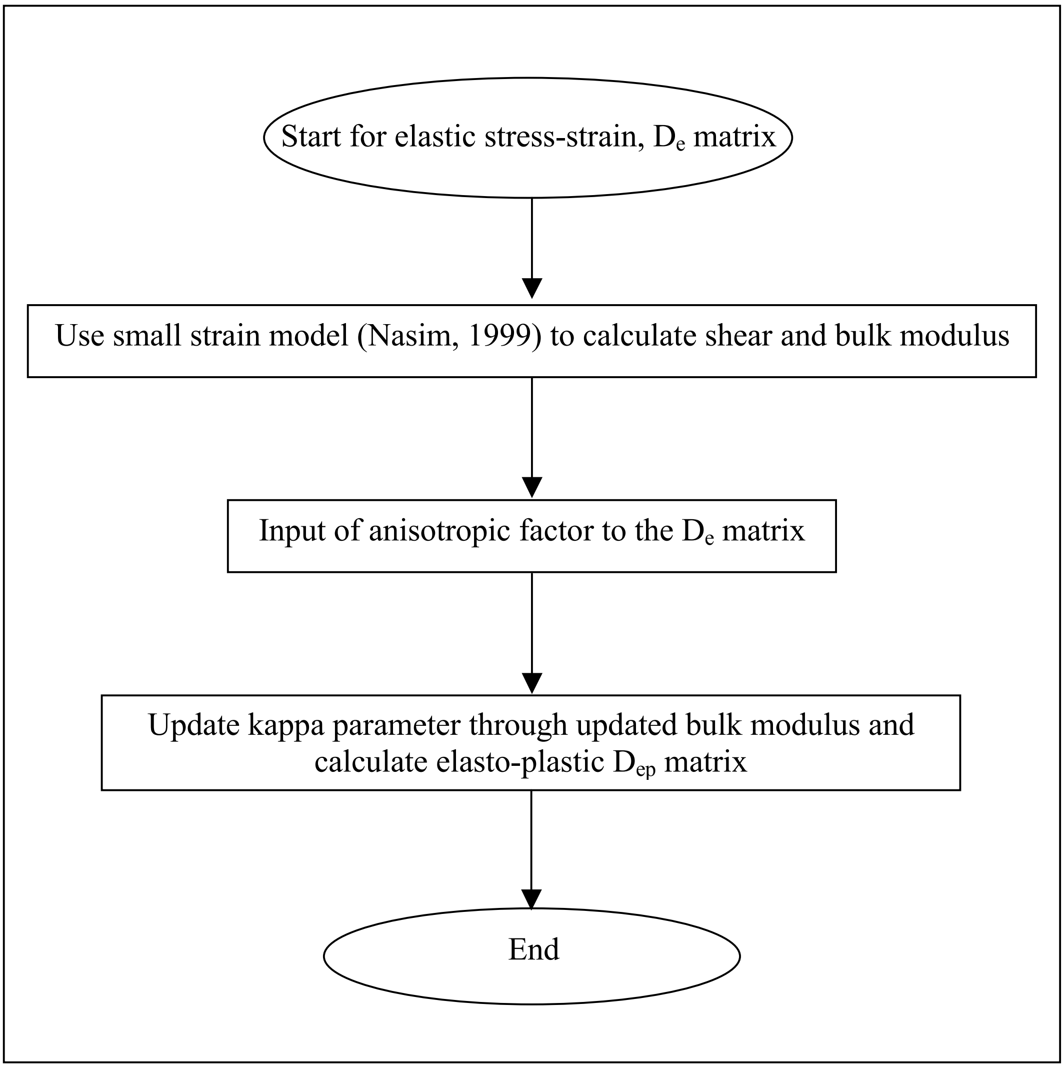

Figure 5.20 Flowchart for hybrid model HMCEA

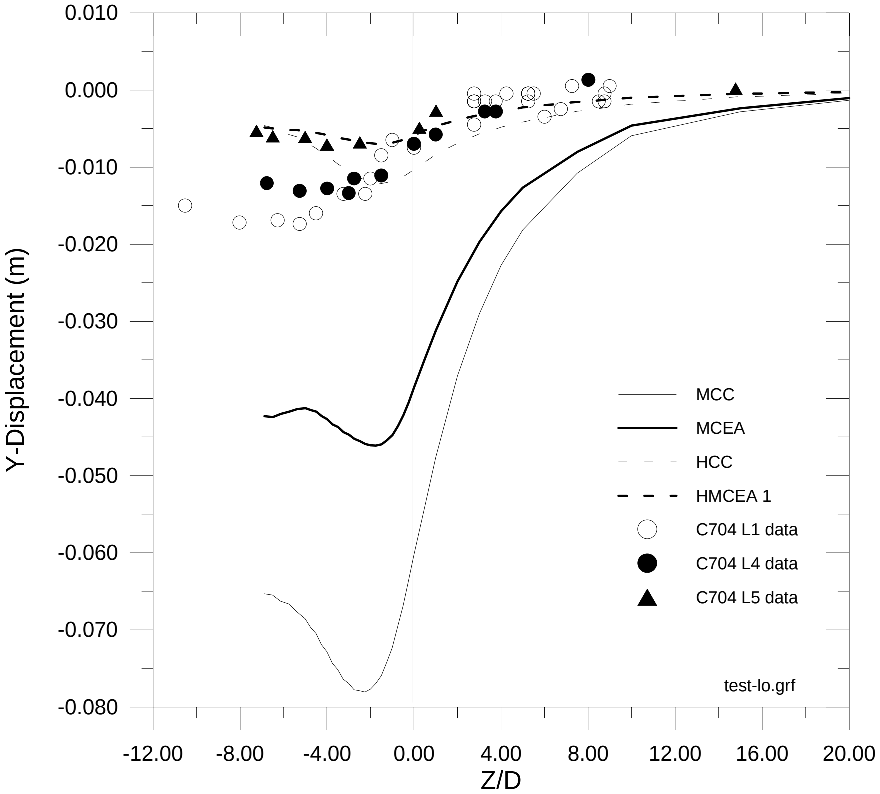

Figure 5.21 Comparison of Trough length for various soil models with field data

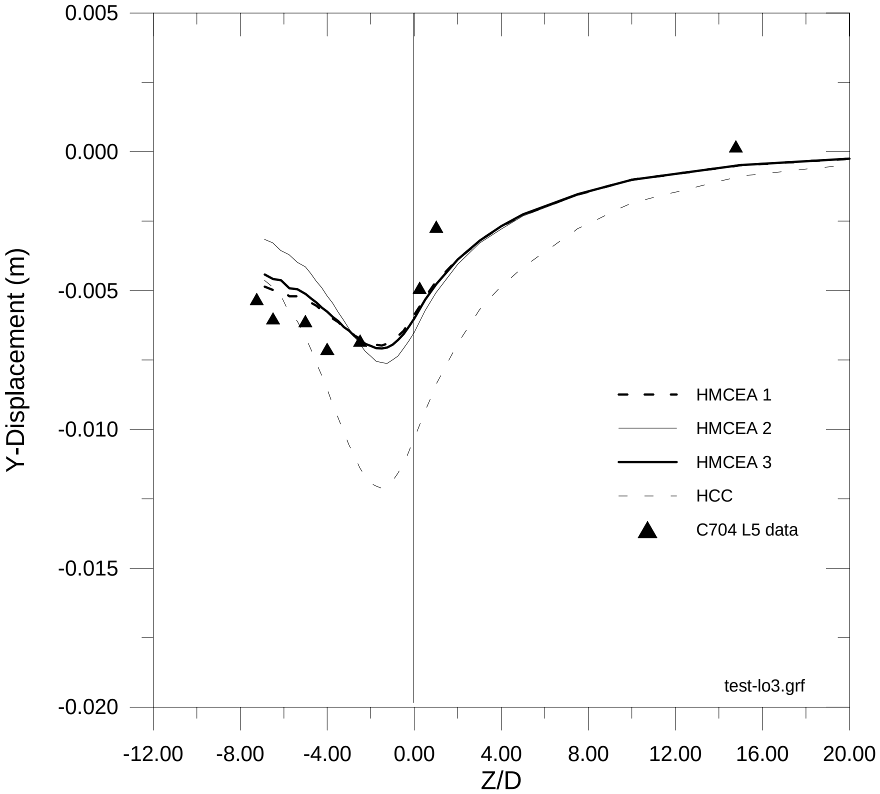

Figure 5.22 Comparison of Trough length for variations of HMCEA model

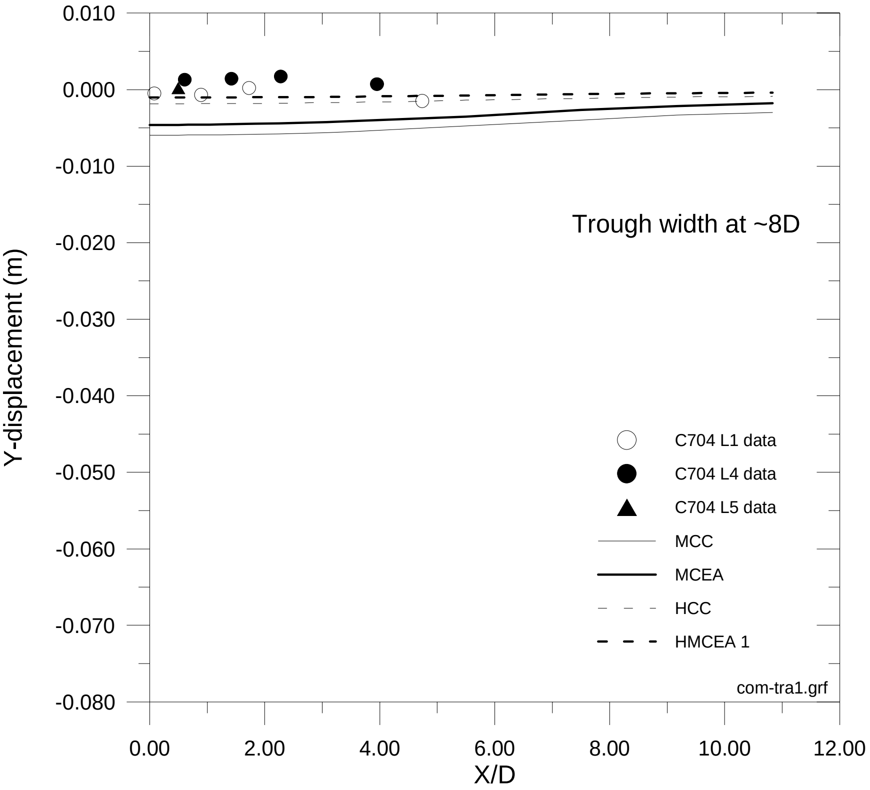

Figure 5.23 Trough width at 8D away from tunnel face

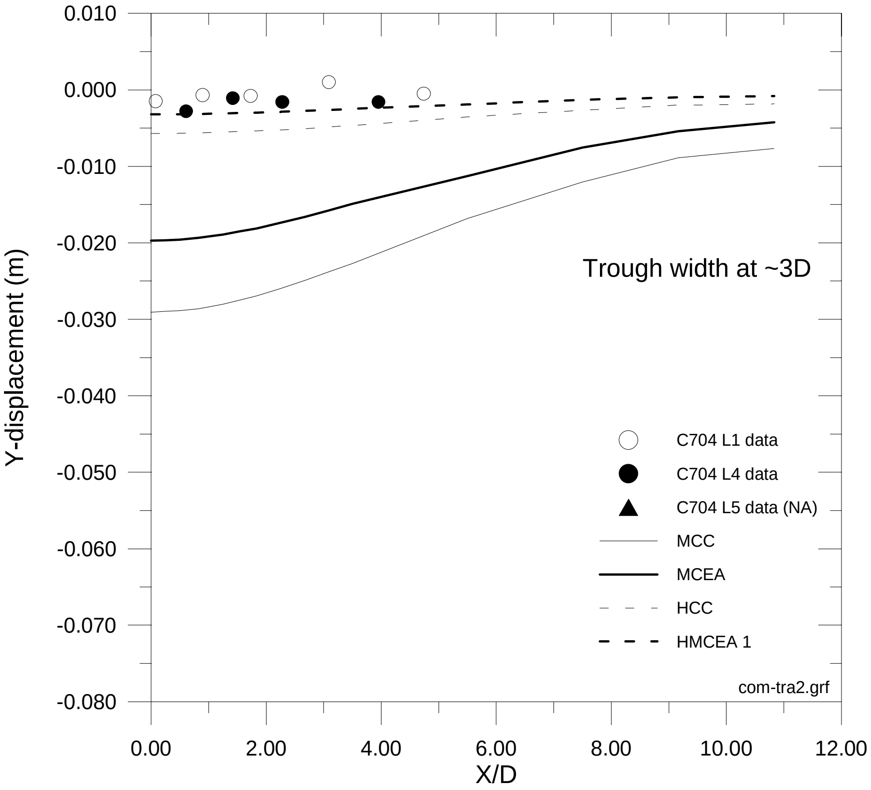

Figure 5.24 Trough width at 3D away from tunnel face

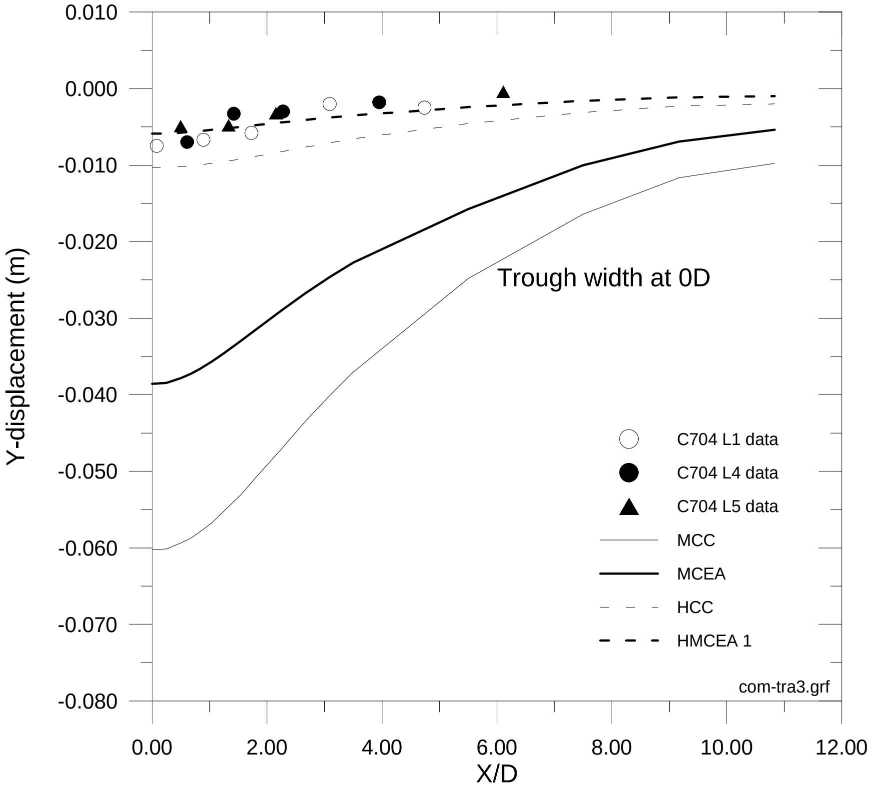

Figure 5.25 Trough width at 0D i.e. at tunnel face

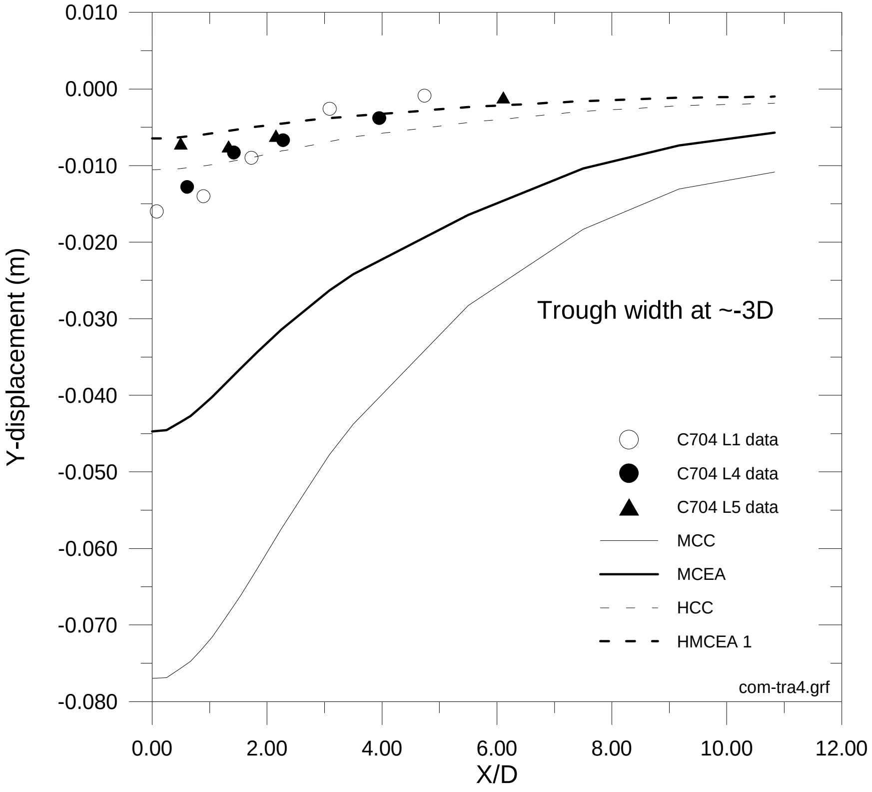

Figure 5.26 Trough width at –3 D away from tunnel face

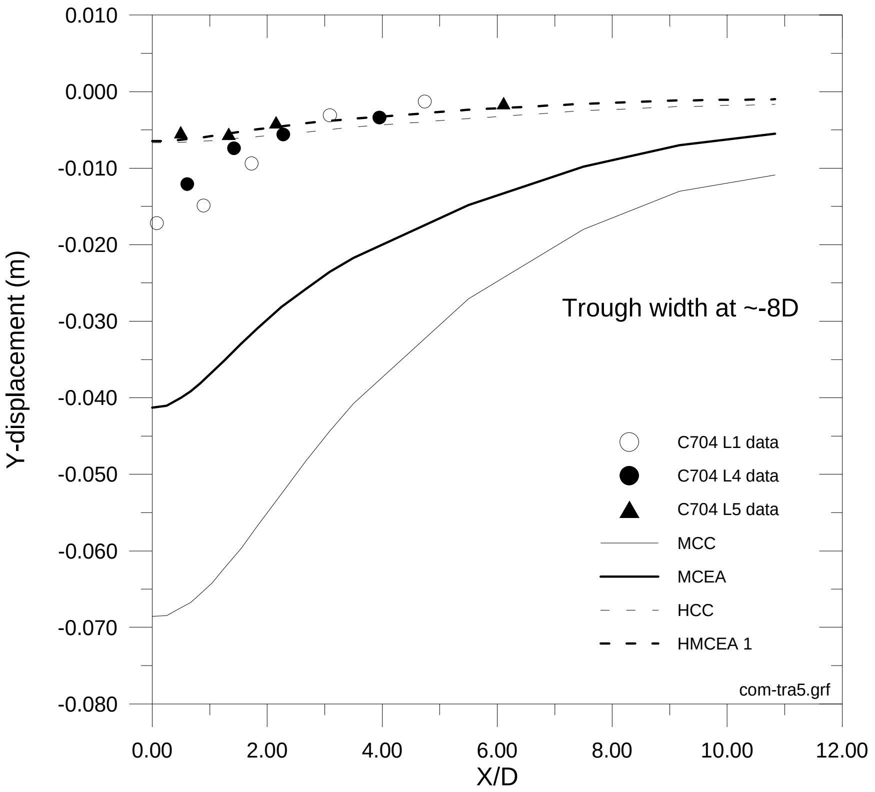

Figure 5.27 Trough width at –8 D away from tunnel face

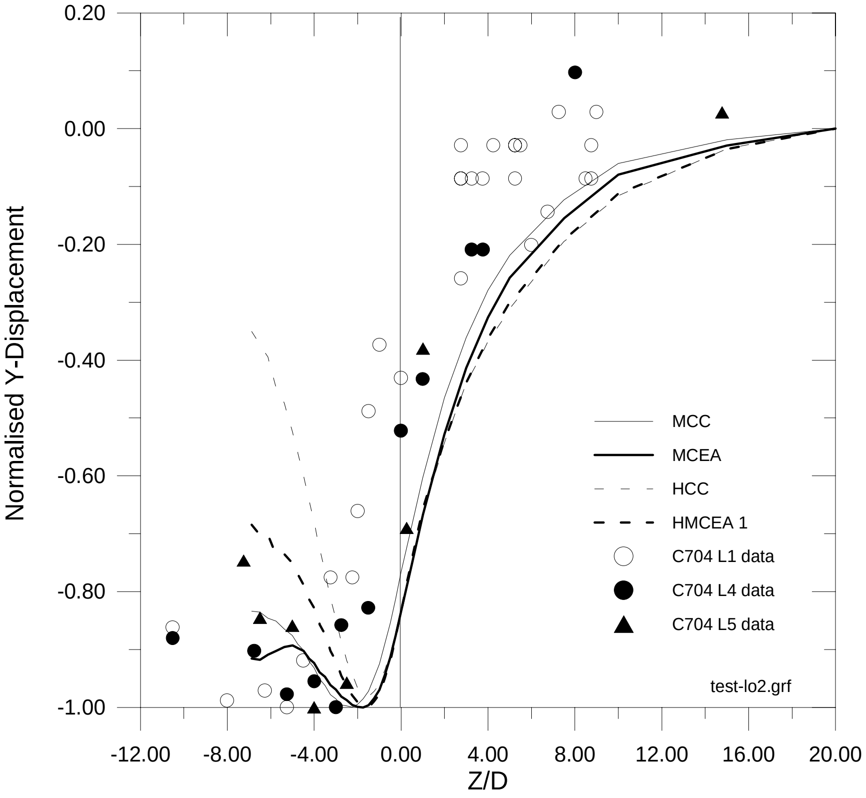

Figure 5.28 Comparison of normalised trough length for various soil models

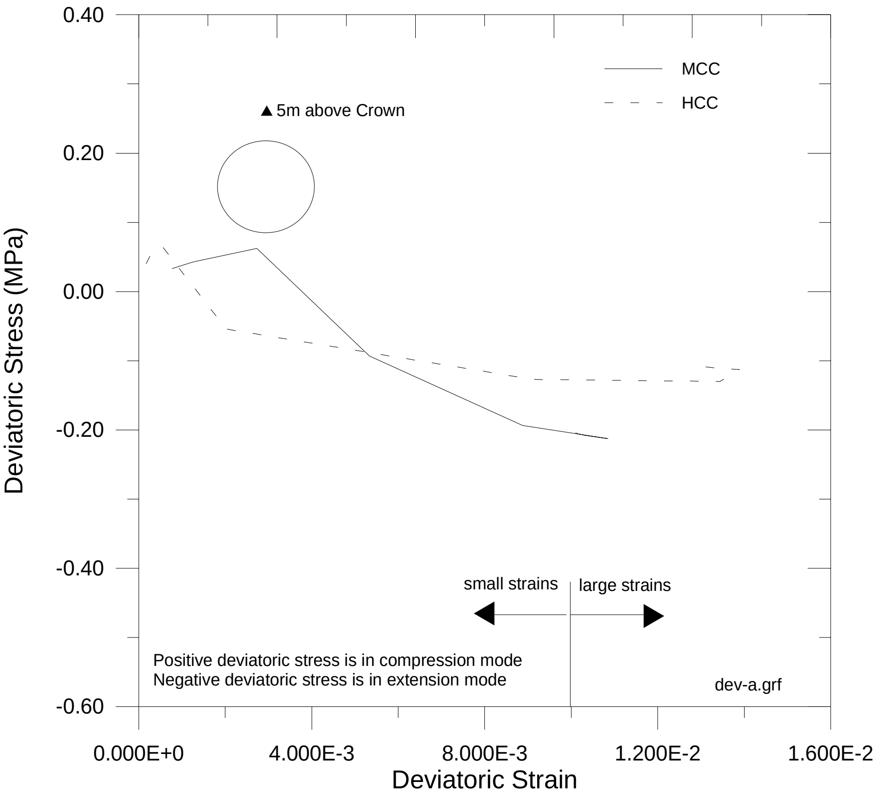

Figure 5.29 Deviatoric stress-strain response for various soil models at the FEM-L1 section, 5m above the Crown of the tunnel

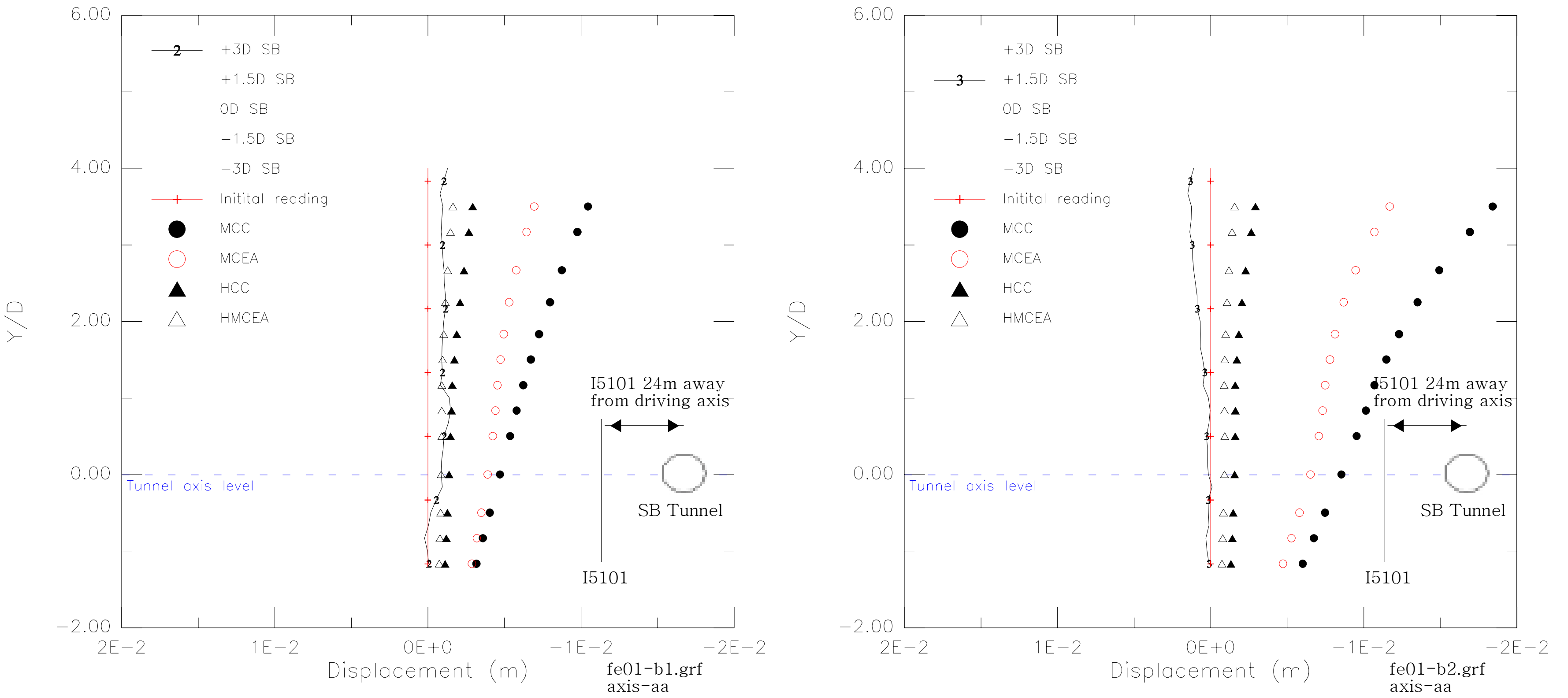

Figure 5.30a

Figure 5.30b

Figure 5.30 Comparison of subsurface lateral response at various distances away from tunnel driving axis a) At +3D, b) At +1.5D

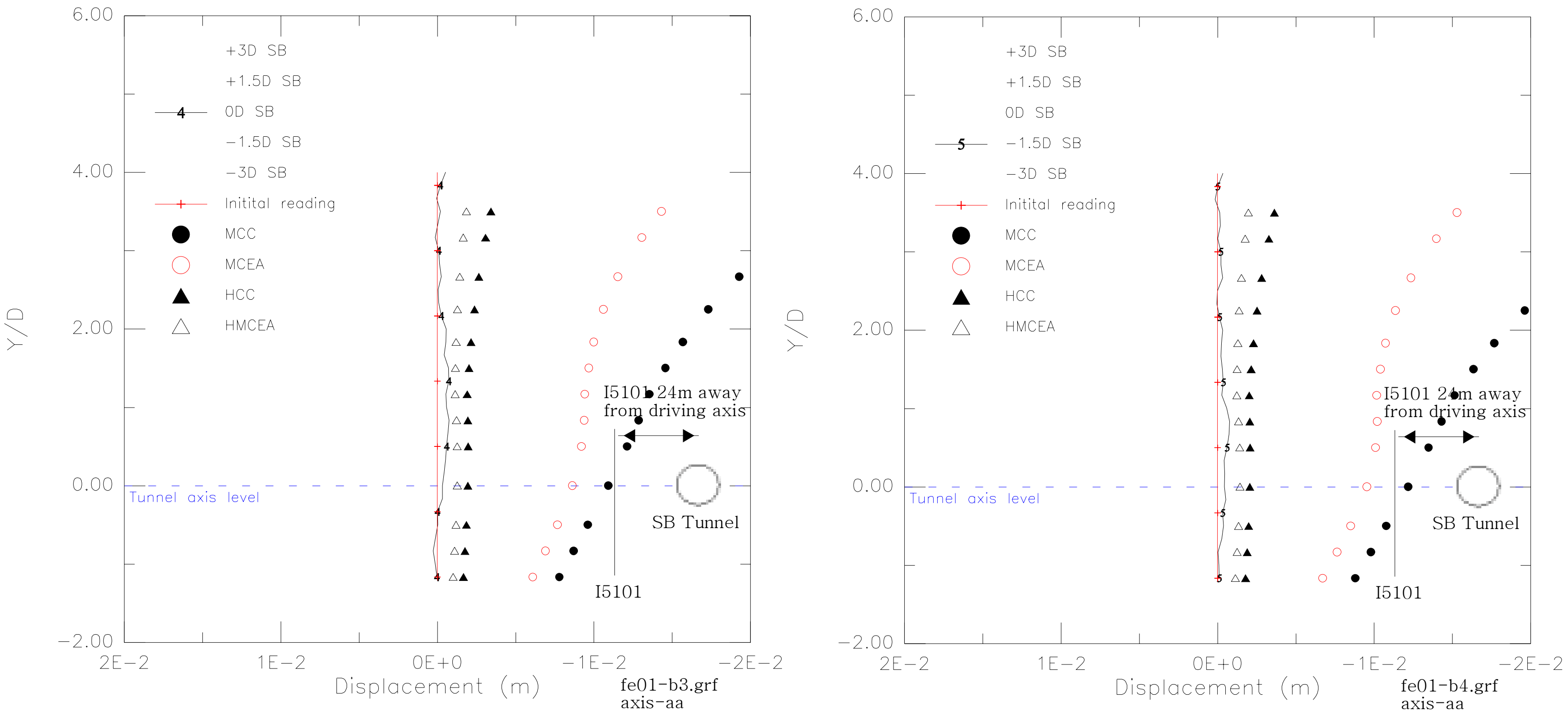

Figure 5.30c

Figure 5.30d

Figure 5.30 Comparison of subsurface lateral response at various distances away from tunnel driving axis c) At 0D, d) At -1.5D

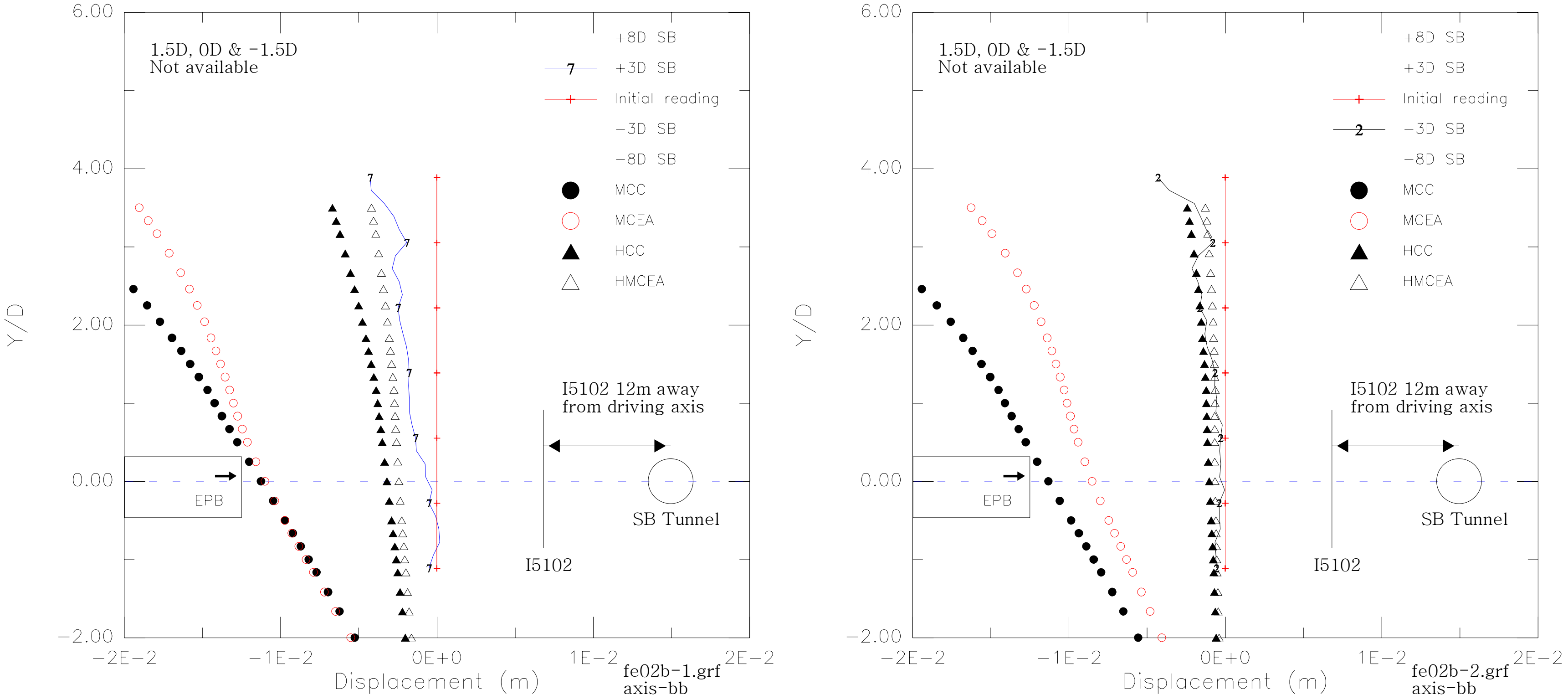

Figure 5.31a

Figure 5.31b

Figure 5.31 Comparison of subsurface longitudinal response at various distances away from tunnel driving axis a) At +3D, b) At -3D

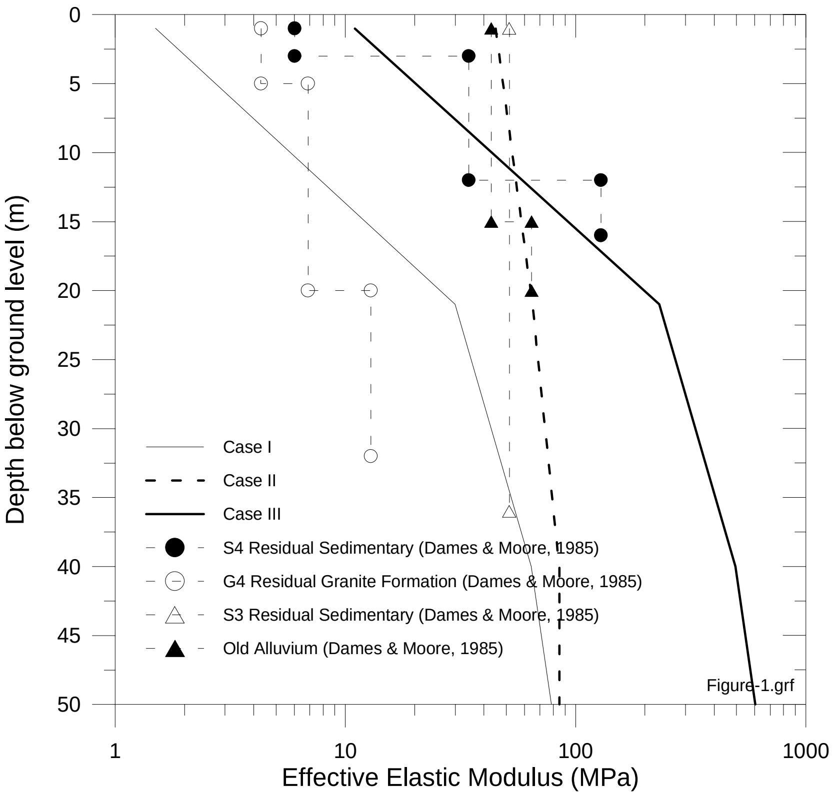

Figure 5.32a Effective E-modulus variations with depth

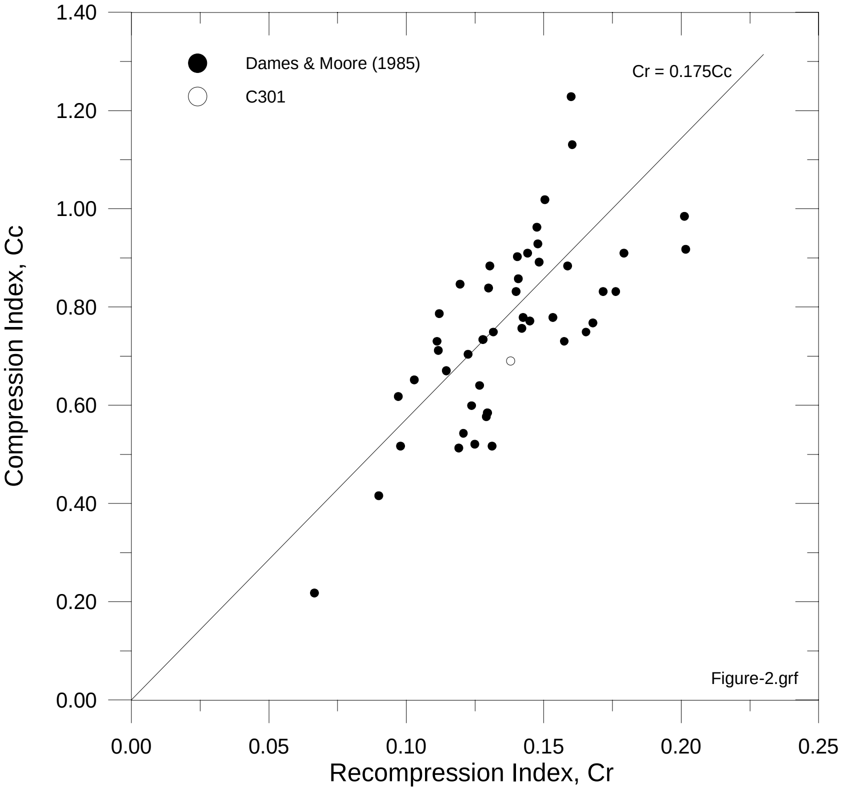

Figure 5.32b Compression and recompression index for Case IV

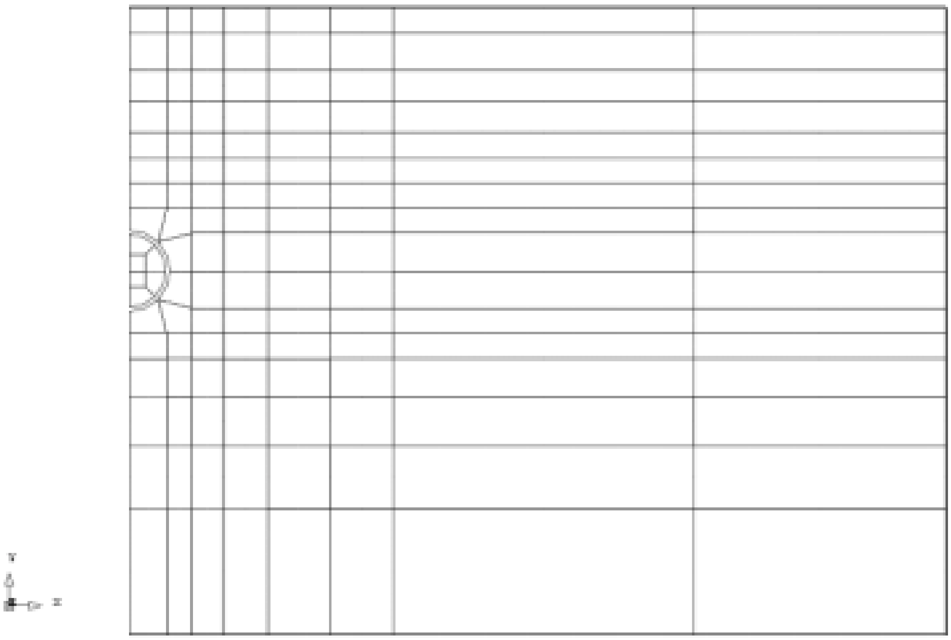

Figure 5.33a 2D meshes from Crisp

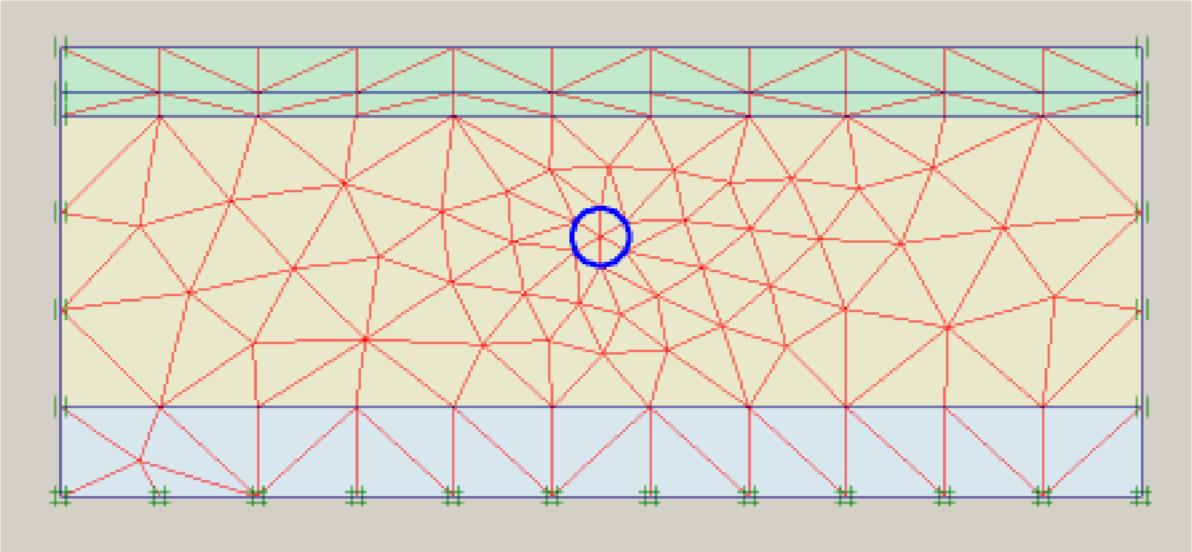

Figure 5.33b 2D meshes from Plaxis

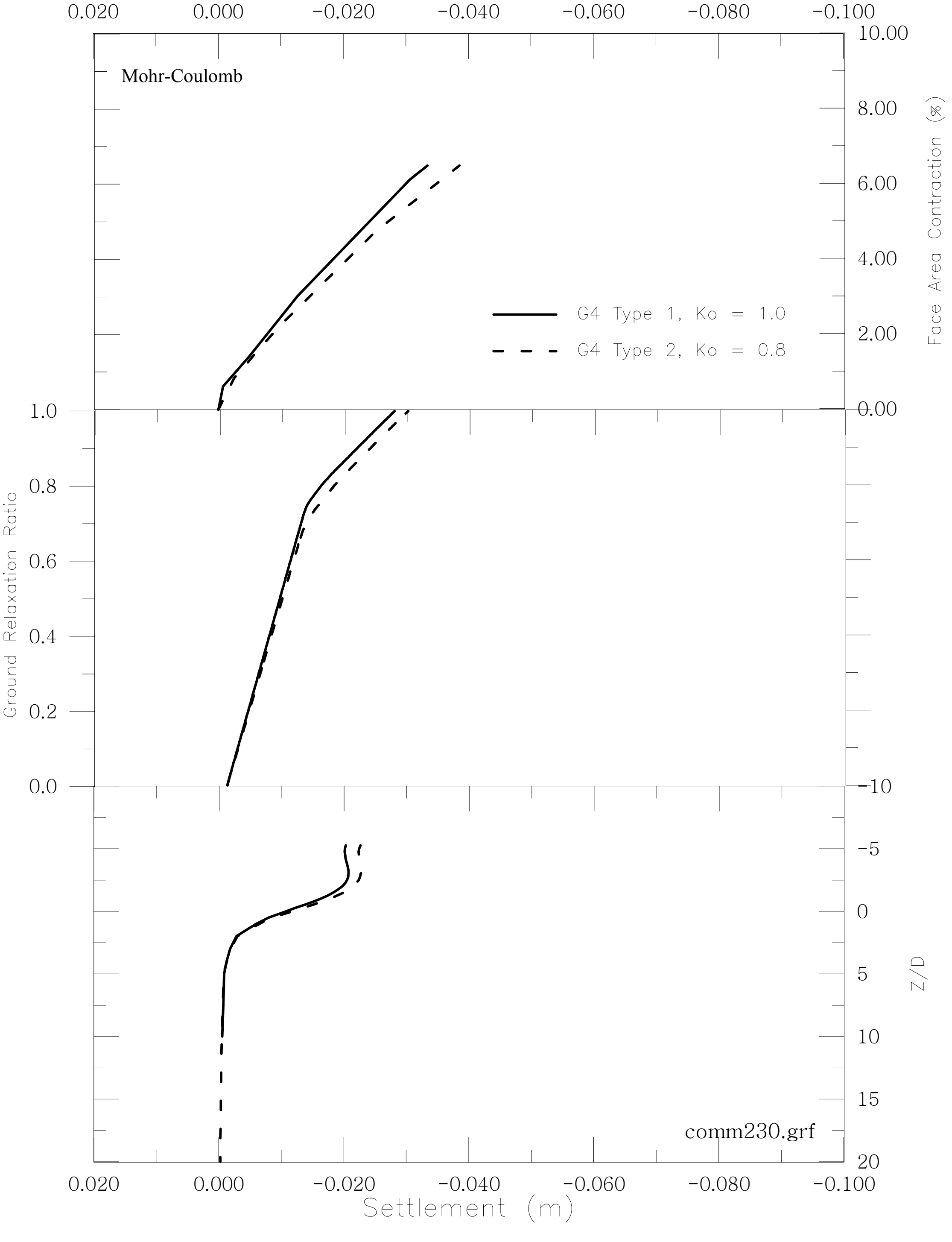

Figure 5.34 Case I 3D & 2D ground response

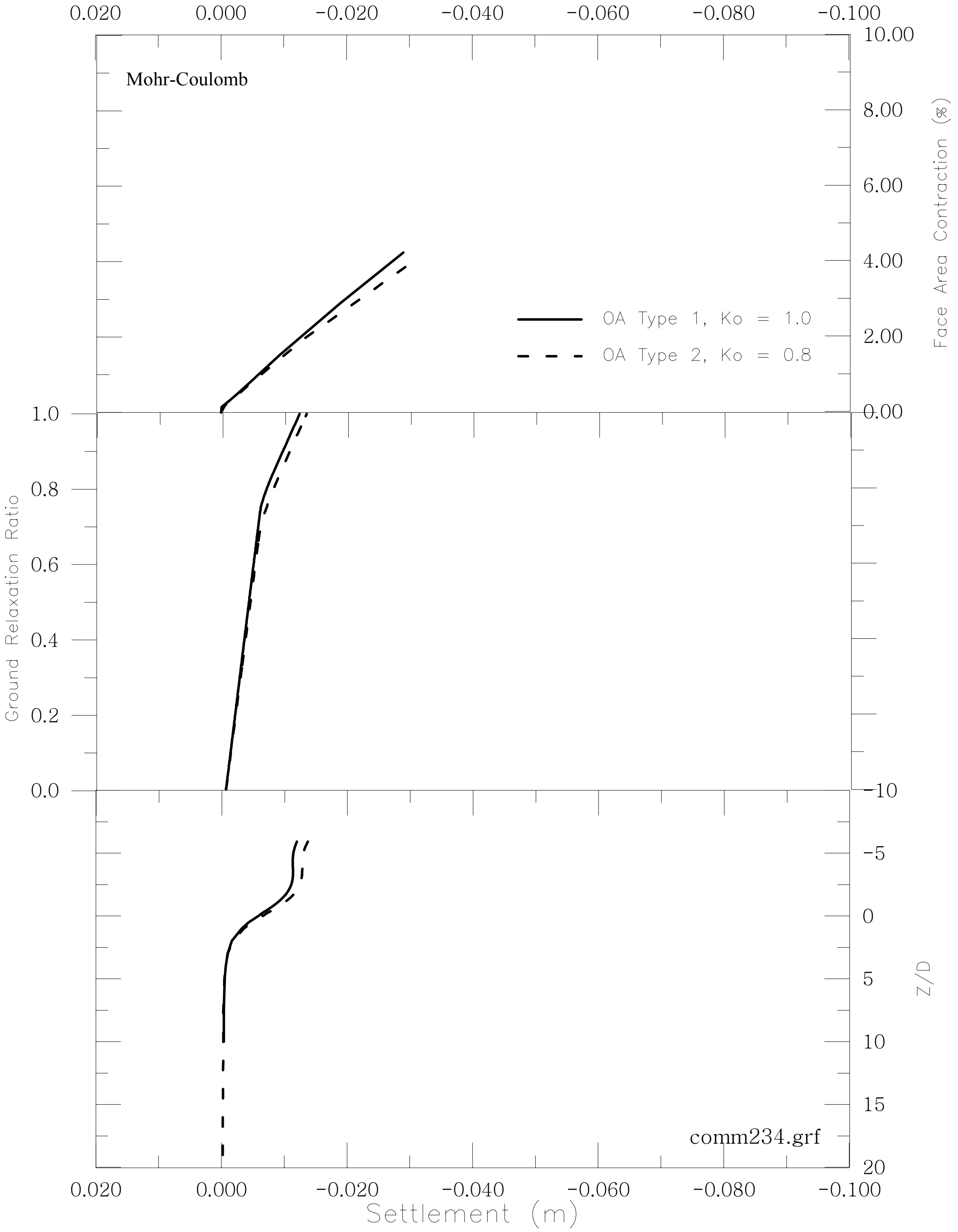

Figure 5.35 Case II 3D & 2D ground response

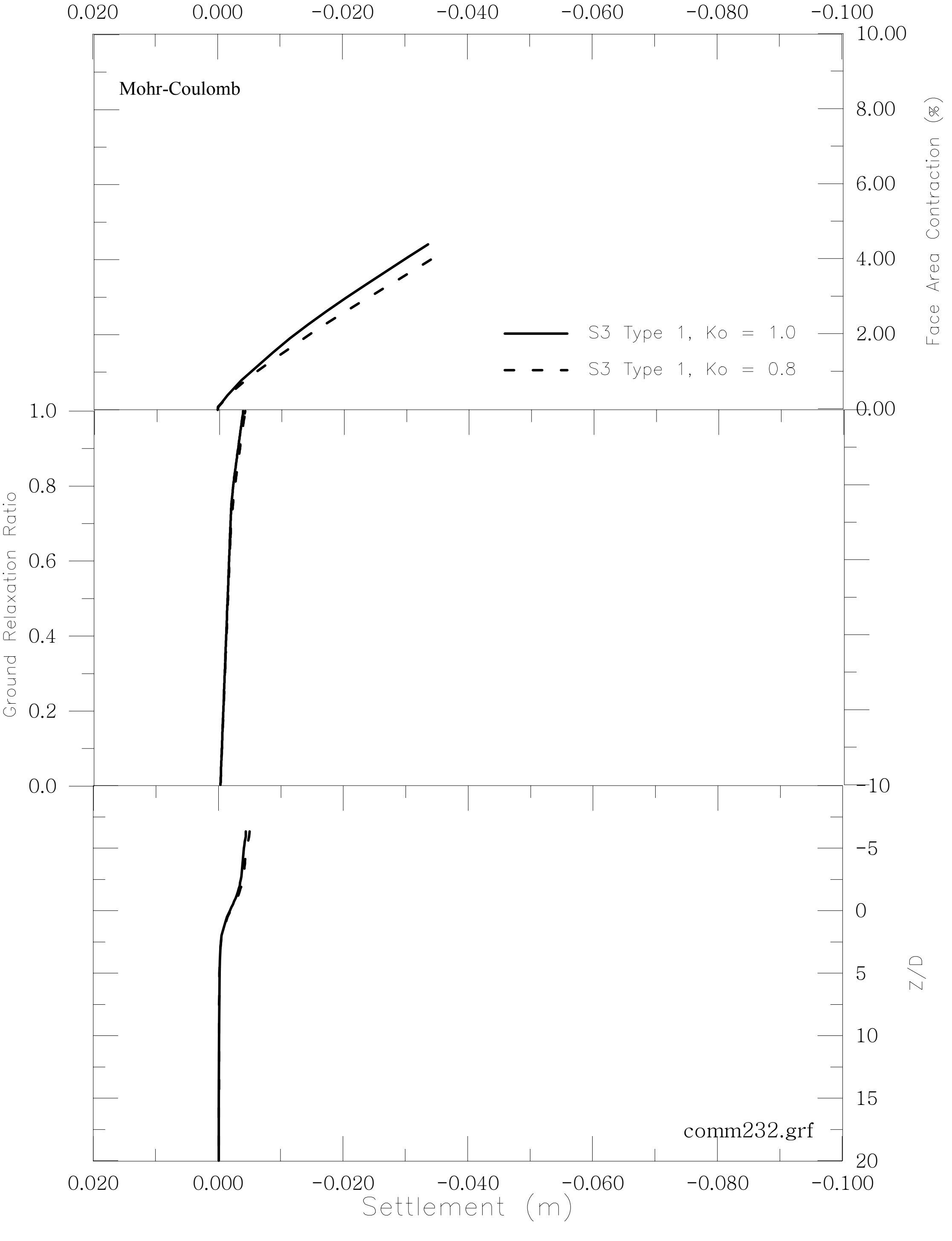

Figure 5.36 Case III 3D & 2D ground response

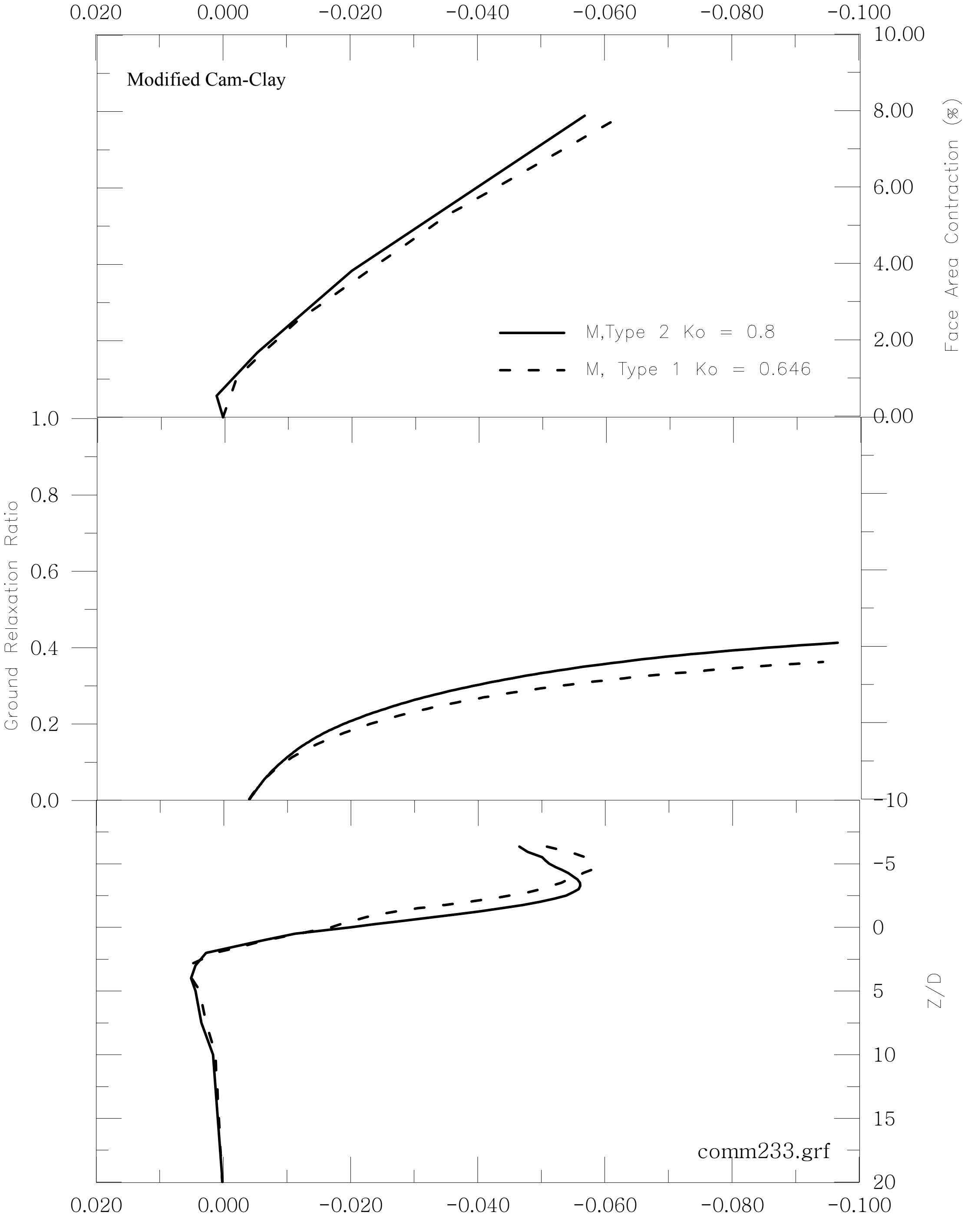

Figure 5.37 Case IV 3D & 2D ground response

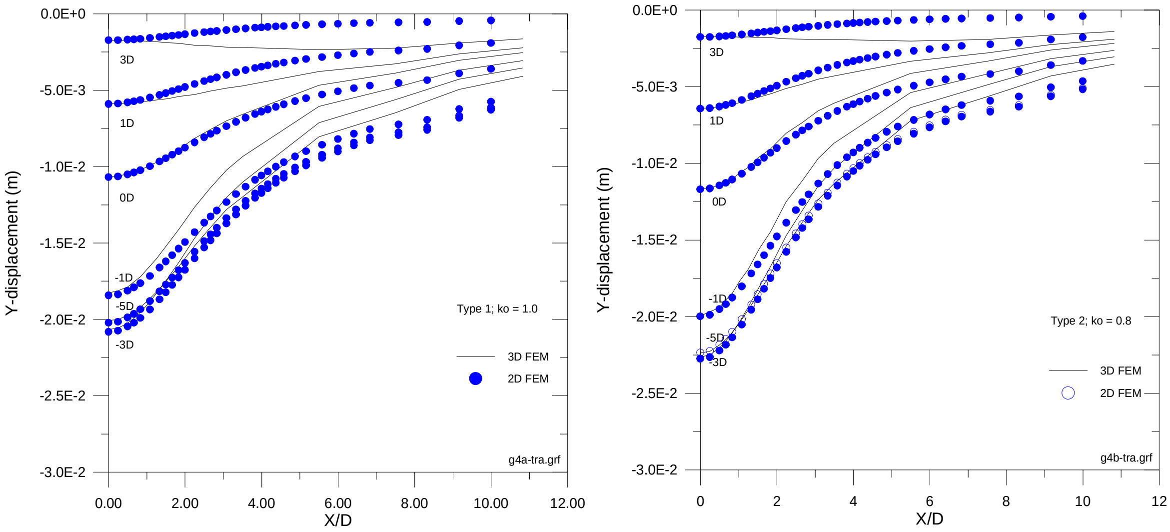

Figure 5.38 (a) $K_0 = 1.0$

Figure 5.38 (b) $K_0 = 0.8$

Figure 5.38 Case I Trough width Response for various K_0

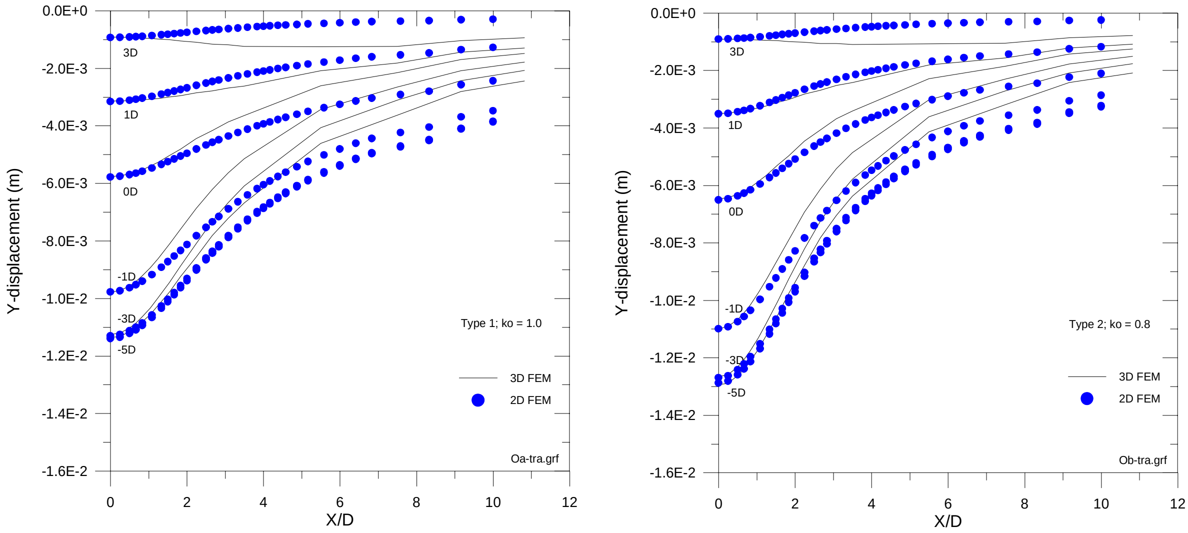

Figure 5.39 (a) $K_0 = 1.0$

Figure 5.39 (b) $K_0 = 0.8$

Figure 5.39 Case II Trough width Response for various K_0

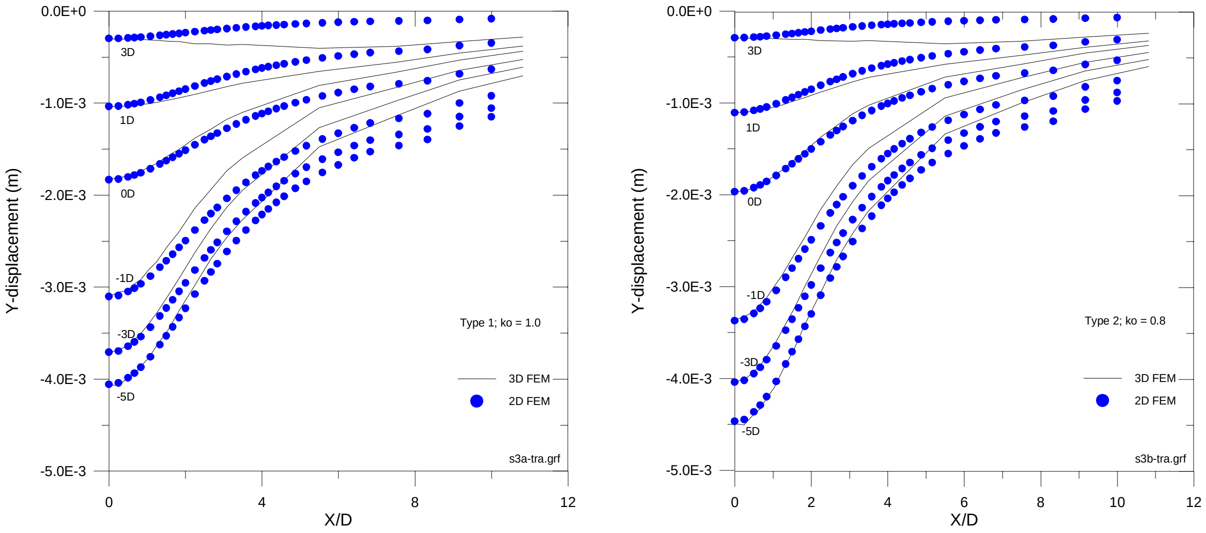

Figure 5.40(a) K$_0$ = 1.0 Figure 5.40(b) K$_0$ = 0.8

Figure 5.40 Case III Trough width Response for various K$_0$

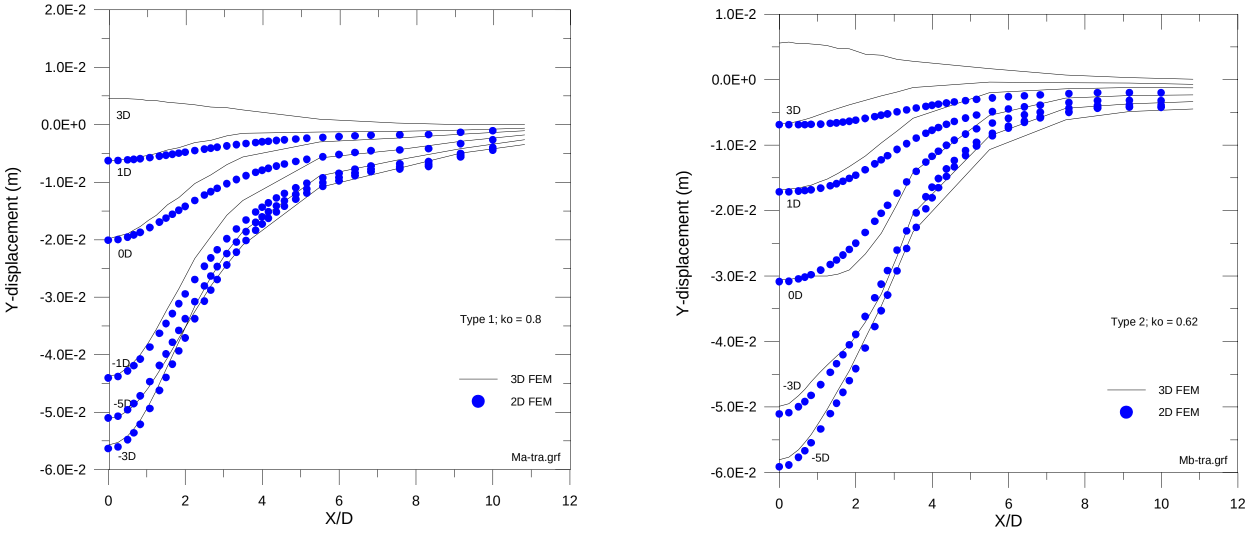

Figure 5.41(a) K$_0$ = 0.8 Figure 5.41(b) K$_0$ = 0.62

Figure 5.41 Case IV Trough width Response for various K$_0$

6 Conclusions & Recommendations

6.1 Conclusions

This study examines the viability of applying three-dimensional finite element analyses to the prediction of ground movement arising from earth pressure balance tunnelling. It seeks to address two of the issues involved in three-dimensional finite element analysis, namely

1. the feasibility of conducting three-dimensional analysis without resorting to inordinate amounts of computer resources and time, and
2. the usefulness of three-dimensional analysis in predicting field movements and its advantages compared to two-dimensional analysis.

To address the first issue, two types of time- and memory-efficient iterative Krylov-subspace solution algorithms were developed on PC platform and their performances for various geotechnical applications were studied. These are the pre-conditioned conjugate gradient (PCG) and the quasi-minimal residual (QMR) methods. The performances of these two algorithms on various types of geotechnical problems were examined using idealised boundary value problems. This performance assessment exercise led to the following findings:

1. The trend and rate of convergence of these algorithms are dependent not only on the condition number but also on the type of analysis, although there is a general trend of decreasing rate of convergence as condition number increases for a given type of analysis. The convergence behaviour of drained problems with "material ill-conditioning" arising from large stiffness ratios between the different material

zones is readily improved by Jacobi preconditioning. This can be explained by the fact that the stiff and soft material zones occupy different spatial sub-domain and are thereby linked to different degrees-of-freedom. By normalising the stiffness coefficients for the degrees-of-freedom by their respective diagonal entries, Jacobi preconditioning, in effect, homogenises the various sub-domains.

2. For undrained problems modelled using a nearly incompressible pore fluid, Jacobi preconditioning appears to be much less effective. The number of iterations needed is far higher than the drained problems, even though the condition number, after preconditioning, may be similar. This is because the material ill-conditioning of an undrained problem arises from the large stiffness ratios between compression/dilatation and shear flow eigenmodes. Jacobi preconditioning changes the eigenvalues for these modes by approximately the same ratio, thus causing little or no compression to the eigenvalue distribution.

3. For consolidation problems, some eigenvalues are displacement-dominated whereas others are excess-pore-pressure-dominated. The Jacobi preconditioner compresses the displacement-dominated eigenvalues in a similar manner to the drained cases. However, the pore pressure eigenvalues appear to be over-scaled. However, if the over-scaling can be compensated for, then significant improvement in the rate of convergence can be achieved.

4. A series of large three-dimensional finite element problems were also analysed by incorporating the developed algorithms into the CRISP code, on a modest PC platform. Because of its high memory-efficiency, the developed Krylov-subspace algorithms were able to address much larger problems than the frontal solver which exists on CRISP. In addition, in a majority of cases, there is also a significant speed-up in the turnaround time of each analysis.

5. To address the second issue, the CRISP code, with the Krylov subspace solvers incorporated, were used to back-analyse an actual three-dimensional tunnel heading problem, namely the tunnelling operation of Contract 704 of the Northeast Mass Rapid Transit Line. This back-analysis exercise leads to the following findings:

6. Parametric studies on the operational parameters indicate that the parameters which have a significant influence on the results are the excavation step length, pore pressure boundary conditions and face pressure. On the other hand, parameters such as the grout stiffness and the tunnel boring machine weight were found not to have a significant influence on the results. These findings allow emphasis to be placed on those significant parameters, thus enabling reasonably realistic simulation to be conducted without undue investment in computer resources.

7. Different soil models were also investigated in the back-analysis. The results show that using the modified Cam Clay without small strain non-linearity and parameters

from conventional triaxial and consolidation tests significantly over-estimates of the ground settlement. This is attributable to the fact that, with Earth Pressure Balance (EPB) control of the face, strain levels in the soil around the tunnel are kept relatively low. The conventionally obtained parameters are obtained under much larger strain conditions; thus they do not reflect the characteristics of the soil around the tunnel under field conditions. By incorporating a hyperbolic description of the soil behaviour below the yield surface, much better agreement can be obtained. This implies that, in earth pressure balance tunnelling of firm to stiff soil, the parameters used should reflect the behaviour of the soil within the correct range of strains.

8. A comparative study was also conducted between three-dimensional and two-dimensional analyses, the latter using the Crisp code as well as the commercially available Plaxis software. The results show that the increase in maximum settlement of a monitored section caused by the approach of a tunnel heading can be replicated in a two-dimensional analysis, either by controlling the rate of relaxation of the equilibrating earth pressure or by controlling the contraction of the tunnel periphery. This points a way forward to the use of two-dimensional analysis to capture some of the three-dimensional characteristics of tunnelling. However, there are some discrepancies between the profiles of the settlement trough computed by the two- and three-dimensional analyses, especially when the tunnel heading is still far away from the monitored section. For stiff soils, before the arrival of the tunnel heading, the two-dimensionally computed settlement trough is often narrower than three-dimensionally computed trough. The reverse occurs after the tunnel heading has passed the monitored section. In particular, much

smaller far-field settlement is predicted by the three-dimensional analysis than the two-dimensional analysis; this being explainable by the stress-transfer effect of the soil in front of the tunnel heading. This is an often-encountered problem with two-dimensional analysis and the study shows that it is at least partially due to the three-dimensional effect of the tunnel heading. For soft soils, the three-dimensionally computed trough is generally narrower than the two-dimensionally computed trough as the tunnel face approaches and passes through the section. However, when the tunnel is near the monitored section (either ahead or behind), the three-dimensionally computed trough may be narrower or wider than the two-dimensionally computed trough, depending upon the in-situ K_0 value. This is due to the effect of face pressure, which is simulated in the three-dimensional analyses but not in the two-dimensional analyses.

6.2 Recommendations for Future Research

Further research may be conducted on the following aspects:

1. Extend the *element-by-element PCG* and *QMR* towards a multi-processor system or a set of several computers each consisting of a CPU, a memory and and I/O system. The current Jacobi preconditioner has a high degree of parallelism and is extremely favourable to the implementations on parallel architectures (Saad, 1996).

2. The test problem (Fig.3.6) model size sensitivity could have been studied so that there could be some indication to the aspect ratios to be adopted for more complex problems.

3. One common discrepancy between simulated and observed settlement trough is the sharpness of the trough. In most cases, the observed settlement trough is distinctly sharper than the computed trough. Although this has been variously attributed to anisotropy e.g. Lee & Rowe (1989) and small strain non-linearity [e.g. Jardine et al. (1986), Gunn (1992), Dasari (1996), Stallebrass and Taylor (1997)]. Few, if any of the studies, including the present have been able to reproduce the sharpness of the empirically-fitted normal distribution curve. This study indicates that three-dimensional effects may at least partially account for the difference. More work is still needed to fully resolve this issue.

4. Much of the emphasis in this study has been placed on ground movement. In practice, there are two aspects of tunnelling which often need attention in design, namely ground movement and lining stresses. The latter aspect has not been studied so far.

5. Many aspects of the current study are still highly idealized. For instance, the grout is assumed to harden instantaneously. In reality, the grout will gain strength and stiffness over a period of time. The implications of the time-dependent grout strength and stiffness on the results should be investigated. Similarly, the effects of imperfect grouting, e.g. caused by voids left in the grout should also be. Thirdly, in the present study, the segmental lining is assigned an equivalent stiffness, based on some rule-of-thumb. The validity of this should also be examined.

6. Finite element studies, perhaps using more sophisticated multi-surface soil models with kinematic hardening, may be conducted to elucidate other aspects of soil structure interaction such as pile-tunnel and tunnel-tunnel interaction. This can potentially lead to a whole range of studies on tunnel-structure configurations in various soil types and formations.

7 Appendix A

A.1. **Claim**: Let $A = [a_{ij}]$ be an *n-by-n* matrix (may be complex-valued).

If $|a_{nn}| \to \infty$, then (i) $\lambda_n \to a_{nn}$ and (ii) $v_n \to \{0, 0, 0, ..., c\}$

Define

$$r_i = \sum_{\substack{j=1 \\ j \neq i}}^{n} \left| a_{ij} \right| \tag{A1}$$

The *i*th disk is defined on the complex plane as:

$$D_i = \{z \in \mathbf{C} \text{ such that } |z - a_{ii}| \leq r_i\} \tag{A2}$$

The Gerschgorin Circle Theorem (Gerschgorin, 1931) states that all eigenvalues are contained in the union of D_1, D_2, …. D_n. In particular, if one disk is disjoint from all others, that disk contains exactly one eigenvalue.

The *n*th disk can be made disjoint from all other disks by ensuring that a_{nn} is much larger than all other a_{ii}. Hence,

$$\left| \lambda_n - a_{nn} \right| \leq r_n \text{ or} \tag{A3}$$

$$\left| \frac{\lambda_n}{a_{nn}} - 1 \right| \leq \frac{r_n}{\left| a_{nn} \right|} = \varepsilon \tag{A4}$$

When $|a_{nn}| \to \infty$, $\varepsilon \to 0$ and $\lambda_n \to a_{nn}$. Hence (i) follows.

For $k \neq n$,

$$\sum_{j=1}^{n} |a_{kj}||v_j| \geq \left|\sum_{j=1}^{n} a_{kj} v_j\right| = |\lambda_n||v_k| \text{ or} \tag{A5}$$

$$\sum_{j=1}^{n} \frac{|a_{kj}|}{|a_{nn}|}|v_j| \geq |v_k| \tag{A6}$$

When $|a_{nn}| \to \infty$, $|a_{kj}|/|a_{nn}| \to 0$ and $|v_k|$ for $k \neq n \to 0$. Hence (ii) follows.

A.2. Claim: Let $A = [a_{ij}]$ be an n-by-n matrix (may be complex-valued) and $A^{*}_{PCG} = E^{-1}AE^{-T}$ where $EE^{T} = M_1$ and $m_{1ij} = 0$ for $i \neq j$, $m_{1ii} = 1$ for $i = 1$ to p, $m_{1ii} = a_{ii}$ for $i = p + 1$ to n.

If $|a_{ii}| \to \infty$ for $i = p + 1$ to n, then

$\lambda \to 1$ with multiplicity $q = n - p$ and

$v \to \{0, 0, 0, \ldots c, \ldots, 0\}$ with a single non-zero entry located at $i = p + 1$ to n for each q eigenvector, respectively.

If $|a_{ii}| \to \infty$ for $i = p + 1$ to n, then

$$A^{*}_{PCG} \to \begin{bmatrix} B & 0_1 \\ 0_2 & I \end{bmatrix} \tag{A7}$$

where B = p-by-p matrix, 0_1 = p-by-q null matrix, 0_2 = q-by-p null matrix and I = q-by-q identity matrix.

$$\begin{bmatrix} B & 0_1 \\ 0_2 & I \end{bmatrix} \begin{Bmatrix} v_1 \\ v_2 \end{Bmatrix} = \lambda \begin{Bmatrix} v_1 \\ v_2 \end{Bmatrix} \qquad \text{(A8)}$$

Clearly, the eigenvalues of I are also eigenvalues of A^*_{PCG}. This is easily seen by setting v_2 = eigenvector of I and v_1 = null vector. Hence the result stated above follows.

Further, note that the eigenvalues of B are also eigenvalues of A^*_{PCG}.

A.3. **Claim**: Let $A = [a_{ij}]$ be an *n-by- n* matrix (may be complex-valued). If $|a_{ii}| \rightarrow \infty$ for $i = p + 1$ to n, then

p of the eigenvalues are equal to the eigenvalues of B (*p-by-p* top diagonal block)

These eigenvalues remain the same after partial pre-conditioning ($E^{-1}AE^{-T}$).

Write

$$A = \begin{bmatrix} B & C \\ D & E \end{bmatrix} \quad \text{(A9)}$$

where B = *p-by-p* matrix, C = *p-by-q* matrix, D = *q-by-p* matrix and E = *q-by-q* matrix.

Define

$S = [s_{ij}]$, where $s_{ij} = 0$ for $i \neq j$, $s_{ii} = 1$ for $i = 1$ to p, $s_{ii} = a_{ii}$ for $i = p + 1$ to n

$F = SAS^{-1}$ will have the same eigenvalues as A since they are similar.

If $|a_{ii}| \rightarrow \infty$ for $i = p + 1$ to n, then

$$F \rightarrow \begin{bmatrix} B & 0_1 \\ D' & E' \end{bmatrix} \tag{A10}$$

where $0_1 = p\text{-}by\text{-}q$ null matrix.

$$\begin{bmatrix} B & 0_1 \\ D' & E' \end{bmatrix} \begin{Bmatrix} v_1 \\ v_2 \end{Bmatrix} = \lambda \begin{Bmatrix} v_1 \\ v_2 \end{Bmatrix} \tag{A11}$$

Clearly, the eigenvalues of B are also eigenvalues of A. This is easily seen by setting v_1 = eigenvector of B and v_2 = null vector.

Hence (i) follows and (ii) follows because eigenvalues of B are also eigenvalues of A^*_{PCG} as noted above.

8 References

Ajiz MA, Jennings A (1984). A robust incomplete Choleski conjugate gradient algorithm. International Journal for Numerical Methods in Engineering, 20, pp. 949-966.

Atzl GV and Mayr JK (1994). FEM analysis of Heathrow NATM trial tunnel. Proceedings of the International Conference on Numerical Methods in Engineering, Manchester, UK, pp. 195-201.

Anderson E, Bai Z, Bischof C, Demmel J, Dongarra J, Du Croz J, Greenbaum A, Hammarling S, McKenney A, Ostrouchov S, Sorensen D (1995). *LAPACK User's Guide*, 2nd edn. SIAM Press: Philadelphia.

Arioli M, Duff I, Ruiz D (2000). A stopping criterion for the conjugate gradient algorithm in a finite element method framework. Technical Report, Istituto di analisi Numerica, #1179.

Atkinson JH and Potts DM (1977) Subsidence above shallow tunnels in soft ground. Journal of Geotechnical Engineering Division, ASCE, Vol. 103, No. GT4, April, pp. 307-325.

Attewell PB and Farmer IW (1974). Ground deformations resulting from shield tunnelling in London clay, Can. Geotech. J., Vol 11, pp. 380-395.

Attewell PB (1977). Large ground movement and structural damage caused by tunnelling below the water table in a silty alluvial clay. Proceedings of the first Conference: "Large ground movements and structures", pp. 307-355.

Attewell PB and Woodman JP (1982). Predicting the dynamics of ground settlement and it's derivatives caused by tunnelling in soil. Ground Engineering, 15, pp. 13-22.

Atzl AZ and Mayr JK (1994). FEM-Analysis of Heathrow NATM Trial tunnel. Numerical Methods in Geotechnical Engineering, pp. 195-201. Smith (ed), Balkema, Rotterdam.

Axelsson, O. (1972), “A generalized SSOR method”, BIT 12, pp. 443-467

Becker DE (1981). Settlement analysis of intermittently-loaded structures founded on clay subsoils. Ph.D. Thesis, University of Western Ontario.

Barrett R, Berry M, Chan T, Demmel J, Donato J, Dongarra J, Eijkhout V, Pozo R, Romine C and H. van der Vorst. Templates for the Solution of Linear Systems: Building Blocks for Iterative Methods. Philadelphia: SIAM Press. 1994.

Barla G. and Ottoviani M (1974). Stresses and displacement around two adjacent circular openings near to ground surface. Proc. Third Int. Congr. On Rock Mechanics, Vol. II, Denver.

Bathe KJ (1996). Finite Element Procedures. Prentice-Hall: Englewood Cliffs.

Beer G, Watson JO, Swoboda G (1987). Three- Dimensional analysis of tunnels using infinite boundary elements. Computers and Geotechnics, 3, pp. 37-58.

Biot MA (1941). General theory of three-dimensional consolidation. Journal of Applied Physics; 12, pp. 155-164.

Boscardin MD and Cording EJ (1989). Building response to excavation induced settlement, ASCE Journal of Geotechnical Engineering, Vol 115, pp. 1-21.

Brendan Reilly (1999). Introduction to Tunnel Design & Construction. Short Course organised by Tunnelling and Underground Construction Society (Singapore) and Land Authority of Singapore (LTA), March.

Britto AM, Gunn MJ (1987) Critical State Soil Mechanics via Finite Elements. Ellis Horwood Ltd.: Chichester, West Sussex , 1987.

Britto AM and Gunn MJ (1990). Crisp90 User's and Programmer's Guide. Cambridge University Engineering Department, Soil Mechanics Group.

Broms BB and Bennermark H (1967). Stability of clay in vertical openings. J. Soil Mech. Fdns. Div. ASCE, Vol.93, No. SM1, pp. 71-94.

BS 1377 (1999). Methods for testing soil for civil engineering purposes. British Standard Institution.

Bulgakov VE, Kuhn G (1995). High-performance multi-level iterative aggregation solver for large finite-element structural analysis problems. International Journal for Numerical Methods in Engineering; 38, pp. 3529-3544.

Burd HJ, Houlsby GT, Augarde CE and Liu G (2000). Modelling tunnelling-induced settlement of masonry buildings. Proc. Instn Civ Engrs, Geotech. Engng, 2000, 143, Jan., pp. 17-29.

Burns & Richard (1964). Attenuation of Stresses for Buried Cylinders. Proceedings, Symposium on soil-structure interaction, Tucson, pp. 378-392.

Paige CC and Saunders MA (1975). Solution of Sparse indefinite systems of linear equations. SIAM, J. Numer. Anal., 12, pp. 617-629.

Chan SH, Phoon KK, Lee FH (2001). A modified Jacobi preconditioner for solving ill-conditioned Biot's consolidation equations using symmetric quasi-minimal residual method. International Journal for Numerical and Analytical Methods in Geomechanics 2001; 25, pp. 1001-1025.

Chan SH (2002). Iterative solution for large indefinite linear systems from Biot's finite element formulation. Ph.D. Thesis, National University of Singapore.

CIRIA (1996). Prediction and effects of ground movements caused by tunnelling in soft ground beneath urban areas. Project Report 30. Construction Industry Research and Information Association. Mott et al. (eds). pp. 130.

Clough GW and Leca E (1989). With focus on use of finite element methods for soft ground tunnelling. Review paper in tunnels et Micro-Tunnels en Terrain Meuble-du Chantier a la Theorie, Presse de Ecole Nationale des Ponts et chausses, Paris, pp. 531-573.

Clough GW and Schmidt B (1977). Design and performance of excavations and tunnels in soft clay. State of the Art report, International Symposium on Soft Clay, Bangkok, Thailand. pp. 980-1032.

Clough GW and Schmidt B (1981). Design and Performance of excavations and tunnels in soft clays. Soft Clay Engineering, Elsevier, Amsterdam, pp. 269-276.

Concus P, Golub GH, O'Leary DP (1976). A generalised conjugate gradient method for the numerical solution of the elliptic partial differential equations. Sparse Matrix Computations, Bunch JR, Rose DJ (eds). Academic Press: New York, pp. 309-332.

Cording, EJ and Hansmire WH (1975) Displacements around soft ground tunnels. General report: Session IV, Tunnels in Soil, 5th Panamerican Congress on Soil Mechanics and Foundation Engineering, Buenos Aires, November.

Coutts DR and Wang J (2000). Monitoring of reinforced concrete piles under horizontal and vertical loads due to tunnelling. Tunnels and Underground structures. Zhao et al (eds), Balkema, pp. 541- 546.

Dasari GR (1996). Modelling the variation of soil stiffness during sequential construction. Ph.D. Thesis. University of Cambridge.

Dames and Moore (1983) Detailed Geotechnical Study, Factual report issued to provisional MRT authority, Singapore.

Davies, EH, Gunn, MJ, Mair, RJ, Seneviratne, HN (1980) The stability of shallow tunnels and underground openings in cohesive material. Geotechnique 30, No.4, pp 397-416.

Dayde MJ, L'Excellent JY, Gould NIM (1997). Element-by-element preconditioners for large partially separable optimisation problems. SIAM Journal of Scientific Computing; 18 (6), pp. 1767-1787.

Gibson RE (1974). The analytical method in soil mechanics. Geotechnique, Vol. 24 (2), pp. 115-140.

Fioravante V (2000). Anisotropy of small strain stiffness of Ticino and Kenya sands from seismic wave propagation measured in triaxial testing. Soils and Foundation, Vol. 40, No. 4, pp. 129-142.

Fitzpatrick L (1980). Lining leakage and consolidation around soft-ground tunnels. Masters' thesis, Cornell University.

Fotieva NN and Sheinin VI (1966). Distribution of stresses in the lining of a circular tunnel when driving a parallel tunnel. Soil Mech. Found. Engng, Vol. 6.

Fox RL, Stanton EL (1968). Developments in structural analysis by direct energy minimization. American Institute for Aeronautics and Astronautics Journal, 6, pp. 1036-1042.

Freund RW and Natchigal NM (1991). A Quasi minimal residual method method for non-hermitian linear systems. Numerical Mathematics, 60, pp. 315-339.

Freund RW and Natchigal NM (1994). An implementation of the QMR method based on coupled two term recurrences. SIAM, Journal of Scientific computing, 15, pp. 313-337

Freund RW, Nachtigal NM (1994). A new Krylov-subspace method for symmetric indefinite linear system. Proceedings of the 14th IMACS World Congress on

Computational and Applied Mathematics, Atlanta, USA, Ames WF (ed), 11-15 July 1994, pp. 1253-1256.

Fried I (1969) More on gradient iterative methods in finite element analysis, AIAA J., Vol 7, pp 565-567.

Golub G and Van Loan C (1989). Matrix Computations, 2nd Edition, The John Hopkins University Press, Baltimore.

George A and Liu JW (1981) Computer Solution of Large Sparse Positive Definite Systems. Prentice-Hall: Englewood Cliffs.

Gerschgorin SA (1931). Uber die Abgrenzung der Eigenwerte einer Matrix. Izv. Akad. Nauk SSSR, Ser. Fiz.-Mat., 6, pp. 749-754.

Ghaboussi J and Ranken RE (1977). Interaction between two parallel tunnels, Int. Journal. for Numerical and Analytical Methods in Geomechanics, Vol I, pp. 75-103.

Ghaboussi J. and Hansmire WH (1983). Finite element simulation of tunnelling over subways. Journal of Geotechnical Engineering, ASCE, Vol. 109, March, pp. 318-333.

Graham J and Houslby GT (1983). Elastic Anisotropy of a natural clay. Geotechnique 33 (2), pp. 165-180.

Gritffiths DV and Smith IM (1991). Numerical Methods for Engineers, Blackwell, Oxford.

Gunn MJ (1993). The prediction of surface settlement profiles due to tunnelling. Predictive Soil Mechanics, Thomas Telford, London, pp. 305 – 316.

Hellings JE (1994). Limiting the damage to historic buildings due to tunnelling: Experience at the Mansion House, London. Tunnelling'94, Institute of Mining and Metallurgy and the British Tunnelling society, Chapman and Hall, pp. 253-278.

Hergarden HJAM, Van der Poel JT, Van der Schrier JS (1996). Ground movements due to tunnelling: Influence on pile foundations. Geotechnical aspect of underground construction in soft ground, Mair RJ & Taylor RN (eds), pp. 519-524.

Hestenes MR and Stiefel E (1952). Methods of conjugate gradient for solving linear systems. Journal of Research of the National Bureau of Standards, pp. 409-436.

Hibbitt, Karlsson & Sorensen, INC, (1997), Abaqus/Standard User's Manual, Volume I, Chapter 8.

Hurell RE (1985). The empirical prediction of long-term surface settlements above shield-driven tunnels in soil. Proc. 3rd Int. Conf. Ground Movements and Structures, Cardiff, 1984. Published as Ground Movements and Ground Structures. Edited by Geddes JD. Pentech Press, Plymouth, pp.161 – 172.

Holtz RD and Kovacs WD (1981) An Introduction to Geotechnical Engineering, Prentice Hall Civil Engineering Mechanics Series, pp. 77.

Hong SH (2002). Behaviour of soldier pile and timber lagging support system. Ph.D. Thesis, National University of Singapore.

Howden (1996). Technical Catalogue: Wirth Howden tunnelling. Operating Division of James Howden & company Limited. Old Govan Road, Renfrew PA4 8XJ.

Irons BM (1970). A frontal solution program for finite element analysis. International Journal for Numerical Methods in Engineering, 12, pp. 5-32.

Jamiolkowski M, Lancellotta R and LoPresti D (eds) (1999). "Pre-failure Deformation Characteristics of Geomaterials (Torino), Balkema, Rotterdam, 1419 pp.

Jardine RJ, Potts DM, Fourie AB and Burland JB (1986). Studies of the influence of non-linear stress-strain characteristics in soil-structure interaction. Geotechnique, Vol XXXVI, No. 3, pp. 377-396.

Johnson C (1987) Numerical solution of partial differential equations by the Finite Element Method. Cambridge University Press: Cambridge.

Johnson OG, Michelli CA and Paul G (1983), Polynomial Preconditioners for conjugate gradient calculations. SIAM Journal Numerical Analysis, Vol 20, pp. 363-376.

Komiya K, Soga K, Akagi H, Hagiwara T, Boltom M (1999). Finite element modelling of excavation and advancement processes of a shield tunnelling machine. Soils and Foundations, Vol 39, No. 3, pp 37-52, June 1999 Japanese Geotechnical Society.

Kreyszig E (1993). Advanced Engineering Mathematics, 7th Ed., John Wiley & Sons.

Lee KM and Rowe RK (1989a). Deformations caused by surface loading and tunnelling: the role of elastic anisotropy. Geotechnique, Vol 39 , pp. 125-140.

Lee KM and Rowe RK (1989b). Effects of undrained strength anisotropy on surface subsidences induced by the construction of shallow tunnels. Canadian Geotechnical Journal, 26, pp. 279-291.

Lee KM and Rowe RK (1990). Finite element modelling of the 3D ground deformations due to tunnelling in soft cohesive soils- Part I/II”, Computers and Geotechnics, 10, pp 87-109, 111-138.

Lee KM and Rowe RK (1991a). An analysis of three-dimensional ground movements: the Thunder Bay tunnel. Canadian Geotechnical Journal, Vol 28, pp. 25-41.

Lee KM and Rowe KR (1991b). An evaluation of simplified techniques for estimating three-dimensional undrained ground movements due to tunnelling in soft soils. Canadian Geoteochnical Journal, Vol 29, 1992, pp 39-52

Lee KM and Rowe KR (1992a) Subsidence owing to tunnelling Part I: Estimating the Gap parameter. Canadian Geoteochnical Journal, Vol 29, 1992, pp 929-940.

Lee KM and Rowe RK (1992b). Subsidence owing to tunnelling II- evaluation of prediction technique. Vol. 29, pp 941-953.

Leong EC, Rahardjo H, Tang SK (2003) Characterisation and engineering properties of Singapore residual soils. Characterisation and Engineering Properties of Natural Soils, Tan et al. (eds.), Balkema, ISBN 90 5809 537 1, Vol. 2, 2003, pp. 1279 – 1304.

Lim KC, Lee FH and Phoon KK (1998). Three dimensional analysis of twin tunnels. Proceedings of the Eighth KKNN Seminar on Civil Engineering, National University of Singapore, Kent Ridge, Singapore. Swaddiwudhipong S, Wang CM, Leung CF (eds), 30th November and 1st December 1998; pp. 452-457.

Lin CC, Chen JC and Chi SY (2001). Optimized back-analysis for ground movement using equivalent ground loss model. Tunnelling and Underground Space Technology. Vol. 16 (3), pp. 159-165.

Loganathan N. and Poulos HG (1998). Analytical Prediction for Tunnelling-induced ground movements in clays. Journal of Geotechnical and geoenvironmental engineering, September 1998, pp. 846-856.

Maidl B, Herrenknecht M., Anheuser L. (1996), Mechanised Shield Tunnelling. ISBN 3-433-01292-X, pp. 197-319.

Mair RJ (1979). Centrifugal Modelling of tunnel construction in soft clay. PhD thesis, Cambridge University.

Mair RJ (1992). Theme Lecture: Bored tunnelling in the urban environment, Proceedings of the Fourteenth International conference on Soil Mechanics and Foundation Engineering, Mair RJ and RN Taylor (eds), Vol. 4, pp 2353-2385.

Mair RJ, Taylor RN, Bracegirdle A (1993). Subsurface Settlement profiles above tunnels in clays, Geotechniques, vol.43, No.2, pp 315-320.

Mair RJ (1996). General report on settlement effects of bored tunnels. Geotechnical Aspects of Underground Construction in Soft Ground (eds Mair RJ and Talyor RN), Blakema, Rotterdam, pp. 43-53.

Mair RJ and Taylor RN (eds) (1996). Geotechnical Apsects of Underground Construction in Soft Ground, Balkema, Rotterdam.

MATLAB, Version 5.3.0.10183 (R11), 1999.

Meurant G (1999) Computer solution of large linear system. In Studies in Mathematics and Its Applications, Vol. 28, Lions JL, Papanicolaou G, Fujita H, Keller HB (eds). Elsevier: Amsterdam.

Mitchell JA, Reddy JN (1998) A multilevel hierarchical preconditioner for thin elastic solids. International Journal for Numerical Methods in Engineering, 43, 1383-1400.

Muir Wood AM (1975). The circular tunnel in elastic ground. Geotechnique, 25, pp. 115-127.

Nachtigal N, Reddy S and Trerethen L (1992). How fast are non-symmetric matric iterations? SIAM, J. Matrix Anal. Appl., 13, pp. 778-795.

Nasim ASM (1999). Corner constraints in strutted excavation. MEng. Thesis, Department of Civil Engineering, CSGE, National University of Singapore.

Nelson PP (1985). Tunnel boring machine performance in sedimentary rock. Ph.D. Thesis, Cornell University.

Nour-Omid B, Parlett BN (1985) Element preconditioning using splitting techniques. SIAM Journal of Scientific and Statistical Computing,6 (3), pp. 761-770.

O'Reilly MP and New BM (1982). Settlements above tunnels in the United Kingdom- Their Magnitude and prediction. Tunnelling'82. The Institution of Mining and Metallurgy, pp. 173-181.

O'Reilly MP and New BM (1991). Tunnelling induced ground movements; predicting their magnitude and effects. Ground movements and structures, Proceedings of the 4th International Conference, pp 671-697.

Oteo CS and Sagaseta C (1982). Prediction of settlements due to underground openings. Int. Symp. On Numerical models in Geomechanics, Zurich. pp. 653-699.

PWD (1976). Geology of the Republic of Singapore, Public Works Department, Singapore 1976

Paige CC and Saunders MA (1975) Solution of sparse indefinite systems of linear equations, SIAM Journal of Numerical Analysis 1975; 12, pp. 617-629.

Palmer JHL and DJ Belshaw (1980). Deformations and pore pressures in the vicinity of a precast, segmented, concrete-lined tunnel in clay. Can. Geo. Jnl., Vol. 17, pp. 174-184.

Papadrakakis M (1993). Solving large-scale linear problems in solid and structural mechanics. Solving Large-scale Problems in Mechanics – The Development and Application of Computational Solution Methods, Papadrakakis M (ed). John Wiley: Chichester, 1-32.

Payer HJ and Mang HA (1997). Iterative strategies for solving systems of linear, algebraic equations arising in 3D BE-FE analyses of tunnel drivings. Numerical Linear Algebra with Applications. 4 (3), pp. 239-268.

Peck RB (1969). State of the Art Report: Deep excavations and tunnelling in soft ground. Proc. 7th Int. Conf. Soil Mech., Mexico, pp. 225-290.

Plaxis (1998). Finite element code for soft and rock analysis. Version 7.

Poh KB, Chua NL and Tan SB (1985). Residual granite soil of Singapore. Proceedings of 8th Southeast Asian Geotechnical Conference, Kuala Lumpur: pp. 3-1 – 3-9.

Potts DM and TI Addenbrooke (1997). A structures's influence on tunnelling-induced ground movements. Proc. Instn Civ. Engrs, Geotech. Engr., Issue 125, Apr., pp 109-125.

Ranken RE and Ghaboussi J (1975). Tunnel Design Consideration: Analysis of Stress and Deformations around Advancing Tunnels. U.S. Department of Transportation, Report FRA-OR&D 75-84, August 1975.

Rankin WJ (1988). Ground movements resulting from urban tunnelling. Proc. Conf. Engng Geol. Underground Movements, Nottingham, pp. 79-92. London Geological Society.

Roscoe KH and Burland JB (1968). On the generalized stress-strain behaviour of an idealised wet clay. Engineering Plasticity. Cambridge University Press.

Saad Y (1985). Practical use of polynomial preconditionings for the conjugate gradient method. SIAM Journal for Scientific and Statistical Computing; 6 (4):865-881.

Saad Y (1996). Iterative method for sparse linear systems. PWS Publishing Company: Boston.

Saad Y and Schultz M (1986). GMRES: A Generalized Minimum Residual Algorithm for solving nonsymmetric linear systems", SIAM, Journal of Scientific and Statistical Computing, 7, 1986, pp. 856-869.

Saad Y and van der Vorst HA (2000). Iterative solution of linear systems in the 20-th century. Journal of Computational and Applied Mathematics ; **123**:1-33.

Sagaseta C (1987). Analysis of undrained soil deformation due to ground loss, Geotechnique, 37, No.3 , pp. 301-320.

Sage Crisp (1997) Finite element analysis program, Version 4.

Schmidt B (1969). Settlements and ground Movements associated with tunnelling in soil. PhD thesis, University of Illinois.

Schmidt B (1982). International conference on Mass Rapid Transit, MRT'82. pp. 3-16.

Sharma JS, Zhao J, Hefny AM (2000) Effect of shotcrete setting time and excavation sequence on surface settlements. Tunnels and Underground Structures. Zhao et al. (eds), pp.535 – 540.

Shahrour I, Mroueh H (1997). Nonlinear three-dimensional analysis of closely spaced twin tunnels. Numerical Models in Geomachanics, pp. 481-487.

Shewchuk JR An introduction to the conjugate gradient method without the agonizing pain. Release version 1.25, August 4, 1994. School of Computer Science, Carnegie Mellon University. FTP: warp.cs.cmu.edu. (IP Adddress: 128.2.209.103), filename <quake-papers/painless-conjugate-gradients.ps>.

Shibuya S, Mitachi T and Miura S, (eds) (1995). Pre-failure deformation of Geomaterials (Sapporo), Balkema, Rotterdam, 1268 pp.

Shirlaw JN (1994). Subsidence owing to tunnelling. Part II. Evalaution of a prediction technique: Discussion. Can. Geotech. J. Vol. 31, pp. 463-366.

Shirlaw JN, Ong JCW, Rosser RB, Osborne NH, Tan CG, Heslop PJE (2001) Immediate Settlements due to tunnelling for the North East Line. Proceedings of Underground Singapore 2001, 29th –30th November, 2001.

Skempton AW and Northey RD (1953). The sensitivity of clays, Geotechnique, Vol. 3 (1), pp. 30-53.

Simpson B (1992). Development and application of a new soil model for prediction of ground movements. Proc. Wroth Memorial Symp., Oxford.

Smith IM (2000). A general-purpose system for finite element analyses in parallel. Engineering Computations, 17, (1), pp. 75-91.

Smith IM and Wong SW (1989). PCG methods in transient FE analysis. Part I: First order problems. International J. for Numerical methods in engineering, Vol 28, pp. 1557-1566.

Smith IM, Griffiths DV Programming the Finite Element Method, 3rd edn. John Wiley: Chichester, 1997.

Sleijpen GLG and Vorst HA (2000). Differences in the effects of rounding errors in Krylov solvers for symmetric indefinite linear systems. SIAM, Journal on Matrix Analysis and Applications, Vol. 22 (3), pp.726-751.

Stallebrass SE and Taylor RN (1997). The development and evaluation of a constitutive model for the prediction of ground movements in overconsolidated clay. Geotechnique, 47, No. 2 , pp. 235-253.

Swoboda G. and Abu-Krisha A. (1999). Three-dimensional numerical modelling for TBM tunnelling in consolidated clay. Tunnelling and underground space technology, Vol. 14 (3), pp. 327-333.

U.S. Army Corp of Engineers (1997) Tunnels and shafts in rock. EM 1110-2-2705. 109 pp.

Verruijt A, Booker JR (1996). Surface Settlement due to deformation of a tunnel in an elastic half plane. Geotechnique, 46, No. 4, pp. 753-756.

Vorst HVD (2002). Lecture notes: Iterative methods for large linear systems. http://www.math.uu.nl/people/vorst/lecture.html , June 24, 2002, 195 pp.

Wang A (1996). Three Dimensional finite element analysis of pile groups and pile-rafts. Ph.D. Thesis, University of Manchester, 1996.

Wang XN (2003). Field monitoring and back –analysis of soldiers piles retaining wall for deep excavation. Ph.D. Thesis, National University of Singapore.

Winget JM, Hughes TJR (1985). Solution algorithms for non-linear transient heat conduction analysis employing element-by-element iterative strategies. Computer Methods in Applied Mechanics and Engineering, 52, pp. 711-815.

Wood DM (1983). Index Properties and Critical State Soil Mechanics. Proceedings, Symposium on recent developments in laboratory and field tests and analysis of geotechnical problems, Bangkok, pp 301-309, December 1983.

Wood DM (1990). Soil behaviour and critical state soil mechanics. Cambridge University Press.

Yeates J (1985). Discussion of ground movement due to parallel trench construction and effects on buried pipeline, in Ground Movements and Structures: Proc. 3rd Int. Conf. Cardiff, 1984, Geddes JD (ed), Pentech Press, London, pp. 798-804.

Yi X, Rowe RK and Lee KM (1993) "Observed and calculated ground pressures and deformations induced by an earth pressure balance shield. Canadian Geotechnical Journal, Vol. 30, pp. 476-490.

Viggiani G (1992). Small strain stiffness of fine grained soils. Ph.D. Thesis. City University, London.

Zienkiewicz OC, Taylor RL (1999). The Finite Element Method, Vol. 1: Basic Formulation and Linear Problems, 4th edn. McGraw-Hill: London, 1999.